2014

Crystal plasticity finite element method simulation of equal channel angular pressing

Guanyu Deng
University of Wollongong

Crystal Plasticity Finite Element Method Simulation of Equal Channel Angular Pressing

A thesis submitted in fulfilment of the requirements
for the award of the degree of

Doctor of Philosophy

from

University of Wollongong

by

Guanyu Deng
BEng, MEng

School of Mechanical, Materials and Mechatronic Engineering
Faculty of Engineering

2014

Declaration

I, Guanyu Deng, declare that this thesis, submitted in fulfillment of the requirements for the award of Doctor of Philosophy, in the school of Mechanical, Materials and Mechatronic Engineering, University of Wollongong, Australia, is wholly my own work unless otherwise referenced or acknowledged, and has not been submitted for qualifications at any other university or academic institution.

Guanyu Deng

August 2014

Acknowledgements

I wish to express my sincere gratitude to my supervisors Professor Anh Kiet Tieu (University of Wollongong), Associate/Professor Cheng Lu (University of Wollongong) and Professor Xianghua Liu (Northeastern University, China) for their excellent supervision and guidance, continuous encouragement and invaluable advice during my PhD study. All my supervisors' implicit trust in my research abilities not only allowed me to freely pursue my goals, but also gave me an opportunity to learn how to manage time and allocate resources. Without their help I could never have finished this work.

I am grateful to Dr. Hongtao Zhu, Dr. Zhijie Jiao, Dr. Liangying Si and Dr. Nam Nhat Huynh for their invaluable advice on my study. I would also like to acknowledge all colleagues in Prof. Tieu's group. We shared our feelings, comfort and support for each other and I liked the discussions with you all during our weekly group meetings, as well as the basketball games.

My thanks are also extended to Bei Wang, Zhe Sun, Jinlin Li, Ziqi Sun, Ting Liao and Jintao Li for your great help and support and I will never forget the time spent together with you guys. I acknowledge my office roommates, EEC and ITS staffs for their kind help.

Special thanks go to Laia Ledo Gomis, Wan Fathul Hakim W. Zamri and Ahmed Saleh for your great help, fruitful discussions and continuous encouragement. I enjoyed all the coffees, dinners, movies and trips together with you and I feel very lucky to have you guys during my study in Wollongong.

Finally, I would like to offer my heartfelt thanks to my family, for their continued love, understanding and devotion. Their encouragements always kept me going forward during my study.

Thank you all,

Guanyu

List of Publications

1. **G.Y. Deng**, C. Lu, L.H. Su, X.H. Liu, A.K. Tieu, Modeling texture evolution during ECAP of copper single crystal by crystal plasticity FEM, Materials Science and Engineering A, 534 (2012) 68-74.

2. **G.Y. Deng**, C. Lu, L.H. Su, A.K. Tieu, X.H. Liu, Crystal plasticity investigation of texture evolution of Al single crystal during extrusion through a bent channel, Journal of Computational and Theoretical Nanoscience, 9 (2012) 1481-1484.

3. **G.Y. Deng**, C. Lu, L.H. Su, A.K. Tieu, H.L. Yu, X.H. Liu, Investigation of sample size effect on the deformation heterogeneity and texture development during equal channel angular pressing, Computational Materials Science, 74 (2013) 75-85.

4. **G.Y. Deng**, C. Lu, L.H. Su, A.K. Tieu, M. Liu, H.T. Zhu, X.H. Liu, Influence of outer corner angle (OCA) on the deformation behavior and texture evolution in equal channel angular pressing, Computational Materials Science, in press, doi: 10.1016/j.commatsci.2013.07.006.

5. **G.Y. Deng**, C. Lu, L.H. Su, J.T. Li, H.T. Zhu, X.H. Liu, A.K. Tieu, A study on the aluminium alloy AA1050 severely deformed by Non-equal channel angular pressing, Advanced Materials Research, 651 (2013) 442-447.

6. **G.Y. Deng**, A.K. Tieu, L.H. Su, C. Lu, H.T. Zhu, P.T. Wei, X.H. Liu, Crystal plasticity FEM study on the influence of crystallographic orientation in copper single crystals subjected to equal channel angular pressing, Steel Research International, in press, doi: 10.1002/srin.201300047.

7. **G.Y. Deng**, A.K. Tieu, L.Y. Si, L.H. Su, C. Lu, H.T. Zhu, H. Wang, M. Liu and X.H. Liu, Influence of cold rolling reduction on the deformation behavior and crystallographic orientation development, Computational Materials Science, in press, doi:10.1016/j.commatsci.2013.06.054.

8. **G.Y. Deng**, C. Lu, L.H. Su, A.K. Tieu, H.L. Yu, L.Y. Si, H.T. Zhu, X.H. Liu, Crystal plasticity finite element analysis of influence of initial crystal orientation on texture evolution of cold rolled aluminium, Steel Research International, special edition: Metal Forming 2012, 1119-1122.

9. C. Lu, **G.Y. Deng**, A.K. Tieu, L.H. Su, H.T. Zhu, X.H. Liu, Crystal plasticity modeling of texture evolution and heterogeneity in equal channel angular pressing of aluminium single crystal, Acta Materialia, 59 (2011) 3581-3592.

10. A.K. Tieu, **G.Y. Deng**, C. Lu, L.H. Su, H.T. Zhu, M. Liu, X.H. Liu, An insight into the deformation and orientation development of severely plastic deformed aluminium, AIP Conference Proceedings, 1532 (2013) 206-213.

List of Contents

Declaration ..... **I**

Acknowledgements ..... **II**

List of Publications ..... **III**

List of Contents ..... **i**

Abstract ..... **iv**

Notations ..... **vii**

List of Tables ..... **xii**

List of Figures ..... **xiv**

Chapter 1 Introduction **1**

Chapter 2 Literature Review **4**

2.1 Severe Plastic Deformation 4

2.2 ECAP 11

2.3 Deformation Models of the ECAP Process 16

2.3.1 Simple Shear Model 16

2.3.2 Analytical Model 16

2.3.3 Physical Model 19

2.3.4 Classic Finite Element Method Model 19

2.4 ECAP Texture Measurement 21

2.4.1 Texture Representation and Measurement Techniques 21

2.4.2 Main Characteristics of Measured ECAP Texture 23

2.5 ECAP Texture Simulations 27

2.5.1 Taylor-type Models 27

2.5.2 Self-consistent Model 32

2.5.3 CPFEM Model 36

2.6 Summary and Research Scope of this Thesis 39

Chapter 3 Development and Verification of the CPFEM Model 41

3.1 Crystal Plasticity Theory 41

3.1.1 Kinematical Theory 41

3.1.2 Constitutive Equations 46

3.1.3 Hardening Model 49

3.2 Development of the CPFEM Model 52

3.2.2 Fundamental Equations of FEM 52

3.2.2 Implementation of Crystal Plasticity Theory in FEM 53

3.3 Verification of the developed CPFEM Model 54

3.3.1 ECAP of Aluminium Single Crystal 55

3.3.2 ECAP of Copper Single Crystal 59

3.4 Summary 61

Chapter 4 Investigation of ECAP of Aluminium Single Crystals 63

4.1 Inhomogeneous Deformation and Texture Evolution 63

4.1.1 Macroscale Deformation Behaviour 63

4.1.2 Crystal Rotation Patterns 65

4.1.3 Slip Trace 68

4.1.4 Heterogeneity along Thickness 70

4.2 Three-dimensional Simulation of ECAP 75

4.3 Influence of Mesh Condition 82

4.4 Influence of Frictional Condition 86

4.5 Influence of Sample Size 91

4.6 Influence of Outer Corner Angle 107

4.7 Influence of Inner Corner Fillet Radius 117

4.8 Summary 127

Chapter 5 Investigation of ECAP of Copper Single Crystals 130

5.1 Influence of Friction 131

5.2 Influence of ECAP Die Channel Angles 140
5.2.1 ϕ = 75° 140
5.2.2 ϕ=105° 147
5.3 Influence of Initial Crystallographic Orientations 153
5.5 Summary 162
Chapter 6 CPFEM Simulation of Multi-pass ECAP Process 164
6.1 Adaptive Meshing Techniques 164
6.1.1 ALE Adaptive Meshing Analysis 164
6.1.2 VT Adaptive Remeshing Analysis 165
6.1.3 MTMS Mapping Analysis 166
6.2 CPFEM Simulation of Route A 168
6.3 CPFEM Simulation of Route C 181
6.5 Summary 192
Chapter 7 CPFEM Simulation of ECAP Process of Aluminium Bicrystals and Polycrystal 194
7.1 CPFEM Simulation of Aluminium Bicrystals 195
7.2 CPFEM Simulation of Aluminium Polycrystal 204
7.3 Summary 217
Chapter 8 Conclusions and Suggestions for Future Work 219
8.1 Conclusions 219
8.2 Suggestions for Future Work 221
References 223

Abstract

Severe plastic deformation (SPD) has been the subject of intensive investigations in recent years because of the unique physical and mechanical properties of ultrafine grained (UFG) materials fabricated by this technique. Equal channel angular pressing (ECAP) is the most frequently used SPD technique due to its efficiency in grain refinement. The deformation mechanism during the ECAP process is very complicated and it has always been assumed to be a simple shear along the intersecting plane of two ECAP channels in most published literatures. A number of experiments and numerical simulations have revealed that the simple shear based theory could not accurately predict the microstructure development, plastic strain (or strain rate) distributions and texture evolutions. Even though many studies have contributed to understanding of the deformation mechanism of the ECAP process, some research areas have still not been fully explored, such as texture modelling. Up to now, few texture simulations in the literatures have been carried out based on the real full-scale ECAP process and most of them were conducted using the simple shear theory. Therefore, a systematic study on modeling of texture evolution of the real ECAP process and investigation of the effects of the ECAP parameters on texture evolution are essential.

In the present study, a crystal plasticity finite element method (CPFEM) model has been developed to offer a systematic understanding of the deformation behavior and texture evolutions of single crystals, bicrystals and a polycrystal during the full scale ECAP processes. The developed CPFEM model has been validated by comparing the simulation results with the experimental observations.

Three-dimensional and two-dimensional simulations have been performed for ECAP of aluminium single crystal using a die with the square cross-section. It has been found that both simulations predict similar textures, plastic strain and strain rates distributions. However, the three-dimensional simulation is very time-consuming. In order to save the computing time, the two-dimensional CPFEM model has been used in the following studies.

Texture simulation has been carried out for ECAP of aluminium single crystal which has the initial slip plane (-1 -1 -1) parallel to the theoretical shear plane, and the slip direction [-1 1 0] parallel to the theoretical shear direction of the ECAP die. It has been seen that the deformation is inhomogeneous along the thickness of the sample and three matrix bands develop after the ECAP process. The predominant crystal rotation is around the transverse direction and the corresponding rotation angles in these matrix bands are 60°, 0° and 90°, respectively. The CPFEM model has been applied to investigations of the influences of mesh conditions, friction conditions, outer corner angle (OCA) and inner corner radius (ICR) of the ECAP die on texture evolution. It has been found that: 1) Coarse meshes (total elements of the sample: 600 and 2400) fail to capture the main texture features observed in the experiment; 2) The gap between the die and the sample in the outer corner decreases with increasing coefficient of friction (μ) and μ=0.05 and 0.1 can predict satisfactory texture; 3) A larger OCA leads to a decrement in the processing load but a larger rigid body rotation region in the bottom part of the deformed samples; 4) A larger ICR leads to a larger strain but less efficiency in grain refinement because the number of matrix bands along the thickness decreases with the ICR.

Deformation and texture evolution of copper single crystal have also been simulated. It has been found that they are significantly influenced by the ECAP die channel angle and initial crystallographic orientations. The magnitudes of strain and the strain rate gradually decrease with increasing the die channel angle and the crystal rotation angles in the bottom part are dependent on the die channel angle.

The CPFEM simulations of the multi-pass ECAP processes with Routes A (90° rotation between two passes) and C (180° rotation between two passes) have been conducted with the help of the mesh-to-mesh solution (MTMS) mapping technique. It has been found that Route C leads to more matrix bands along the billet thickness direction than Route A after four ECAP passes. This indicates that Route C is more effective in grain refinement.

The ECAP process of bicrystals has been simulated using the CPFEM model. The initial crystallographic orientations of two grains are [1 2 3] II extrusion direction, [-4 -1 2] II insertion

direction and [1 2 3] II extrusion direction, [4 1 -2] II insertion direction, respectively. Different results are obtained when the same bicrystal is rotated by 180° in the entry channel before the ECAP process. The grain boundary leads to a large variation of plastic strain, and stress and shear strength.

A polycrystalline structure has been implemented in the CPFEM model to simulate the ECAP process of aluminium polycrystal. The simulation results show that predicted textures are in good agreement with the experimental results. It has been found that the strain in the polycrystal is comparable to those in the single crystals and bicrystals. However, the crystallographic rotation patterns are different to the single crystals. In addition to large crystallographic rotation around the transverse direction in ECAP of single crystals, large rotations around the extrusion direction and insertion direction have also been observed in ECAP of polycrystal.

Notations

ARB	Accumulative roll bonding
a_1	Constant for $f_{\alpha\beta}$ (no junction)
a_2	Constant for $f_{\alpha\beta}$ (Hirth lock)
a_3	Constant for $f_{\alpha\beta}$ (coplanar junction)
a_4	Constant for $f_{\alpha\beta}$ (glissile junction)
a_5	Constant for $f_{\alpha\beta}$ (sessile junction)
$\boldsymbol{B}$	Symmetrical part of the coefficient matrix of velocity gradient
BCC	Body centered cubic
$\boldsymbol{C}$	Fourth order tensor of the elastic modulus
$\boldsymbol{C}_0$	Tensor of elastic moduli
C_i	Deformation inhomogeneity index
CCC	Cylinder covered compression
CEC	Cyclic extrusion compression
CPFEM	Crystal plasticity finite element method
$\boldsymbol{D}$	Stretch rate tensor
$\boldsymbol{D}^*$	Elastic part of the stretch rate tensor
$\boldsymbol{D}_{\mathrm{L}}$	Rate of the elastic stretching in the lattice coordinate system
$\boldsymbol{D}^{\mathrm{P}}$	Plastic part of the stretch rate tensor
$\delta\boldsymbol{D}$	Virtual form of the rate of deformation
$\boldsymbol{E}$	Grain strain tensor
$\dot{\boldsymbol{E}}$	Rate of Grain strain tensor
EBSD	Electron backscatter diffraction

ECAE	Equal channel angular extrusion
ECAP	Equal channel angular pressing
ED	Extrusion direction
$\boldsymbol{F}$	Total deformation gradient
$\dot{\boldsymbol{F}}$	Time derivative of the total deformation gradient
$\boldsymbol{F}^{*}$	Elastic part of the total deformation gradient
$\dot{\boldsymbol{F}}^{*}$	Time derivative of the total deformation gradient
$\boldsymbol{F}^{*-1}$	Inverse of $\boldsymbol{F}^{*}$
$\boldsymbol{F}^{\mathrm{P}}$	Plastic part of the total deformation gradient
$\dot{\boldsymbol{F}}^{\mathrm{P}}$	Time derivative of the plastic part of the total deformation gradient
$\boldsymbol{F}^{\mathrm{P}-1}$	Inverse of $\boldsymbol{F}^{\mathrm{P}}$
$\boldsymbol{F}^{(\alpha)\mathrm{P}}$	Contribution of slip system α to $\boldsymbol{F}^{\mathrm{P}}$
$\boldsymbol{F}^{\mathrm{T}}$	Transposition of $\boldsymbol{F}$
FCC	Face centered cubic
FSW	Frictional stir welding
$f_{\alpha\beta}$	Strength of a particular slip interaction between two slip systems α and β
$\boldsymbol{G}$	Skewed part of the coefficient matrix of velocity gradient
g	Orientation matrix
$\boldsymbol{H}$	Fourth order hardening parameter tensor
HCP	Hexagonal close packed
HPT	High pressure torsion
HPTT	High pressure tube twisting
$h_{\alpha\beta}$	Instantaneous hardening moduli
h_{s}	Hardening modulus during easy glide

h_0	Hardening modulus just after the initial yield
$\boldsymbol{I}$	Second order unit tensor
ICR	Inner corner fillet radius
$\boldsymbol{K}$	Jacobian matrix
$\boldsymbol{L}$	Velocity gradient
$\boldsymbol{L}^*$	Elastic part of velocity gradient
$\boldsymbol{L}^{\mathrm{P}}$	Plastic part of velocity gradient
$\boldsymbol{L}^{\mathrm{T}}$	Transposition of $\boldsymbol{L}$
MDE	Multiple direct extrusion
MDF	Multidirectional forging
$\boldsymbol{m}^{(\alpha)}$	Normal vector of slip plane of α-th slip system in the current configuration
$\boldsymbol{m}_0^{(\alpha)}$	Normal vector of slip plane of α-th slip system in the reference configuration
N	Number of active slip systems
N	Shape functions
n	Rate sensitive exponent
ND	Normal direction
OCA	Outer corner angle
OIM	Orientation imaging microscopy
ODF	Orientation distribution function
PDZ	Plastic deformation zone
$\boldsymbol{p}^{(\alpha)}$	Symmetrical part of Schmid factor
q	Latent hardening parameter
$\boldsymbol{q}^{(\alpha)}$	Asymmetrical part of Schmid factor

$\boldsymbol{R}$	Orthogonal rotation tensor
RD	Rolling direction
SFE	Stacking fault energy
SPD	Severe plastic deformation
$\boldsymbol{s}^{(\alpha)}$	Slip direction vector of slip plane of α-th slip system in the current configuration
$\boldsymbol{s}_0^{(\alpha)}$	Slip direction vector of slip plane of α-th slip system in the reference configuration
$\boldsymbol{s}^{(\alpha)} \otimes \boldsymbol{m}^{(\alpha)}$	Schmid factor
TD	Transverse direction
TE	Twist extrusion
THPS	Tube high pressure shearing
Δt	Time increment
$\boldsymbol{t}_0$	Kirchhoff stress in the reference configuration
$\dot{\boldsymbol{t}}$	Material rate of Kirchhoff stress
$\dot{\boldsymbol{t}}_1^*$	Rate of the Kirchhoff stress in the intermediate configuration
$\dot{\boldsymbol{t}}_{\mathrm{L}}$	Material rate of the Kirchhoff stress in the lattice coordinate system
$\nabla \boldsymbol{t}$	Kirchhoff stress
$\nabla^* \boldsymbol{t}$	Jaumann rate of Kirchoff stress
$\boldsymbol{U}$	Right stretch tensor
UFG	Ultrafine grained
$\boldsymbol{V}$	Left stretch tensor
$\boldsymbol{v}$	Velocity of the material point
$\boldsymbol{v}^{\mathrm{n}}$	Nodal velocities

$\delta \boldsymbol{v}$	kinematically admissible virtual velocity field
VPSC	Visco-plastic self-consistent
$\boldsymbol{W}$	Spin tensor
$\boldsymbol{W}^{*}$	Elastic part of spin tensor
$\boldsymbol{W}^{\mathrm{P}}$	Plastic part of spin tensor
$\boldsymbol{X}$	Position of material point in the initial configuration
$\boldsymbol{x}$	Position of material point in the current configuration
$\otimes$	Tensor product
α	Slip system α
β	Slip system β
$\gamma^{(\alpha)}$	Shear strain of slip system α
$\gamma_0^{(\alpha)}$	Reference value of shear strain of slip system α
$\dot{\gamma}^{(\alpha)}$	Shear rate of slip system α
$\dot{\gamma}_0^{(\alpha)}$	Reference value of shear rate of slip system α
$\tau^{(\alpha)}$	Resolved shear stress of slip system α
$\tau_{\mathrm{c}}^{(\alpha)}$	Current strength of slip system α
τ_1	Breakthrough stress where large plastic flow begins
τ_0	Initial critical resolved shear stress
$\boldsymbol{\sigma}$	Cauchy stress
ϕ	ECAP die channel angle
$\varphi 1$, φ, $\varphi 2$	Three Euler angles
ψ	Outer corner angle
μ	Friction coefficient

List of Tables

Table 2.1 Euler angles and Miller indices for the ideal orientations of FCC materials after one ECAP pass with ϕ=90°die [2, 31]. 25

Table 2.2 Maximum intensity in {1 1 1} pole figure (P) and texture index (T) of the experimental and simulated textures at different thickness positions in the deformed billet after the first pass [59]. 35

Table 3.1 The strain rate sensitivity component and parameters of aluminium single crystal used in the hardening model as Equation (3.60). 55

Table 3.2 Notations of the slip systems for the FCC materials considered in this study. 57

Table 3.3 The strain rate sensitivity component and parameters in the hardening law for copper single crystal. 59

Table 4.1 The average values of the effective plastic strain (ε), shear strength (τ_c), von Mises stress (σ), peak force, and the deformation inhomogeneity index (C_i) along the width of the sample after the ECAP process. 95

Table 4.2 Detailed parameters in the simulations used to study the influence of OCAs. 108

Table 4.3 The average values of the effective plastic strain (ε), shear strength (τ_c), von Mises stress (σ), peak force, and the deformation inhomogeneity index (C_i) for different OCAs. 111

Table 4.4 The required peak force, average values of effective plastic strain, von Mises stress and shear strength, and the deformation inhomogeneity index. 121

Table 5.1 The relationship between the crystallographic orientations of four studied copper single crystals and the coordinate system X-Y-Z during the ECAP process. 154

Table 5.2 The angle of the outer corner gap, average value of the effective plastic strain (ε) and deformation inhomogeneity index (C_i) for all four copper single crystals after the ECAP process. 156

Table 6.1 The details of parameters used in the simulations of Route A. 169

Table 7.1 Chemical composition of aluminium alloy AA1050 used in this study [22]. 205

Table 7.2 The list of average values of effective plastic strain (ε), von Mises stress (σ), shear strength (τ_c), and the deformation inhomegeneity index (C_i) along the billet thickness at three selected planes in the ECAP processed aluminium polycrystal..... 214

List of Figures

Fig. 2.1 Schematic illustration of the HPT process [86]. 5

Fig. 2.2 (a) Microhardness profiles of nickel processed by the HPT process at two different applied pressures [88] and (b) Contour map of the microhardness across the surface of high purity Al processed by the HPT process at a pressure of 2.5 GPa for 5 turns [89]. 6

Fig. 2.3 TEM microstructures of nickel processed by HPT through N=5 turns, (a) edge, P=1 GPa, (b) center, P=1 GPa, (c) edge, P=3 GPa, (d) center, P=3 GPa, (e) edge, P=9 GPa, and (f) center, P=9 GPa [86]..... 7

Fig. 2.4 Schematic illustration showing the principle of the ARB process [19]. 8

Fig. 2.5 TEM microstructures and the matching SAD patterns of ARB processed AA5083 by (a) 2, (b) 4, and (c) 6 cycles [90]. 9

Fig. 2.6 The variation of microhardness along the thickness of the ARB processed AA5083 [90]. 10

Fig. 2.7 Schematic illustration of the ECAP process [50]. 11

Fig. 2.8 The four fundamental processing routes in the ECAP process: (a) Route A, (b) Route Ba, (c) Route Bc, and (d) Route C [104]. 12

Fig. 2.9 The slip systems viewed on the X, Y, and Z planes for the consecutive ECAP passes using processing Routes A, Ba, Bc and C [1]..... 13

Fig. 2.10 (a) Principle of ECAP with parallel channels where ϕ is the intersecting angle and K is displacement between two channels, and (b) general view of the die set [107]. 14

Fig. 2.11 Schematic illustration of the rotary die ECAP process at (a) the initial state, (b) after one pass, and (c) after rotating the die 90° [109]..... 15

Fig. 2.12 Deformation history of material elements during the ECAP process based on an analytical analysis [5]. 17

Fig. 2.13 Description of the flow field by flow lines, n indicates the value of the exponent in the proposed flow function determined by finite element calculations [43]. 18

Fig. 2.14 Diagram showing how rotation through the Euler angles φ_1, φ, φ_2, in the order 1, 2, 3 as shown describes rotation between the sample and crystal axes [152]. 22
Fig. 2.15 {1 1 1} pole figures showing the main ideal orientations and fiber textures for FCC materials after one ECAP pass with ϕ=90°. (the arrows indicate the direction of shear) [31]. ... 24
Fig. 2.16 {1 1 0} pole figures showing the main ideal orientations and fiber textures for BCC materials after one ECAP pass with ϕ=90°. (the arrows indicate the direction of shear) [31]. ... 24
Fig. 2.18 {1 1 1} pole figures of textures in the deformed billets after various passes via Route Bc. (a) experimental results, (b) simulation results with FC-Taylor model based on simple shear deformation, and (c) simulation results with FC-Taylor model based on FEM calculated deformation history [41]..... 28
Fig. 2.19 {1 1 1} pole figures of textures in the deformed billets after 1 to 4 passes via Route C. (a) experimental results, (b) simulation results with the Taylor model based on simple shear deformation, and (c) simulation results with the Taylor model based on FEM calculated deformation history [41]..... 30
Fig. 2.20 The Taylor model predicted (a, c, e) and experimental (b, d, f) measured {1 1 1} pole figures for (a-b) one pass, (c-d) four passes in Route A, and (e-f) four passes in Route C for the high purity Al0.5Cu alloy [47]..... 31
Fig. 2.21 {1 1 0} pole figures of textures in the deformed IF steel after 1-4 passes of ECAP process (120° die) via Routes (a) A, (b) Bc and (c) C simulated by the VPSC model using the FEM predicted deformation history for each pass [60]. 33
Fig. 2.22 {1 1 1} pole figures of the experimental textures and simulated textures using the Taylor model and VPSC models with the shear increment of 0.005 for (a) the first pass, and (b) the second pass [38]. 35
Fig. 2.23 {1 1 1} pole figures and ODFs for the textures in the Al after one pass of ECAP process: (a) experimental results, (b and c) simulated by the CPFEM model using the 1EPG and 8 EPG meshes, (d and e) simulated by the VPSC model without and with enforcing grain co-rotation [58]. 37
Fig. 2.24 Lattice rotation fields in the range of 20° × 20° × 20° around ideal orientations for FCC materials in ECAP deformation: (a) $A_{1\theta}^{*}$, (b) $A_{2\theta}^{*}$, (c) $A_{1\theta}^{*}$, (d) A_{θ}, (e) B_{θ}, and (f) C_{θ}. Left:

phi2=constant section, and right: phi2=constant section. The direction and length of an arrow signify, respectively, the direction and magnitude of the rotation vector [166]. 38

Fig. 3.1 Multiplicative decomposition of the deformation gradient $\boldsymbol{F}$ into elastic deformation part and plastic deformation part. 42

Fig. 3.2 A typical curve of resolved shear stress versus shear strain in a slip system for a FCC single crystal. (Point 'A' denotes where secondary slip commences) [246] 50

Fig. 3.3 Geometry of the ECAP die, initial mesh and {1 1 1} pole figure of aluminium single crystal used in this simulation. 56

Fig. 3.4 Comparisons of the {1 1 1} pole figures between the CPFEM simulation and experimental measurements (upper panel: simulation results; lower panel: experiment results [33]): (a) Initial crystallographic orientation, (b) Position P1, (c) Position P2, (d) Position P3, and (e) Position P4. 58

Fig. 3.5 Comparisons of the {1 1 1} pole figures between the experimental measurements [178] (upper panel) and the CPFEM simulation (lower panel): (a) Position 1, (b) Position 2, and (c) Position 3. 60

Fig. 4.1 Mesh distortions and distribution of effective plastic strain rate in the deformed billet: (a) mesh distortions, and (b) effective plastic strain rate. 64

Fig. 4.2 Distributions of crystal rotation angles in the billet: (a) contour map of crystal rotation angle around the X axis, (b) contour map of crystal rotation angle around the Y axis, (c) contour map of crystal rotation angle around the Z axis, and (d) crystal rotation angle along line AA' marked in (a). 67

Fig. 4.3 Simulated slip traces in the aluminium single crystal during the ECAP process. 69

Fig. 4.4 Results for tracer-element I as functions of moving distance from initial position: (a) crystal rotation angles, (b) shear strain rates, (c) stresses, and (d) strain rates. 71

Fig. 4.5 Results for tracer-element II as functions of moving distance from initial position: (a) crystal rotation angles, (b) shear strain rates, (c) stresses, and (d) strain rates. 72

Fig. 4.6 Results for tracer-element III as functions of moving distance from initial position: (a) crystal rotation angles, (b) shear strain rates, (c) stresses, and (d) strain rates. 74

Fig. 4.7 Mesh distortions in the three-dimensional CPFEM simulation of the ECAP process of aluminium single crystal. 76
Fig. 4.8 Contour of strain distribution in the cross-section (X=6 mm) of the deformed aluminium single crystal during the ECAP process. 77
Fig. 4.9 Variation of the effective plastic strain and logarithmic strian components along the Z axis and Y axis in the steady-state deformation region. (a) on the line of Y=3.6 mm, (b) on the line of Y=2 mm, (c) on the line of Y=0.4 mm, and (d) comparison of the effective plastic strain along the thickness direction between two-dimensional and three-dimensional simulations. (LE33 is normal component of logarithmic strain along the Z axis, LE13 and LE23 are shear components on the Y and X planes, respectively)..... 78
Fig. 4.10 Simulated {1 1 1} pole figures for the selected positions marked in Fig. 4.8 according to the three-dimensional CPFEM simulation of the ECAP process of aluminium single crystal. 80
Fig. 4.11 Variation of crystal rotation angles around the X, Y and Z axes along the thickness direction in the steady-state deformation region. (a) on the line of Z=-1.8 mm; (b) on the line of Z=0 mm; (c) on the line of Z=1.8 mm; (d) comparison of the crystal rotation angles around the Z axis on the three selected lines Z=-1.8, 0 and 1.8 mm. 81
Fig. 4.12 Comparison of mesh distortions in the deformed aluminium single crystal between different mesh conditions. (a) Mesh 600, (b) Mesh 2400, (c) Mesh 6369, and (d) Mesh 12000. 83
Fig. 4.13 Variation of (a) effective plastic strain, and (b) von Mises stress along the thickness at different mesh conditions..... 84
Fig. 4.14 Influence of mesh condition on the {1 1 1} pole figures for the selected positions as marked in Fig. 4.12(b). (a) Mesh 600, (b) Mesh 2400, (c) Mesh 6369, and (d) Mesh 12000. 86
Fig. 4.15 Distribution of effective plastic strain rate in the billet during the ECAP process. (a) μ=0, (b) μ=0.05, (c) μ=0.1, and (d) μ=0.15. 88
Fig. 4.16 Comparison of the {1 1 1} pole figures between the CPFEM simulations and experiment. The upper panel is for Position 1 and the lower panel is for Position 2. (a) Experiment [33], (b) μ=0, (c) μ=0.05, (d) μ=0.1, and (e) μ=0.15. 89
Fig. 4.17 Crystal rotation angles around the transverse direction (Z axis) during the ECAP process for different coefficients of friction. (a) μ=0, (b) μ=0.05, (c) μ=0.1, and (d) μ=0.15. 91

Fig. 4.18 Simulated load curves for aluminium single crystals having different sample widths varying from 2 mm to 40 mm during the ECAP process. 94
Fig. 4.19 The deformation history of the ECAP process and the simulated mesh distortions for the sample width of d=2 mm. 95
Fig. 4.20 Distribution of calculated shear strength along the width of the sample of aluminium single crystals with d=2-40 mm after the ECAP process. 96
Figure 4.21 Distribution of the calculated effective plastic strain along the width of the sample of aluminium single crystals with d=2-40 mm after the ECAP process. 97
Fig. 4.22 Distribution of the calculated von Mises stress along the width of the sample of aluminium single crystals with d=2-40 mm after the ECAP process. 97
Fig. 4.23 (a) The deviation of the average values of shear strength and von Mises stress along the width of the sample for all four cases. (b) Comparison between the calculated effective strain and theoretical value during the ECAP process. 99
Fig. 4.24 Distribution of the effective plastic strain rate component εX in the plastic deformation zone for different sample widths during the ECAP process. 100
Fig. 4.25 The shear rates for three selected elements in the deformed sample with d=2 mm as a function of ECAP time: Element-I belongs to the upper region, Element-II belongs to the center region and Element-III belongs to the lower region. 101
Fig. 4.26 The shear rates for three selected elements in the deformed sample with d=10 mm as a function of ECAP time: Element-I belongs to the upper region, Element-II belongs to the center region, and Element-III belongs to the lower region. 102
Fig. 4.27 The shear rates for three selected elements in the deformed sample with d=40 mm as a function of ECAP time: Element-I belongs to the upper region, Element-II belongs to the center region, and Element-III belongs the lower region. 103
Fig. 4.28 Contour maps of crystal rotations around the Z axis during the ECAP process for all four samples. (a) d=2 mm, (b) d=4 mm, (c) d=10 mm, and (d) d=40 mm. 104
Fig. 4.29 Crystal rotations around X, Y, and Z axes along the width of the sample in the deformed aluminium single crystals with d varying from 2 mm to 40 mm during the ECAP process. 105

Fig. 4.30 The simulated {1 1 1} pole figures at three selected positions in the deformed samples as marked in Fig. 4.28(a). (a) d=2 mm, (b) d=4 mm, (c) d=10 mm, and (d) d=40 mm. 106
Fig. 4.31 The geometry of an ECAP die with, (a) very sharp outer corner angle [4], and (b) with a non-zero outer corner angle [103]. 107
Fig. 4.32 The pressure required for processing different OCAs in terms of deformation time. 109
Fig. 4.33 Distribution of the effective plastic strain for different OCAs along the thickness in the deformed billet. 109
Fig. 4.34 Average values of the effective plastic strain for different OCAs during the ECAP process. 110
Fig. 4.35 Distribution of the plastic strain rates for different OCAs. (a) OCA=0°, (b) OCA=10°, (c) OCA=20°, (d) OCA=30°, (e) OCA=40°, (f) OCA=60°, and (g) OCA=90°. 113
Fig. 4.35 Continued. 114
Fig. 4.36 Simulated {1 1 1} pole figures at three selected positions for different OCAs. (a) OCA=0°, (b) OCA=10°, (c) OCA=20°, (d) OCA=30°, (e) OCA=40°, (f) OCA=60°, and (g) OCA=90°.115
Fig. 4.37 Crystal rotation angles about the transverse direction (Z axis) along the thickness after the ECAP process. 116
Fig. 4.38 The required processing pressures for different ICRs in terms of deformation time. 118
Fig. 4.39 Distribution of (a) effective plastic strain and (b) von Mises stress for different ICRs along the thickness in the deformed aluminium single crystals. 119
Fig. 4.40 Distribution of effective plastic strain for different ICRs along the thickness direction in the deformed billets. 121
Fig. 4.41 Distribution of plastic strain rates for different ICRs. (a) ICR=0 mm, (b) ICR=0.3 mm, (c) ICR=0.5 mm, (d) ICR=1 mm, (e) ICR=2 mm, (f) ICR=3 mm, and (g) ICR=4 mm. 122
Fig. 4.41 Continued. 123
Fig. 4.42 Simulated {1 1 1} pole figures at three selected positions for (a) ICR=0 mm, (b) ICR=0.3 mm, (c) ICR=0.5 mm, (d) ICR=1 mm, (e) ICR=2 mm, (f) ICR=3 mm, and (g) ICR=4 mm. 125
Fig. 4.43 Influence of ICR on the Z-axis rotation angles along the thickness of the deformed aluminium single crystals after the ECAP process. 126

Fig. 5.1 Mesh distortions of copper single crystals during the ECAP process under frictional conditions of (a) μ=0.05, and (b) μ=0.1. 132
Fig. 5.2 Distributions of the simulated plastic strain rates in the deformed copper single crystals during the ECAP process with (a) μ=0.05 and (b) μ=0.1. 134
Fig. 5.3 Variation of the (a) effective plastic strain, and the logarithmic plastic strain components for (b) μ=0.05 and (c) μ=0.1 along the sample thickness in the ECAP processed copper single crystals. 135
Fig. 5.4 Comparisons of the {1 1 1} pole figures for five selected positions P1-P5 marked in Fig. 5.5(c) between simulation results with different friction coefficients (a) μ=0.05 and (b) μ=0.1. 136
Fig. 5.5 Contour of crystal rotation angles in the steady-state deformation region of the ECAP processed copper single crystals. (a), (b), and (c) indicate the rotation components around the X, Y, and Z axes for μ=0.05, respectively and (d) indicates the rotation component around the Z axis for μ=0.1. The numbers (1)-(5) marked in (c) indicates the selected positions P1-P5. Matrix bands and transition bands are marked as 'M' and 'T', respectively. 138
Fig. 5.6 Crystal rotation angles around the X, Y, and Z axes along the sample thickness in the exit channel at 1.5 mm away from the intersecting zone. (a) μ=0.05 and (b) μ=0.1. 139
Fig. 5.7 Mesh distortions and plastic strain distribution in the deformed copper single crystal during the ECAP process with a die channel angle of 75°. 141
Fig. 5.8 Distribution of the plastic strain rate components (a) ε_X and (b) ε_{XY} in the deformed copper single crystal during the ECAP process with a die channel angle of 75°. 142
Fig. 5.9 Plastic strain rates for four tracked elements as function of the deformation time during the ECAP process with a die channel angle of 75°..... 143
Fig. 5.10 Logarithmic plastic strain components for four tracked elements as function of the deformation time during the ECAP process with a die channel angle of 75°. 144
Fig. 5.11 Variations of the Logarithmic plastic strain components along the sample thickness (line L-L) in the deformed copper single crystal during the ECAP process with a die channel angle of 75°. 145

Fig. 5.12 Simulated {1 1 1} pole figures for eight selected positions in the deformed copper single crystal during the ECAP process with a die channel angle of 75°. (Positions P1-P4 are located in the entry channel and positions P5-P8 are located in the exit channel marked in Fig. 5.6(b)) 146

Fig. 5.13 Variation of crystal rotation angles along the thickness of the sample (line L-L) in the deformed copper single crystal during the ECAP process with a die channel angle of 75°. 147

Fig. 5.14 Mesh distortions and plastic strain distribution in the deformed copper single crystal during the ECAP process with a die channel angle of 105°. 148

Fig. 5.15 Distribution of the plastic strain rate components (a) ε_X and (b) ε_{XY} in the deformed copper single crystal during the ECAP process with a die channel angle of 105°. 149

Fig. 5.16 Plastic strain rates for four tracked elements as function of the deformation time during the ECAP process with a die channel angle of 105°. 150

Fig. 5.17 Variation of the Logarithmic plastic strain components along the thickness of the sample (line L-L') in the deformed copper single crystal during ECAP with a die channel angle of 105°. 151

Fig. 5.18 Predicted {1 1 1} pole figures for eight selected positions in the deformed copper single crystal during the ECAP process with a die channel angle of 105°. 152

Fig. 5.20 Mesh distortions for four copper single crystals with different initial crystallographic orientation after ECAP with a 90° ECAP die: (a) Crystal A; (b) Crystal B; (c) Crystal C, and (d) Crystal D. 155

Fig. 5.21 Contour of distribution of the plastic strain rates in (a) Crystal A, (b) Crystal B, (c) Crystal C, and (d) Crystal D. (the upper panel shows the ε_X and the lower panel shows the ε_{XY}) 157

Fig. 5.22 Distribution of the effective plastic strain along the billet thickness for all four copper single crystals after ECAP. 158

Fig. 5.23 Comparisons of the CPFEM simulated {1 1 1} pole figures at selected positions for copper single crystals during the ECAP process: (a) Crystal A, (b) Crystal B, (c) Crystal C, and (d) Crystal D. 159

Fig. 5.24 The contour of crystal rotation angles around the Z axis in the ECAP processed copper single crystals with different initial crystallographic orientations. (a) Crystal A, (b) Crystal B, (c) Crystal C, and (d) Crystal D. 160
Fig. 5.25 Distribution of crystal rotation angles around three axes along the thickness of the sample during the ECAP process: (a) Crystal A, (b) Crystal B, (c) Crystal C, and (d) Crystal D.... 161
Fig. 6.1 (a) The deformed mesh after the first pass of ECAP process, (b) New mesh based on the MTMS mapping analysis from the steady-state region of deformed mesh in (a), (c) {1 1 1} pole figure along line A-B marked in (a), and (d) {1 1 1} pole figure along line A'-B' marked in (b). . 168
Fig. 6.2 Scheme of the Route A of the ECAP process used in the simulations. 170
Fig. 6.3 Effective plastic strain distribution along the thickness of the billet after ECAP in Route A. ('top' means close to the inner corner and 'bottom' means close to the outer corner). 171
Fig. 6.4 Comparison of effective plastic strain between the FEM simulation and empirical theoretical calculations for Route A during up to 4 ECAP passes. 171
Fig. 6.5 Distribution of plastic strain rate ε_X and ε_{XY} in the deformed billet during the (a) first pass, (b) second pass, (c) third pass, and (d) fourth pass of ECAP in Route A. 172
Fig. 6.6 Variation of plastic strain rates of (a) Element 1, (b) Element 2, (c) Element 3, and (d) Element 4 during the first pass of ECAP as a function of the processing time. 174
Fig. 6.7 Variation of plastic strain rates of (a) Element 1, (b) Element 2, (c) Element 3, and (d) Element 4 during the second pass of ECAP in Route A as a function of the processing time.... 175
Fig. 6.8 The history of crystallographic orientations development of four tracked elements (a) Element 1, (b) Element 2, (c) Element 3, and (4) Element 4 during the ECAP process in Route A up to four passes. (N indicates the pass number) 176
Fig. 6.9 The shear strain rates of four tracked elements (a) Element 1, (b) Element 2, (c) Element 3, and (d) Element 4 during the ECAP process of 2-4 passes in Route A. 178
Fig. 6.9 Continued. 179
Fig. 6.10 Crystal rotation angles along the billet thickness during ECAP in Route A. (a) second pass, (b) third pass, and (c) fourth pass. 181
Fig. 6.11 Scheme of Route C in the ECAP process used in the simulations. 182

Fig. 6.12 Varitation of effective plastic strain along the sample thickness after ECAP during up to four passes in Route C. ('top surface' means close to the inner corner) 183
Fig. 6.13 Comparison of the effective plastic strain between the CPFEM simulations and empirical theoretical calculations after ECAP in Route C. 183
Fig. 6.14 Distribution of plastic strain rates ε_X and ε_{XY} in the deformed billet during the (a) first pass, (b) second pass, (c) third pass, and (d) fourth pass of ECAP in Route C. 185
Fig. 6.15 Variation of the strain rates of (a) Element 1, (b) Element 2, (c) Element 3, and (d) Element 4 during the second pass of ECAP in Route C as a function of the processing time. ... 186
Fig. 6.16 The development history of crystallographic orientations of four selected elements (a) Element 1, (b) Element 2, (c) Element 3, and (4) Element 4 during ECAP in Route C. 187
Fig. 6.17 The shear strain rates of four tracked elements during ECAP in Route C. (a) Element 1, (b) Element 2, (c) Element 3, and (d) Element 4..... 189
Fig. 6.17 Continued. 190
Fig. 6.18 Crystal rotation angles along the billet thickness direction during ECAP in Route C. (a) second pass, (b) third pass and (c) fourth pass. 191
Fig. 7.1 Illustration of the sample geometry, initial crystallographic orientations of two component grains in the aluminium bicrystal (Case 1). 196
Fig. 7.2 Mesh distortions of the aluminium bicrystals: (a) Case 1 and (b) Case 2 during the ECAP process. (the grain denoted as Crystal1 is highlighted in red). 197
Fig. 7.3 Distributions of (a) von Mises stress and plastic strain rate components (b) ε_X, (c) ε_Y and (d) ε_{XY} in the deformed specimen of Case 1. 198
Fig. 7.4 Distributions of (a) von Mises stress and plastic strain rate components (b) ε_X, (c) ε_Y and (d) ε_{XY} in the deformed specimen of Case 2. 199
Fig. 7.5 Variation of effective plastic strains along the thickness in both bicrystals. 200
Fig. 7.6 Variation of the (a) von Mises stress, (b) shear component of the stress (S12), and (c) shear strength along the thickness in both simulation cases. 201
Fig. 7.7 Simulated {1 1 1} pole figures of three selected positions (P1-P3 marked in Fig. 7.2(a)) in both component grains in Case 1. 202

Fig. 7.8 Simulated {1 1 1} pole figures of three selected positions (P1-P3 marked in Fig. 7.2(a)) in both component grains in Case 2. 203

Fig. 7.10 (a) The experimental measured distribution of grain size and (b) the calculated distribution of grain size for the simulation based on the experimental result, and (c) the simulated grain shapes and initial meshes of the billet in the model before the ECAP process. 206

Fig. 7.11 Initial {1 1 1} pole figure of the annealed AA1050 alloy before ECAP: (a) experimental measurement [22] and (b) Matlab program generated result used for simulation. 207

Fig. 7.12 Initial texture of the annealed AA1050 before the ECAP process in terms of φ_2=0° ODF section (a) experimental measurement [22] and (b) Matlab program generated result used for simulation. 208

Fig. 7.13 (a) Mesh distortion and (b) Distribution of the plastic strain in the aluminium polycrystal during the ECAP process at t=480 s..... 209

Fig. 7.14 Distributions of (a) von Mises stress and plastic strain rates (b) ε_X, (c) ε_Y and (d) ε_{XY} in the deformed polycrystal during the ECAP process. 210

Fig. 7.15 Variation of (a) Effective plastic strain, (b) von Mises stress and (c) Shear strength along the thickness in the ECAP processed aluminium polycrystal. 211

Fig. 7.16 Variation of the logarithmic plastic strains at (a) X=6, (c) X=10, and (e) X=14 and the stress components at (b) X=6, (d) X=10, and (f) X=14 along the thickness in the ECAP processed aluminium polycrystal..... 212

Fig. 7.17 {1 1 1} pole figures of the aluminium polycrystal of (a) CPFEM simulation result, (b) experimental measurement [22] and (c) the main ideal orientations in FCC materials after the ECAP process [31]. 214

Fig. 7.18 Simulated {1 1 1} pole figures of ECAP processed aluminium polycrystal at four different positions of (a) Position P1, (b) Position P2, (c) Position P3, and (d) Position P4 as marked in Fig. 7.13(a). 215

Fig. 7.19 Simulated {1 1 1} pole figures of ECAP processed aluminium polycrystal at four different positions of (a) Position P5, (b) Position P6, (c) Position P7, and (d) Position P8 as marked in Fig. 7.13(a). 216

Fig. 7.20 Crystal rotation angles around three axes along the thickness in the ECAP processed aluminium polycrystal at plane X=6..... 217

Chapter 1 Introduction

Over the last two decades, severe plastic deformation (SPD) techniques have attracted a lot of interest due to their abilities of the synthesis of bulk ultra-fine grained (UFG) materials [1-3]. Up to now, many different SPD techniques have been proposed and developed, including equal channel angular pressing (ECAP) [4-7], high pressure torsion (HPT) [8-16], accumulative roll bonding (ARB) [17-23], conshearing [24-27], cyclic extrusion-compression (CEC) [28-30] and so on. The ECAP process is one of the most widely used SPD techniques [4].

Material texture is defined as a microstructural property describing the crystallographic orientation distribution of the grains. Texture can influence many aspects of material behavior including plastic anisotropy, formability, fracture and work hardening [2]. Unlike conventional large plastic deformation techniques, texture evolution during the ECAP process is very complicated. The ECAP process is often idealized as a simple shear deformation along the intersecting plane of the two channels in a negative sense [31]. For the face centered cubic (FCC) materials, ideal ECAP textures are often described by two partial fibers, namely {1 1 1}||SP (A fiber) and <1 1 0>||SD (B fiber), where SP and SD are the ideal shear plane and shear direction, respectively [2, 31, 32]. Many experimental studies [33-45] revealed that the difference between the measured ECAP textures and theoretical simple shear textures is significant. A second shear plane (perpendicular to the intersecting plane of two channels) model has been proposed to interpret the above-mentioned difference by Starink and co-workers [46]. However, satisfactory results have not been achieved. Therefore, a systematic study of texture evolution during the ECAP process is very necessary.

In addition to the experimental measurement, texture modeling offers a unique opportunity to investigate how texture evolves during plastic deformation [2]. Most of the ECAP texture simulations were carried out based on the Taylor-type model [43, 45, 47-49] and self-consistent model [43, 50-53]. Several studies [54-58] were conducted using the decoupled crystal plasticity finite element method (CPFEM) model. The simulation results [41, 47, 59] revealed that the

Taylor model always failed to give good quantitative predictions and led to the significant overestimations of the texture strengths compared to the experimental results. A better prediction of the positions of the ideal ECAP texture components can be obtained by the self-consistent model [38, 43, 60], but the predicted texture strength is still not in satisfactory. Thus far the CPFEM model has been recognized as one of the best models for predicting the deformation textures [61]. Unfortunately, all the CPFEM simulations in the published literatures were conducted in a decoupled manner. For a decoupled CPFEM method: a FEM simulation is carried out first to predict the deformation history, and then the deformation history is used as input parameters in a texture model to predict texture evolution during deformation. Therefore, the influence of crystallographic orientation on the strain distributions at each material point cannot be considered. By contrast, the deformation history will be updated together with texture in a coupled CPFEM model which leads to a better texture evolution and strain distributions. Therefore, the fully-coupled CPFEM simulations of the full-scale ECAP process by considering the real deformation history, frictional condition and ECAP die geometry are essential for a better understanding of the deformation behavior and texture evolution during the ECAP process, for the aim of future industrial engineering application of ECAP.

This thesis consists of 8 chapters set out as follows:

Chapter 2 presents a brief overview of the ECAP process. The existing models used in the ECAP research, including the simple shear model, analytical model, physical model and finite element method model, are introduced. The advantages and disadvantages of the ECAP texture simulation methods have been reviewed.

Chapter 3 introduces the crystal plasticity theory and rate-dependent hardening model which will be used to simulate texture evolutions during the ECAP process. The procedures describing the development of the CPFEM model have been outlined. For the first time, texture evolutions of aluminium single crystal and copper single crystal during ECAP have been simulated and the developed CPFEM models have been verified by comparing the simulation results with the experimental measurements.

Chapter 4 presents the CPFEM simulations of aluminium single crystals during the ECAP process. The influences of plane strain assumption, mesh condition, frictional condition, sample dimension and ECAP die geometries, including the outer corner angle and inner corner fillet radius, on the deformation behavior and texture evolution are investigated in detail.

Chapter 5 presents the CPFEM simulations of the ECAP process of copper single crystals. The influences of the frictional condition, ECAP die geometry and initial crystallographic orientations of copper single crystals are carefully examined.

Chapter 6 shows the CPFEM simulations of aluminium single crystals during the multi-pass ECAP process. The deformation behavior and texture evolution history in Route A and Route C are compared.

Chapter 7 extends the CPFEM simulation of the ECAP process from single crystal to bicrystals and polycrystal. The influence of grain boundaries in the bicrystals will be discussed and simulated textures of an aluminium polycrystal will be investigated in detail.

Chapter 8 summarizes the research findings obtained in this thesis and some suggestions for future research are also offered.

Chapter 2 Literature Review

This chapter contains a substantial amount of information on topics considered essential to understanding of deformation mechanism and simulation of texture evolution during the equal channel angular pressing process.

2.1 Severe Plastic Deformation

UFG materials are defined as polycrystalline materials having very small grains, with average grain sizes between 100 nm and ~1 μm [1]. In recent years, UFG materials have attracted a lot of interest due to their unusual physical and mechanical properties, such as high strength and damping properties, lower temperature superplasticity and elevated toughness and high magnetic properties [8, 9]. These materials are very attractive for use in a range of applications from biomedical to aerospace industries.

There are two basic and complementary approaches used to fabricate the UFG materials [1, 62]. The first approach is 'bottom-up' approach, which fabricates the UFG materials from individual atoms or nanoscale building blocks such as nano-particles. The major 'bottom-up' approaches are gas condensation, ball milling, and electrodeposition [63, 64]. Another approach is called 'top-down' approach, which fabricates the UFG structures from coarse grained materials. The first approach is often limited by production of fairly small samples, together with some degrees of residual porosity and contamination. In contrast, the 'bottom-up' approach has overcome the above mentioned problems [1, 9].

The 'top-down' approach mainly adopts severe plastic deformation techniques. Up to now, many different SPD techniques have been developed, such as HPT [1-3, 8-16], ECAP [1-9, 62, 65], ARB [17-23], conshearing [24-27], multidirectional forging (MDF) [66-68], cyclic extrusion-compression (CEC) [28-30], cyclic expansion-extrusion (CEC) [69], multiple direct extrusion (MDE) [70], twist extrusion (TE) [71, 72], axisymmetric forward spiral extrusion (AFSE) [73], simple shear extrusion (SSE) [74-76], high pressure tube twisting (HPTT) [77-79], frictional stir

welding (FSW) [80-83], cylinder covered compression (CCC) [84, 85] and tube high pressure shearing (THPS) [86]. These techniques are fundamentally different, but they all introduce large plastic strain during deformation to achieve significant grain refinement. In the following text, several frequently used SPD techniques, namely HPT, ARB and ECAP will be summarized.

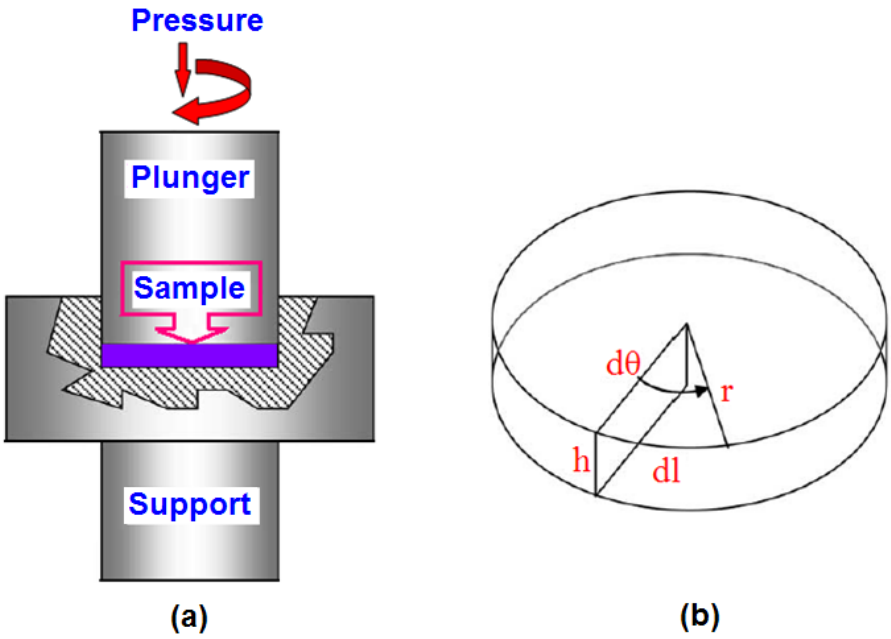

Fig. 2.1 Schematic illustration of the HPT process [87].

The HPT process was first proposed by Bridgeman in 1952 [88], but it only attracted scientific interest within last fifteen years. Fig. 2.1(a) shows a schematic illustration of the HPT process where the sample is usually machined into a thin disk, as shown in Fig. 2.1(b) [87]. The radius (r) and thickness (h) of the sample are normally less than 20 mm and 0.8 mm, respectively. During the HPT process the sample is located between the plunger and the support and then subjected to a compressive pressure (P) of several GPas. Shear strain will be introduced into the disk by rotating the plunger with the help of friction, as indicated in Fig. 2.1(a). The deformed sample does not break even at very high strains due to high imposed pressure [8]. With this method, a mean grain size of ~100 nm can be obtained subjected to a pressure of 6 GPa and with an overall strain of ~7 from an initial single crystal [10]. However, the microhardness and microstructures of the HPT processed sample are extremely inhomogeneous, as shown in Fig. 2.2 [89, 90] and Fig. 2.3 [87], respectively.

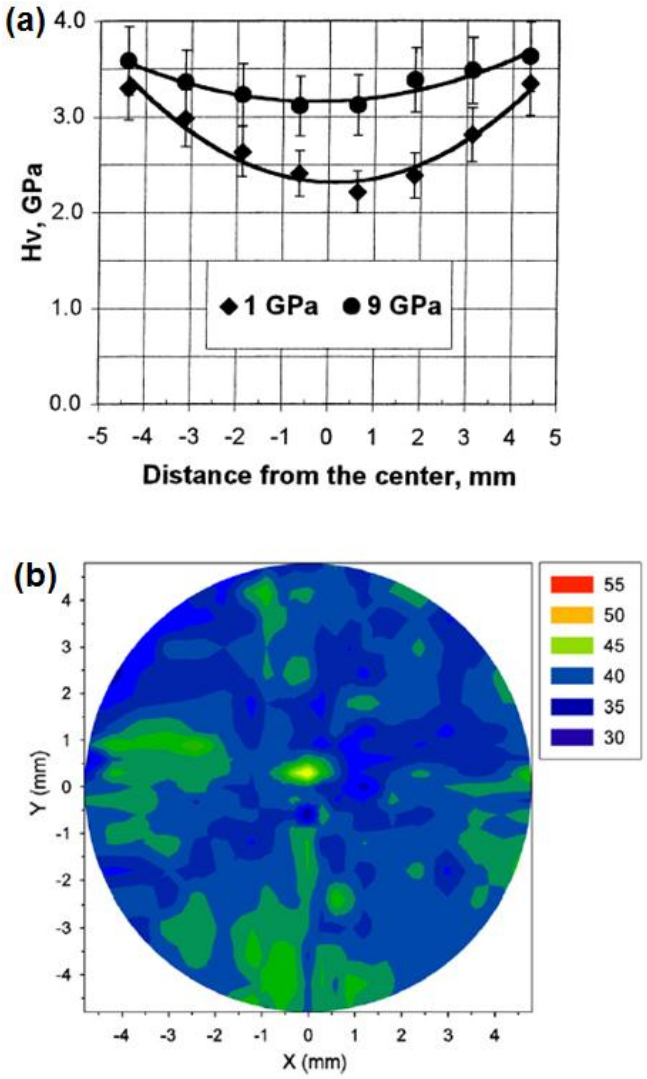

Fig. 2.2 (a) Microhardness profiles of nickel processed by the HPT process at two different applied pressures [89] and (b) Contour map of the microhardness across the surface of high purity Al processed by the HPT process at a pressure of 2.5 GPa for 5 turns [90].

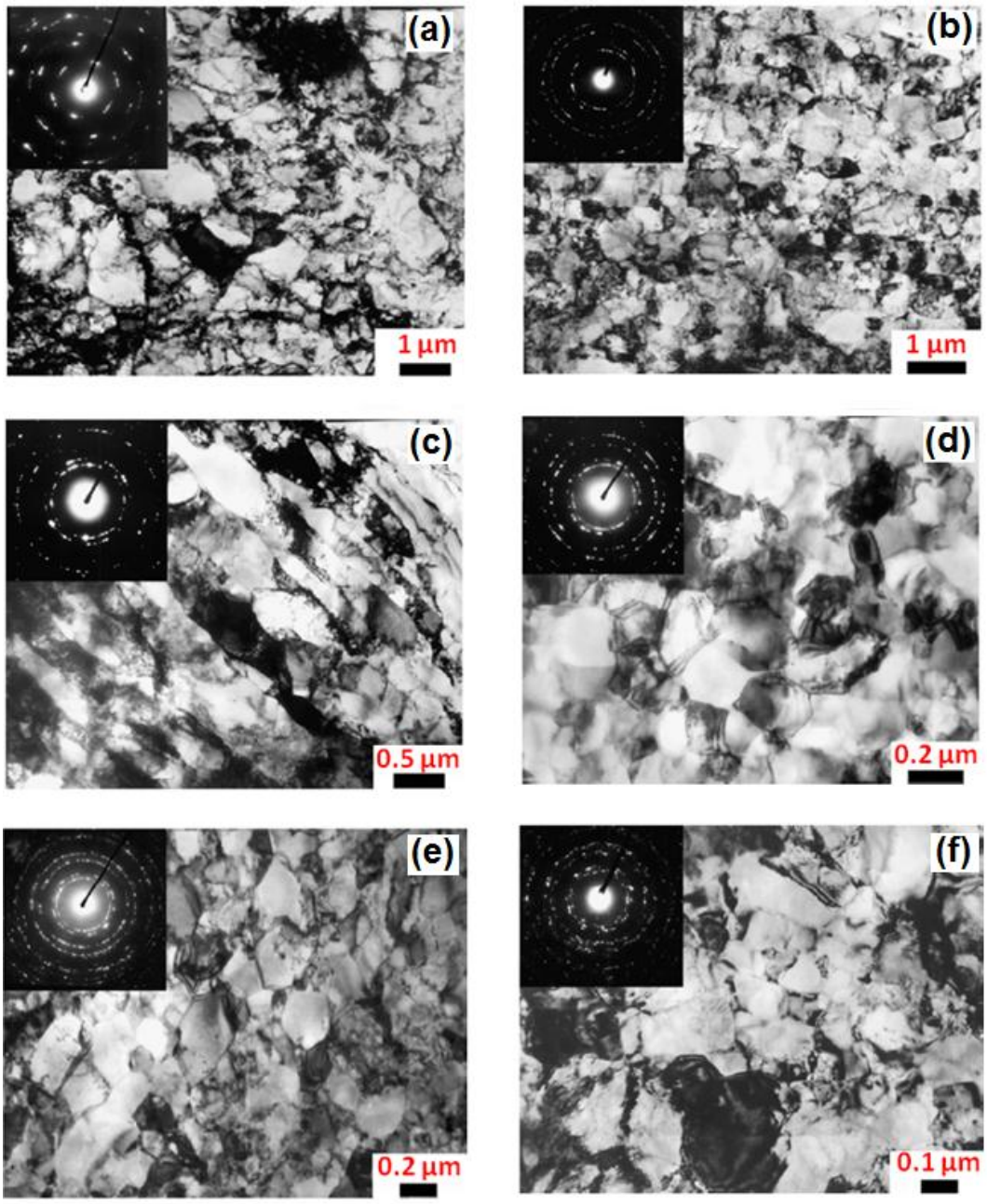

Fig. 2.3 TEM microstructures of nickel processed by HPT through N=5 turns, (a) edge, P=1 GPa, (b) center, P=1 GPa, (c) edge, P=3 GPa, (d) center, P=3 GPa, (e) edge, P=9 GPa, and (f) center, P=9 GPa [87].

During the HPT process, the shear strain is proportional to the distance from the center of the disk. The true logarithmic strain (ε_{true}) can be estimated by [89]

$$\varepsilon_{\text{true}} = \ln\left(\frac{2\pi \text{Nr}}{\text{h}}\right) \tag{2.1}$$

where h is the thickness of the disk, r is the radius and N is the number of revolutions, as shown in Fig. 2.2(b).

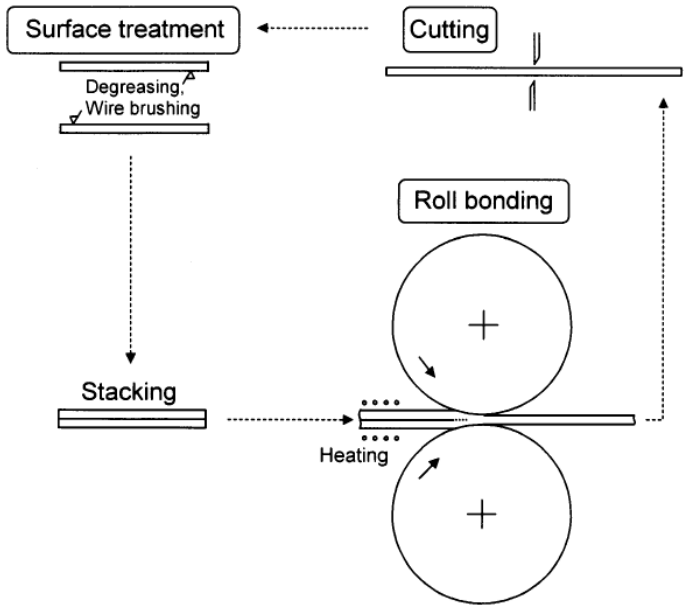

Fig. 2.4 Schematic illustration showing the principle of the ARB process [19].

Compared with the HPT process, the ARB process is a recently developed SPD technique used to manufacture the UFG sheet material. It was first proposed by Saito et al. [19, 20]. Fig. 2.4 is a schematic illustration of the ARB process where two sheets of similar dimensions are joined together by rolling. This rolled sheet is then cut in half, and the two halves are placed together and rolled again. This process can be repeated without decreasing the thickness of the sheet if the reduction is maintained to 50% for every rolling pass. Ultra-high plastic strain can be obtained by the ARB process and in theory, there is no limit.

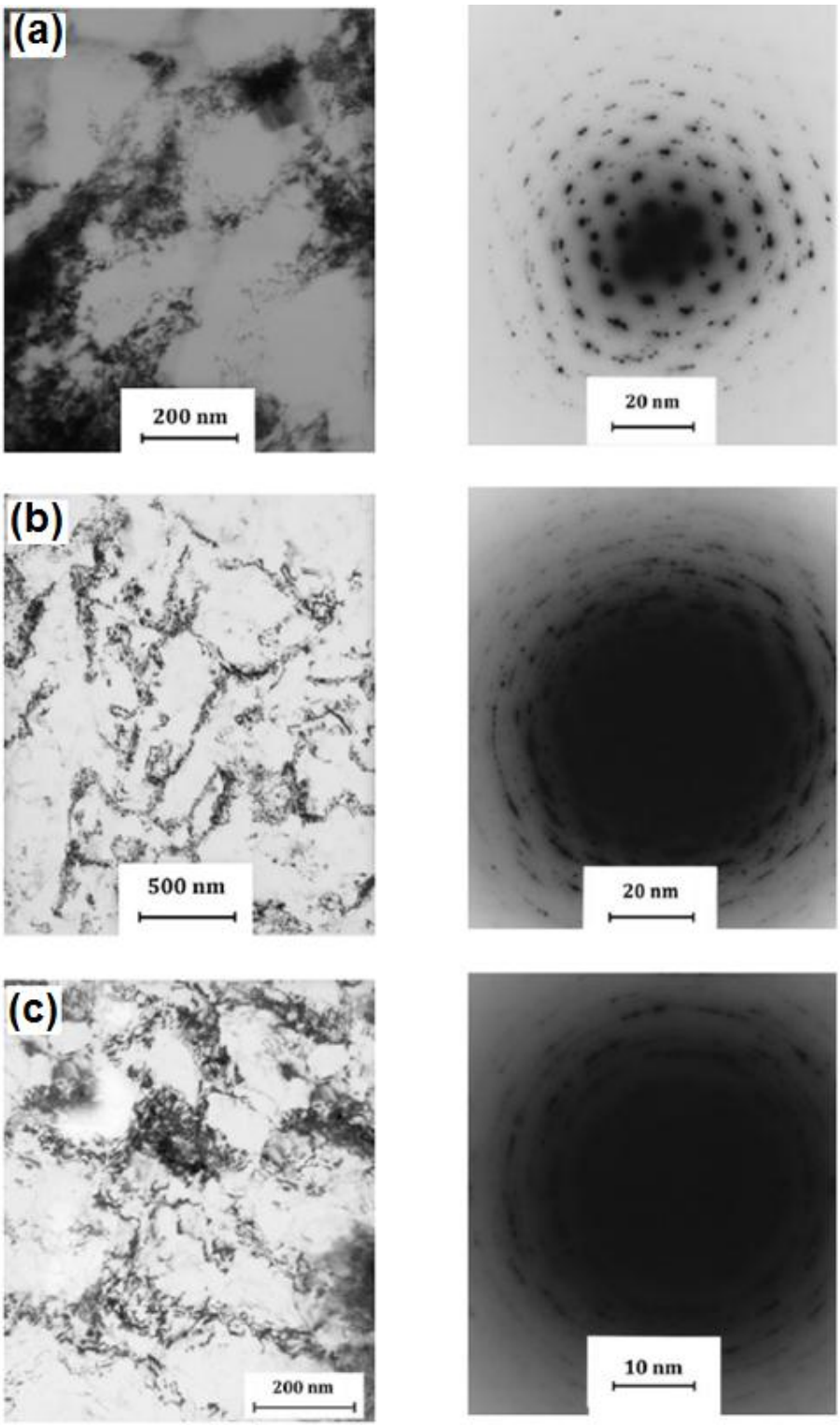

Fig. 2.5 TEM microstructures and the matching SAD patterns of ARB processed AA5083 by (a) 2, (b) 4, and (c) 6 cycles [91].

The ARB process is very effective in grain refinement, and the average grain sizes of about 200 nm and 80 nm can be obtained in AA5083 with an initial average grain size of 25 μm after four and six rolling cycles respectively, as shown in Fig. 2.5 [91]. During the ARB process the microhardness increases rapidly after the first rolling cycle and then it dwindles until it becomes saturated by further ARB cycles, as shown in Fig. 2.6 [91]. The saturation of hardness at high cycles is caused by the steady-state density of dislocation due to a dynamic balance between the generation and annihilation of dislocation caused by the dynamic restoration phenomena [91]. The main drawback of the ARB process is its poor bond strength, although it can be improved by the application of nano-particles before stacking [17, 22].

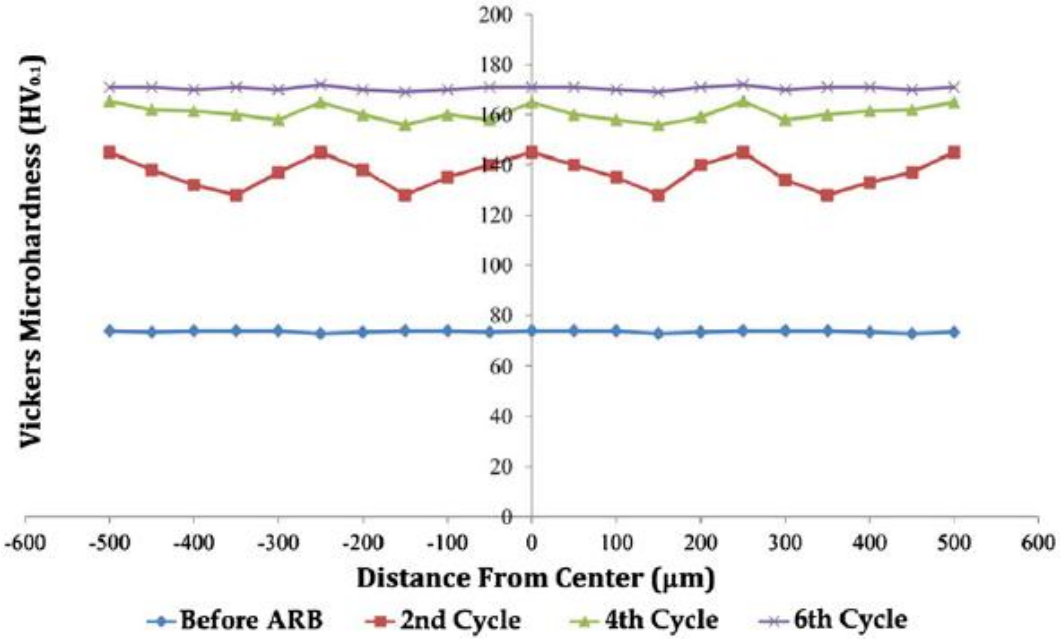

Fig. 2.6 The variation of microhardness along the thickness of the ARB processed AA5083 [91].

In practice ARB can be assumed as a plane strain deformation process, which means that the effective plastic strain during ARB can be estimated by [22]

$$\varepsilon = \frac{2}{\sqrt{3}} N \ln \frac{h_0}{h_f} \tag{2.2}$$

where h_0 is the initial thickness of the stacked sheets, h_f is the final thickness after the ARB process and N is the number of rolling cycles. If the reduction per rolling cycle can be maintained at 50%, Equation (2.2) can be simplified to the form [20]

$$\varepsilon = 0.8\mathrm{N} \tag{2.3}$$

The HPT process is only suitable for small disk samples, while the ARB process is only suitable for sheet metals.

2.2 ECAP

ECAP, also called equal channel angular extrusion (ECAE), was first proposed by Segal and his co-workers who wanted to transform simple shear into ordinary and effective production operations [4]. The ECAP process has drawn significant attention since the early of 1990s [1, 3-6, 8, 9, 92]. The principle of ECAP is illustrated schematically in Fig. 2.7 [93]. In ECAP, a bar shaped billet is pressed through a die that has two channels with an equal cross-section intersecting at an angle ϕ which varies from 60° to 150° [2]. During the ECAP process, the sample undergoes no change in its cross-section so it can be processed repeatedly to attain exceptionally high strains. Compared to the HPT and ARB processes, ECAP is capable to fabricate large bulk UFG materials and thus it is the focus of this study.

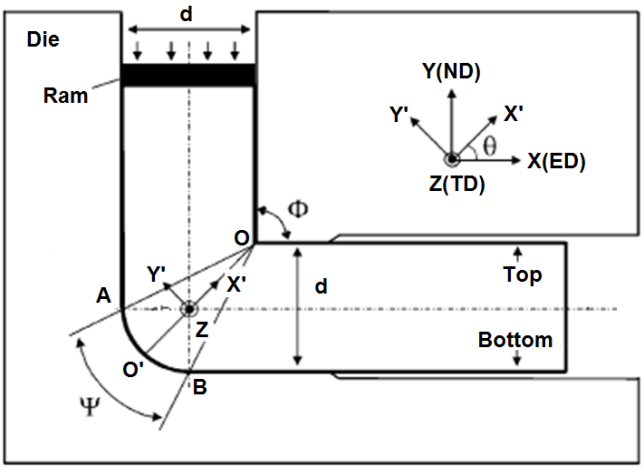

Fig. 2.7 Schematic illustration of the ECAP process [50].

The microstructure evolution during the ECAP process is influenced by different factors such as stacking fault energy [1, 94-96], die channel angle [97, 98], outer corner angle [1], number of ECAP passes [1, 3, 22, 94, 99, 100], extrusion speed [1, 93, 101], deformation temperature [22, 102, 103] and so on.

The effective plastic strain during ECAP can be calculated by [104]

$$\varepsilon_N = \frac{\mathrm{N}}{\sqrt{3}}\left[2\cot\left(\frac{\phi}{2}+\frac{\psi}{2}\right)+\psi\mathrm{cosec}\left(\frac{\phi}{2}+\frac{\psi}{2}\right)\right] \tag{2.4}$$

where ε_N is the accumulated equivalent plastic strain, N is the number of ECAP passes, ϕ is the die channel angle and ψ is the outer corner angle.

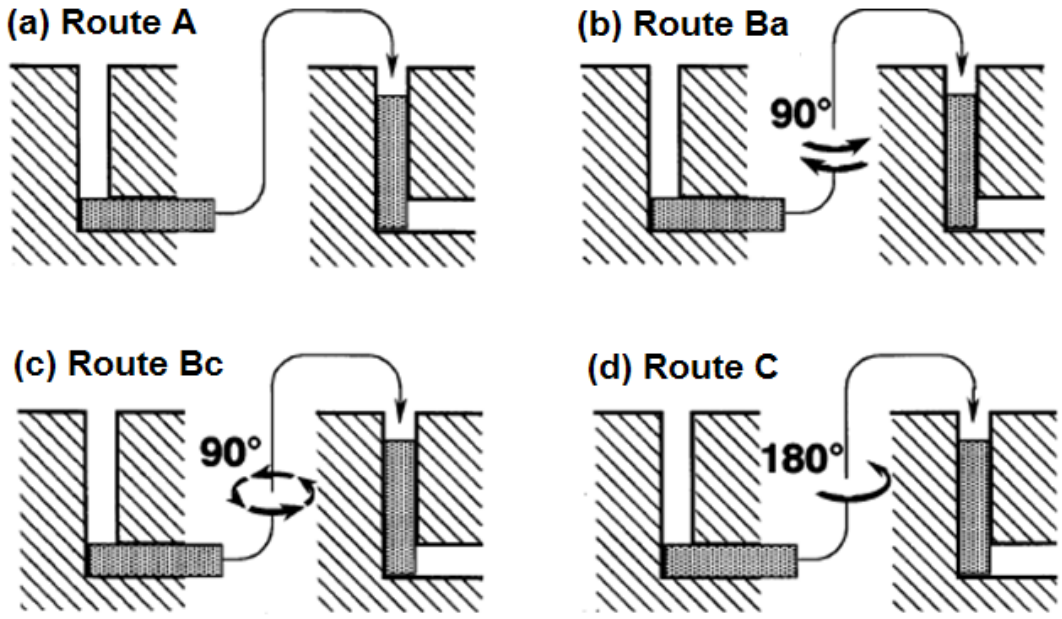

Fig. 2.8 The four fundamental processing routes in the ECAP process: (a) Route A, (b) Route Ba, (c) Route Bc, and (d) Route C [105].

During the ECAP process, the sample typically has a square or circular cross-section, which means it can be rotated clockwise or counter-clockwise about the longitudinal axis prior to the following processing passage. There are four basic processing routes as summarized in Fig. 2.8, where in Route A the sample is processed repetitively without any rotation; in Route Ba the sample is rotated 90° in alternate directions between each pass; in Route Bc the sample is

rotated 90° in the same direction between consecutive passes; and in Route C the sample is rotated 180° between two passes [105].

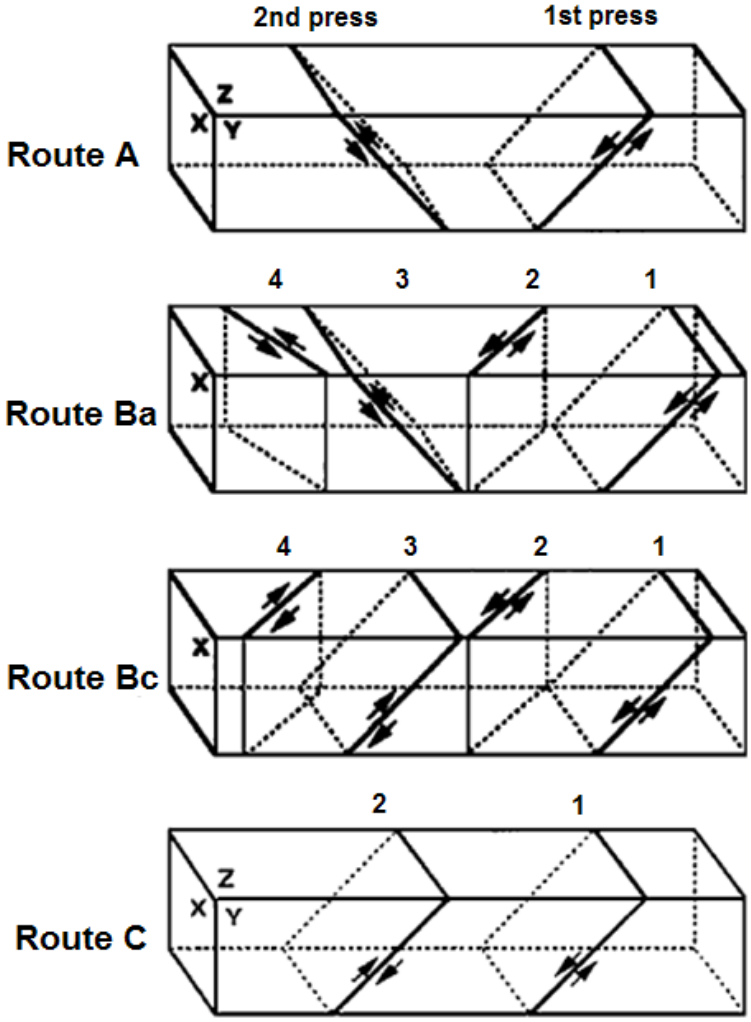

Fig. 2.9 The slip systems viewed on the X, Y, and Z planes for the consecutive ECAP passes using processing Routes A, Ba, Bc and C [1].

The slip systems for different ECAP routes are schematically shown in Fig. 2.9 [1]. In Route A there are two separate shearing planes that intersect at 90° between two passes, in Route Ba there are four separate shearing planes that intersect at 120° between two passes, while in Route Bc the shear in the first pass is cancelled by shear in the third pass, and shear in the second pass is cancelled by shear in the fourth pass. In Route C the shear continues on the same plane in each consecutive pass but the shear direction is reversed. Therefore, the cubic

element is restored every 4 passes in Route B_C and every 2 passes in Route C, while the distortions become more acute when using routes A and Ba [106].

It is obvious that the ECAP process is a discontinuous process where a sample needs to be reinserted into the die after each ECAP pass. From an industrial application perspective these operations are both labor intensive and time consuming [1]. In order to improve the efficiency of fabrication, the modified ECAP processes have been developed.

The first development is called equal cross-section lateral extrusion (ECSLE), which uses two parallel channels [107-109]. Fig. 2.12 shows the principles of this process, where ϕ is the intersecting angle and K is the displacement between two parallel channels [108]. During this process average subgrain size of ~0.4 μm can be obtained when the strain is about 10 [107]. The required number of processes can obviously be reduced to form UFG structures with this approach, but the inhomogeneity depends on the parameters ϕ and K [108, 109].

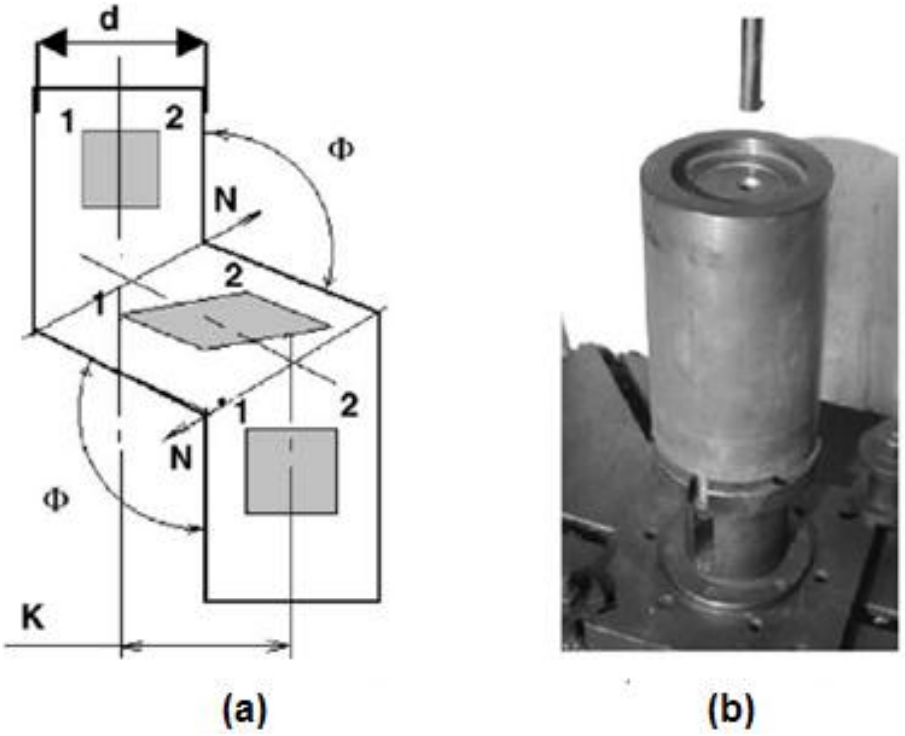

Fig. 2.10 (a) Principle of ECAP with parallel channels where ϕ is the intersecting angle and K is displacement between two channels, and (b) general view of the die set [108].

The second development is the rotary die ECAP process [110-112], or called the side extrusion process [113]. A schematic illustration of the rotary die ECAP process is shown in Fig. 2.11 [110]. Two channels with equal cross-sections intersecting at 90° are placed into the die. Three punches with equal lengths are inserted in the channel, one in the vertical channel and the other two in the horizontal channels, as shown in Fig. 2.11(a). The left punch can move freely but the other two are confined. The sample is inserted into the vertical channel and then pressed with a plunger. The die is rotated 90° after the first cycle so that the sample can be pressed again, as shown in Fig. 2.11(b-c). The process of manufacturing Al-11mass%Si alloy up to a maximum of 32 passes was successfully conducted at 623 K [111]. The main disadvantage of this process is that more processing cycles are required than conventional ECAP to obtain a sufficiently homogeneous microstructure [112].

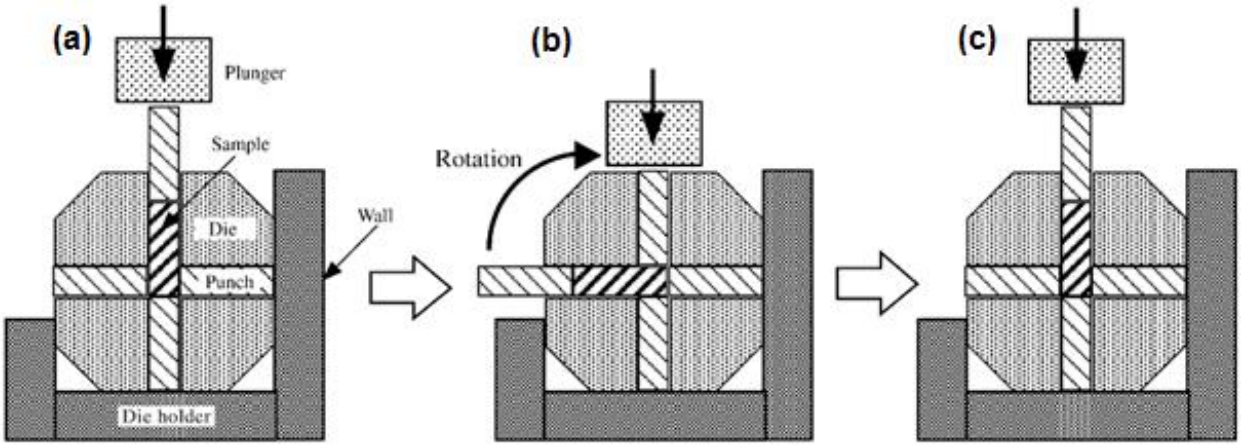

Fig. 2.11 Schematic illustration of the rotary die ECAP process at (a) the initial state, (b) after one pass, and (c) after rotating the die 90° [110].

The third development is continuous ECAP, including continuous confined strip shearing (C2S2) [114], conshearing [24-27] and equal channel angular rolling (ECAR) [115]. The common feature of these approaches is the combination of conventional rolling and ECAP. However, only limited results with small range of materials has been reported till now for these techniques. More work is needed to provide a detailed assessment of any potential industrial application of these techniques to produce large quantities of materials [1].

2.3 Deformation Models of the ECAP Process

2.3.1 Simple Shear Model

The simple shear model has been widely used to describe the material deformation during the ECAP process [44, 45, 47, 57, 58, 116-120]. It was proposed by Segal et al. [4-7] for ideal ECAP conditions, including no rounding of the inner and outer corners, perfectly plastic material, and frictionless surfaces [2]. According to the simple shear model, the sample undergoes simple shear along the intersecting plane of two channels during the ECAP process. However, it is almost impossible to meet these ideal conditions in practice.

Generally, simple shear on the intersecting plane can be represented by the displacement gradient tensor ($\mathbf{G}_{\mathrm{SS}}$) as (X'-Y'-Z' reference system in Fig. 2.8)

$$\mathbf{G}_{\mathrm{SS}} = \begin{pmatrix} 0 & \gamma & 0 \\ 0 & 0 & 0 \\ 0 & 0 & 0 \end{pmatrix} \tag{2.9}$$

where γ is the shear strain. Accordingly, the corresponding displacement gradient in the ECAP reference ($\mathbf{G}_{\mathrm{ECAP}}$) can be derived from $\mathbf{G}_{\mathrm{SS}}$ by a clockwise rotation of θ=ϕ/2 around the transverse direction and written as (X-Y-Z reference system in Fig. 2.7)

$$\mathbf{G}_{\mathrm{ECAP}} = \gamma \begin{pmatrix} -\sin\theta\cos\theta & \cos^2\theta & 0 \\ -\sin^2\theta & \sin\theta\cos\theta & 0 \\ 0 & 0 & 0 \end{pmatrix} \tag{2.10}$$

For the ECAP die with channel angle of ϕ=90°, the magnitude of the shear strain is about γ=2.

2.3.2 Analytical Model

In order to understand the deformation mechanism of the ECAP process, many analytical analyses [4, 5, 43, 48, 51-53, 104, 121-132] have been carried out. For example, a strain estimation equation (Equation (2.4)) that considers the influence of the die channel angle, the outer corner angle, and the number of ECAP passes, has been widely used since it was proposed by Iwahashi et al. [104]. This equation was improved by Luis [126, 127] based on an upper bound solution by considering the influence of the inner corner. In 1999, Segal [5]

proposed an analytical model using a slip line field and velocity hodograph. It has been found that there are three different systems of macroslip planes that occur during ECAP and the deformation history can be divided into three different steps: (i) simple shear along slip line AO, (ii) simple shear along α-slip lines inside the central fan AOB (or called 'shear fan' [2]), and (iii) simple shear along the slip line BO, as shown in Fig. 2.12 [5]. According to the slip line solution [121], round corner channels result in the reduction of pressure and increment of friction in the outlet channel.

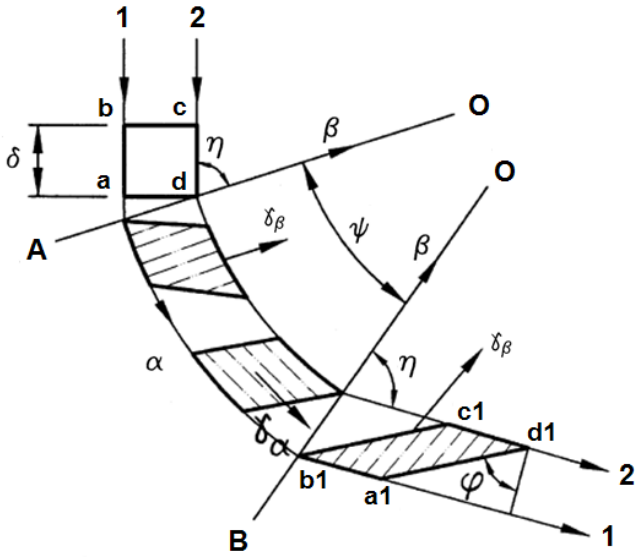

Fig. 2.12 Deformation history of material elements during the ECAP process based on an analytical analysis [5].

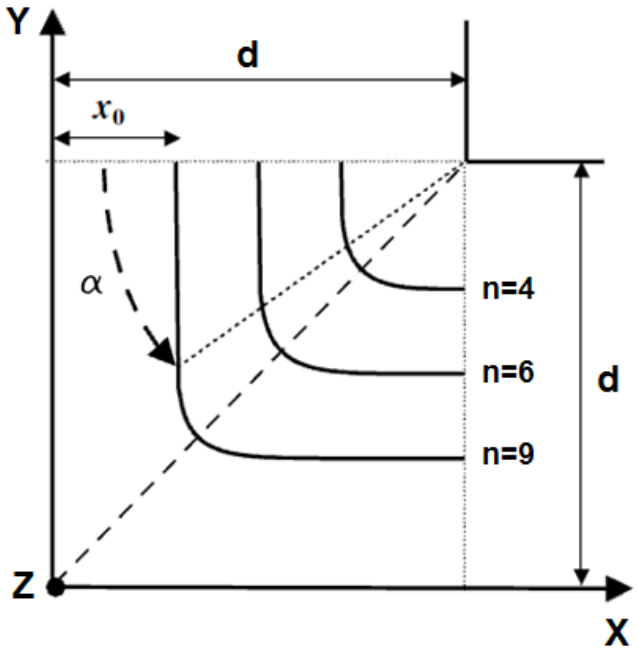

Fig. 2.13 Description of the flow field by flow lines, n indicates the value of the exponent in the proposed flow function determined by finite element calculations [43].

A flow line model is recently proposed by Toth and co-authors [43]. It uses a flow line function to describe material deformation during ECAP for a 90° die in order to avoid discontinuity of the deformation process in the classical simple shear model. The material flow in the ECAP die can be better approximated by the following flow function

$$\phi = (d - x)^n + (d - y)^n = (d - x_0)^n \tag{2.11}$$

where d is the diameter of the die, x_0 defines the incoming (and outgoing) position of the flow line, and n is a parameter used to describe the possible shapes of the flow lines as indicated in Fig. 2.13 [43]. The flow line is circular when n=2 and it is a simple shear model when n is infinity. The flow field has been validated by comparison with finite element calculations of the ECAP process. It has also been seen that the flow line model performed well in texture predictions [43, 48, 51-53, 125].

2.3.3 Physical Model

Physical modeling with a suitable material is very important because a clear observation of the material flow pattern during the ECAP process, the influence of ECAP die wall friction and a true representation of the starting microstructure of the feedback are all possible with this method. However, only limited work is available on physical modeling [133-138] so far.

The first physical model of the ECAP process was reported by Wu et al. [134] in 1997. Then this model was used to examine the methods of estimating strain [4, 104], where layered plasticine billets of different colors were pushed through plexiglass extrusion jigs allowing the process to be observed in operation. It has been found that only the experimental data from the center of the billets matched reasonably well with the theoretical values, but there were significant differences near the jig walls. Han et al. [138] conducted an in-situ physical modeling experiment to investigate the geometrical aspect of deformation during the ECAP process. It has been revealed that deformation only takes place in a fan shaped region and the basic mechanism of shear deformation is the difference in the flow route or flow path induced by the geometrical character of the ECAP die. In practice, the initial shape of the constituents of the billet did not affect the final refinement of the microstructure [136] and the strain rate of process did not essentially affect the character of non-uniformity in the distribution of shear strain [133, 137].

The disadvantage of the physical model is that the material used is generally plasticine which may not have a mechanical behavior that is identical to metal [136].

2.3.4 Classic Finite Element Method Model

The classic finite element method (FEM) model has been widely used to simulate the ECAP process. The first FEM study was conducted by Prangnell et al. [139] who reported that a corner gap in the outer corner leads to a non-uniform distribution of strain in the deformed sample. It has been proven in many experiments [1] that the development of a corner gap significantly influences the inhomogeneous grain refinement and microstructure evolution. The size of the corner gap is measured by the angle about the inner corner that subtends the points where the

billets make contact with the entry and exit channel [140]. The corner gap usually decreases in size with an increasing outer corner angle. The classic FEM analysis can be used to investigate the effects of different factors, such as number of passes, processing route, ECAP die geometry, material constitutive behavior, frictional condition, back-pressure, thermal condition and so on, on the strain, strain rate, and stress distributions in the deformed sample. These analyses are very important and valuable for design as well as for defining the processing limits for producing large volumes of homogeneously UFG materials. However, the classic FEM model is unable to predict textures.

There is no doubt that the frictional condition between the sample and channels in the die has a strong influence on the required processing loads, development of corner gaps, plastic deformation heterogeneity, inhomogeneous grain refinements and texture evolution. However, there are some contradictory results and the study is still essential. For instance, it has been found that strain and inhomogeneous deformation increase with the friction according to the study [139], but Yang and Lee [141] stated that the frictional condition does not affect the distribution of strain, while Li et al. [142] reported that when the material fills the die, it has little influence on the shape of plastic deformation zone (PDZ) but some influence on the local variation of strain rates at the inner and outer corner regions. Specifically, an increase of friction leads to a higher plastic strain rate in the inner corner and variation of the strain rates near the outer corner region. Besides, Wei et al. [143] revealed that the strain distribution is relatively more uniform with friction than without friction and they attributed this to the back pressure induced by friction. Therefore, they have concluded that friction is not the source of non-uniform strain distribution. In addition, Balasundar and Raghu [144] stated that they have found obvious differences between the Coulomb friction model and the shear friction model during the simulation of ECAP process.

The FEM mesh is important, but few studies have considered this influence. As can be seen in Ref. [142], there is a large difference between mesh with 839 elements and mesh with 3379 elements. In order to save computing time, most of the FEM studies were carried out based on the assumption of plane strain condition in the middle longitudinal plane of the billet, and

reasonable results have been obtained. However, three-dimensional simulations to evaluate the deformation heterogeneity in the transverse direction [145-150] and simulate the routes Ba and Bc [146, 148, 151] are still very important because they cannot be simulated using two-dimensional models at all. Generally, three-dimensional simulations predict similar trends of heterogeneity along the X and Y directions with the two-dimensional simulations. It has been found that with the rounded corner dies, the undeformed bottom layer was larger in the three-dimensional FEM model than in the two-dimensional model [152]. In addition, the deformation heterogeneity along the Z direction decreases with an increasing outer corner angle [152] and it changes with the number of ECAP pass [151]. This deformation may not be symmetrical about the central plane for a circular cross-section, and the average plastic strain and the deformation inhomogeneity index along the Z direction increase with the coefficient of friction [150].

2.4 ECAP Texture Measurement

2.4.1 Texture Representation and Measurement Techniques

Texture is defined as preferred orientation and it is very important due to its influence on material properties such as Young's Modulus, Poisson's ratio, strength, ductility, toughness, electrical conductivity, and so on [153]. Texture is commonly represented by Miller indices, the pole figure, the inverse pole figure or orientation distribution function (ODF).

The main advantage of the Miller indices notation is that it highlights important planes {h k l} and directions <u v w> which are parallel to the principle directions in the sample. For example, the notation of {h k l}<u v w> during rolling indicates that the direction <h k l> is parallel to the normal direction (ND) and the direction <u v w> is parallel to the rolling direction (RD). The pole figure is a two-dimensional representation of three-dimensional orientation information projected from the reference sphere. One direction must be chosen as a pole during projection and ND is typically chosen to be in the north pole of the sphere during rolling. The inverse pole figure is similar to the pole figure and it is the orientation that represents the sample coordinate system in the crystal coordinate system. Inverse pole figures are often used for axial symmetric samples, where only one of the axes is prescribed. ODF is a three-dimensional

representation of textures and it is able to offer a quantitative evaluation with the help of Euler angles, which are shown in Fig. 2.14 [153]. It should be noted that there are several different conventions for describing the Euler angles, with the most widely used being the Bunge's convention [154].

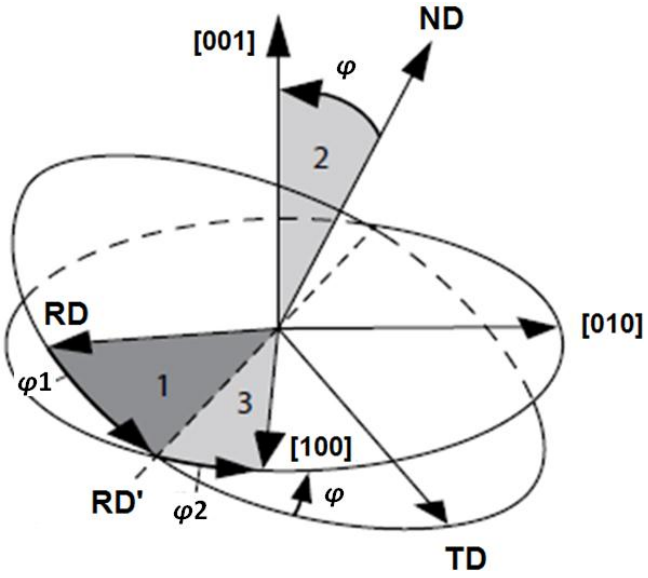

Fig. 2.14 Diagram showing how rotation through the Euler angles φ_1, φ, φ_2, in the order 1, 2, 3 as shown describes rotation between the sample and crystal axes [153].

The orientation matrix (g) can be expressed with the three Euler angles as [153]

$$g = g_{\varphi_2} \cdot g_{\varphi} \cdot g_{\varphi_1} \tag{2.5}$$

where the three rotation matrices (g_{φ_2}, g_{φ}, g_{φ_1}) can be written as

$$g_{\varphi_2} = \begin{pmatrix} \cos\varphi_2 & \sin\varphi_2 & 0 \\ -\sin\varphi_2 & \cos\varphi_2 & 0 \\ 0 & 0 & 1 \end{pmatrix} \tag{2.6}$$

$$g_{\varphi} = \begin{pmatrix} 1 & 0 & 0 \\ 0 & \cos\varphi & \sin\varphi \\ 0 & -\sin\varphi & \cos\varphi \end{pmatrix} \tag{2.7}$$

$$g_{\varphi_1} = \begin{pmatrix} \cos\varphi_1 & \sin\varphi_1 & 0 \\ -\sin\varphi_1 & \cos\varphi_1 & 0 \\ 0 & 0 & 1 \end{pmatrix} \tag{2.8}$$

According to the scale of the measured area, texture measurement can be divided into two groups, namely macrotexture analysis and microtexture analysis. Macrotexture represents the bulk texture of a particular sample and is measured from a large number of grains by means of X-ray diffraction or neutron diffraction. Microtexture is measured by Kikuchi patterns with the electron diffraction under an electron microscope and represents the texture of individual grains. The most widely used measurement is the electron backscatter diffraction (EBSD) technique.

2.4.2 Main Characteristics of Measured ECAP Texture

Up to now, texture evolution during the ECAP process has been studied for a wide range of metals and alloys, such as Al single crystals and alloys [2, 22, 33, 34, 46, 47, 49, 96, 119, 135, 155-171], Ni single crystals [172-176], Nb single crystals [177, 178], Cu single crystals, bi-crystal and alloys [2, 36, 38-41, 59, 96, 98, 159, 179-190], low carbon steels [42, 45, 60, 167, 191-193], magnesium alloys [44, 194-200], Ti alloys [44, 148, 201-203] and so on. It has been found that the ideal textures of polycrystalline materials after ECAP can be defined directly from those in simple shear by counter-clockwise rotation of $\theta=\phi/2$ around the transverse direction, assuming that simple shear takes place along the plane of intersection of the two channels in a negative direction [2, 4, 31, 32]. ECAP textures depend strongly on the crystal structures and ideal texture components have been determined for face-centered cubic (FCC) and body-centered cubic (BCC) polycrystalline materials in terms of pole figures as shown in Fig. 2.15 and Fig. 2.16, respectively [31].

It should be noted that during the ECAP process, the Miller index {h k l}<u v w> denotes an orientation that has an {h k l} plane parallel to the normal plane (or Y plane) and an <u v w> direction parallel to the extrusion direction (or X direction), and {h k l}<u v w>$_\theta$ indicates an counter-clockwise rotation of θ around the transverse direction (or Z direction) (Fig. 2.7). For FCC structures, there are two partial fibers {1 1 1}$_\theta$ and <1 1 0>$_\theta$. The fiber {1 1 1}$_\theta$ contains four ideal components of A_θ, $\overline{A}_\theta$, $A^*_{1\theta}$ and $A^*_{2\theta}$, while the fiber <1 1 0>$_\theta$ contains A_θ, $\overline{A}_\theta$, B_θ, $\overline{B}_\theta$, C_θ. The corresponding Miller indices and Euler angles have been summarized in Table 2.1 [2, 31].

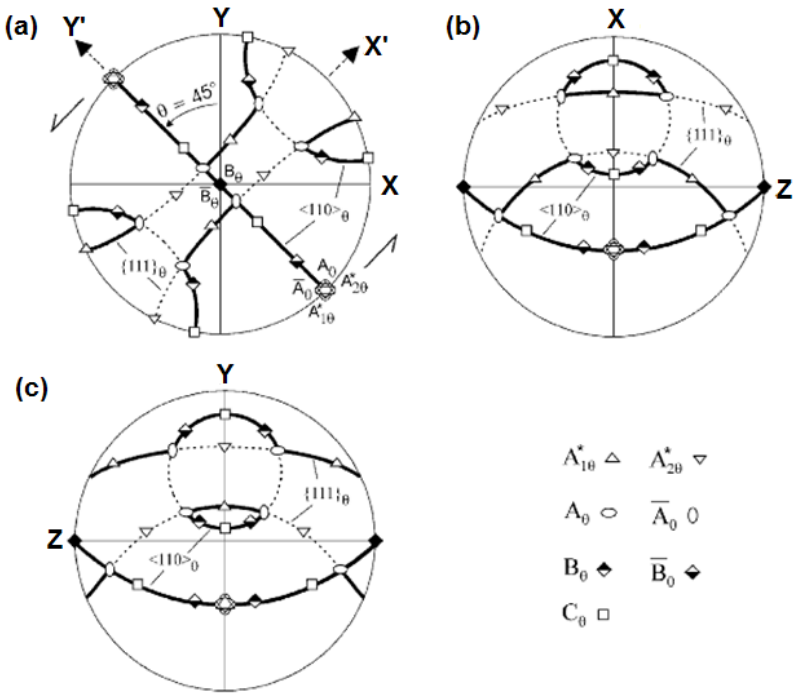

Fig. 2.15 {1 1 1} pole figures showing the main ideal orientations and fiber textures for FCC materials after one ECAP pass with ϕ=90°. (the arrows indicate the direction of shear) [31].

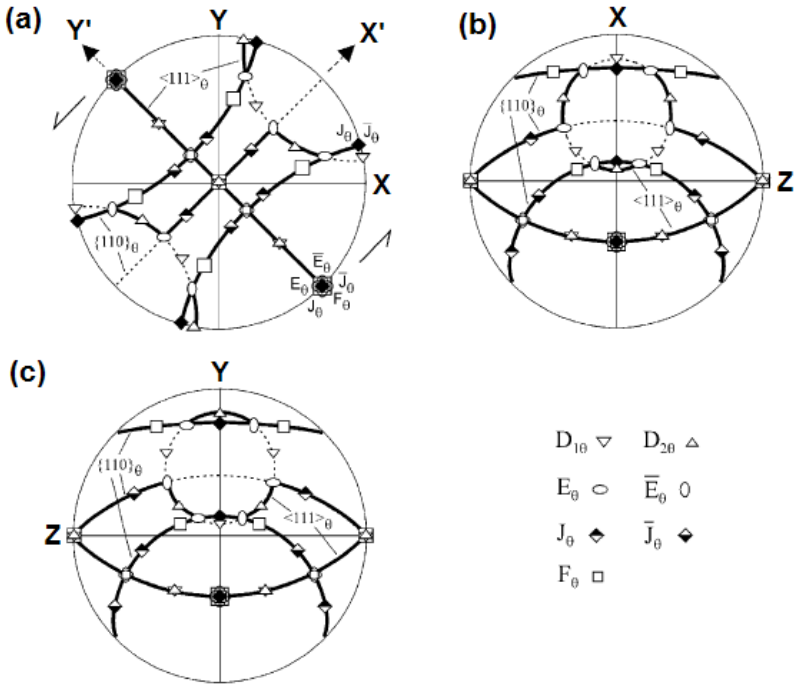

Fig. 2.16 {1 1 0} pole figures showing the main ideal orientations and fiber textures for BCC materials after one ECAP pass with ϕ=90°. (the arrows indicate the direction of shear) [31].

Table 2.1 Euler angles and Miller indices for the ideal orientations of FCC materials after one ECAP pass with ϕ=90°die [2, 31].

Notation	Euler angles (°)			Miller index
	φ_1	φ	φ_2	{h k l}<u v w>
A_θ	45	35.26	45	(9 1 4)[1 11 -5]
$\overline{A}_\theta$	225	35.26	45	(-1 -11 5)[-9 -1 -4]
$A_{1\theta}^*$	80.26/260.26	45	0	(8 1 -1)[1 -4 4]
	170.26/350.26	90	45	
$A_{2\theta}^*$	9.74/189.74	45	0	(1 -4 4)[8 1 -1]
	99.74/279.74	90	45	
B_θ	45/165/285	54.74	45	(15 4 11)[7 26 -19]
$\overline{B}_\theta$	105/225/345	54.74	45	(-7 -26 19)[-15 -4 -11]
C_θ	135/315	45	0	(3 3 4)[2 2 -3]
	45/225	90	45	

The fibers and ideal orientations for BCC materials can be found in Fig. 2.16 and they can be related to those for FCC materials in Fig. 2.15 by an exchange of the slip planes {h k l} and slip directions <u v w>. Experimental results have shown significant influence of the processing routes, number of passes, substructure evolution, temperature, stacking fault energy, and ECAP die geometry on the development of ECAP textures [2]. For example the components $B_\theta/\overline{B}_\theta$ has been strengthened continuously with the increasing number of passes in pure copper processed in Route A [40]. In addition, the orientation distribution along the $\{1\ 1\ 0\}_\theta$ and $<1\ 1\ 1>_\theta$ fibers is more uniform in Routes A and C than Ba and Bc [42]. Fig. 2.17 shows the ODF sections of textures for aluminium and copper after one ECAP pass [50]. As shown, textures are quite different to each other in that differences are primarily attributed to their initial textures,

material properties and microstructure evolution, all of which will decrease with an increasing number of passes.

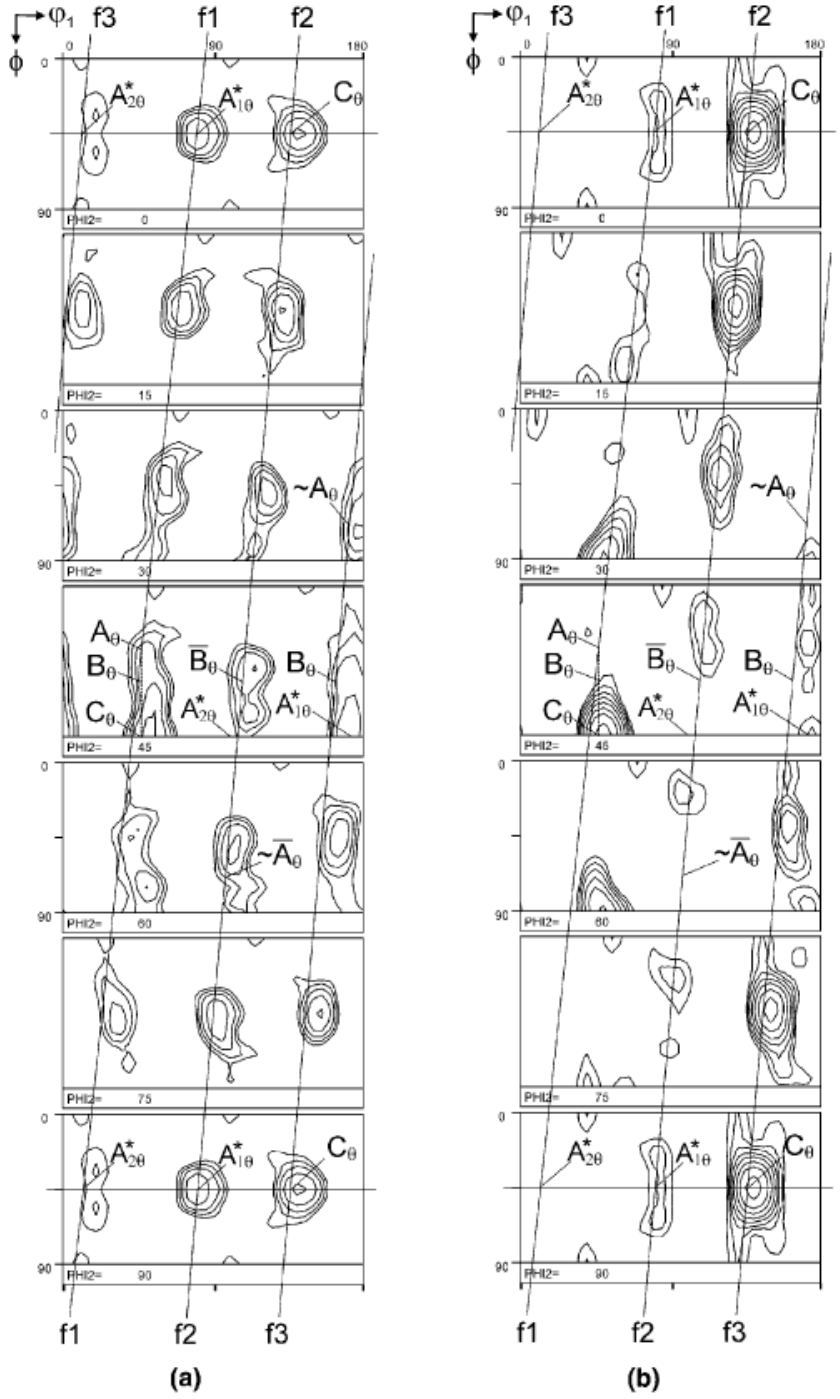

Fig. 2.17 φ_2=constant ODF sections of textures measured after one ECAP pass for (a) copper, and (b) aluminium [50].

It is worthy to note that, texture evolutions in single crystals are different to the polycrystalline materials during the ECAP process, particular after the first pass. The experimental results revealed only two orientation components (initial orientation and the 60° rotated component) in the deformed aluminium and copper single crystals [33, 179, 181], where the slip plane (-1 -1 -1) was parallel to the theoretical shear plane and the slip direction [-1 1 0] was parallel to the theoretical shear direction. The relationship between the crystallographic orientation and theoretical shear plane was observed in Refs. [161, 179, 181] by rotating the crystals around the transverse direction. Al 20° crystal led to a 40° rotated orientation component [204] and Al -20° led to a 60° rotated component [161] after the ECAP process where '-' indicated the counter-clockwise rotation.

2.5 ECAP Texture Simulations

Up to now, a lot of effort has been devoted to simulating texture evolutions during the ECAP process and these studies can be categorized into three groups. The first group was based on the Taylor-type texture models, the second group used the self-consistent models, and the last group used the CPFEM model.

2.5.1 Taylor-type Models

One of the earliest and most widely used texture models, referred as fully constrained (FC) model, was proposed by Taylor [205]. This model is based on the assumption that each grain is subjected to the same plastic strain as the macroscopic plastic strain. In the FC model, five components of the plastic strain increment need to be prescribed and five independent slip systems are generally necessary to comply with these conditions. As a consequence of its assumption, the FC-Taylor model often leads to an upper-bound estimate for the overall strength of textures. It is widely recognized that textures predicted by the FC-Taylor model are in a fairly good qualitative agreement with those experimentally observed for both FCC and BCC materials. However, there are two main discrepancies, including the shift of major texture components and the excessive stronger intensity than the actual measurements [206, 207]. In addition, the FC-Taylor model rapidly becomes inaccurate at large strains [2].

In order to improve the FC-Taylor model, the relaxed constraints (RC) theory has been proposed [206-208]. The RC-Taylor model allows for some of the strain components in the grain to differ from the average one. It has been found that predicted textures based on the RC-Taylor model are in better agreement with experiments than the FC-Taylor model, particularly for large strain rolling and torsion. However, the relaxation is based on the grain shape and stress continuity considerations and not in the relative stiffness of grain and matrix [209]. In practice, the RC-Taylor model does not resolve the problem of nonuniqueness in the choice of active systems and there is the added task of specifying model criteria for relaxing compatibility requirements.

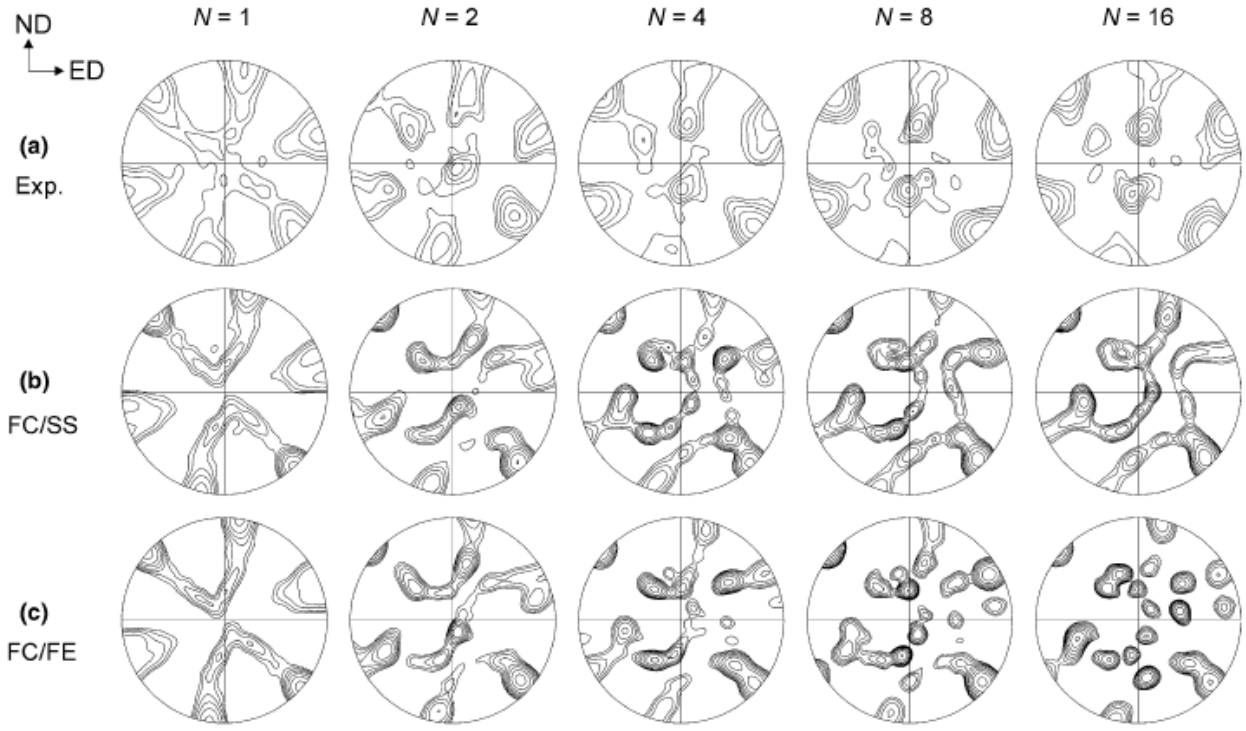

Fig. 2.18 {1 1 1} pole figures of textures in the deformed billets after various passes via Route Bc. (a) experimental results, (b) simulation results with FC-Taylor model based on simple shear deformation, and (c) simulation results with FC-Taylor model based on FEM calculated deformation history [41].

Up to now, the Taylor models have been widely used to simulate texture evolution during the ECAP process [38, 39, 41, 43, 45, 47-49, 59, 60, 191, 210-215]. For example Pithan et al. [210] used the FC-Taylor model to explain the existence of the copper-orientation {1 1 2}<1 1 1> and brass-orientation {1 1 0}<1 1 2> in the ECAP processed AA5056. Gholinia et al. [49] applied this

model to simulate deformation textures in aluminium alloy after the ECAP process with die channel angles of 90° and 120°. Messemaeker et al. [45] calculated the rotation fields for IF steel subjected to the ECAP process via Routes A, Ba, Bc and C up to 4 passes. It has been found that the results for Routes Ba and Bc are less self-evident, due to the change of shear plane between two passes. Li et al. [59] simulated texture along three flow lines at the top, middle and bottom regions in the processed copper after 16 passes. The influence of strain path in copper alloy was also examined by Li et al. [41] using FC-Taylor model based on the deformation histories calculated by simple shear model (FC/SS) and FEM (FC/FEM). Their simulation results have been compared with the experimental results for Route Bc as shown in Fig. 2.18 and for Route C as shown in Fig. 2.19. It has been found that the measured texture indices after 16 passes in Route Bc is 4.3, while the simulated values are 16.5 with FC/SS and 25.4 with FC/FEM, respectively. In another study, even larger difference in the texture strength by two and three orders in magnitude between simulations and experiments have been observed by Ferrasse et al. [47], where the simulated material was high purity Al0.5Cu alloy and the influences of strain path, number of passes and initial textures were considered. Their simulation results revealed a continuous texture strengthening with the number of passes, as shown in Fig. 2.20.

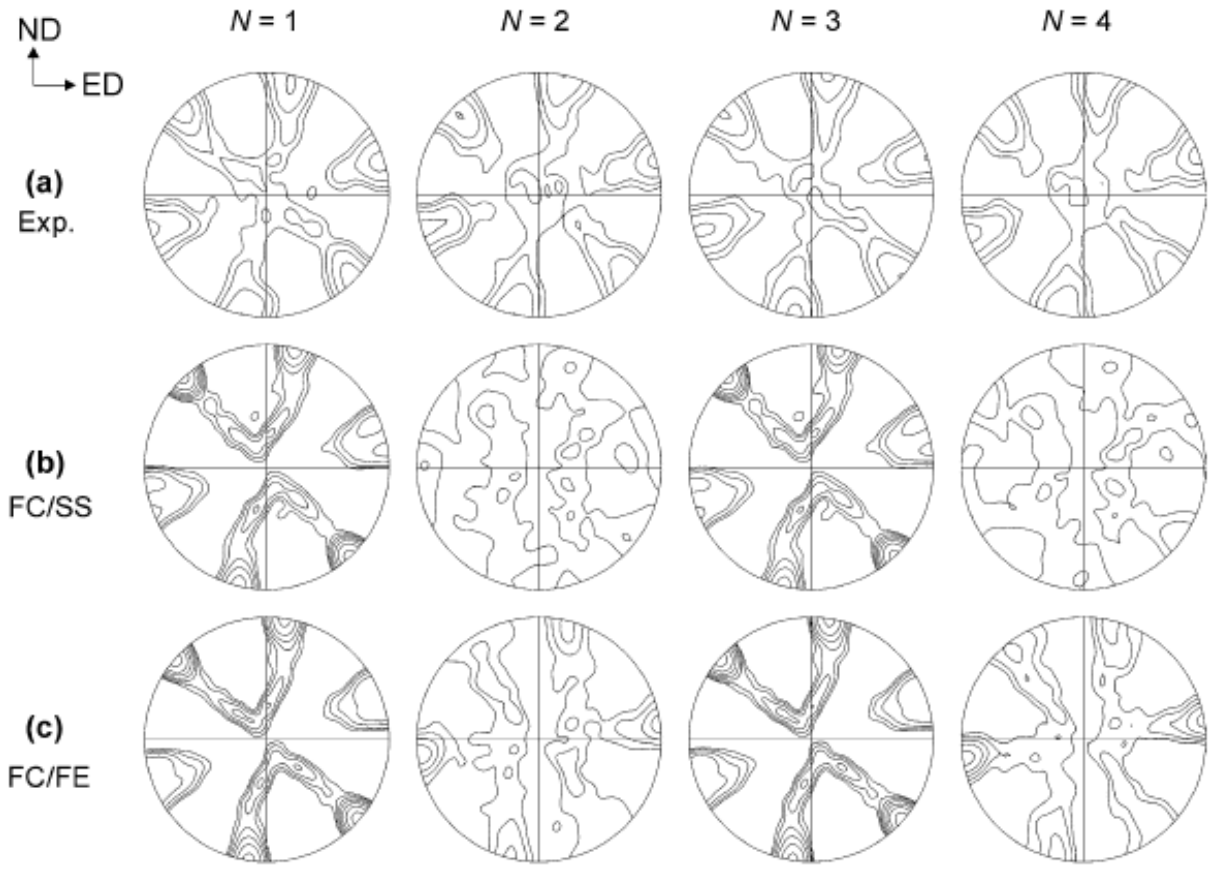

Fig. 2.19 {1 1 1} pole figures of textures in the deformed billets after 1 to 4 passes via Route C. (a) experimental results, (b) simulation results with the Taylor model based on simple shear deformation, and (c) simulation results with the Taylor model based on FEM calculated deformation history [41].

In order to improve prediction of the deformation fields in ECAP, a flow line model was developed by Toth et al. [43]. It has been found that the Taylor constitutive laws implemented into this flow line model could give a better texture prediction, at least up to two ECAP passes. The results revealed that the measured intensities of texture components were well reproduced and the differences in the tilts from the ideal positions did not exceed 5°. Simulation results of IF steel in Ref. [60] indicated that textures developed during the ECAP processes with different die channel angles can be approximately related by a rotation about the axis normal to the flow plane. In a recent report, Gu and Toth [38] used a Taylor-type model to simulate the texture development in polycrystalline oxygen-free high conductivity (OFHC) copper deformed in route C for up to two passes. Their results showed that the magnitude of

the shear strain increment played an important role in predicting texture evolution during strain reversal. However, the acceptable agreement between simulations and experiments can only be obtained when the strain increment is very large.

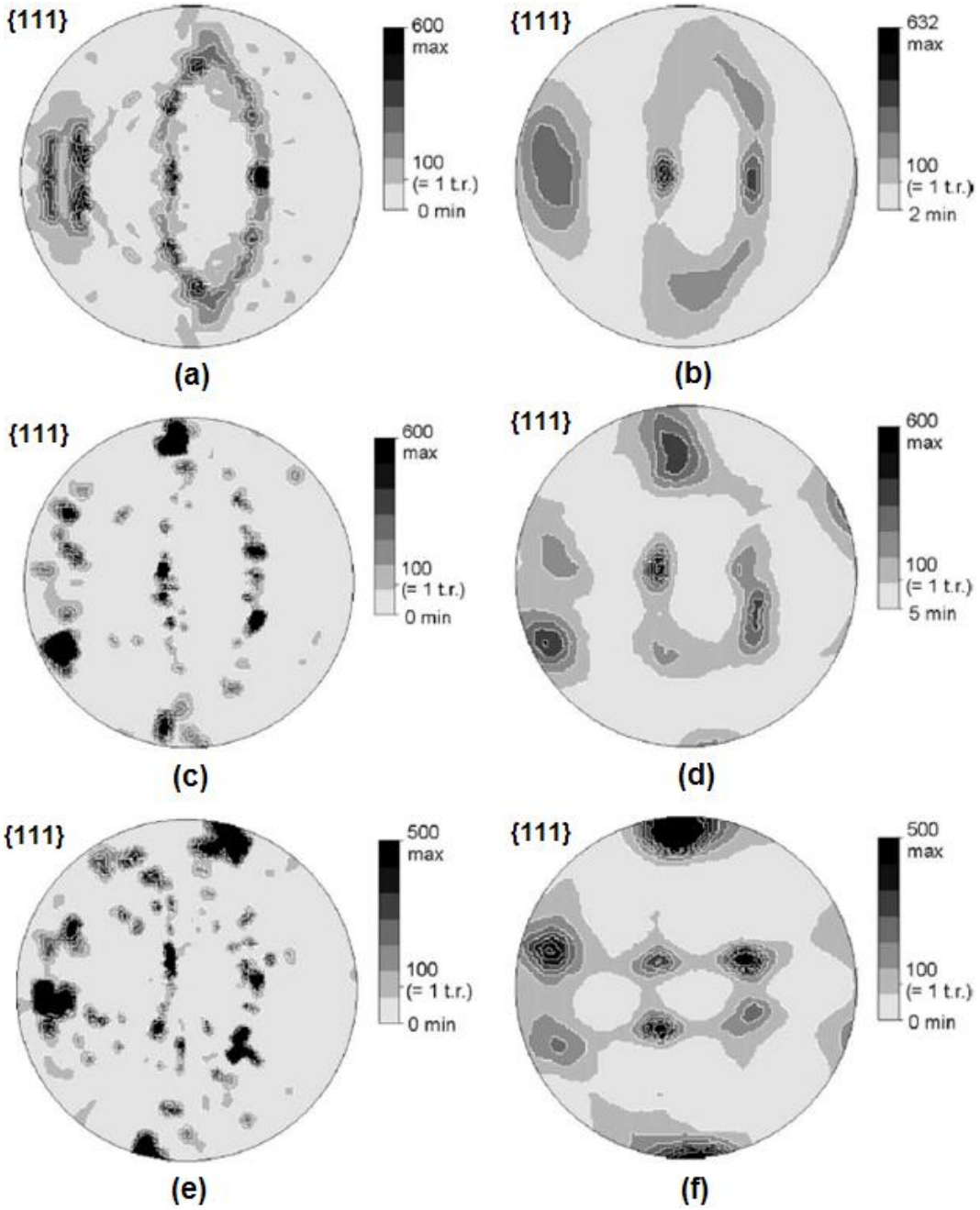

Fig. 2.20 The Taylor model predicted (a, c, e) and experimental (b, d, f) measured {1 1 1} pole figures for (a-b) one pass, (c-d) four passes in Route A, and (e-f) four passes in Route C for the high purity Al0.5Cu alloy [47].

Although the Taylor-type models could give reasonable description of ECAP textures, but they failed to give good quantitative predictions. Significant overestimations of the texture strengths in all cases except for the even-numbered passes in route C have been obtained. It should be noted that, even the method FC/FEM performed better in predicting the texture characteristics, but it led to more texture strength than the method FC/SS, and both methods failed to accurately predict textures for even-numbered passes in Route C in both the strength and characteristics.

2.5.2 Self-consistent Model

In the Taylor theory, the strain uniformity fulfills the compatibility condition but not the equilibrium condition at the grain boundaries. In order to overcome this limitation, self-consistent approaches have been proposed by Hill [216], Hutchinson [217], and Iwakuma and Nemat-Nasser [218]. In Ref. [219], a large deformation viscoplastic self-consistent (VPSC) polycrystal theory was formulated, where each grain was assumed to be a single ellipsoidal inclusion in a homogeneous equivalent medium to predict textures in tension, compression, rolling, and torsion. Based on this assumption, the average stress and strain rate over all the grains is consistent with the equivalent microscopic magnitudes. Therefore, each grain can deform differently in the VPSC model depending on its directional properties and the strength of the interaction with its surroundings. However, self-consistent methods must struggle with the non-linearity of the relationship between stress and plastic strain or strain rate, because they implicitly use linearizations of this material model for the strain field surrounding the inclusion [61].

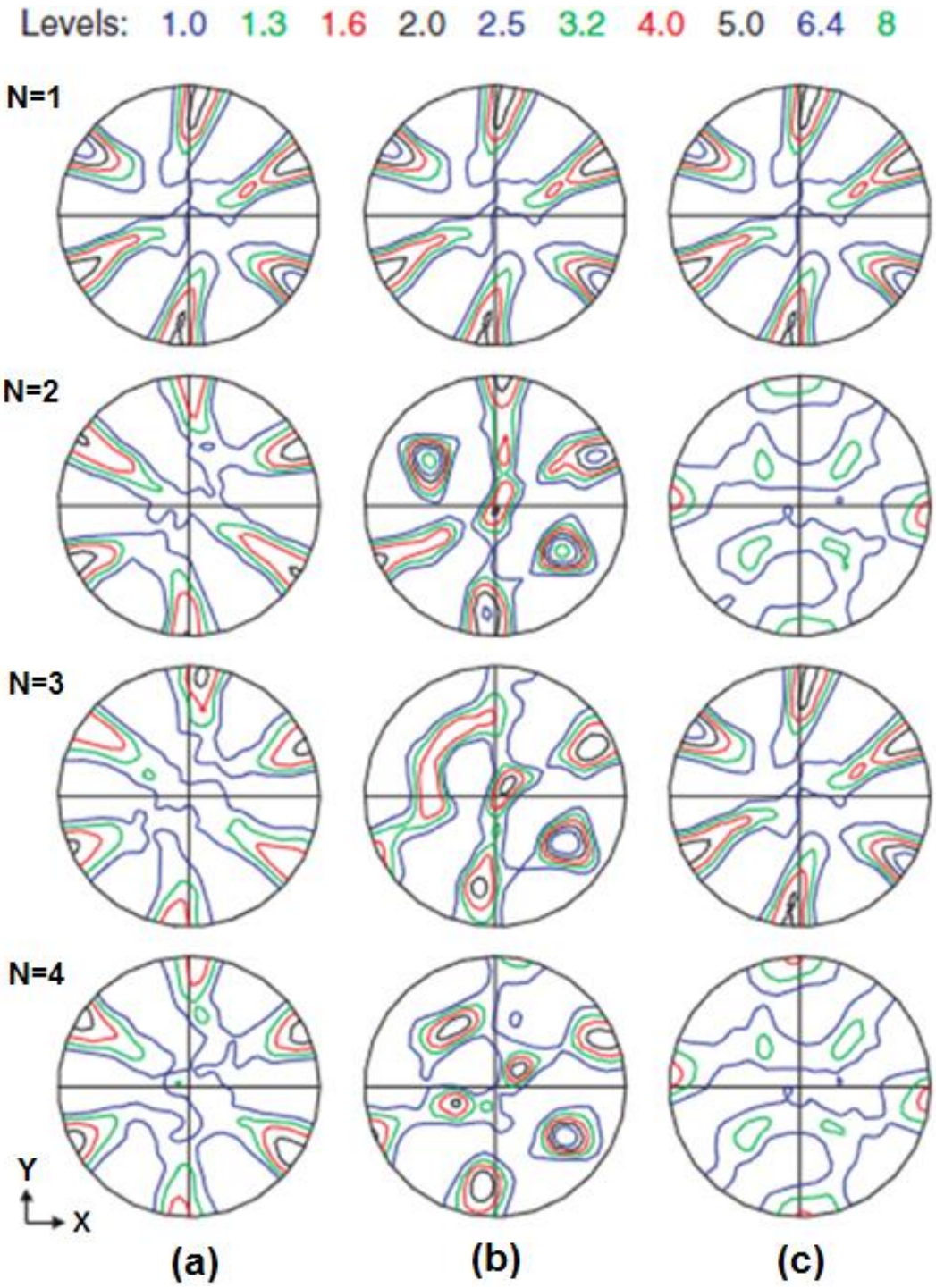

Fig. 2.21 {1 1 0} pole figures of textures in the deformed IF steel after 1-4 passes of ECAP process (120° die) via Routes (a) A, (b) Bc and (c) C simulated by the VPSC model using the FEM predicted deformation history for each pass [60].

The VPSC model has been applied to simulate texture evolution of the ECAP process [38, 41, 43, 50-53, 59, 60, 170, 182, 194, 195, 215, 220-230]. Toth et al. [43] used this model to simulate texture evolution of copper up to three passes in route A. Their results revealed that the VPSC model was able to reproduce textures well for the first two passes, but failed in the third pass performing as the Taylor-type models. In the VPSC simulations [59], the advances including a grain co-rotation scheme and an implementation of an empirical criterion for grain subdivisions based on grain shape were applied. As shown in Table 2.2, the VPSC model led to better agreement with the experimentally measured textures than the Taylor-type models for all the positions, except for s=0.5 and 0.9 where the two models were approximately similar. The simulations were extended from the Routes A and C in Ref. [59] to the Route Bc in Ref. [41]. The VPSC model was also applied to simulation of the ECAP process of IF steel under Routes A, Bc and C [60]. Their results revealed that the VPSC/FEM model reproduced well the main features and satisfactorily predicted the texture strengths in Routes Bc and C and, to a lesser extent, route A as shown in Fig. 2.21. However, according to the report [38], both the Taylor and VPSC models failed to predict the strain reversal texture in Route C and they returned texture to initial state every second pass. In addition to the FCC and BCC materials, the HCP materials such as magnesium single crystal [230] and alloy ZK60 [228] have also been simulated by the VPSC model.

In general, improvement of texture prediction has been achieved by the self-consistent model compared to the Taylor-type models. However, the predicted texture strength is still not in satisfactory. As shown in Fig. 2.22(b), both the Taylor-type model and VPSC model predicted wrong textures compared to the experimental results.

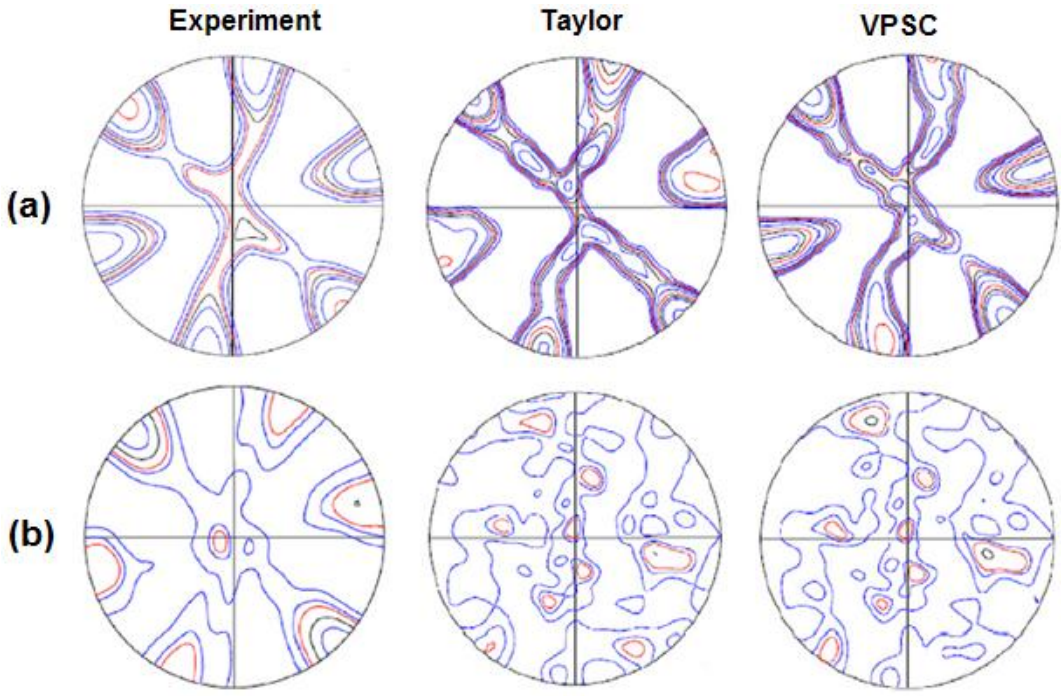

Fig. 2.22 {1 1 1} pole figures of the experimental textures and simulated textures using the Taylor model and VPSC models with the shear increment of 0.005 for (a) the first pass, and (b) the second pass [38].

Table 2.2 Maximum intensity in {1 1 1} pole figure (P) and texture index (T) of the experimental and simulated textures at different thickness positions in the deformed billet after the first pass [59].

Position	P			T		
	Experiment	Taylor	VPSC	Experiment	Taylor	VPSC
s=0.1	6.8	12.2	6.9	5.5	7.7	4.5
s=0.5	10.4	12.2	7.6	7.9	7.5	4.4
s=0.7	7.1	11.8	7.4	6.1	6.8	3.9
s=0.8	5.9	11.3	7.1	4.7	6.0	3.3
s=0.9	6.0	6.5	6.3	3.1	1.8	1.7

2.5.3 CPFEM Model

In contrast to the Taylor-type model and VPSC model, another texture modeling approach is to implement the crystal plasticity constitutive laws in the finite element framework. This method is called the crystal plasticity finite element method (CPFEM) model and has been recognized as the best model for simulating texture evolution during plastic deformation [61]. In the CPFEM model, local heterogeneity can be considered. Therefore, the deformation and orientation rotation of a material point depend on both its initial crystallographic orientation and the crystallographic orientations of its neighbors. According to the reports [231, 232], the main advantage of the CPFEM model is its ability to solve crystal mechanical problems under complicated internal and external boundary conditions. In addition, various constitutive formulations for plastic flow and hardening, based on not only dislocation mechanism [233, 234], but also other mechanisms such as mechanical twinning [235, 236], can be added. This could result in that one type of deformation mechanism occurs at some material points, while other deformation mechanisms or a mixed mechanism may occur at remaining material points [231]. However, the requirement of huge calculation time limits the extensive use of the CPFEM model in engineering applications.

Compared to the Taylor-type models and VPSC model, limited studies based on the CPFEM model have been conducted to investigate texture development during the ECAP process. The first application was performed by Li et al. to simulate the texture evolution in one ECAP pass of pure aluminium and copper [58]. They have evaluated the performance of the CPFEM model by comparing the simulation results with experimental measurements by neutron diffraction. At the same time, comparison with predictions by the VPSC model was also carried out, as shown in Fig. 2.23. It has been found that the CPFEM predictions agreed better with the experimental textures than those simulated using the VPSC model with or without enforcing grain co-rotation. On the other hand, Wu et al. [120] used the CPFEM model to study grain refinement and texture evolution in route C during multiple-pass of ECAP. Texture evolution in route C has also been simulated by Li et al. [57] for one to four passes, while another study examined up to 20 ECAP passes [120]. Based on the CPFEM simulations [56], the influences of the processing route

and the die channel angle on slip activities and grain refinement have been successfully explained.

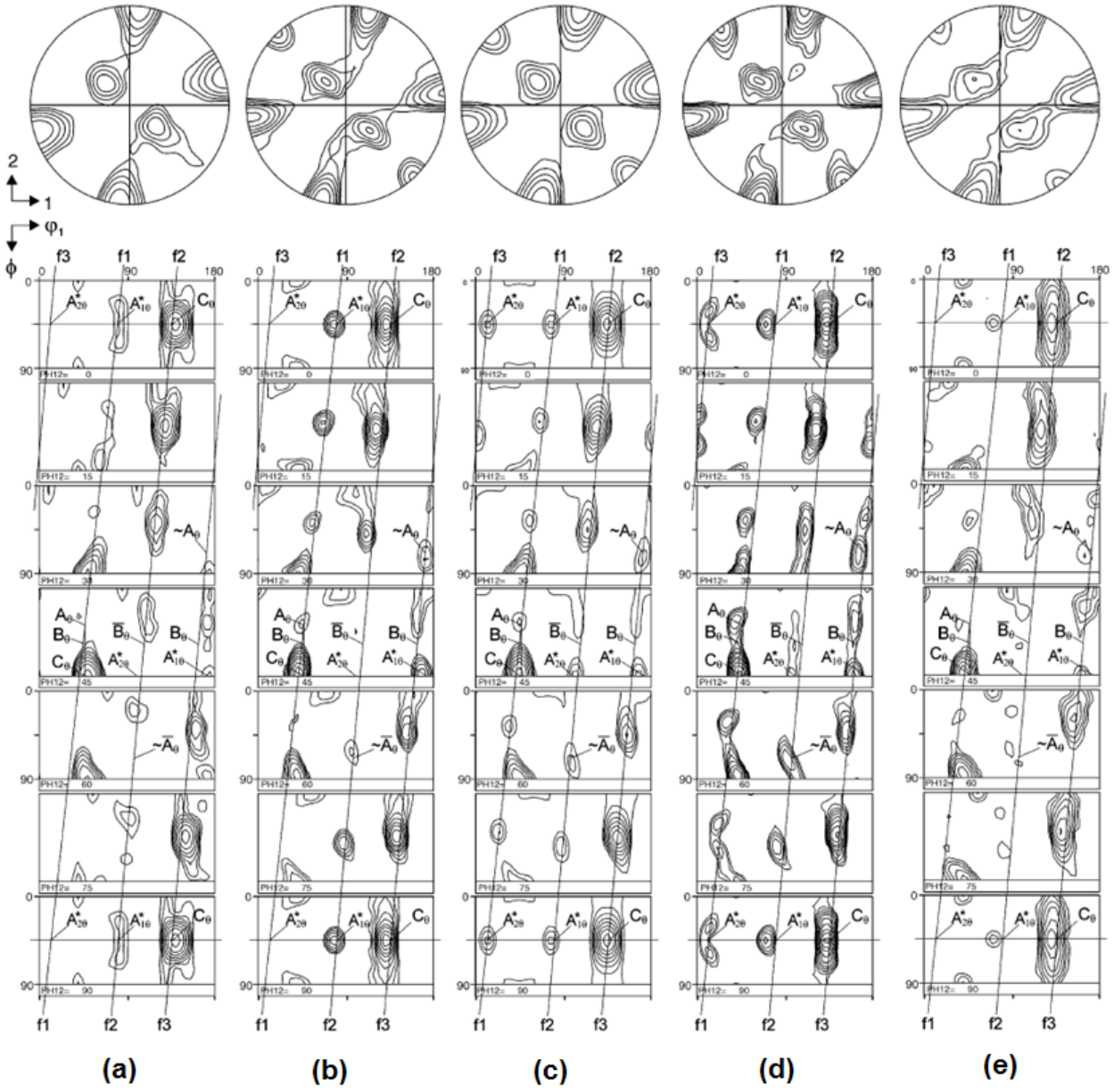

Fig. 2.23 {1 1 1} pole figures and ODFs for the textures in the Al after one pass of ECAP process: (a) experimental results, (b and c) simulated by the CPFEM model using the 1EPG and 8 EPG meshes, (d and e) simulated by the VPSC model without and with enforcing grain co-rotation [58].

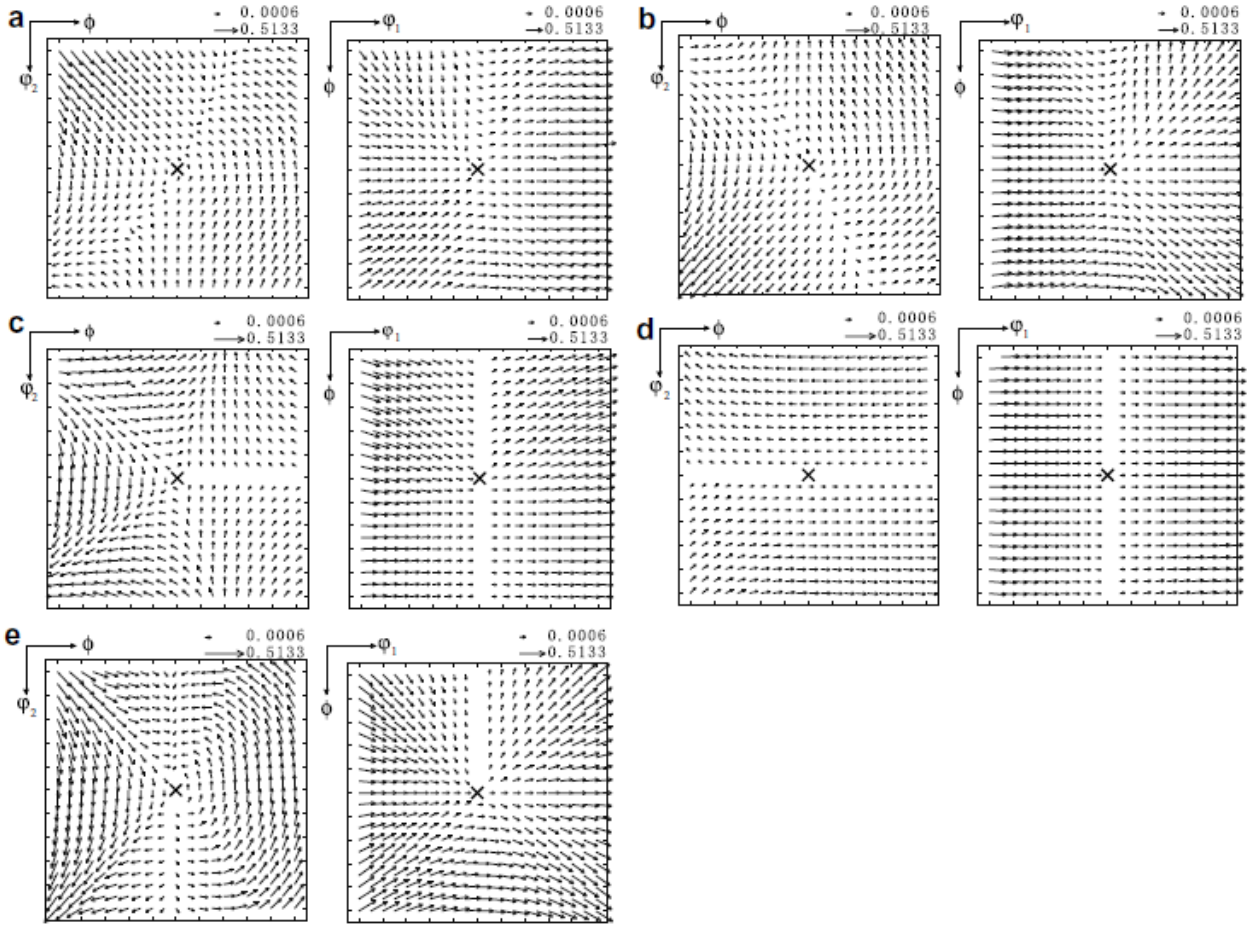

Fig. 2.24 Lattice rotation fields in the range of 20° × 20° × 20° around ideal orientations for FCC materials in ECAP deformation: (a) $A_{1\theta}^{*}$, (b) $A_{2\theta}^{*}$, (c) $A_{1\theta}^{*}$, (d) A_{θ}, (e) B_{θ}, and (f) C_{θ}. Left: phi2=constant section, and right: phi2=constant section. The direction and length of an arrow signify, respectively, the direction and magnitude of the rotation vector [167].

Recently, Li studied the orientation stability in ECAP for FCC and BCC polycrystalline materials in [167, 192] and for HCP polycrystalline materials [44] using the CPFEM model. Fig. 2.24 shows the lattice rotation fields around ideal orientations in ECAP deformation. The results revealed that the ideal orientations are meta-stable under rate-sensitive conditions, and their stability generally increases with the decrease of strain rate sensitivity. The CPFEM model was also adopted by Jung et al. [54] to investigate texture evolution and deformation heterogeneity during the ECAP process and the upsetting of pure aluminium AA1050 by implementing a rate-dependent polycrystalline theory into an in-house program, CAMPform3D. It has been found

that friction was the crucial factor to govern anisotropic deformation. Besides, Kalidindi et al. [55] conducted a CPFEM simulation and assumed that the macroscale deformation field could be represented by a set of equi-spaced streamlines. They stated that their results showed better agreement with the measuremental results compared against the other reported model in the literature when the same deformation history was used.

2.6 Summary and Research Scope of this Thesis

The ECAP process is one of the most widely used SPD techniques and is very effective in grain refinement and improving the strength of materials. The main advantage of this technique is its capability to introduce large amounts of plastic strain without changing the overall dimensions of the billets. A number of experimental researches on the microstructure evolution and texture development during the ECAP process have been conducted for a wide range of materials, including aluminium single crystals and alloys, Cu single crystals, bicrystal and alloys, interstitial-free steels, titanium alloys, magnesium alloys and so on. Many models have been developed to help understanding the deformation mechanism of the ECAP process. Simple shear along the intersecting plane of the entry channel and exit channel is the most frequently used model to represent the deformation mode during the ECAP process. In practice, a simple shear model is only suitable for the ideal conditions, including the frictionless condition, and ECAP dies with sharp angles, and perfect plastic materials. These ideal conditions are very difficult to achieve because deformation always deviates from simple shear due to the significant influences of the ECAP die channel angle, outer corner angle, inner corner angle, processing route, number of passes, frictional condition, material property, and initial crystallographic orientation, and so on.

FEM simulations have revealed the fan shaped PDZ due to the development of a dead zone in the outer corner region during the ECAP process which leads to a non-uniform plastic strain distribution, inhomogeneous grain refinement and texture evolution in the deformed billet. The dead zone obviously decreased with the increasing friction coefficient and the application of back pressure. Generally, the plastic strain in the bottom part of the billet was much lower than

the upper region after deformation. Meanwhile, many studies on the predictions of ECAP texture have also been conducted to gain a better knowledge of the texture evolutions and the influencing factors during this specific deformation technique by comparing the simulated textures with the experimental results. Generally, the predicted textures based on the FEM deformation history are stronger than those obtained by the simple shear model due to the larger shear strain component in the FEM predicted displacement gradient.

However, most of the ECAP textures in the literature have been simulated by a combination of the Taylor model or VPSC model with the deformation histories provided by the simple shear model, or the flow line model or FEM simulations, and even then they failed to capture the main features and intensities of experimental textures in the even numbered passes in Route C. Even the application of the advanced texture model, namely CPFEM model, only improved slightly compared to the VPSC model when the deformation history was predicted from the simple shear model. However, none of the CPFEM simulations of the ECAP process in the literature were carried out based on the deformation history of the real full-scale ECAP process. All these simulations have been conducted in a decoupled manner and the influence of crystallographic orientations on the strain distributions at each material point during the ECAP process has been neglected when they predict the deformation history. In practice, the simulated texture will be significantly influenced by the degree of accuracy in describing the ECAP deformation. Furthermore, the texture predictions of initial single crystals and differences in texture between two-dimensional and three-dimensional model during the ECAP process have never been reported. Studies on the influence of frictional condition, sample dimension, ECAP die geometry, processing routes and initial crystallographic orientations on the texture evolutions in single crystals are essential for these fundamental investigations.

Chapter 3 Development and Verification of the CPFEM Model

A CPFEM model has been developed in the thesis to simulate the ECAP process. This chapter presents the basic concepts of crystal plasticity theory and implementation of crystal plasticity laws into a commercial FEM framework. The experimental measured results [33, 179] have been used to validate the capability of the developed CPFEM model.

3.1 Crystal Plasticity Theory

As a general scheme of notation, vectors in the subsequent context are written as boldface lowercase letters (e.g., **a**), tensor and matrices are written as boldface capital letters (e.g., **A**). Cartesian components of vectors and tensors are written as, a_i and A_{ij}, respectively. All inner products are indicated by a single dot and the tensor product is indicated as '⊗'. The superscript '-1' of a matrix (e.g., $\mathbf{A}^{-1}$) indicates the inverse and the superscript 'T' of a matrix ((e.g., $\mathbf{A}^{T}$)) denotes the transposition of this matrix. The summation convention is used for Latin indices but summations over crystallographic slip systems are indicated explicitly. Time derivatives are denoted by superposed dots.

3.1.1 Kinematical Theory

The quantitative description of kinematical theory for the mechanics of elastic-plastic deformation of crystals stems from the early work of Taylor [205] and Hill [237], where they proposed that material flows through the crystal lattice via dislocation motion. The kinematical theory used in the present CPFEM model follows the procedures used by Asaro [238], Asaro and Rice [239], and more recently by Si and Huynh [233, 240].

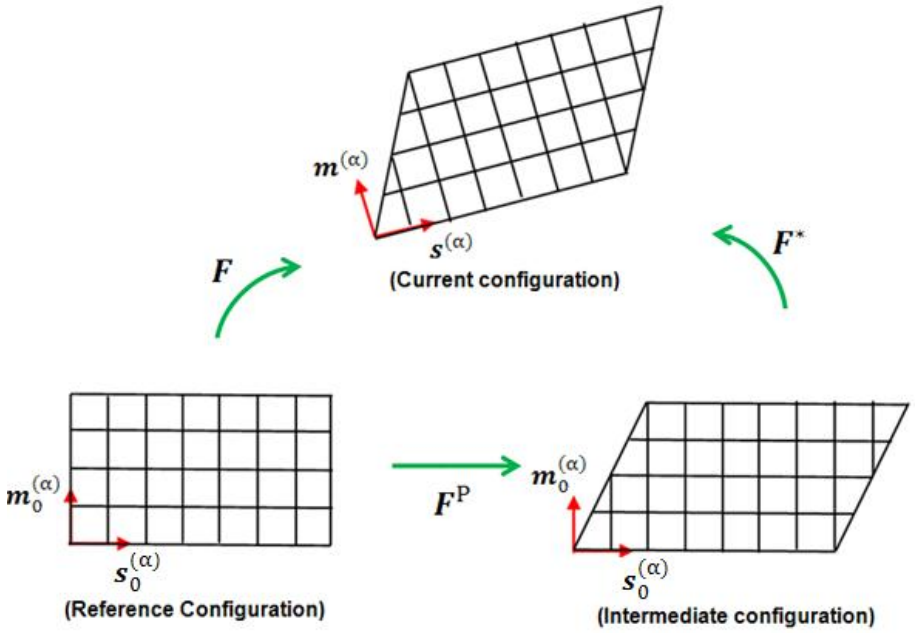

Fig. 3.1 Multiplicative decomposition of the deformation gradient $\boldsymbol{F}$ into elastic deformation part and plastic deformation part.

It has been assumed in this study that crystalline material under load undergoes a crystallographic slip due to dislocation motion on the active slip systems and elastic deformation including stretching and rotating of the crystal lattice [233, 238-243]. Three configurations are used for mathematical convenience as shown in Fig. 3.1. The initial configuration corresponds to the undeformed state of the element and the current configuration to the deformed state of the element. The intermediate configuration is obtained from the current configuration when relaxing the lattice elastic stretching and rotation. Therefore, the total deformation gradient can be decomposed into two components as

$$\boldsymbol{F} = \frac{\partial \boldsymbol{x}}{\partial \boldsymbol{X}} = \boldsymbol{F}^* \cdot \boldsymbol{F}^{\mathrm{P}} \tag{3.1}$$

where $\boldsymbol{F}$ is the total deformation gradient, $\boldsymbol{x}$ is the position of the material point in the current configuration, $\boldsymbol{X}$ is the position of material point in the initial configuration, $\boldsymbol{F}^*$ is the deformation gradient combined the stretching and rotation of the crystal lattice, and $\boldsymbol{F}^{\mathrm{P}}$ is the deformation due to plastic shearing on crystallographic slip systems and can be written as

$$\boldsymbol{F}^{\mathrm{P}} = \sum_{\alpha=1}^{\mathrm{N}} \boldsymbol{F}^{(\alpha)\mathrm{P}} = \sum_{\alpha=1}^{\mathrm{N}} \boldsymbol{I} + \gamma^{(\alpha)}\left(\boldsymbol{s}_0^{(\alpha)} \otimes \boldsymbol{m}_0^{(\alpha)}\right) \tag{3.2}$$

where $\boldsymbol{F}^{(\alpha)\mathrm{P}}$ is the contribution of α-th slip system to $\boldsymbol{F}^{\mathrm{P}}$, $\gamma^{(\alpha)}$ is the shear strain of α-th slip system, $\boldsymbol{I}$ is a second-order unit tensor and N is the number of active slip systems.

The Green strain tensor can be expressed by

$$\boldsymbol{E} = \frac{1}{2}(\boldsymbol{F}^{\mathrm{T}}\boldsymbol{F} - \boldsymbol{I}) \tag{3.3}$$

In the initial configuration, the crystal slip system α consists of a slip direction $\boldsymbol{s}_0^{(\alpha)}$ lying in a slip plane with normal vector of $\boldsymbol{m}_0^{(\alpha)}$. Both $\boldsymbol{s}_0^{(\alpha)}$ and $\boldsymbol{m}_0^{(\alpha)}$ are taken to be unit vectors and are orthogonal.

$$\boldsymbol{s}_0^{(\alpha)} \cdot \boldsymbol{m}_0^{(\alpha)} = 0 \tag{3.4}$$

They do not change during crystallographic slip from the initial configuration to the intermediate configuration but convert with the lattice when the lattice is stretched and rotated. The slip direction vector $\boldsymbol{s}_0^{(\alpha)}$ can be given in a deformed configuration by

$$\boldsymbol{s}^{(\alpha)} = \boldsymbol{F}^{*} \cdot \boldsymbol{s}_0^{(\alpha)} \tag{3.5}$$

The normal to the slip plane $\boldsymbol{m}_0^{(\alpha)}$ after deformation can be written as

$$\boldsymbol{m}^{(\alpha)} = \boldsymbol{m}_0^{(\alpha)} \cdot \boldsymbol{F}^{*-1} \tag{3.6}$$

It should be noted that $\boldsymbol{s}^{(\alpha)}$ and $\boldsymbol{m}^{(\alpha)}$ are generally not in unit vectors, but remain orthogonal.

$$\boldsymbol{s}^{(\alpha)} \cdot \boldsymbol{m}^{(\alpha)} = 0 \tag{3.7}$$

The current velocity gradient is evaluated from the deformation gradient by

$$\boldsymbol{L} = \frac{\partial \boldsymbol{v}}{\partial \boldsymbol{x}} = \frac{\partial \boldsymbol{v}}{\partial \boldsymbol{X}}\frac{\partial \boldsymbol{X}}{\partial \boldsymbol{x}} = \dot{\boldsymbol{F}}\boldsymbol{F}^{-1} = \boldsymbol{L}^{*} + \boldsymbol{L}^{\mathrm{P}} \tag{3.8}$$

$$\boldsymbol{L}^{*} = \dot{\boldsymbol{F}}^{*} \cdot \boldsymbol{F}^{*-1} \tag{3.9}$$

$$\boldsymbol{L}^{\mathrm{P}} = \boldsymbol{F}^{*} \cdot \dot{\boldsymbol{F}}^{\mathrm{P}} \cdot \boldsymbol{F}^{\mathrm{P}-1} \cdot \boldsymbol{F}^{*-1} \tag{3.10}$$

where $\boldsymbol{v}$ is the velocity of the material point, $\boldsymbol{L}^{*}$ is the elastic part of the velocity gradient and $\boldsymbol{L}^{\mathrm{P}}$ is the plastic part of the velocity gradient. $\boldsymbol{L}^{\mathrm{P}}$ is related to the shear strain rate $\dot{\gamma}^{(\alpha)}$ of the α-th slip system by

$$\boldsymbol{L}^{\mathrm{P}} = \sum_{\alpha=1}^{\mathrm{N}} \dot{\gamma}^{(\alpha)}\, \boldsymbol{s}^{(\alpha)} \otimes \boldsymbol{m}^{(\alpha)} \tag{3.11}$$

$$\boldsymbol{F}^{\mathrm{P}} = \boldsymbol{I} + \gamma^{(\alpha)} \boldsymbol{s}^{(\alpha)} \otimes \boldsymbol{m}^{(\alpha)} \tag{3.12}$$

The velocity gradient can be uniquely decomposed into a symmetrical part and a skewed-symmetrical part as

$$\boldsymbol{L} = \boldsymbol{D} + \boldsymbol{W} \tag{3.13}$$

$$\boldsymbol{D} = \frac{1}{2}(\boldsymbol{L} + \boldsymbol{L}^{\mathrm{T}}) \tag{3.14}$$

$$\boldsymbol{W} = \frac{1}{2}(\boldsymbol{L} - \boldsymbol{L}^{\mathrm{T}}) \tag{3.15}$$

where $\boldsymbol{D}$ and $\boldsymbol{W}$ are called the stretch rate tensor and spin tensor, respectively. $\boldsymbol{D}$ is generally called the rate of deformation. The tensors $\boldsymbol{D}$ and $\boldsymbol{W}$ can also be decomposed into the elastic stretching and lattice rotation part ($\boldsymbol{D}^{*}$ and $\boldsymbol{W}^{*}$), and the plastic part ($\boldsymbol{D}^{\mathrm{P}}$ and $\boldsymbol{W}^{\mathrm{P}}$), as follows:

$$\boldsymbol{D} = \boldsymbol{D}^{*} + \boldsymbol{D}^{\mathrm{P}} \tag{3.16}$$

$$\boldsymbol{W} = \boldsymbol{W}^{*} + \boldsymbol{W}^{\mathrm{P}} \tag{3.17}$$

The components of the two tensors ($\boldsymbol{D}$ and $\boldsymbol{W}$) can be expressed by the velocity $\boldsymbol{v}$ and the coordinate $\boldsymbol{x}$ as,

$$D_{\mathrm{ij}} = \frac{1}{2}\left(\frac{\partial v_{\mathrm{i}}}{\partial x_{\mathrm{j}}} + \frac{\partial v_{\mathrm{j}}}{\partial x_{\mathrm{i}}}\right) \tag{3.18}$$

$$W_{\mathrm{ij}} = \frac{1}{2}\left(\frac{\partial v_{\mathrm{i}}}{\partial x_{\mathrm{j}}} - \frac{\partial v_{\mathrm{j}}}{\partial x_{\mathrm{i}}}\right) \tag{3.19}$$

According to Equations (3.8), (3.10), (3.16) and (3.17), $\boldsymbol{L}^{\mathrm{P}}$ can be derived as

$$\boldsymbol{L}^{\mathrm{P}} = \boldsymbol{D}^{\mathrm{P}} + \boldsymbol{W}^{\mathrm{P}} = \boldsymbol{F}^{*} \cdot \dot{\boldsymbol{F}}^{\mathrm{P}} \cdot \boldsymbol{F}^{\mathrm{P}-1} \cdot \boldsymbol{F}^{*-1} \tag{3.20}$$

And then $\boldsymbol{D}^{\mathrm{P}}$ in Equation (3.16) and $\boldsymbol{W}^{\mathrm{P}}$ in Equation (3.17) can be expressed as

$$\boldsymbol{D}^{\mathrm{P}} = \sum_{\alpha=1}^{\mathrm{N}} \boldsymbol{p}^{(\alpha)} \dot{\gamma}^{(\alpha)} \tag{3.21}$$

where $\boldsymbol{p}^{(\alpha)}$ has been defined as

$$\boldsymbol{p}^{(\alpha)} = \frac{1}{2}\left(\boldsymbol{s}^{(\alpha)} \otimes \boldsymbol{m}^{(\alpha)} + \boldsymbol{m}^{(\alpha)} \otimes \boldsymbol{s}^{(\alpha)}\right) \tag{3.22}$$

Similar to $\boldsymbol{D}^{\mathrm{P}}$, the tensor $\boldsymbol{W}^{\mathrm{P}}$ in Equation (3.17) can also be expressed as

$$\boldsymbol{W}^{\mathrm{P}} = \sum_{\alpha=1}^{\mathrm{N}} \boldsymbol{q}^{(\alpha)} \dot{\gamma}^{(\alpha)} \tag{3.23}$$

where $\boldsymbol{q}^{(\alpha)}$ has been defined as

$$\boldsymbol{q}^{(\alpha)} = \frac{1}{2}\left(\boldsymbol{s}^{(\alpha)} \otimes \boldsymbol{m}^{(\alpha)} - \boldsymbol{m}^{(\alpha)} \otimes \boldsymbol{s}^{(\alpha)}\right) \tag{3.24}$$

For convenience, $\boldsymbol{s}^{(\alpha)} \otimes \boldsymbol{m}^{(\alpha)}$ is usually called the Schmid factor. Therefore, $\boldsymbol{p}^{(\alpha)}$ and $\boldsymbol{q}^{(\alpha)}$ are the symmetrical and asymmetrical part of the Schmid factor, respectively.

The derivatives of Equations (3.5) and (3.6) yield

$$\dot{\boldsymbol{s}}^{(\alpha)} = \boldsymbol{L}^{*} \boldsymbol{s}^{(\alpha)} \tag{3.25}$$

$$\dot{\boldsymbol{m}}^{(\alpha)} = -\boldsymbol{m}^{(\alpha)} \boldsymbol{L}^{*} \tag{3.26}$$

By differentiating Equation (3.3), the rate of change of Green's Lagrangian strain can be written as

$$\dot{\boldsymbol{E}} = \frac{1}{2}\left(\dot{\boldsymbol{F}}^{\mathrm{T}} \boldsymbol{F} + \boldsymbol{F}^{\mathrm{T}} \dot{\boldsymbol{F}}\right) = \boldsymbol{F}^{\mathrm{T}} \boldsymbol{D} \boldsymbol{F} \tag{3.27}$$

According to the polar decomposition theory, the deformation gradient $\boldsymbol{F}$ in Equation (3.1) can be expressed by two alternative forms as

$$\boldsymbol{F} = \boldsymbol{R}\boldsymbol{U} \tag{3.28}$$

$$\boldsymbol{F} = \boldsymbol{V}\boldsymbol{R} \tag{3.29}$$

where $\boldsymbol{R}$ is the orthogonal rotation tensor, $\boldsymbol{U}$ is the right stretch tensor, $\boldsymbol{V}$ is the left stretch tensor. Both tensors $\boldsymbol{U}$ and $\boldsymbol{V}$ are positive definite symmetric tensors. And they satisfy the condition of

$$\boldsymbol{R}^{\mathrm{T}} = \boldsymbol{R}^{-1} \tag{3.30}$$

$$\boldsymbol{U} = \boldsymbol{U}^{\mathrm{T}} \tag{3.31}$$

Therefore, $\boldsymbol{W}$ in Equations (3.14) and (3.16) can be expressed as

$$\boldsymbol{W} = \dot{\boldsymbol{R}}\boldsymbol{R}^{-1} \tag{3.32}$$

And then $\boldsymbol{R}$ can be expressed by

$$\boldsymbol{R} = \left(\boldsymbol{I} + \tfrac{1}{2}\boldsymbol{W}\Delta\mathrm{t}\right)\left(\boldsymbol{I} - \tfrac{1}{2}\boldsymbol{W}\Delta\mathrm{t}\right)^{-1} \tag{3.33}$$

where Δt is the time increment. Accordingly, Equation (3.32) can also be expressed as

$$\boldsymbol{W} = \tfrac{2}{\Delta\mathrm{t}}(\boldsymbol{R} - \boldsymbol{I})(\boldsymbol{R} - \boldsymbol{I})^{-1} \tag{3.34}$$

3.1.2 Constitutive Equations

It has been assumed that the crystal's elasticity is unaffected by slip. According to the description of Hill and Rice, the elastic constitutive law takes the form

$$\overset{\nabla}{\boldsymbol{t}^*} = \boldsymbol{C} : \boldsymbol{D}^* \tag{3.35}$$

$$\boldsymbol{C} = (\boldsymbol{R}_{\mathrm{L}} \otimes \boldsymbol{R}_{\mathrm{L}}) \cdot \boldsymbol{C}_0 \cdot \left(\boldsymbol{R}_{\mathrm{L}}^{\mathrm{T}} \otimes \boldsymbol{R}_{\mathrm{L}}^{\mathrm{T}}\right) \tag{3.36}$$

where $\boldsymbol{C}$ is the fourth order tensor of the elastic modulus, $\overset{\nabla^*}{\boldsymbol{t}}$ is the Jaumann rate of Kirchoff stress. It has been assumed that $\boldsymbol{t}_0$ is the Kirchhoff stress in the reference configuration at a time t+Δt, and it is also the Kirchhoff stress in the current configuration at a time t. According to the description in Section 3.1.1, deformation occurs first by crystallographic slip from the reference configuration to the intermediate configuration, and then lattice stretching and rotation from the intermediate configuration to the current configuration. It is assumed that

the change in stress caused by the slip and lattice stretching is $\dot{\boldsymbol{t}}_0\Delta t$, where $\dot{\boldsymbol{t}}_0$ is the stress rate in the reference configuration. The stress $\boldsymbol{t}_0 + \dot{\boldsymbol{t}}_0\Delta t$ will be rotated to the current configuration. The rotation tensor is $\boldsymbol{R}$. The Kirchhoff stress $\boldsymbol{t}$ in the configuration can be expressed by

$$\boldsymbol{t} = \boldsymbol{R}(\boldsymbol{t}_0 + \dot{\boldsymbol{t}}_0\Delta t)\boldsymbol{R}^{\mathrm{T}} \tag{3.37}$$

Taking the time derivative of Equation (3.33) it can be obtained as

$$\dot{\boldsymbol{t}} = \boldsymbol{R}\dot{\boldsymbol{t}}_0\boldsymbol{R}^{\mathrm{T}} + \dot{\boldsymbol{R}}(\boldsymbol{t}_0 + \dot{\boldsymbol{t}}_0\Delta t)\boldsymbol{R}^{\mathrm{T}} + \boldsymbol{R}(\boldsymbol{t}_0 + \dot{\boldsymbol{t}}_0\Delta t)\boldsymbol{R}^{\mathrm{T}} = \boldsymbol{R}\dot{\boldsymbol{t}}_0\boldsymbol{R}^{\mathrm{T}} + \boldsymbol{W}\boldsymbol{t} - \boldsymbol{t}\boldsymbol{W} \tag{3.38}$$

where $\dot{\boldsymbol{t}}$ is the material rate of Kirchhoff stress. $\boldsymbol{R}\dot{\boldsymbol{t}}_0\boldsymbol{R}^{\mathrm{T}}$ is defined as the Jaumann rate of Kirchhoff stress ($\overset{\nabla}{\boldsymbol{t}}$) on axes that rotate with the material. Therefore, Equation (3.34) can be written as

$$\overset{\nabla}{\boldsymbol{t}} = \dot{\boldsymbol{t}} - \boldsymbol{W}\boldsymbol{t} + \boldsymbol{t}\boldsymbol{W} \tag{3.39}$$

If deformation from the intermediate to the current configuration alone is taken into account then Equation (3.35) can be rewritten as

$$\overset{\nabla}{\boldsymbol{t}^*} = \dot{\boldsymbol{t}} - \boldsymbol{W}^*\boldsymbol{t} + \boldsymbol{t}\boldsymbol{W}^* = \boldsymbol{R}\dot{\boldsymbol{t}}_1^*\boldsymbol{R}^{\mathrm{T}} \tag{3.40}$$

where $\overset{\nabla}{\boldsymbol{t}^*}$ is the Jaumann rate of Kirchhoff stress on axes that rotate with the lattice and $\dot{\boldsymbol{t}}_1^*$ is the rate of the Kirchhoff stress in the intermediate configuration.

The difference between Equations (3.35) and (3.36) can be obtained as

$$\overset{\nabla}{\boldsymbol{t}^*} - \overset{\nabla}{\boldsymbol{t}} = \sum_{\alpha=1}^{\mathrm{N}} \boldsymbol{\beta}^{(\alpha)}\dot{\gamma}^{(\alpha)} \tag{3.41}$$

where $\boldsymbol{\beta}^{(\alpha)}$ is defined by

$$\boldsymbol{\beta}^{(\alpha)} = \boldsymbol{W}^{(\alpha)}\boldsymbol{t} - \boldsymbol{t}\boldsymbol{W}^{(\alpha)} \tag{3.42}$$

The lattice is elastically stretched along the lattice axis. The lattice stretching can be described in the lattice coordinate system by

$$\dot{\boldsymbol{t}}_{\mathrm{L}} = \boldsymbol{C}_0 : \boldsymbol{D}_{\mathrm{L}} \tag{3.43}$$

where $\dot{\boldsymbol{t}}_{\mathrm{L}}$ is the material rate of the Kirchhoff stress in the lattice coordinate system, $\boldsymbol{D}_{\mathrm{L}}$ is the rate of the elastic stretching in the lattice coordinate system, $\boldsymbol{C}_0$ is the elastic moduli tensor.

Provided the rotation tensor between the lattice coordinate system and the current configuration is $\boldsymbol{R}_{\mathrm{L}}$, the elastic deformation rate $\boldsymbol{D}^*$ in the current configuration can be linked to $\boldsymbol{D}_{\mathrm{L}}$ by the following equation

$$\boldsymbol{D}^* = \boldsymbol{R}_{\mathrm{L}} \boldsymbol{D}_{\mathrm{L}} \boldsymbol{R}_{\mathrm{L}}^{\mathrm{T}} \tag{3.44}$$

The rate of Kirchhoff stress in the intermediate configuration can be expressed by

$$\dot{\boldsymbol{t}}_1^* = \boldsymbol{R}^{\mathrm{T}} \boldsymbol{R}_{\mathrm{L}} \dot{\boldsymbol{t}}_{\mathrm{L}} \boldsymbol{R}_{\mathrm{L}}^{\mathrm{T}} \boldsymbol{R} \tag{3.45}$$

Therefore, according to Equations (3.27) and (3.42), the Jaumann rate $\overset{\nabla}{\boldsymbol{t}}^*$ in Equation (3.37) can be written as

$$\overset{\nabla}{\boldsymbol{t}}^* = \boldsymbol{R}_{\mathrm{L}} \dot{\boldsymbol{t}}_{\mathrm{L}} \boldsymbol{R}_{\mathrm{L}}^{\mathrm{T}} \tag{3.46}$$

Equations (3.41) and (3.43) can be rewritten as

$$\boldsymbol{D}_{\mathrm{L}} = \left(\boldsymbol{R}_{\mathrm{L}}^{\mathrm{T}} \otimes \boldsymbol{R}_{\mathrm{L}}^{\mathrm{T}}\right) : \boldsymbol{D}^* \tag{3.47}$$

$$\dot{\boldsymbol{t}}_{\mathrm{L}} = \left(\boldsymbol{R}_{\mathrm{L}}^{\mathrm{T}} \otimes \boldsymbol{R}_{\mathrm{L}}^{\mathrm{T}}\right) : \overset{\nabla}{\boldsymbol{t}}^* \tag{3.48}$$

Substituting Equations (3.44) and (3.45) into Equation (3.40) yields Equation (3.32).

According to Equations (3.32) and (3.37), we can have

$$\overset{\nabla}{\boldsymbol{t}} = \boldsymbol{C} : \boldsymbol{D} - \sum_{\alpha=1}^{\mathrm{N}} \left(\boldsymbol{C} : \boldsymbol{p}^{(\alpha)} + \boldsymbol{\beta}^{(\alpha)}\right) \dot{\gamma}^{(\alpha)} \tag{3.49}$$

It was assumed that slip is the only plastic deformation mechanism. The resolved shear stress on each slip system can be used as the vital variable to evaluate plastic flow. The resolved shear stress $\tau^{(\alpha)}$ can be calculated from

$$\tau^{(\alpha)} = \boldsymbol{p}^{(\alpha)} : \boldsymbol{t} \tag{3.50}$$

Taking the time derivative gives

$$\dot{\tau}^{(\alpha)} = \left(\boldsymbol{C} : \boldsymbol{P}^{(\alpha)} + \boldsymbol{\beta}^{(\alpha)}\right) : (\boldsymbol{D} - \sum_{\beta=1}^{N} \boldsymbol{p}^{(\beta)} \dot{\gamma}^{(\beta)}) \tag{3.51}$$

The relationship of the Cauchy stress $\boldsymbol{\sigma}$ and the Kirchhoff stress is

$$\boldsymbol{t} = \mathrm{J}\boldsymbol{\sigma} \tag{3.52}$$

and J is defined as

$$\mathrm{J} = \frac{1}{|\boldsymbol{F}|} \tag{3.53}$$

Therefore, the constitutive law based on Cauchy stress can be expressed as

$$\boldsymbol{\sigma} = \boldsymbol{R}\left(\boldsymbol{\sigma}_0\left(1 + \mathrm{tr}(\boldsymbol{D})\right)\right)\boldsymbol{R}^{\mathrm{T}} + \overset{\nabla}{\boldsymbol{\sigma}_0}\Delta \mathrm{t} \tag{3.54}$$

$$\overset{\nabla}{\boldsymbol{\sigma}} = \boldsymbol{C} : \boldsymbol{D} - \mathrm{tr}(\boldsymbol{D})\boldsymbol{\sigma} - \sum_{\alpha=1}^{N}(\boldsymbol{C} : \boldsymbol{p}^{(\alpha)} + \boldsymbol{W}^{(\alpha)}\boldsymbol{\sigma} - \boldsymbol{\sigma}\boldsymbol{W}^{(\alpha)})\dot{\gamma}^{(\alpha)} \tag{3.55}$$

$$\dot{\tau}^{(\alpha)} = \left(\boldsymbol{C} : \boldsymbol{p}^{(\alpha)} + \boldsymbol{W}^{(\alpha)}\boldsymbol{\sigma} - \boldsymbol{\sigma}\boldsymbol{W}^{(\alpha)}\right) : (\boldsymbol{D} - \sum_{\beta=1}^{N} \boldsymbol{p}^{(\beta)} \dot{\gamma}^{(\beta)}) \tag{3.56}$$

3.1.3 Hardening Model

The rate-dependent theory has been extensively and successfully applied in crystal plasticity studies to overcome the long standing problem of non-uniqueness in the choice of the active slip systems which are inherent in conventional rate-independent theory [233, 238, 239, 241-245]. The rate-dependent power law was first introduced by Hutchinson [246] in 1976 to study the steady creep properties of face centered cubic and ionic polycrystals. Since then it has been successfully used by Asaro [238, 242], Asaro and Needleman [243], and Toth [244], in their researches. It has been noted by Peirce et al. [241] that the rate-independent plasticity can be treated as the limit of rate-dependent plasticity. This study follows the above mentioned rate-dependent power law, which relates the resolved shear stress $\tau^{(\alpha)}$ to the shear strain rate $\dot{\gamma}^{(\alpha)}$ on a slip system identified by the index α, as follows:

$$\dot{\gamma}^{(\alpha)} = \dot{\gamma}_0^{(\alpha)} \mathrm{sgn}(\tau^{(\alpha)}) \left| \frac{\tau^{(\alpha)}}{\tau_c^{(\alpha)}} \right|^n \tag{3.57}$$

and

$$\mathrm{sgn}(x) = \begin{cases} -1, & x < 1 \\ 1, & x \geq 1 \end{cases} \tag{3.58}$$

where $\dot{\gamma}_0^{(\alpha)}$ is the reference value of the shear strain rate which is taken to be a constant for all slip systems. n denotes the rate sensitive exponent and the rate insensitivity limit is n →infinit. Both parameters $\dot{\gamma}_0^{(\alpha)}$ and n are the material characters. Parameter $\tau_c^{(\alpha)}$ is a variable used to describe the current strength of the slip syatem α.

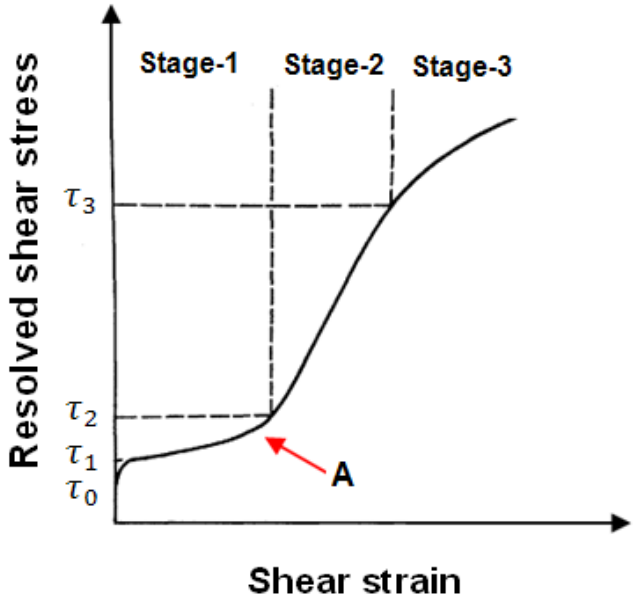

Fig. 3.2 A typical curve of resolved shear stress versus shear strain in a slip system for a FCC single crystal. (Point 'A' denotes where secondary slip commences) [247]

Fig. 3.2 shows a typical shear stress and shear strain curve for a FCC crystal with the tensile axis oriented with a standard triangle, and where it reflects three different stages [247]. Stage-1 is the easy glide stage where the corresponding hardening rate is very low and almost constant. By contrast, Stage-2 is a rapid hardening stage where the hardening rate is also almost constant, but much higher than in Stage-1. Stage-3 is a parabolic hardening region where the hardening

rate decreases continuously until fracture occurs [247]. According to Basinski et al. [248], layered structures are formed in Stage-1 while more cell structures develop in Stage-3. To complete the hardening model, the rate of hardening of the critical resolved shear stress on each slip system is assumed to be a linear combination of the shear strain rates on all systems as

$$\dot{\tau}_{\mathrm{c}}^{(\alpha)} = \sum_{\beta=1}^{\mathrm{N}} h_{\alpha\beta}\dot{\gamma}^{(\beta)} \tag{3.59}$$

The self-hardening and latent hardening moduli are shown in Equations (3.60) and (3.61) as

$$h_{\alpha\alpha} = \left[(h_0 - h_{\mathrm{s}})\mathrm{sech}^2\left(\frac{(h_0-h_{\mathrm{s}})\gamma^{(\alpha)}}{\tau_1-\tau_0}\right) + h_{\mathrm{s}}\right]\left[1 + \sum_{\substack{\beta=1;\\ \beta\neq\alpha}}^{\mathrm{N}} f_{\alpha\beta}\tanh\left(\frac{\gamma^{(\beta)}}{\gamma_0}\right)\right] \tag{3.60}$$

$$h_{\alpha\beta} = q h_{\alpha\alpha} \text{ for } \alpha=\beta \tag{3.61}$$

$h_{\alpha\beta}$ is instantaneous hardening moduli that include the self-hardening of each system (α=β) and latent hardening (α≠β). The parameter q is a latent hardening parameter and γ_0 is the reference value of slip. γ is the shear strain and τ_0 is the initial critical resolved shear stress. τ_1 is the breakthrough stress where large plastic flow begins and h_0 is the hardening modulus just after the initial yield, while h_{s} is the hardening modulus during easy glide. Parameter $f_{\alpha\beta}$ represents the magnitude of the strength of a particular slip interaction between two slip systems α and β and it depends on the geometric relationship between two slip systems. The factors $f_{\alpha\beta}$ are given in terms of five constants [247]:

(i) a_1 (no junction): the resultant Burgers vector from slip systems α and β is parallel to the original one;

(ii) a_2 (Hirth lock): the resultant Burgers vector is not energetically admissible;

(iii) a_3 (coplanar junction): the resultant Burgers vector is on the same slip plane as the original ones;

(iv) a_4 (glissile junction): the resultant Burgers vector is energetically admissible and on one of the two slip planes;

(v) a_5 (sessile junction): the resultant Burgers vector is energetically admissible but not on either of the two slip planes;

3.2 Development of the CPFEM Model

3.2.2 Fundamental Equations of FEM

It is well known that the equilibrium for problems neglecting the body forces can be expressed by the virtual work principle in rate form

$$\int_V \boldsymbol{\sigma} : \delta\mathbf{D}\mathrm{d}V = \int_S \mathbf{f} \cdot \delta\mathbf{v}\mathrm{d}S \tag{3.62}$$

where V is the volume of the solid body in the current configuration; S is the bounding surface of the volume V; σ is the Cauchy stress; f is the surface traction per unit of the current area; δv is the kinematically admissible virtual velocity field and δD is the virtual form of the rate of deformation.

According to FEM theory, a solid body is divided into n elements, where each element is associated with m nodal points. The velocity field in each element is interpolated by interpolation functions $\mathbf{N}$ (shape functions), which link the velocity field ($\boldsymbol{v}$) to the nodal velocities ($\boldsymbol{v}^{\mathrm{n}}$) as follws,

$$\boldsymbol{v} = \mathbf{N}\boldsymbol{v}^{\mathrm{n}} \tag{3.63}$$

The deformation rate $\boldsymbol{D}$ and spin tensor $\boldsymbol{W}$ can be expressed as

$$\boldsymbol{D} = \boldsymbol{B}\boldsymbol{v}^{\mathrm{n}} \tag{3.64}$$

$$\boldsymbol{W} = \boldsymbol{G}\boldsymbol{v}^{\mathrm{n}} \tag{3.65}$$

$\boldsymbol{B}$ and $\boldsymbol{G}$ are the symmetrical part and the skewed part of the coefficient matrix of velocity gradient, respectively.

Therefore, the equilibrium equation (Equation (3.)) can be rewritten as

$$\int_V \mathbf{B}^T \boldsymbol{\sigma} dV : \delta \mathbf{v}^n = \int_S \mathbf{N}^T \mathbf{f} dS : \delta \mathbf{v}^n \tag{3.66}$$

Accordingly, the constitutive relationship for the rate-dependent materials can be described in incremental form as follows

$$\overset{\nabla}{\boldsymbol{\sigma}} = \boldsymbol{H} : \boldsymbol{D} \tag{3.67}$$

$\boldsymbol{H}$ is the fourth order hardening parameter tensor. The derivative of the Cauchy stress with respect to $\boldsymbol{v}^n$ can be calculated as follows

$$\frac{d\boldsymbol{\sigma}}{d\boldsymbol{v}^n} = \frac{d\overset{\nabla}{\boldsymbol{\sigma}}}{d\boldsymbol{v}^n} + \frac{d\boldsymbol{W}}{d\boldsymbol{v}^n}\boldsymbol{\sigma} - \boldsymbol{\sigma}\frac{d\boldsymbol{W}}{d\boldsymbol{v}^n} \tag{3.68}$$

The Jacobian matrix ($\boldsymbol{K}$) can be expressed as

$$\mathbf{K} = \int_V \mathbf{B}^T (\mathbf{G}\boldsymbol{\sigma} - \boldsymbol{\sigma}\mathbf{G} + \mathbf{H} : \mathbf{B}) dV - \int_S \mathbf{N}^T \mathbf{T} dS \tag{3.69}$$

The hardening parameter tensor $\boldsymbol{H}$ must be calculated based on the constitutive law to determine $\boldsymbol{K}$.

3.2.2 Implementation of Crystal Plasticity Theory in FEM

In this study, the crystal plasticity constitutive model is implemented into the implicit finite element code Abaqus/Standard using the user material subroutine (UMAT), where the material properties can be defined and the data can be exchanged with Abaqus [249] UMAT has two functions. The first one is to make sure that the stress state of the material is at the current increment and calculate all state variables. The second function is to calculate the Jacobian matrix of the current material configuration. The stability and rate of convergence are significantly influenced by the material constitutive model.

In the developed CPFEM model, the following seven groups of data need to be provided in the input file [250]:

(i) Elastic moduli of materials;

(ii) Number of sets of potentially activated slip systems considered;

(iii) Initial crystallographic orientations in the sample coordinate system;

(iv) Shear strain rate depending on the resolved shear stress and current strength;

(v) Self and latent hardening moduli;

(vi) The forward gradient time integration parameter and the parameter determining whether the small deformation theory or the theory of finite strain and finite rotation is used in the analysis;

(vii) Parameters for the iteration method;

The loading history has been divided into many steps where deformation is assumed to be static in each step. When the UMAT is first called, the step will be initialized and the orientation and slip systems will be defined. The linear system within the iterative Newton-Raphson scheme is solved using LU decomposition. At the starting time t of the incremental step the stresses, logarithmic strains, rotation increments, time increment and solution dependent variables are provided. Then the slip systems will be determined according to the input parameters and the spin tensor will be calculated. Then the slip direction and normal of the slip plane will be calculated. Accordingly, all the variables and Jacobian matrix can be obtained by the related equations, as shown in Section 3.1. All the values of state variables will be updated and transferred to the next step if the Jacobian matrix converges, and then the iteration of the next increment will be calculated. Otherwise, the time increment will be estimated and iterated. This procedure will be repeated and finally terminated until the deformation is finished.

3.3 Verification of the developed CPFEM Model

Two-dimensional CPFEM simulations of the ECAP process of aluminium and copper single crystals have been carried out. In order to verify the developed CPFEM model for the ECAP process, the simulated textures will be compared with the experimental results.

3.3.1 ECAP of Aluminium Single Crystal

(*This part has already been published in Acta Materialia (2011)*)

An aluminium single crystal was processed by the ECAP process in a recent work [33]. The experimental ECAP die has a square cross-section with dimensions of 4 × 4 mm^2, 90° die channel angle and 30° outer corner angle. The initial crystallographic orientation of the aluminium single crystal is an ideal shear texture component 'A', which means the slip plane (-1 -1 -1) is parallel to the theoretical shear plane of the ECAP die and the slip direction [-1 1 0] is parallel to the theoretical shear direction, respectively.

In order to save computing time, a two-dimensional CPFEM simulation is conducted to model the above mentioned experiment with assumption of plane strain condition on the central plane of the sample. The ECAP die geometry used in Ref. [33] is set in the CPFEM model, as illustrated in Fig. 3.3. During FEM simulation the punch and die channels are considered as rigid bodies and the sample is defined as deformable body. The sample has an initial rectangular geometry of 23.2 (in length) × 4 (in width) mm^2 and it is meshed into 6369 plane strain four-node elements (element id: CPE4R), with 33 elements along the width of sample, as shown in Fig. 3.3. The coordinate system is also depicted in the figure, namely the X, Y, and Z axis representing the extrusion direction (ED), normal (or vertical) direction (ND) and transverse direction (TD), respectively. It should be noted that the coordinate system in the experiment [33] was left-hand, while the system in the present study is right-hand. During the ECAP process, a constant processing velocity of 2.4 mm/s along the –Y axis is applied. The frictional condition between the sample and the ECAP die is considered by setting the coefficient of friction μ=0.1 according to the study by Li and co-authors [142].

Table 3.1 The strain rate sensitivity component and parameters of aluminium single crystal used in the hardening model as Equation (3.60).

n	$\dot{\gamma}_0$ (s^{-1})	h_0 (MPa)	h_s (MPa)	τ_1 (MPa)	τ_0 (MPa)
300	0.0001	100	0.01	6.3	6

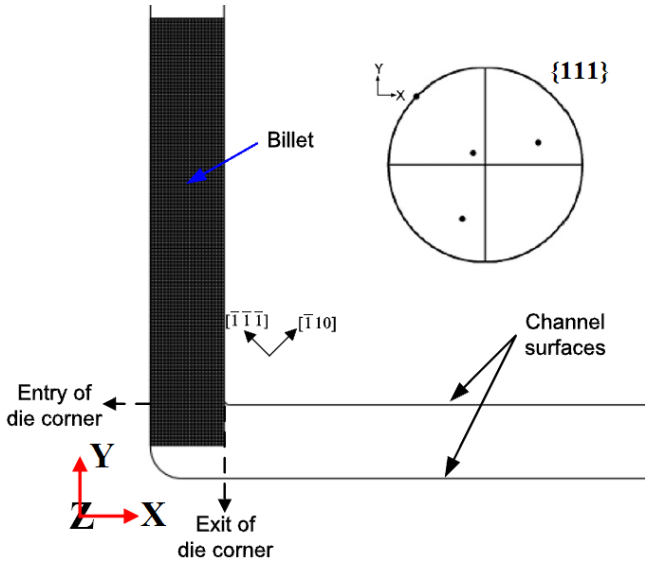

Fig. 3.3 Geometry of the ECAP die, initial mesh and {1 1 1} pole figure of aluminium single crystal used in this simulation.

The simulated material is an aluminium single crystal with an identical initial crystallographic orientation to the experiment, as shown in Fig. 3.3 in terms of the {1 1 1} pole figure. According to the study by Franciosi et al. [251], the factors $f_{\alpha\beta}$ for aluminium in the Equation (3.22) are set as: a1=a2=a3=1.75, a4=2, and a5=2.25. The other material parameters used in the hardening model are listed in Table 3.1. They are evaluated by fitting the simulated stress-strain curve with the experimental results under plane strain compression. The elastic moduli tensor for aluminium has been expressed as

$$C_{ij} = \begin{bmatrix} C_{11} & C_{12} & C_{12} & 0 & 0 & 0 \\ C_{12} & C_{11} & C_{12} & 0 & 0 & 0 \\ C_{12} & C_{12} & C_{11} & 0 & 0 & 0 \\ 0 & 0 & 0 & C_{44} & 0 & 0 \\ 0 & 0 & 0 & 0 & C_{44} & 0 \\ 0 & 0 & 0 & 0 & 0 & C_{44} \end{bmatrix} \tag{3.70}$$

where C_{11}=112000 MPa, C_{12}=112000 MPa, and C_{44}=112000 MPa, respectively. In the deformed materials with FCC structure, it is assumed that slips occur on the {1 1 1} slip planes along the

<1 1 0> slip directions. Their combination defines 12 different slip systems as indicated in the Table 3.2.

Table 3.2 Notations of the slip systems for the FCC materials considered in this study.

Number	Slip system	Slip plane	Slip direction
1	a1	(1 1 1)	[0 -1 1]
2	a2	(1 1 1)	[1 0 -1]
3	a3	(1 1 1)	[-1 1 0]
4	b1	(-1 1 1)	[1 0 1]
5	b2	(-1 1 1)	[1 1 0]
6	b3	(-1 1 1)	[0 -1 1]
7	c1	(1 -1 1)	[0 1 1]
8	c2	(1 -1 1)	[1 1 0]
9	c3	(1 -1 1)	[1 0 -1]
10	d1	(1 1 -1)	[0 1 1]
11	d2	(1 1 -1)	[1 0 1]
12	d3	(1 1 -1)	[-1 1 0]

The simulation is terminated when the majority of the aluminium single crystal has passed through the intersecting zone of the entry channel and exit channel. Simulation is performed using the HPC cluster of the University of Wollongong and the computing time has been compared using different number of CPU at the same time. It has been found that the application of four CPUs at the same time is the best choice which takes about 150 hours to finish this simulation. Ref. [33] reported the measured {1 1 1} pole figures for four selected positions labeled as 1-4 in their deformed sample. To validate the developed CPFEM model for the ECAP process of aluminium single crystal, the {1 1 1} pole figures based on the simulation results at the similar positions are plotted and compared in Fig. 3.4. Those positions 1-4 in the experiment [33] are denoted as Positions P1 – P4 in Fig. 3.4.

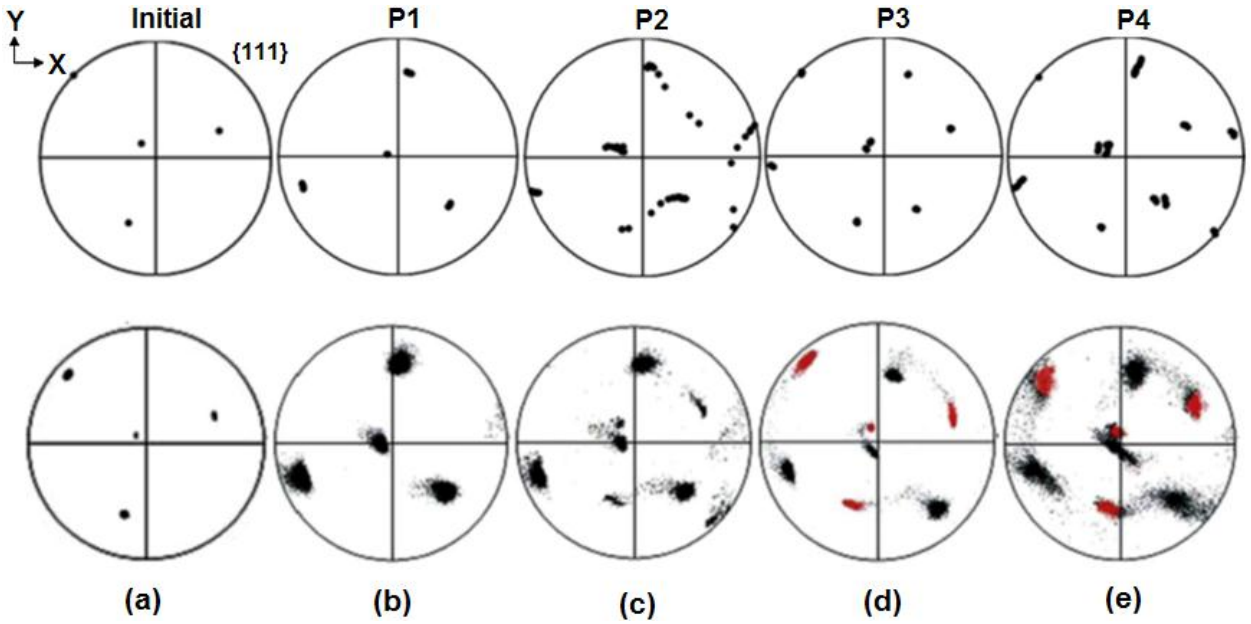

Fig. 3.4 Comparisons of the {1 1 1} pole figures between the CPFEM simulation and experimental measurements (upper panel: simulation results; lower panel: experiment results [33]): (a) Initial crystallographic orientation, (b) Position P1, (c) Position P2, (d) Position P3, and (e) Position P4.

Fig. 3.4(a) shows the initial crystallographic orientations used in the simulation and experiment while Fig. 3.4(b-e) shows that the simulated pole figures have captured all the features shown in the experimentally measured pole figures. It should be mentioned that there is much less resolution in the simulated pole figures than in the measured ones because the dimension of the elements is much larger than the resolution used in the experiment [33]. In Fig. 3.4(b) for Position P1, the structure remains a single crystal and the crystallographic orientation is rotated from the initial orientation. Fukuda et al. [33] interpreted that the rotation angle was about 60° around the Z axis (Y axis in their paper) in the counter-clockwise sense. This rotation angle is confirmed by this simulation. The pole figure measured at Position P2 reveals a strong rotated component together with a weak initial crystallographic orientation. The simulation predicts both crystallographic orientations at almost the same positions in the pole figure. The initial crystallographic orientation and the rotated orientation can also be seen in the measured and predicted pole figures at Positions P3 and P4. The good agreement between the simulation and the experiment demonstrates that the CPFEM model of the ECAP process in this study can predict accurate textures for the aluminium single crystal.

3.3.2 ECAP of Copper Single Crystal

(*This part has already been published in Materials Science and Engineering A (2012)*)

In this study, the ECAP process experiment of copper single crystal [179] has also been simulated to validate the developed CPFEM model. The ECAP die used for ECAP of copper single crystal in Ref. [179] was the same as the one used for ECAP of aluminium single crystal in Ref. [33]. According to the studies [247, 252], the factors $f_{\alpha\beta}$ for copper can be chosen as a1=a2=a3=8, a4=15, and a5=20. Three elastic moduli are C_{11}=168400 MPa, C_{12}=121400 MPa, and C_{44}=75400 MPa. The other parameters used for the hardening law are listed in Table 3.3. The initial crystallographic orientation for copper single crystal is designed as: the slip plane of (-1 -1 -1) and the slip direction of [-1 1 0] are parallel to the theoretical shear plane and shear direction of the ECAP die, respectively.

Table 3.3 The strain rate sensitivity component and parameters in the hardening law for copper single crystal.

n	$\dot{\gamma}_0$ (s^{-1})	h_0 (MPa)	h_s (MPa)	τ_1 (MPa)	τ_0 (MPa)
20	0.0001	90	1.5	1.3	1

For the convenience of simulation, the ECAP die and punch are modeled as rigid body and the sample is defined as deformable body. It is meshed into 6369 elements as the same as the aluminium single crystal described in the last Section. A constant punch speed of 0.04 mm/s along –Y direction is used and the processing is terminated when approximately three-fourths of the sample is pressed through the intersection part of two channels. The Coulomb friction model with coefficient of 0.1 is used to consider the real frictional condition and the processing is assumed at room temperature. The simulation is terminated when the majority of the copper single crystal has passed through the intersecting zone of the entry channel and exit channel.

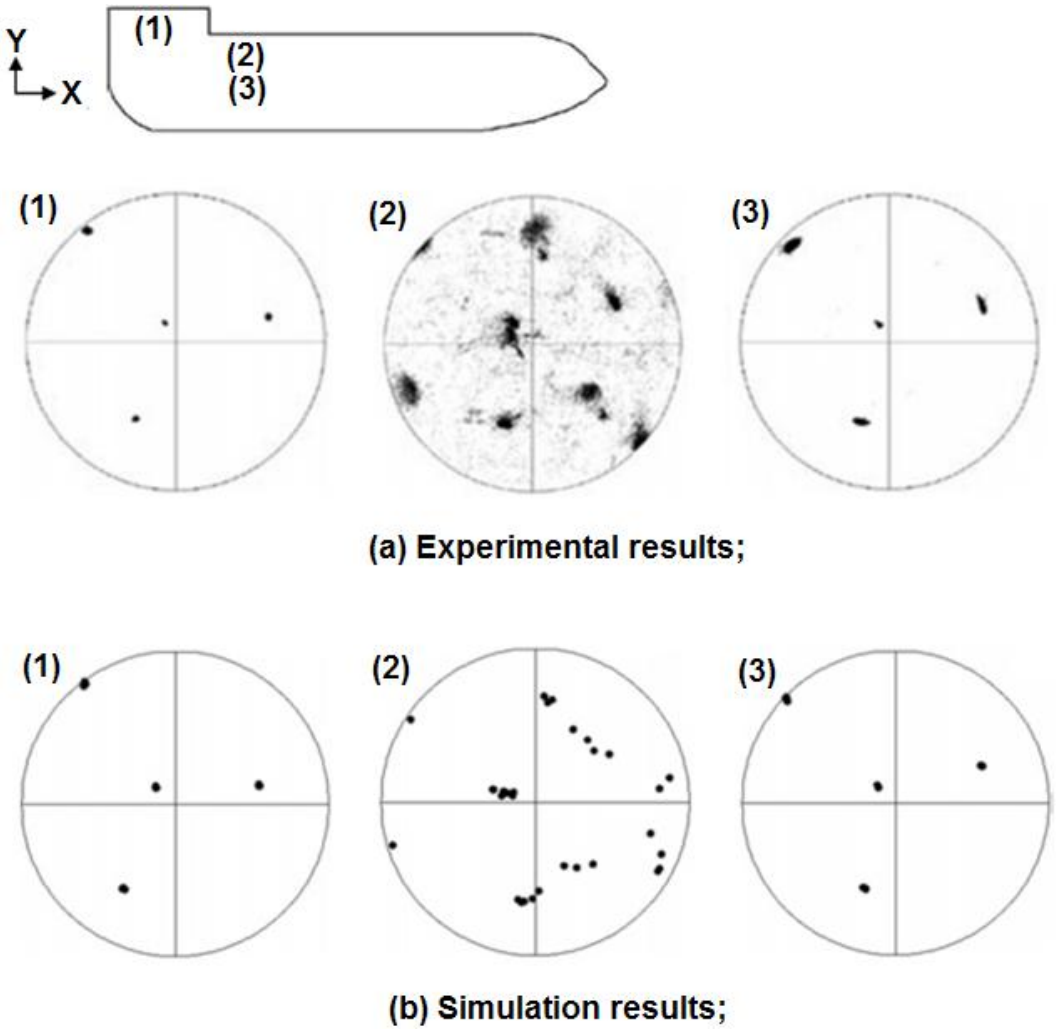

Fig. 3.5 Comparisons of the {1 1 1} pole figures between the experimental measurements [179] (upper panel) and the CPFEM simulation (lower panel): (a) Position 1, (b) Position 2, and (c) Position 3.

In the experiment [179], the textures after the ECAP process were examined using the orientation imaging microscopy (OIM) for three selected positions, as shown in Fig. 3.5. The labels of 1-3 in this figure correspond to the Labels 0, 3, and 4, respectively, in Ref. [179]. It is obvious that the Position 1 is located in the entry channel while Positions 2 and 3 are located in the exit channel. Both the experiment and simulation at Position 1 reveal an almost the initial crystallographic orientation which confirms that the crystal lattices do not significantly rotate at this position before entering the main PDZ. The experimental measurement at Position 2 shows the initial crystallographic orientation together with a rotated orientation by 60° around the Z axis in a counter-clockwise direction from the initial orientation. Furukawa et al. [159, 180]

states that the counter-clockwise rotation is due to the shear plane spreading at the outer arc of curvature at the point where the two channels intersect. In Fig. 3.5(b), both the initial orientation and the 60° rotated component have been observed at this position, but some extra orientation scattering in the simulated {1 1 1} pole figure exists, which indicates the influence of frictional condition on the texture heterogeneity at Position 2. It should be noted that the experiment was conducted using a MoS2 lubricant which could reduce the frictional effect between the sample and the ECAP die channels. The simulated {1 1 1} pole figure at Position 3 in Fig. 3.5(b) is consistent with the experiment result in Fig. 3.5(a), which indicates an orientation rotated about 60° around the Z axis from the initial crystallographic orientation. Therefore, it can be concluded that the CPFEM model developed in this study can predict accurate texture evolution during ECAP of copper single crystal.

3.4 Summary

This chapter is summarized as follows:

(1) The development of a CPFEM model has been introduced. In the model used in this study the deformation has been decomposed into two parts: crystallographic slip due to dislocation on the active slip systems and elastic deformation that includes stretching and rotation of the crystal lattice. The rate-dependent material constitutive law has been applied to overcome the problem of non-uniqueness in the choice of active slip systems which is inherent in the rate-independent theory [233, 238, 240-245]. The hardening model proposed by Wu and Bassani [247, 252] has also been used because it can accurately capture the three different hardening stages in a slip system, namely low hardening in Stage-1, rapid hardening in Stage-2, and parabolic hardening in Stage-3.

(2) A detailed implementation of crystal plasticity theory into the commercial finite element code (Abaqus) has been described. Abaqus/Standard offers a user subroutine interface where the mechanical constitutive behavior of material different from the Abaqus program library can be defined.

(3) For the first time CPFEM simulations of ECAP of aluminium single crystal and copper single crystal have successfully been conducted. The simulation results have been compared with the reported experimental results. It has been found that the simulated results agree well with the experimental observations. This clearly indicates that the developed model can be used to accurately predict the texture evolutions for FCC materials during the ECAP process.

Chapter 4 Investigation of ECAP of Aluminium Single Crystals

The aim of this chapter is to carry out a systematic study on ECAP of aluminium single crystals. Difference between two-dimensional and three-dimensional simulations has been investigated. The effects of mesh conditions, frictional conditions, sample size, outer corner angle and inner corner fillet radius of an ECAP die on the inhomogeneous plastic deformation and texture evolution will be discussed in details.

4.1 Inhomogeneous Deformation and Texture Evolution

(*This part has already been published in Acta Materialia (2011)*)

The CPFEM simulation procedure of ECAP of aluminium single crystal has been given in Chapter 3 in details. In this section, the nature of inhomogeneous deformation and texture evolution of aluminium single crystal during the ECAP process will be analysed.

4.1.1 Macroscale Deformation Behaviour

Fig. 4.1(a) shows the mesh in the deformed billet at the time step where the top surface of the billet is 4.2 mm away from the entry of the die corner. The shape of the billet in the die corner shown in the figure is similar to the experimental observation by an optical microscope in Ref. [33]. It seems that the billet has filled in the whole die. However, a careful inspection indicates that there is a non-contact area, as marked in the figure, in the outer corner of the die. The deformed mesh in Fig. 4.1(a) shows that deformation heterogeneity exists along the X axis before point 'S' but after point 'S' the deformation tends to be homogeneous along the X axis, indicating that the billet was deformed under a steady-state condition. The region behind point 'S' is now called the steady-state deformation region and herein most of the analyses will be conducted in this region.

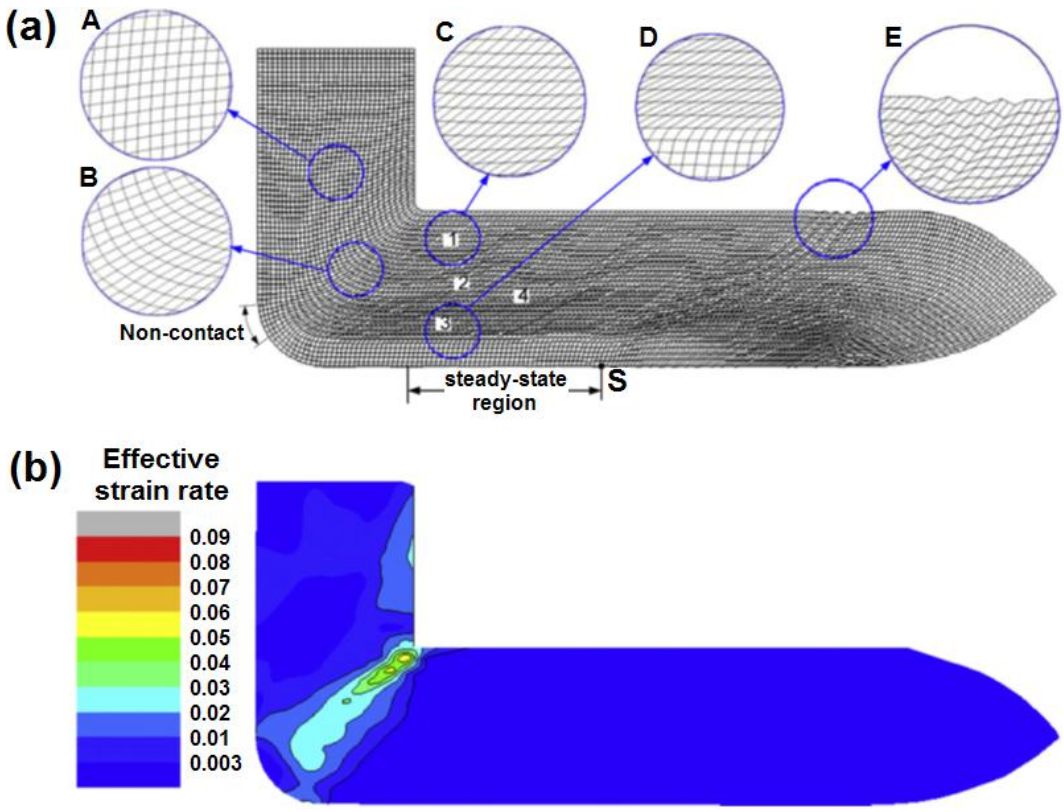

Fig. 4.1 Mesh distortions and distribution of effective plastic strain rate in the deformed billet: (a) mesh distortions, and (b) effective plastic strain rate.

Five circular regions, marked as 'A-E' in Fig. 4.1(a), have been enlarged to give more details of the mesh distortions. Region A is located in the entry channel and shows that the elements in this region are slightly distorted, indicating that deformation has already taken place in the entry channel. Region 'B' was chosen from the die corner. The elements in this region are subjected to shear deformation. Another feature in Region 'B' is that the elements are stretched, which means that the deformation is not simple shear deformation, and that tension and compression deformation has also been imposed onto the billet. Regions 'C' and 'D' represent the upper part and lower part of the deformed billet in the steady-state deformation region respectively. It is clear that after deformation the elements have been distorted and oriented at certain angles with respect to the X axis, as shown in Region 'C'. The rotation angle of the element decreases as the distance (d) from the top surface increases, until d=3.3 mm. It is interesting to observe that the elements in Region 'D' exhibit different deformation

behaviour, such that the elements in the upper part of Region 'D' are highly distorted, whereas in the lower part the elements are slightly distorted. It was reported from a number of experiments that the undistorted region encompasses 5~20% of the billet thickness [253]. In our simulation the thickness of this region is 17.5% of the billet. Region 'E' is located in the unstable deformation region. An undulating localized flow band can be seen in this region. The band is roughly parallel to the intersecting line between two channels, which is consistent with the experimental observation [5]. Segal [5] and Figueiredo et al. [254] attributed the reason for flow localization to the flow softening, but we observed this phenomenon using the work hardening model, as shown in Equation (3.57). As can be seen, the flow localization band includes alternate layers of highly sheared and rotated elements. Large local stress gradients exist in the unstable deformation region which activate different slip systems in the neighbouring elements and induce elements to rotate in different directions. Some elements become softer, while others become harder. The former are subjected to more shear deformation while the lattices in the latter need more rotation to accommodate local strain.

Fig. 4.1(b) shows the distribution of effective plastic strain rate ($\dot{\bar{\varepsilon}}$) in the deformed billet. The main plastic deformation zone (PDZ) spreads about the intersecting plane in the die corner. It can be seen that the deformation in the entry channel extends from the surface to the middle of the billet and the material near the right hand side surface of the entry channel is subjected to more deformation than the left hand side surface. As with the prediction by the VPSC model, ($\dot{\bar{\varepsilon}}$) significantly changes from the inner corner to the outer corner and the PDZ can be divided into two parts based on the pattern of the strain rate. The upper part of the PDZ has a fan-like shape that covers the major portion of the PDZ. The lower part of the PDZ includes two small deformation regions near the surface of the billet, between which a rigid body rotation region exists that in turn corresponds to the non-contact region shown in Fig. 4.1(a).

4.1.2 Crystal Rotation Patterns

In order to analyze the rotation of the crystallographic orientation during the ECAP process, the misorientation of each node relative to the initial crystallographic orientation has been partitioned into three components which represent the crystal rotation angles around the X, Y

and Z axes, respectively. The partitioned method proposed by Wert et al. [234] has been adopted in this study. Contour maps of crystal rotation angles around the X, Y, and Z axes are shown in Fig. 4.2(a-c), respectively. The positive value means the counter-clockwise (CCW) rotation and the negative value indicates the clockwise (CW) rotation. It can be seen from Fig. 4.2 that the crystallographic orientation rotates along all three directions. The crystal rotation angle around the Z axis (TD) is much larger than the other two rotation directions. This is consistent with the experimental observations of single crystal and polycrystalline materials [33, 253]. According to Equation (3.32), the rate of material rotation ($\dot{\boldsymbol{R}}$) can be expressed as

$$\dot{\boldsymbol{R}} = \boldsymbol{W}\boldsymbol{R} \tag{4.1}$$

where $\boldsymbol{R}$ is the material rotation tensor and $\boldsymbol{W}$ is the spin tensor, as defined in Section 3.1. According to Equation (3.17), the component $\boldsymbol{W}^{\mathrm{P}}$ caused by the slip and $\boldsymbol{W}^{*}$ caused by the lattice rotation and stretching. Therefore, $\boldsymbol{W}^{\mathrm{e}}$ represents the rate of rotation of the crystallographic orientation. Under a plane strain condition $\boldsymbol{W}$ for rotations around the X and Y axes are zero. Since the slip directions are oriented in all three dimensions, the slip rotation components ($\boldsymbol{W}^{\mathrm{P}}$) around the X and Y axes always exist. To retain zero material rotations around X and Y axes, the lattices must rotate around the X and Y axes to compensate for the rotation induced by slips. Therefore, the lattice rotations around the X and Y axes are non-zero. It can be seen that in the steady-state deformation region the distributions of crystal rotations around all three axes are heterogeneous. In Fig. 4.2(a), the crystal rotation angles around the X axis in the middle part of the billet are larger than those in the top and bottom parts. The distribution of the rotation angle around the Y axis is different from that around the X axis. The large rotation area in Fig. 4.2(b) locates in the top part of the billet, while in the bottom part the rotation angle around the Y axis is small. According to the distribution of the rotation angle around the Z axis, as shown in Fig. 4.2(c), the steady-state deformation region can be divided into three sub-regions: the top half part with about 60° Z-axis rotation, the region between 1/2 and 3/4 of the billet thickness from the top surface with about 0° Z-axis rotation and the remaining region with about 90° Z-axis rotation.

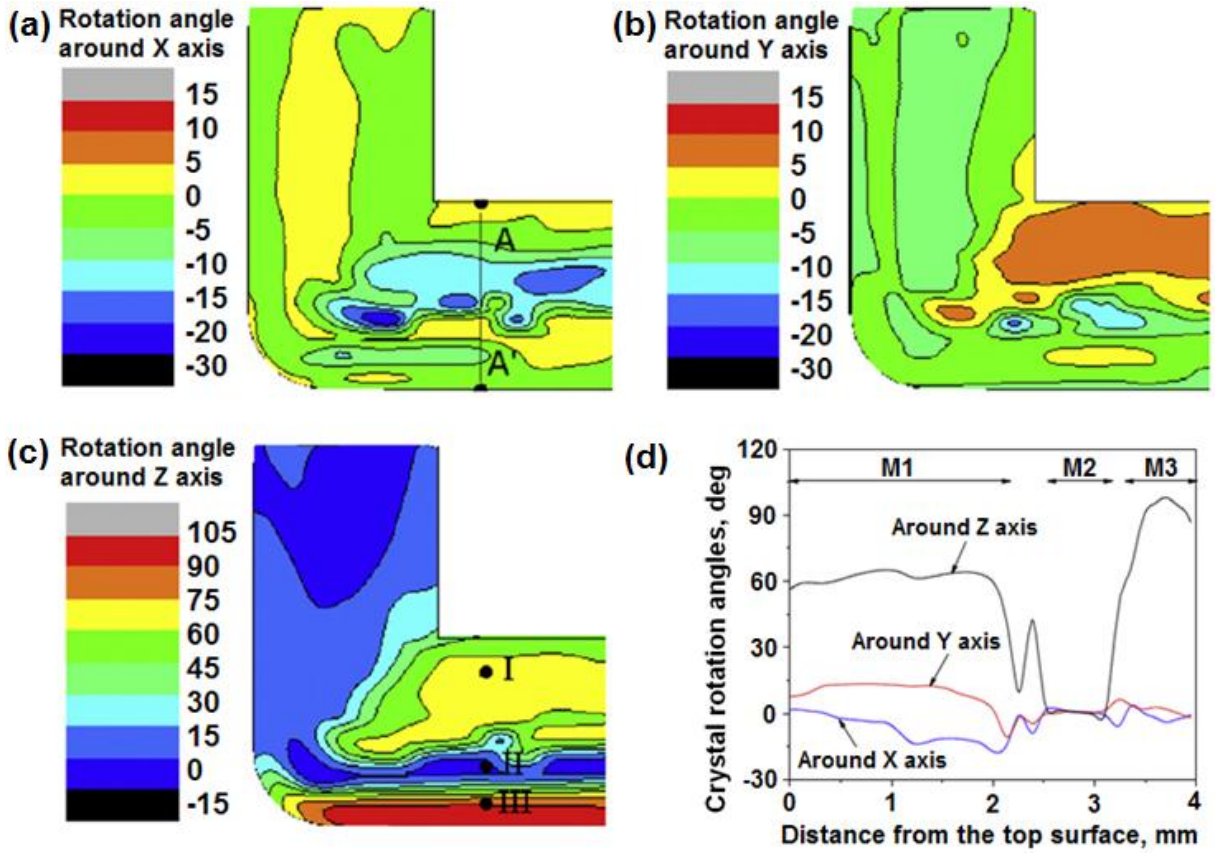

Fig. 4.2 Distributions of crystal rotation angles in the billet: (a) contour map of crystal rotation angle around the X axis, (b) contour map of crystal rotation angle around the Y axis, (c) contour map of crystal rotation angle around the Z axis, and (d) crystal rotation angle along line AA' marked in (a).

The crystal rotation angles along the line AA' marked in Fig. 4.2(a) were selected and shown in Fig. 4.2(d). All rotation angles vary along the billet thickness and the crystal rotation around the Z axis is larger than those around the X and Y axes. It is clear that there are three regions with distinct rotation angles around Z axis. Liu et al. [255] conducted cold rolling of aluminium single crystal with initial Cube orientation. They found that the crystal rotated mainly around TD and the crystal was subdivided macroscopically and symmetrically into four parts, designated matrix bands, along the thickness by the TD rotation. The crystal rotation angle varies significantly in the regions between the matrix bands, defined as transient bands. Fig. 4.2(d) depicts three matrix bands M1, M2, and M3 through the thickness of the ECAP processed billet. The TD (Z-axis) rotation angles in three matrix bands are about 60°, 0° and 90°, respectively. Position P1 marked in Fig. 4.1(a) is located in M1. Therefore, a nearly 60° Z-axis rotation was observed in

the {1 1 1} pole figure, as shown in Fig. 3.5(b). Since positions P2-P4 are located in the transient bands, both 0° and 60° rotations have been seen in the corresponding {1 1 1} pole figures. Ref. [33] did not show any result near the bottom surface (M3 region) nor discussed the sub-grain formation in the experimental work. However, the sub-grain formation can be quantified by the misorientation angles predicted by the current simulation. It can be seen from Fig. 4.2 that the misorientation angles around the Z axis are about 60° between M1 and M2 and 90° between M2 and M3, respectively. These misorientation angles are greater than the angle of 15° commonly used to define a large-angle grain boundary. This indicates that the initial single crystal has been split into three grains after one pass of the ECAP process.

4.1.3 Slip Trace

Fig. 4.3 shows the simulated slip traces in the billet based on the CPFEM model. Three slip systems with the larger magnitudes of the accumulative shear strain are selected for each element. The intersecting line between a slip plane and the transverse plane (Z plane) is plotted by a segment of straight line centered at the integration point of the element, the direction of which infers the orientation of the slip trace. The length of the straight line represents the relative magnitude of accumulated shear strain. The black, blue and red colors refer to the slip systems with the first largest magnitude, the second largest magnitude and the third largest magnitude of the accumulative shear strain, respectively. Six selected regions, marked as ‘A-F’, are enlarged to give details of the slip traces. In Region ‘A’, the single slip system a3 (defined in Table 3.2) is activated. In Region ‘B’, the primarily activated slip system is d1. However, in the area near the surface another slip system (a3) is also activated, which may be due to friction. The evolution of the slip traces can be observed through Region ‘C’, which is located in the upper part of the PDZ. Accompanying the lattice rotation, the slips tend to occur simultaneously on different systems. It can be seen that the activated slip develops from a single-slip system or a double-slip systems to a multi-slip system. Region ‘D’, also located in the PDZ, exhibits a different slip trace pattern. Only one slip system (a3) is active for the majority portion of Region ‘D’ and the accumulative shear strain on this slip system increases as the material moves through the PDZ. It can be observed that most slip traces in Region ‘D’ are parallel to each other,

indicating that the lattice rotation is negligible. Region 'E' and 'F' were chosen from the deformed billet. The main difference between these two regions is that the material in Region 'E' is subjected to multiple slips, while the deformation in Region 'F' is governed by one dominant slip. It is also found that the magnitude of the accumulative shear strain of the primary slip system in Region 'F' is larger than in Region 'E'.

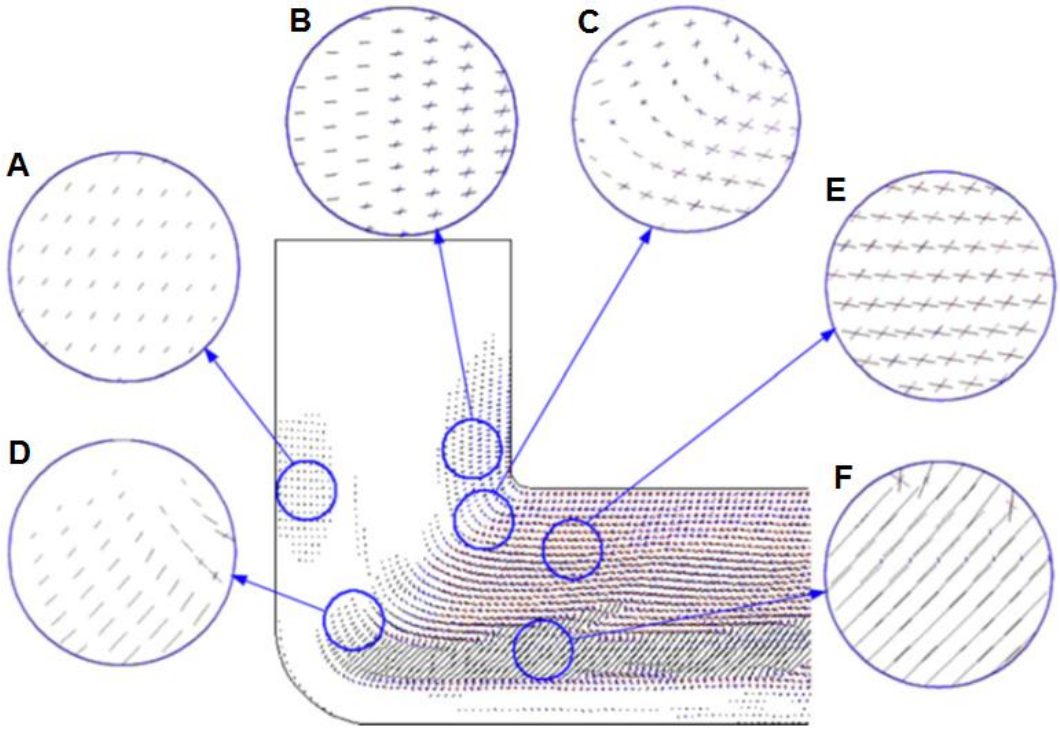

Fig. 4.3 Simulated slip traces in the aluminium single crystal during the ECAP process.

In the experiment of Ref. [33] the crystal was oriented so that the {1 1 1} slip plane was parallel to the ideal shear plane of the ECAP die and the <1 1 0> slip direction lays parallel to the direction of shear. This orientation was expected to be stable during the ECAP process if the billet was deformed by the slip on the desired slip system, as predicted by simple shear theory. However, the experimental observation showed both initial crystallographic orientation and a 60° rotated orientation in the deformed billet. Fukuda et al. [33] interpreted these results using shear factors which are based only on the initial positions of the slip systems with respect to the applied shear. As pointed out by Beyerlein and Toth [2], shear factors cannot give precise information on slip activity, the latter being dependent on the stress state as well.

4.1.4 Heterogeneity along Thickness

According to the results shown in the last section, it is natural to ask the question: what is the basic mechanism behind the observed phenomena? To answer this question, three tracer elements marked by 'I-III' in Fig. 4.2(c) will be analysed in this section. They belong to three matrix bands M1, M2, and M3, respectively.

Fig. 4.4 shows the crystal rotation angles around three axes, shear strain rates on 12 slip systems, three stress components (σ_X: normal stress along the X axis; σ_Y: normal stress along the Y axis; σ_{XY}: shear stress on the Z plane) and three strain rate components ($\dot{\varepsilon}_X$: normal strain rate along the X axis; $\dot{\varepsilon}_Y$: normal strain rate along the Y axis; $\dot{\varepsilon}_{XY}$: shear strain rate on the Z plane) for tracer-element I as functions of the moving distance from its initial position. The positions at the entry and exit of the die corner are marked by dashed lines in the figure. It can be seen from Fig. 4.4(a) that the lattice starts to rotate at the moving position of ~10 mm. The change of the Z-axis rotation angle is faster than the others. In the die corner the lattice rotation around the X axis changes the direction from CW to CCW, while the rates of change of the Z-axis rotation angle and the Y-axis rotation angle increase monotonically. This increase in the Z-axis rotation angle is more significant and it becomes the dominant rotation component at the exit of the die corner. The Z-axis rotation occurs roughly in two regions with regard to the moving distance: 10-14 mm (before the die corner) and 14-15.3 mm (within the die corner). In the 10-14 mm region, the magnitudes of normal stresses increase significantly and the shear stress (τ_{XY}) remains at a relatively large value of 50 MPa. This leads to multiple slips. Five active slip systems have been observed in Fig. 4.4(b) for the 10-14 mm region. Fig. 4.4(d) shows that the magnitude of shear strain rate ($\dot{\varepsilon}_{XY}$) is larger than those of normal strain rates ($\dot{\varepsilon}_X$ and $\dot{\varepsilon}_Y$). This indicates that friction plays an important role in this region. It is interesting to see that seven slip systems are activated in the die corner (14-15.3 mm region), some of which have large shear strain rates, as shown in Fig. 4.4(b). It is reasonable to expect that the Z-axis rotation is affected by multiple slips which correspond to the abrupt increase of the Z-axis rotation angle in the 14-15.3 mm region.

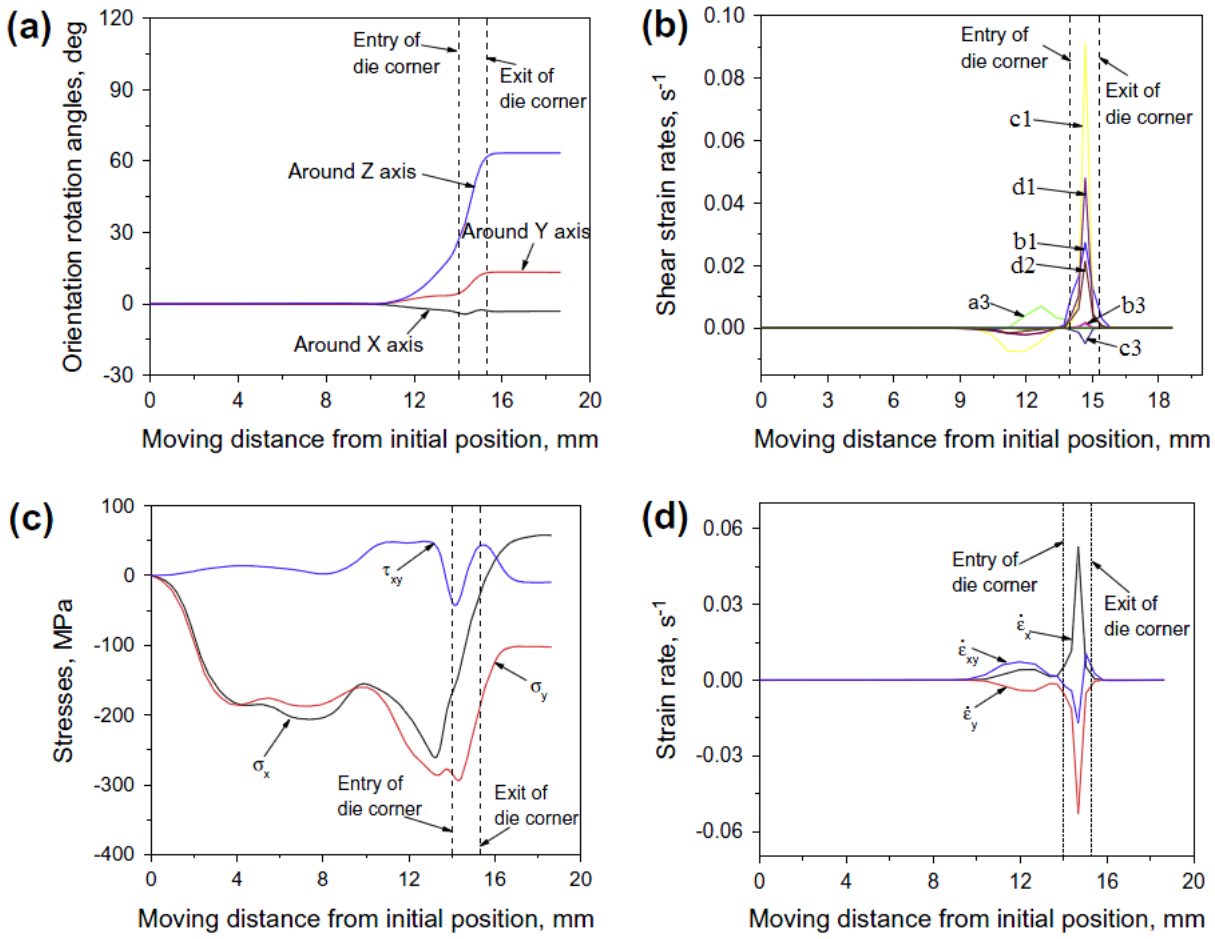

Fig. 4.4 Results for tracer-element I as functions of moving distance from initial position: (a) crystal rotation angles, (b) shear strain rates, (c) stresses, and (d) strain rates.

Fig. 4.5 shows the results for tracer-element II. The Z-axis rotation angle of tracer-element II slightly increases before the element moves into the die corner. The major difference in the Z-axis rotation angle between tracer-element I and II exists in the die corner. Unlike the significant increase in the Z-axis rotation angle for tracer-element I, the Z-axis rotation angle of tracer-element II decreases in the die corner and then stabilizes at a very small value. This gives a near-initial orientation in the matrix band M2. The major feature in Fig. 4.5(b) is that a single-slip system dominates the plastic deformation, even though multi-slip occurs before and within the die corner. The magnitude of the shear strain rate of the dominant slip system in Fig. 4.5(b) is smaller than that of tracer-element I in Fig. 4.5(b). Since tracer-element II is located lower than tracer-element I, the activation distance of the former is larger than the latter, and

therefore the accumulated shear strain on the primary slip system of tracer-element II is larger than tracer-element I, as shown in Region 'F' of Fig. 4.3. In the die corner, both the stresses and strains of tracer-element II are smaller than their counterparts in Fig. 4.4.

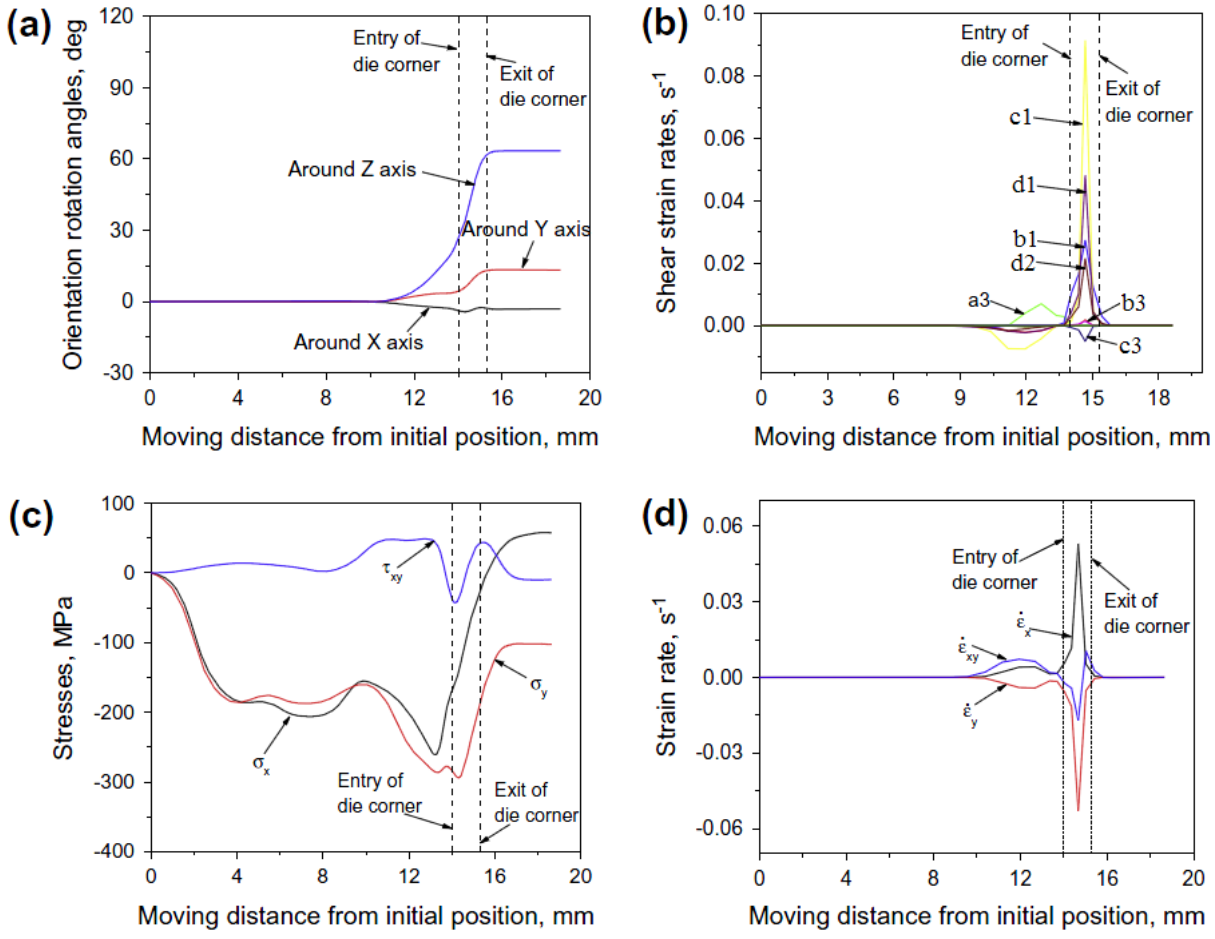

Fig. 4.5 Results for tracer-element II as functions of moving distance from initial position: (a) crystal rotation angles, (b) shear strain rates, (c) stresses, and (d) strain rates.

Fig. 4.6 shows the results for tracer-element III. It can be seen from Fig. 4.6(a) that the Z-axis rotation angle increases dramatically from 15° to 90° as the element moves within the moving distance range of 11.5-14 mm. This range corresponds to the rigid body rotation region locating between two small deformation regions in the lower part of the PDZ, as shown in Fig. 4.1(b). Close inspection reveals that the multi-slip mainly occurs in two small deformation regions. The shear strain rate of the primary slip system has opposite directions in these two regions. This results in near-zero slip after the element leaves the die corner. A comparison of stresses and

strains in Figs. 4.4-6 indicates that tracer-element III has similar magnitude of stresses and strains in the die corner as tracer-element II, but both of them have smaller magnitudes of stresses and strains than tracer-element I.

The calculated material rotation angles for tracer-elements I and II are 63.5° and 58.3°. For tracer-element I, the plastic deformation in the die corner is completed within a short distance, resulting in a larger local strain gradient (or strain rate) and shear strain rates on the slip systems, as shown in Fig. 4.4(b) and (d). From the hardening model (Equation (3.60)), the resolved shear stress on the primary slip system is much larger than the critical shear stress. This also leads to larger resolved shear stresses on other slip systems. The consequence is that several slip systems are activated simultaneously. It can be seen from Region 'E' of Fig. 4.3 that the activated slip systems orientate along different slip directions. They provide opposing contributions to $\boldsymbol{W}^{\mathrm{P}}$, resulting in a small $\boldsymbol{W}^{\mathrm{P}}$. The lattice must rotate to accommodate the material rotation required by deformation, namely the lattice rotation angle is close to the material rotation angle (63.5° for tracer-element I). For tracer-element II, the deformation zone in the die corner has been enlarged so the strain gradients (or strain rates) have been reduced, resulting in a small shear strain rate on the primary slip system. According to the hardening model, a smaller shear strain rate requires a resolved shear stress slightly larger than the critical value, which is not high enough to generate visible shear strains on other slip systems. This results in a dominant slip system observed in the die corner for tracer-element II (Fig. 4.5(b)). The single dominant slip can generate a large rotation ($\boldsymbol{W}^{\mathrm{P}}$) to accommodate the whole material rotation ($\boldsymbol{W}$). Therefore, the lattice rotation ($\boldsymbol{W}^{*}$) is not needed for tracer-element II, leading to almost initial orientation after deformation. In the lower part of the die corner such as tracer-element III, the materials are mainly subjected to deformation in two small regions, between which a rigid body rotation region exists. It can be seen from Fig. 4.6(b) that the shear strain rates are relatively small and slips in two small deformation regions occur in the opposite directions. In the rigid body rotation region, the billet loses contact with the die, leading to the stresses being too small to induce large slip. This results in a very small $\boldsymbol{W}^{\mathrm{P}}$. However, without large slips in the lower part of the die corner the die geometry requires a 90° material rotation.

Therefore, the lattice must rotate about 90° around Z axis to accommodate the required material rotation.

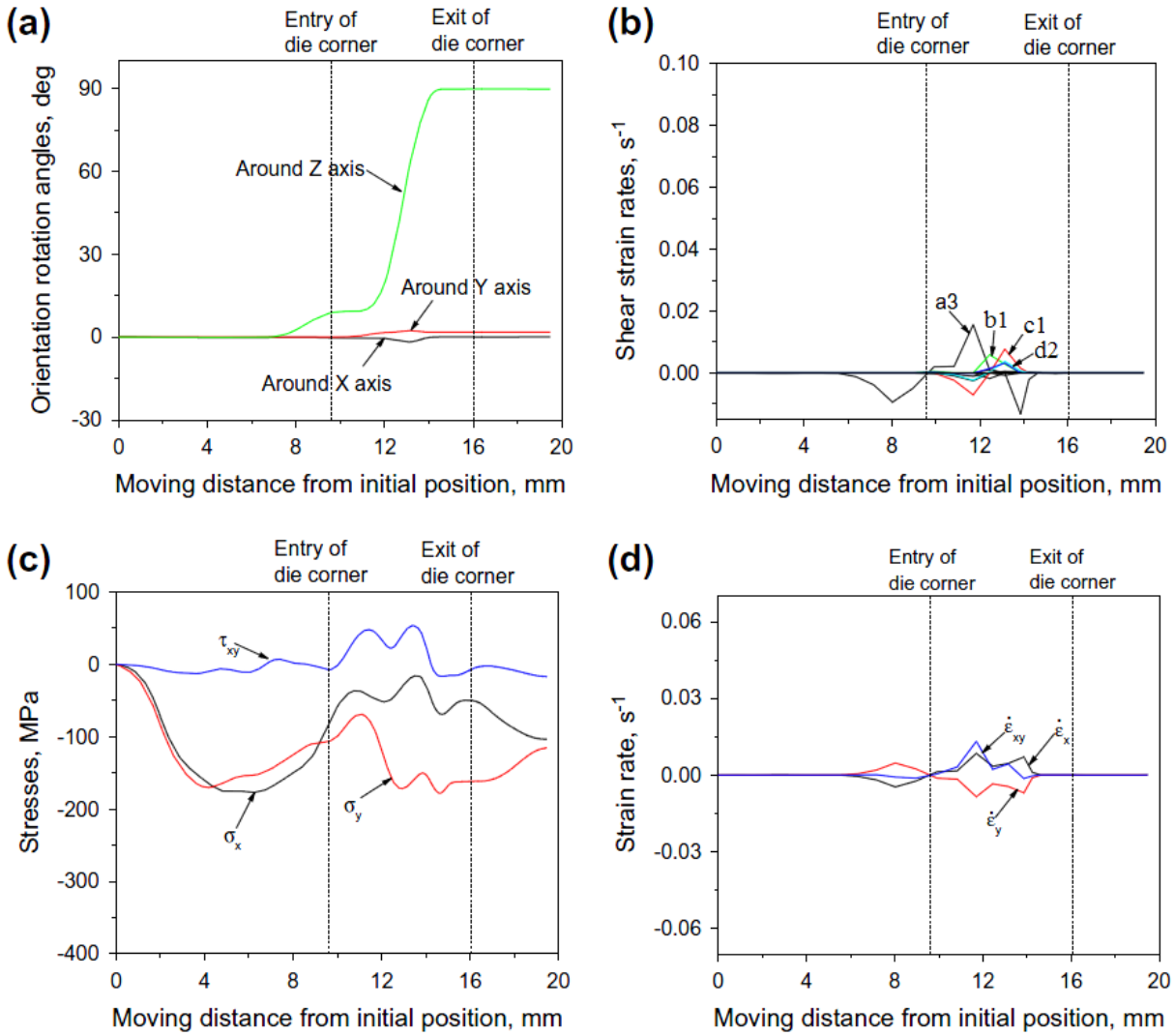

Fig. 4.6 Results for tracer-element III as functions of moving distance from initial position: (a) crystal rotation angles, (b) shear strain rates, (c) stresses, and (d) strain rates.

Based on the above analysis, it can be demonstated that the geometry of the die plays a very important role in the texture evolution and heterogeneity along the thickness direction during ECAP process. When the strain gradient is large (such as tracer-element I), multi-slip can be activated. The material rotation induced by slips is negligible and the lattice rotation dominantes the whole material rotation requested by deformation. When the strain gradient is

small (such as tracer-element II), the single dominant slip is the main slip mechanism, which can satisfy the required material rotation in the absence of the lattice rotation. Therefore, the lattice remains at the initial orientation after deformation. There is a rigid body rotation region in the lower part of the die corner where the lattice rotates by the die channel angle in this region. The inhomogeneous texture evolution along the thickness direction of such oriented aluminium single crystal during the ECAP process is obvious shown in Fig. 3.2.

4.2 Three-dimensional Simulation of ECAP

In order to examine the accuracy of two-dimensional plane strain assumption, a three-dimensional CPFEM simulation of the ECAP process has been carried out. Three-dimensional classical FEM simulation of the ECAP process [145, 148-150, 256] have been reported. However, to the author's knowledge this is the first three-dimensional CPFEM simulation of the ECAP process.

In the three-dimensional simulation, the simulated ECAP die geometry is exactly the same as the one used in Section 3.3.1. The ECAP die has a square cross-section with dimensions of 4 × 4 mm^2 and is assumed as rigid body in the simulation. The die channel angle is 90° and the outer corner angle is 30°. The aluminium single crystal has a total length of about 24 mm and is defined as deformable body in the simulation. It has been meshed into 27945 C3D8R elements, which is defined as an 8-node linear brick and reduced integration with hourglass control [249]. To provide the consistency of the previous simulations, the friction coefficient μ is set to 0.1. The initial crystallographic orientation and the other material parameters for aluminium single crystal can be found in Chapter 3.

Fig. 4.7 shows the mesh in the deformed crystal. As can be seen, the deformation is not uniform along both the X axis and Y axis. Along the X axis, similar distorted elements to the two-dimensional simulation in Fig. 4.1(a) can be observed. In contrast along the Y axis, the elements in the upper part have been sheared more than in the lower part. Apart from the inhomogeneous deformation in the leading head, steady-state deformation region has been obtained and all the results will be analyzed in this region.

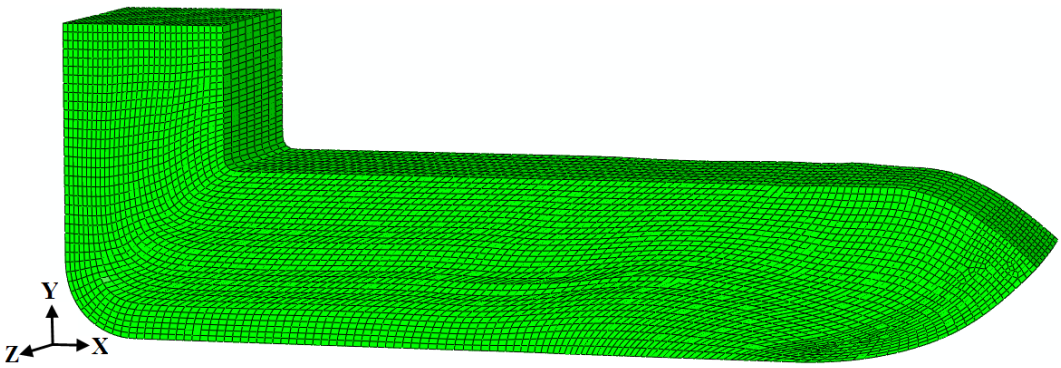

Fig. 4.7 Mesh distortions in the three-dimensional CPFEM simulation of the ECAP process of aluminium single crystal.

Fig. 4.8 shows the distribution of plastic strain in the cross-section of the deformed billet (2 mm away from the exit of the die corner, namely X=6 mm). It is obvious that the strain distribution is not uniform along the thickness direction (or Y axis), but homogeneous along the transverse direction (or Z axis). According to the distribution of strain along the Y axis, three regions can be distinguished, namely part of the upper half, the middle 1/4 thickness, and the lower 1/4 thickness. The strain in the upper region is slightly smaller than the middle part, where the deformation pattern is very complicated and includes shearing, tension and compression. The smallest strain is located in the bottom part. This should be attributed to the outer corner angle of the ECAP die which leads to the rigid body rotation.

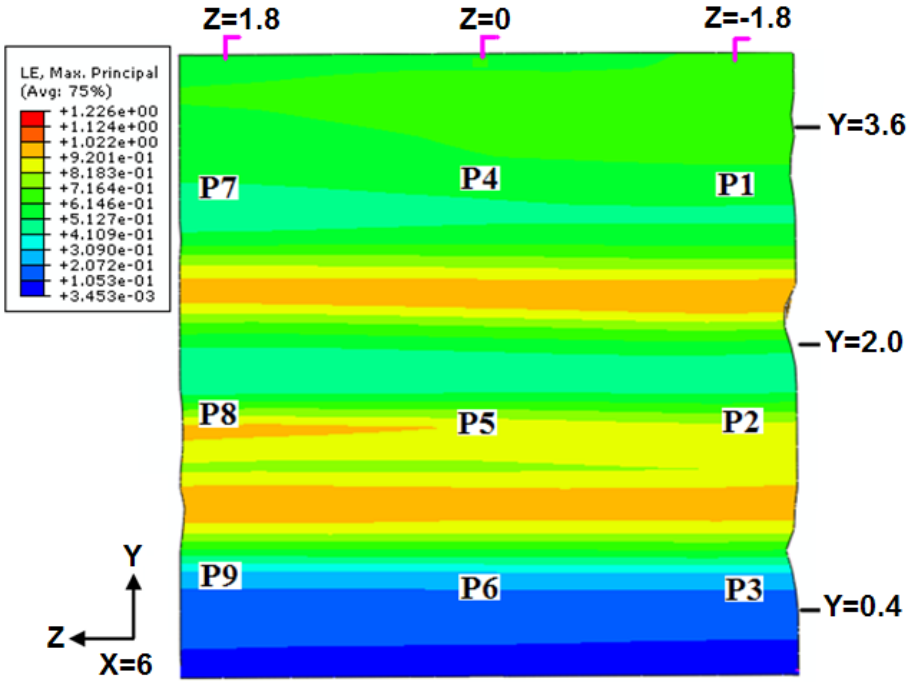

Fig. 4.8 Contour of strain distribution in the cross-section (X=6 mm) of the deformed aluminium single crystal during the ECAP process.

Fig. 4.9(a-c) shows the variation of the effective plastic strain and strain components along three selected lines parallel to the Z axis (lines of Y=3.6, 2 and 0.4 mm representing different parts along thickness direction) as marked in Fig. 4.8. It is clear that the strain components ε_Z, γ_{XZ} and γ_{YZ} are almost zero for all three lines. The effective plastic strain on the line of Y=3.6 mm in the upper region is slightly smaller than that of Y=2 mm in the middle part, but larger than that of Y=0.4 mm in the lower region. Fig. 4.9(d) shows the variation of the effective plastic strain between three selected lines parallel to the Y axis (line of Z=-1.8, 0, and 1.8 mm representing different planes along transverse direction) as marked in Fig. 4.8 and the results agree with each other.

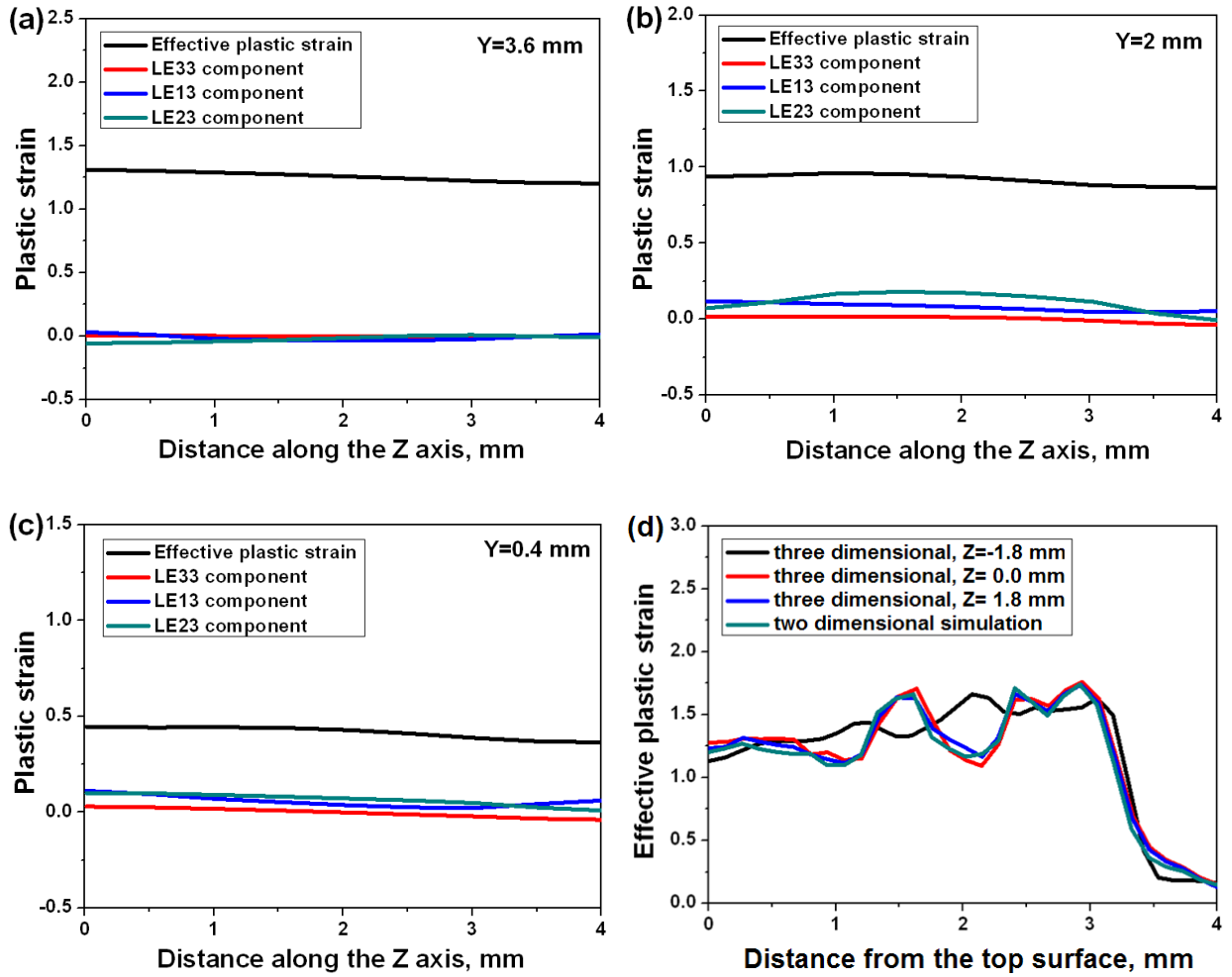

Fig. 4.9 Variation of the effective plastic strain and logarithmic strian components along the Z axis and Y axis in the steady-state deformation region. (a) on the line of Y=3.6 mm, (b) on the line of Y=2 mm, (c) on the line of Y=0.4 mm, and (d) comparison of the effective plastic strain along the thickness direction between two-dimensional and three-dimensional simulations. (LE33 is normal component of logarithmic strain along the Z axis, LE13 and LE23 are shear components on the Y and X planes, respectively)

A deformation inhomogeneity index, C_i, was defined to quantify the degree of deformation inhomogeneity along the Z axis after the ECAP process proposed by Li et al. [142] as:

$$C_i = \left(\frac{\varepsilon_{\max} - \varepsilon_{\min}}{\bar{\varepsilon}}\right) \tag{4.1}$$

where $\varepsilon_{\max}$, $\varepsilon_{\min}$ and $\bar{\varepsilon}$ represent, respectively, the maximum, minimum and average of the effective plastic strains along the Z axis.

Calculation reveals that the indexes C_i for three lines of Y=3.6, 2 and 0.4 mm are very small, with a corresponding index of 0.09, 0.1, and 0.12, respectively. These results indicate a relatively homogeneous deformation along the transverse direction when the die has a square cross-section. However, the index for the lines of Z=-1.8, 0 and 1.8 mm are very large. The corresponding indexes are 1.42, 1.39, and 1.41, respectively, which shows significant inhomogeneous deformation along the Y axis.

Fig. 4.9(d) shows a comparison of the effective plastic strain between the three-dimensional and two-dimensional simulations, with the result being very good agreement. Therefore, according to the results shown in Fig. 4.8 and Fig. 4.9, it can be concluded that similar strain distribution can be obtained from both the three-dimensional and two-dimensional simulations when the ECAP die has a square cross-section.

Nine different positions marked P1 to P9 in Fig. 4.8 are selected to study texture evolution along the thickness direction (Y axis) and the transverse direction (Z axis). Positions P1-P3 are located in the line of Z=-1.8 mm. Positions P4-P6 are located in the middle line of Z=0 mm and Positions P7-P9 are located in the line of Z=1.8 mm. The texture has been studied in terms of {1 1 1} pole figures, as shown in Fig. 4.10. It is obvious that texture evolution is not uniform along the Y axis as predicted by the two-dimensional simulation shown in Section 4.1. A crystallographic orientation rotated about 60° from the initial component around the Z axis has been observed for Positions P1, P4, and P7 which are located in the upper region along the thickness direction. Both the initial and rotated crystallographic orientations exist in the middle region (Positions P2, P5, and P8) and a nearly 90° rotated orientation component in the bottom part (Positions P3, P6, and P9). The {1 1 1} pole figures along three lines Y=3.6, 2, and 0.4 mm shown in Fig. 4.10 are similar, which indicate that uniform texture evolution along the transverse direction for aluminium single crystal was deformed by ECAP with the die having a square cross-section.

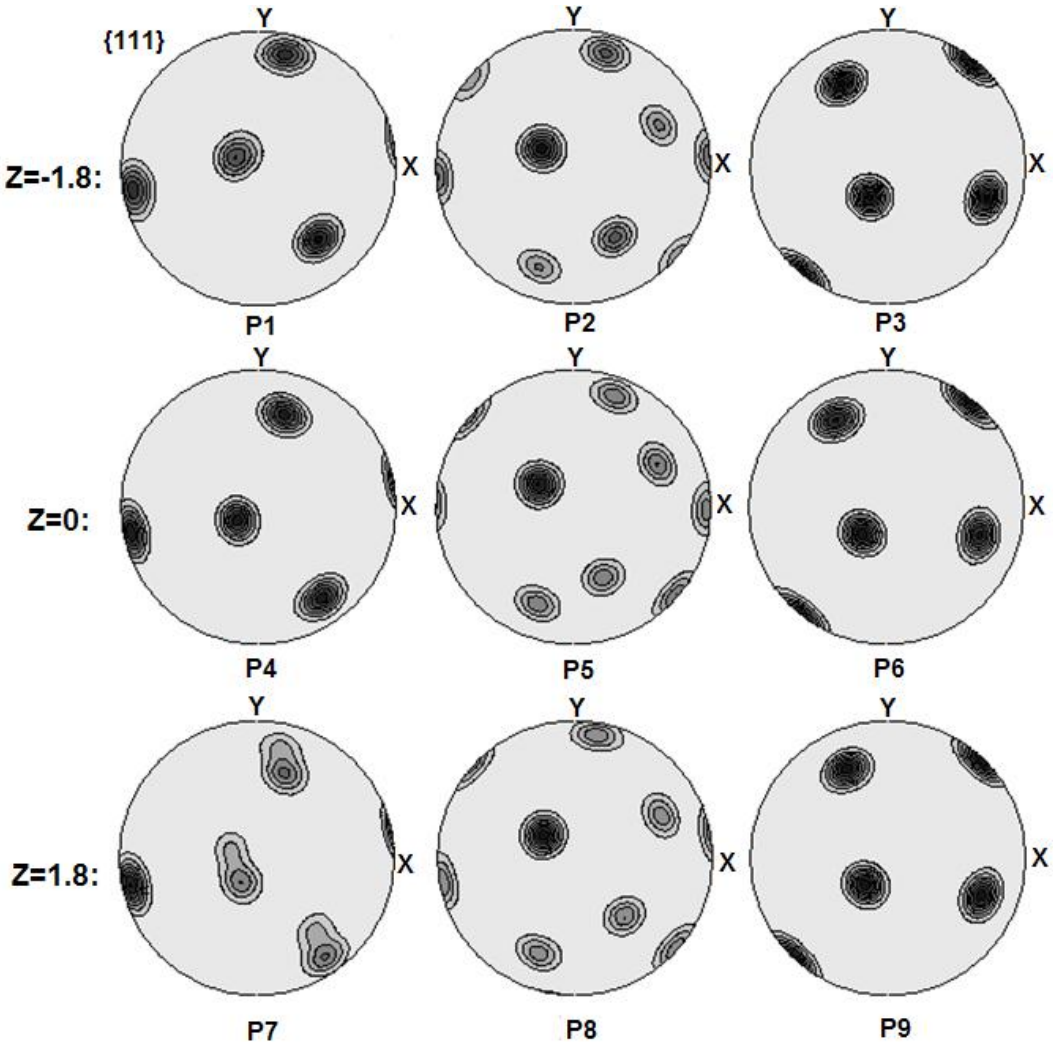

Fig. 4.10 Simulated {1 1 1} pole figures for the selected positions marked in Fig. 4.8 according to the three-dimensional CPFEM simulation of the ECAP process of aluminium single crystal.

The crystal rotation patterns of aluminium single crystal are analyzed based on the three-dimensional CPFEM simulation results using the method proposed by Wert and et al. [234]. Figs. 4.5(a), (b) and (c) show the results for lines of Z=-1.8, Z=0 and Z=1.8, respectively. As can be seen, there are similar crystal rotations for three lines, which are also similar to the result from the two-dimensional CPFEM simulation. The predominant crystal rotation is around the Z axis and the crystal rotation angles around X axis and Y axis are much smaller. Three matrix bands predicted by two-dimensional simulation, marked in Fig. 4.11(d), are also seen by three-

dimensional simulation. The corresponding Z-axis crystal rotation angles are about 60°, 0°, and 90°, respectively.

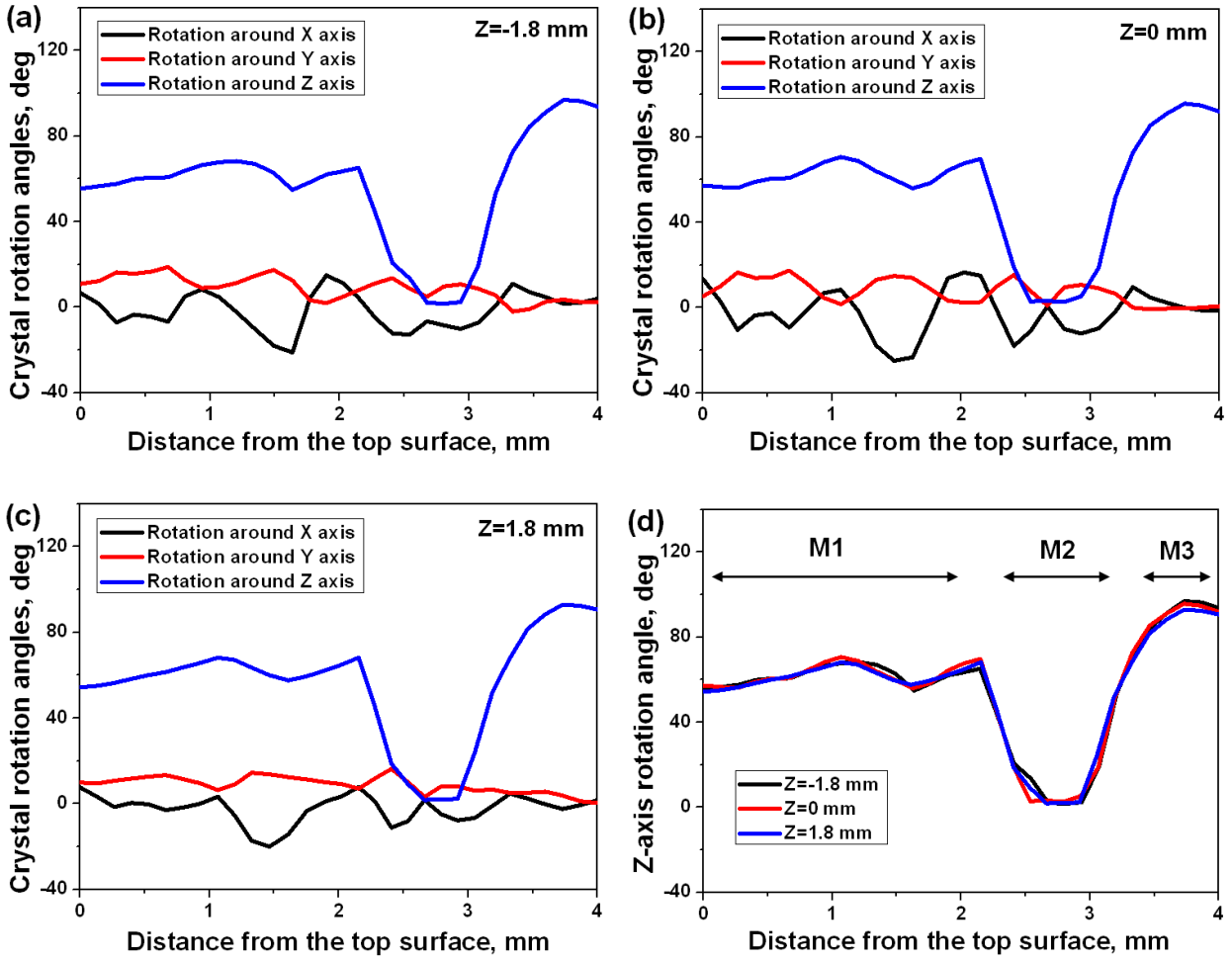

Fig. 4.11 Variation of crystal rotation angles around the X, Y and Z axes along the thickness direction in the steady-state deformation region. (a) on the line of Z=-1.8 mm; (b) on the line of Z=0 mm; (c) on the line of Z=1.8 mm; (d) comparison of the crystal rotation angles around the Z axis on the three selected lines Z=-1.8, 0 and 1.8 mm.

In this section, it has been found that the three-dimensional CPFEM simulation leads to a similar distribution of strain and texture evolution along the thickness direction to the two-dimensional simulation. However, the CPU time for the three-dimensional simulation is about 7.5 times more than the two-dimensional simulation which is around one week. Therefore, it is reasonable to assume the plane strain condition in the simulations of the ECAP process for the

die with a square cross-section and all the remaining simulations will be two-dimensional to save computing time. It should be mentioned that, the other solid elements have been tried during the simulation and the results indicated that the elements CPE4R (two dimensional model) and C3D8R (three dimensional model) lead to shorter computation time and reasonable agreement with experimental measurements.

4.3 Influence of Mesh Condition

According to Li et al. [142], the strain distribution is sensitive to the mesh conditions, even in a steady state deformation region during the ECAP process. This section will examine the influence of mesh condition on deformation behaviour and texture evolution using the CPFEM model introduced in Chapter 3.

The simulated material is still aluminium single crystal with the same initial crystallographic orientation as Sections 3.3.1. The same geometries of the ECAP die and sample are used. Four different meshes are studied, using 10, 20, 34, and 60 elements along the thickness direction, respectively. The corresponding number of the total elements are 600, 2400, 6369, and 12000, as shown in Fig. 4.12. They will be called Mesh 600, Mesh 2400, Mesh 6369 and Mesh 12000 in the following text, respectively.

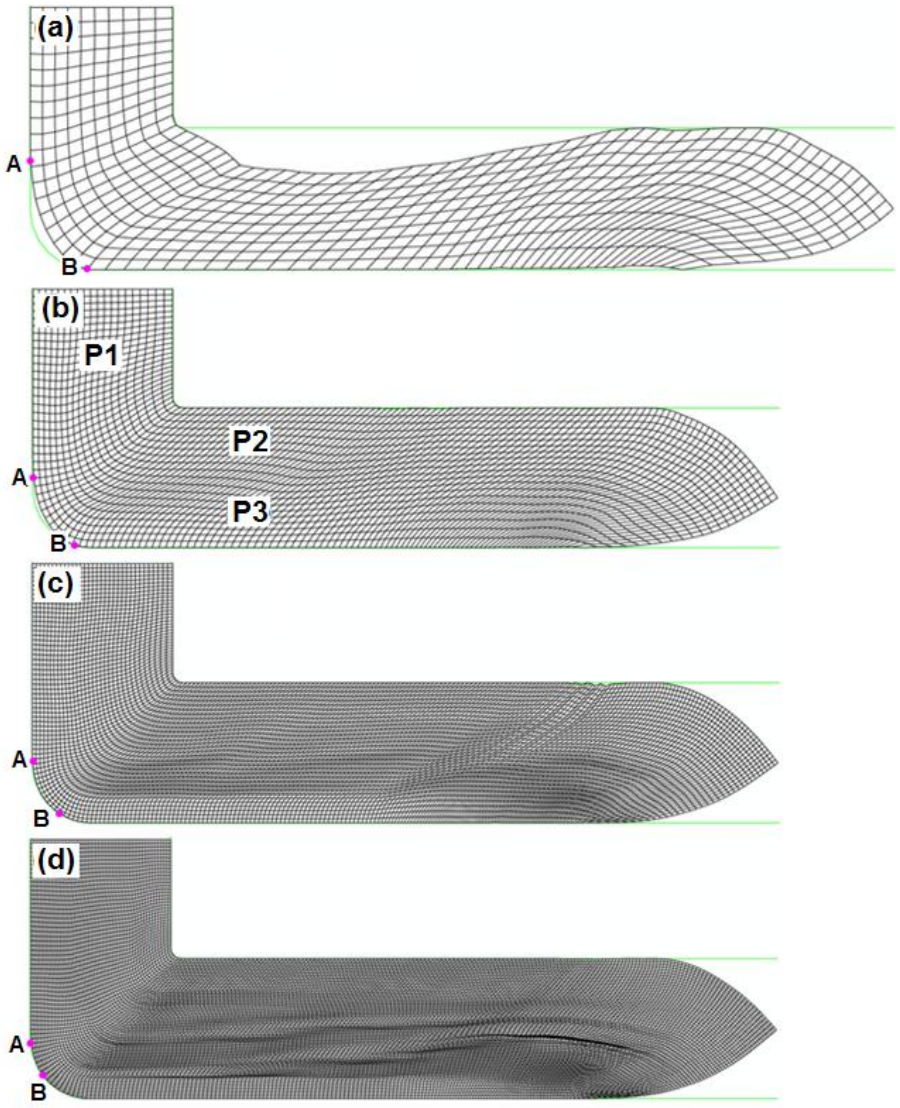

Fig. 4.12 Comparison of mesh distortions in the deformed aluminium single crystal between different mesh conditions. (a) Mesh 600, (b) Mesh 2400, (c) Mesh 6369, and (d) Mesh 12000.

Fig. 4.12(a-d) shows the mesh distortions in the deformed billet for 600, 2400, 6369, and 12000 meshes, respectively. The significant difference between Mesh 600 and the other three meshes has been observed. In Fig. 4.12(a), very coarse mesh leads to a failure of filling the ECAP die. There is a large gap between the sample and the ECAP die in the outer corner and exit channel. The outer corner gap is represented by the arc of 'AB', as marked in Fig. 4.12(a). For Mesh 600 the sample undergoes both shear and bending during ECAP, and the corner gap decreases obviously as the number of elements increase from 600 to 6369. Mesh 12000 leads to a similar

corner gap to Mesh 6369, as shown in Fig. 4.12(c) and (d). Note that the mesh distortions in the bottom for Mesh 600 and 2400 are similar and they have been sheared more than those of Mesh 6369 and 12000, where the obvious rigid body rotation part can be observed.

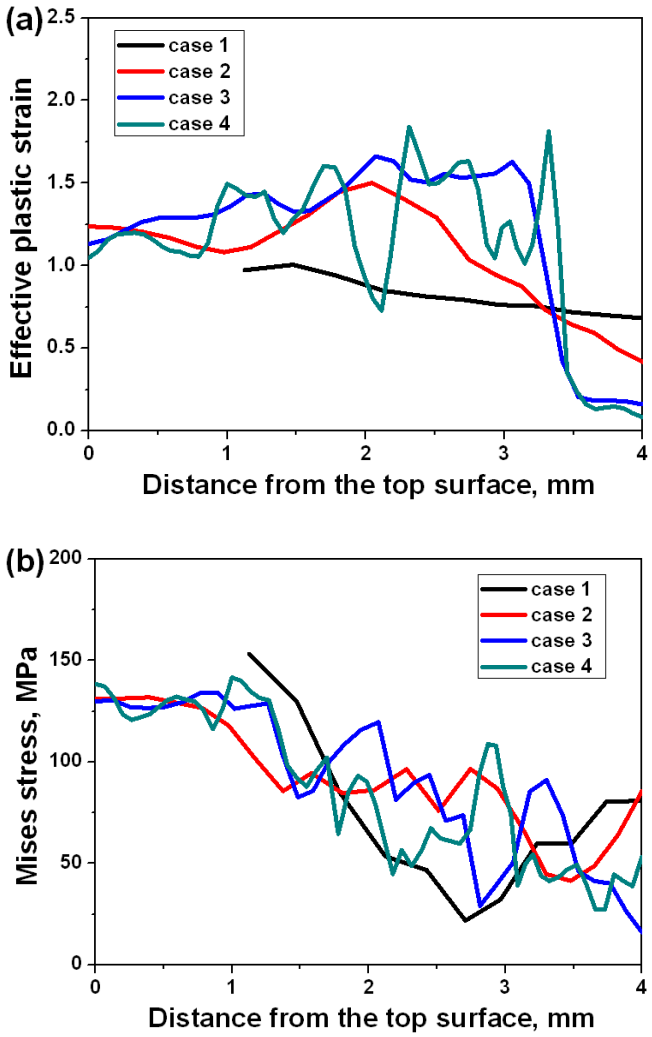

Fig. 4.13 Variation of (a) effective plastic strain, and (b) von Mises stress along the thickness at different mesh conditions.

Fig. 4.13 shows a comparison of plastic strain along the thickness direction for different meshes. It is obvious that Mesh 600 and Mesh 2400 fail to simulate the rigid body rotation part in the bottom of the sample and both of them lead to a smaller strain than Meshes 6369 and 12000. The average values of the effective plastic strain along the thickness direction for Meshes 600, 2400, 6369, and 12000 are 0.818, 0.926, 1.287, and 1.275, respectively.

The influence of the mesh condition on texture evolution of aluminium single crystal during the ECAP process has also been studied. Three positions as marked in Fig. 4.12(b) are selected to plot {1 1 1} pole figures. As can be seen, Position P1 is in the entry channel before entering the PDZ area and Positions P2 and P3 are located in the exit channel. The corresponding {1 1 1} pole figures are shown in Fig. 4.14 and Position P1 is characterized as the initial crystallographic orientation for all the mesh conditions. For Mesh 600, as shown in Fig. 4.14(a), Positions P2 and P3 have similar crystallographic orientations which is an ~50° rotated component from the initial orientation around the Z axis in a counter-clockwise direction. Slightly larger rotation angles are observed in Fig. 4.14(b) for Mesh 2400 at both Positions P2 and P3 than for Mesh 600. The rotation angle is about 60° and a slight orientation scattering can also be observed at Position P3. In contrast, Fig. 4.14(c) shows similar pole figures for Mesh 6369 to Fig. 4.14(d) for Mesh 12000 at Positions P2 and P3. The {1 1 1} pole figure at Position P2 reveals a single crystallographic orientation with about 60° rotation from the initial orientation while the pole figure at Position P3 indicates the presence of both initial crystallographic orientation and the rotated orientations. Therefore, it can be concluded that texture evolution during the ECAP process has been significantly influenced by the mesh condition. Meshes 6369 and 12000 are able to capture the main characters of texture evolution of aluminium single crystal during ECAP and lead to a good agreement with the experimental results, as observed by Fukuda et al. [33]. In contrast, Meshes 600 and 2400 fail to predict accurate textures.

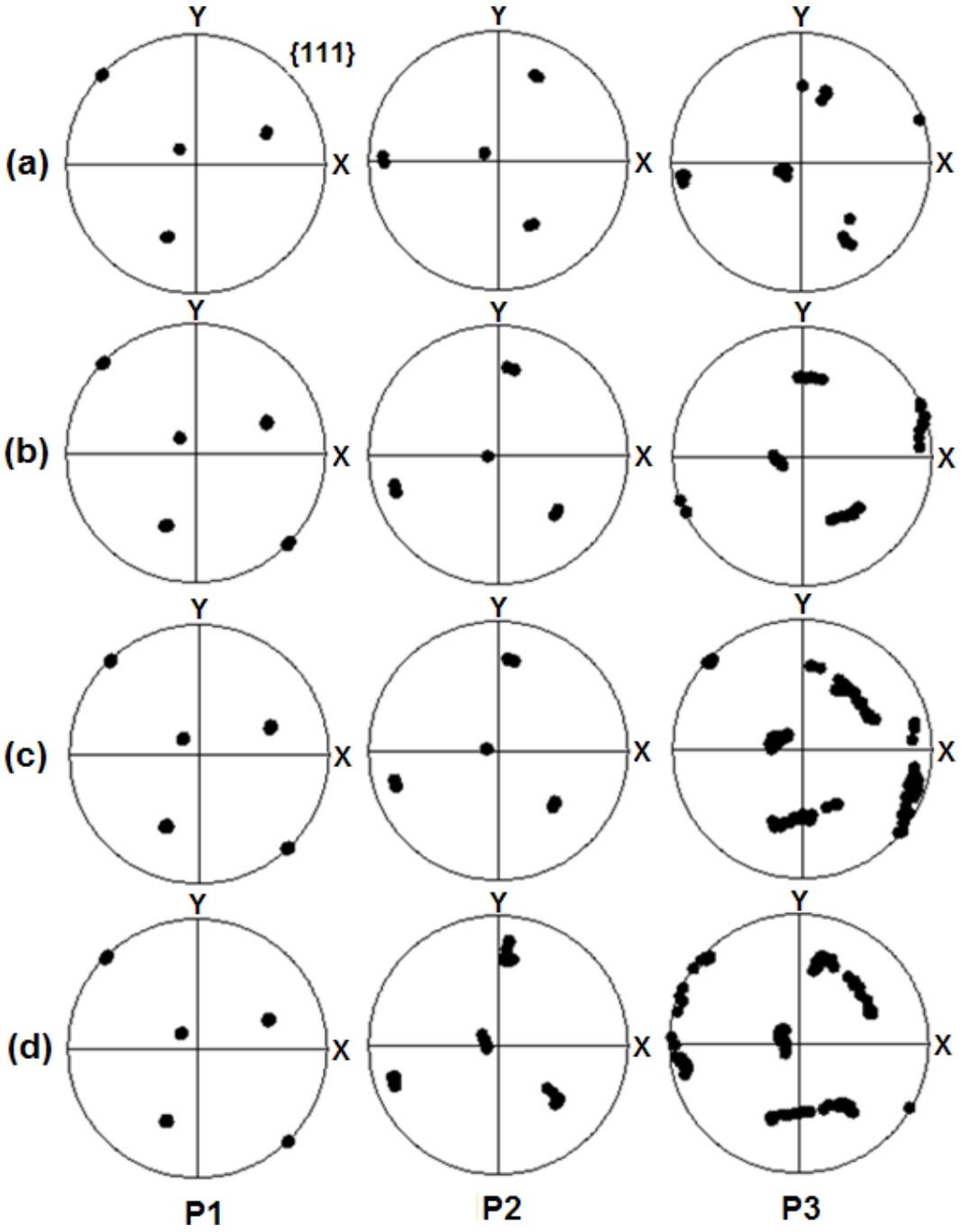

Fig. 4.14 Influence of mesh condition on the {1 1 1} pole figures for the selected positions as marked in Fig. 4.12(b). (a) Mesh 600, (b) Mesh 2400, (c) Mesh 6369, and (d) Mesh 12000.

4.4 Influence of Frictional Condition

(*This part has already been published in Journal of Materials Science (2010)*)

Up to now a number of classic FEM simulations have been conducted to investigate the influence of the frictional condition between the sample surfaces and die walls during the ECAP process [139, 141-144, 257]. All these studies adopted the classic constitutive law for plastic deformation, which is unable to predict texture evolution. One of the main objectives of this section is to investigate the influence of frictional condition on texture evolution during the ECAP process, which has not been seen in the published literature.

The Coulomb friction model is used in the simulations. The coefficient of friction varies from 0 to 0.2 with an increment of 0.05. Other simulation conditions are the same as the previous study in Section 4.2 and 4.3. Two-dimensional CPFEM simulations are carried out with Mesh 6369 to save computing time.

It is worthy of noting that the simulation with μ=0.2 could not be finished due to very poor convergence caused by severe mesh distortion. Discussion in the following text will be conducted for μ=0-0.15.

Fig. 4.15 shows the distributions of effective plastic strain rate ($\dot{\varepsilon}$), in the billets for different frictional conditions. It can be seen that deformation already occurs in a small area within the entry channel even for the frictionless condition shown in Fig. 4.15(a). When friction is applied to the interface between the wall of the die and the surface of the billet (Fig. 4.15(b)-(d)), deformation is induced in the vicinity of the right side interface in the entry channel which extends from the right side to the left side. Under a frictionless condition, the PDZ is relatively narrow but with friction the PDZ can be divided into two parts based on the pattern of $\dot{\varepsilon}$. The upper part of the PDZ is fan shaped and covers a major portion of the PDZ. The lower part of the PDZ includes two small deformed regions near the surface of the billet between which there is a region of rigid body rotation. A large corner gap exists for the frictionless case, while the corner gap almost disappears when the coefficient of friction is increased to 0.05. The billet has filled the whole corner of the die for cases with μ=0.1 and 0.15, which is consistent with results reported by Li et al. [59]. However, a careful inspection indicates that there is a non-contact area between points A and B in the outer corner of the die. This will intensify the inhomogeneous deformation in the billet.

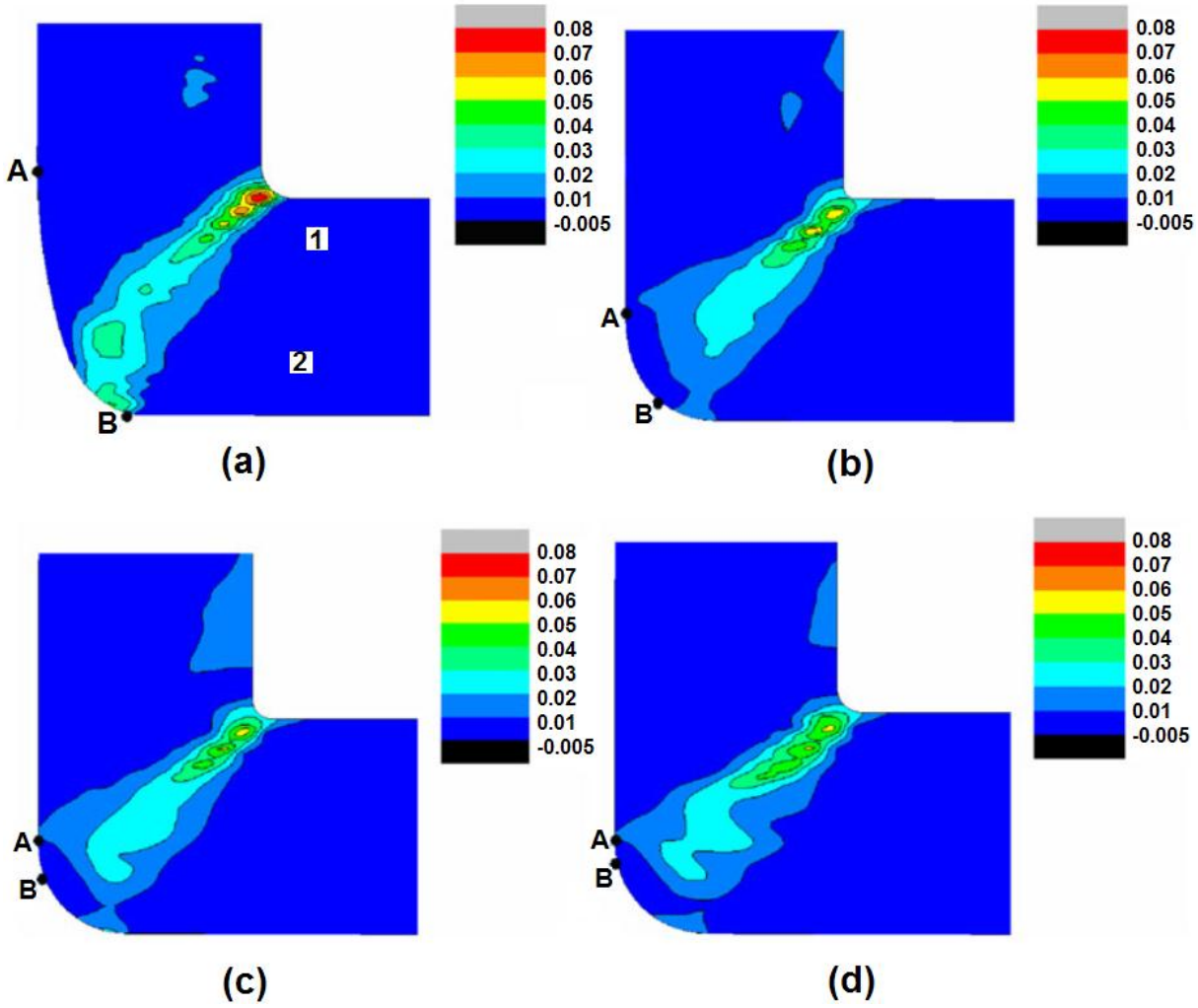

Fig. 4.15 Distribution of effective plastic strain rate in the billet during the ECAP process. (a) μ=0, (b) μ=0.05, (c) μ=0.1, and (d) μ=0.15.

The simulated {1 1 1} pole figures for four different friction coefficients were compared in Fig. 4.16 with the experimentally measured results at two selected positions labelled 1 and 2 in Fig. 4.15(a). At Position 1 (upper panel of Figure 4.16), the experimental observation shows that the structure remains a single crystal and the crystallographic orientation has been rotated from the initial orientation. Fukuda et al. [33] found that the rotation angle is 60° around the Z axis (Y axis in their paper) in a counter-clockwise sense. Fig. 4.16 shows that all the simulation results agree with the experimental measured result at Position 1. The measured pole figure at Position 2 reveals a rotated orientation and an initial orientation, but the simulation for the frictionless case only predicts the rotated orientation and the rotation angle is larger than the

experimental value shown in Fig. 4.16(b). By contrast, the simulations with μ=0.05 and 0.1 predict both the initial orientation and rotated component. When the friction coefficient is increased to 0.15, except for the initial orientation, an unexpected orientation appears in the pole figure (lower panel in Figure 4.16(e)). Comparisons in Figure 4.16 indicate that the coefficient of friction between 0.05 and 0.1 can provide good texture predictions.

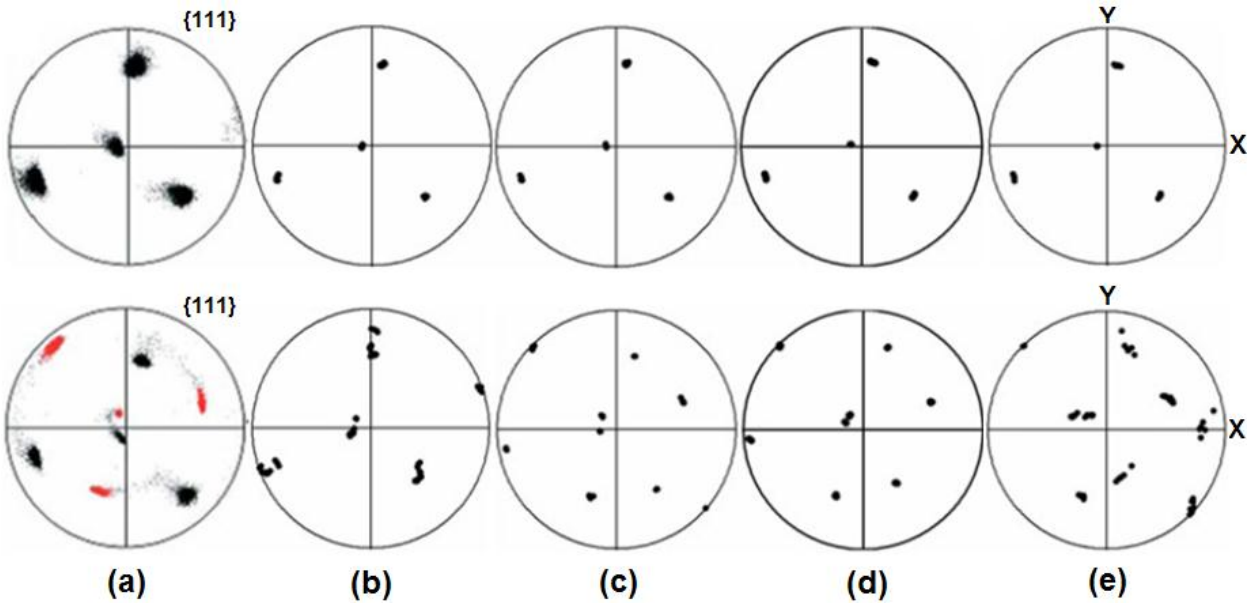

Fig. 4.16 Comparison of the {1 1 1} pole figures between the CPFEM simulations and experiment. The upper panel is for Position 1 and the lower panel is for Position 2. (a) Experiment [33], (b) μ=0, (c) μ=0.05, (d) μ=0.1, and (e) μ=0.15.

A quantitative analysis regarding the influence of the frictional condition on the crystallographic rotation angles was carried out using the partition method proposed by Wert et al. [234]. According to the results shown in Section 4.2, the crystallographic orientation rotates in three dimensions for this initial crystallographic orientation so only the rotation around the transverse direction (Z axis) will be considered and discussed in this section. Fig. 4.17 shows the contour maps of the crystallographic orientation rotation angles for all cases. As mentioned before, a positive value of the rotation angle indicates a counter-clockwise rotation and a negative value indicates a clockwise rotation. For the convenience of analysis, the billet is divided into three regions marked as A, B, and C, along the billet thickness as shown in Fig.

4.17(a). Regions A, B, and C roughly correspond to the three matrix bands M1, M2, and M3 shown in Fig. 4.2(d), respectively. All the simulations predict a similar 60° Z-axis rotation in the upper part of the deformed billet, namely Region A. It seems that friction does not affect the texture in the main portion of Region A. A careful inspection reveals that the Z-axis rotation angle in the vicinity of the top surface of the deformed billet increases slightly with the coefficient of friction due to the direct frictional effect on the top surface. The comparison in Fig. 4.17 shows that friction significantly affects texture evolution in the lower part of the deformed billet, namely Regions B and C. As shown in Fig. 4.17(a), the frictionless condition does not generate the initial orientation in Region B. A striation with a Z-axis rotation angle of about 25° is inserted in the region with 60° Z-axis rotation. In addition, the Z-axis rotation angle in Region C for the frictionless case is smaller than other cases while Fig. 4.17(b) and (c) shows that cases of μ=0.05 and 0.1 exhibit similar results. Three matrix bands for both cases are parallel to the X axis which indicates that the texture is heterogeneous along the billet thickness, but it is relatively homogeneous along the X axis, at least in the steady state region. When a higher friction (μ=0.15) is applied, as shown in Fig. 4.17(d), Region C near the bottom surface has a similar rotation angle to μ=0.05 and 0.1, but the case of μ=0.15 has a different texture pattern in Region B where the texture is no longer homogeneous along the X axis. This region is partitioned into several small matrix bands. Based on above analysis, it can be found that the major difference in texture for various friction coefficients are located in Region B where the frictionless condition even does not generate an initial orientation. Continuous matrix bands with an initial orientation are formed in the cases of μ=0.05 and 0.1, while a higher friction (μ=0.15) leads to the development of separate small matrix bands in Region B. It is clear that texture evolution in Region B was inherited from the PDZ so it can be concluded that the frictional condition affects the texture in Region B through the PDZ. The inhomogeneous matrix bands in Region B also results in slightly more crystallographic rotation around the X and Y axes in the {1 1 1} pole figure, as shown in Fig. 4.16(e). Friction increases the back pressure in the exit channel and results in a smaller outer corner gap. The difference in the corner gap significantly affects the distribution of stresses in the lower part of the PDZ, but it has very little effect in the upper part of the PDZ. Therefore, texture in Region B depends on the frictional

condition, while texture in Region A does not change. Texture in Region C is mainly determined by the rigid body rotation, which is strongly relative to the die geometry. Therefore, a slight influence of friction on texture in Region C is observed.

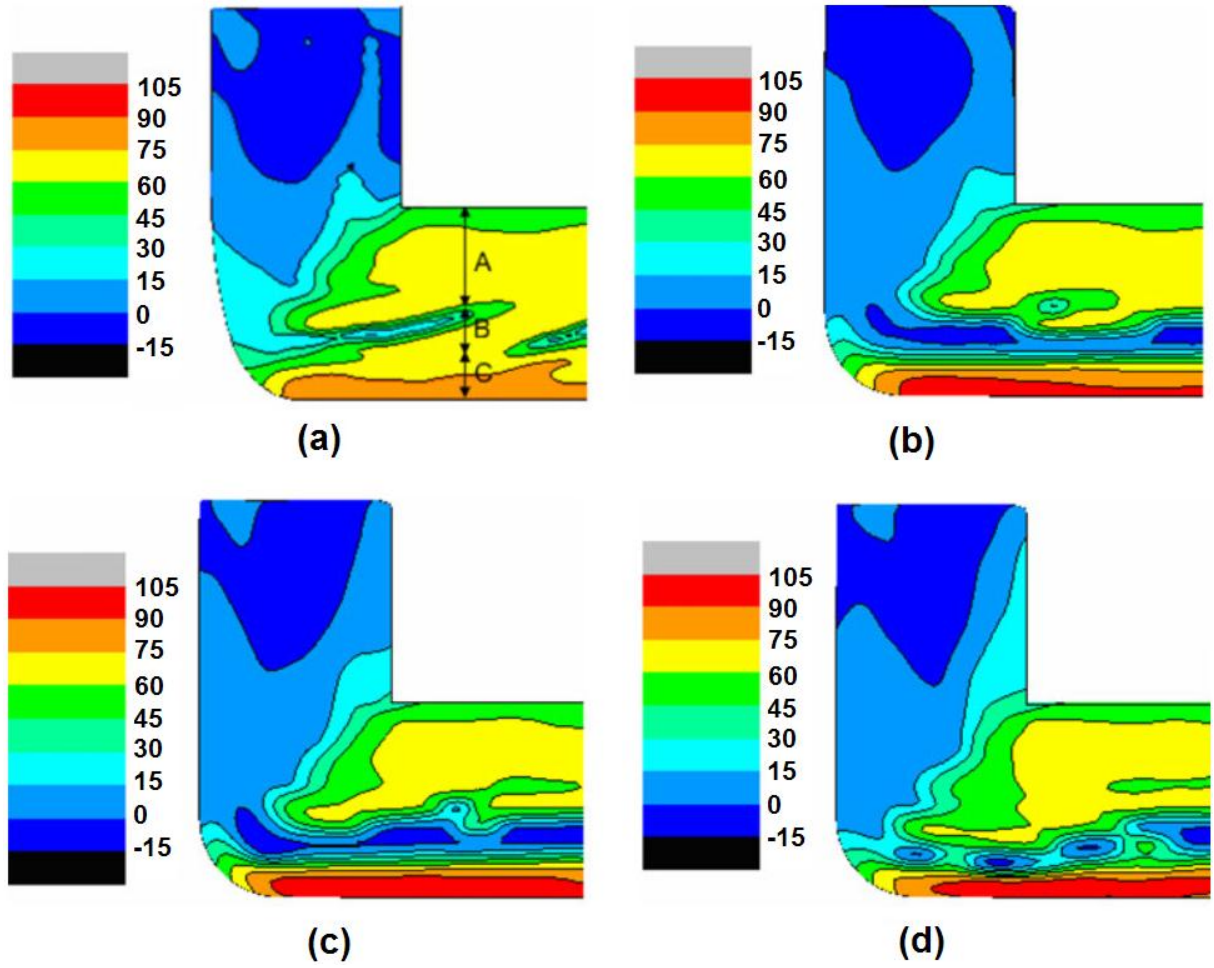

Fig. 4.17 Crystal rotation angles around the transverse direction (Z axis) during the ECAP process for different coefficients of friction. (a) μ=0, (b) μ=0.05, (c) μ=0.1, and (d) μ=0.15.

According to the distributions of the effective plastic strain rate and crystal rotation angles, it can be concluded that μ=0.05 performs better so the remaining study of the ECAP process of aluminium single crystals will be conducted using the coefficient of friction of μ=0.05.

4.5 Influence of Sample Size

(*This part has already been published in Computational Materials Science (2013)*)

Due to the promising properties of UFG materials produced by the ECAP process, a few successful attempts to scale up the sample to a larger size for potential use in industrial applications [258-263] have been reported. Till now, the mass of the largest ECAP sample can reach 32.7 kg for aluminium alloy and 110 kg for copper alloy [263], but the influence of sample size during the ECAP process has only recently been discussed and very few studies have been reported. Berbon et al. [93] was the first one to investigate the sample size and stated that the result was significantly influenced by friction when the cross-section of the sample was less than 5 mm. This has not been confirmed in the experiment by Fukuda et al. [33, 157, 179] and Furukawa et al. [96, 158, 160, 161, 180]. In addition, the previous study [264] suggested that 5 mm was not the lowest limit for a satisfactory ECAP process. Meanwhile, Horita et al. [258] have experimentally investigated the effect of the sample dimension on the grain refinement and mechanical properties of aluminium alloys with diameters ranging from 6 mm to 40 mm. Suo and co-workers have examined the strain inhomogeneity by classic FEM simulation with sample varying in diameter from 8 mm to 20 mm [262]. However, the influence of the sample size on texture evolution during the ECAP process has not been reported.

This section studies how the sample size influences the deformation and texture evolution of aluminium single crystals during the ECAP process. To the author's knowledge, this is the first crystal plasticity FEM study to investigate the relationship between texture and sample dimension during ECAP. The initial crystallographic orientation is the same as that described in Section 3.3.1 and the coefficient of friction is set to 0.05. The two-dimensional simulations have been conducted and all the samples meet the condition where the length (l) is not less than five times the width of the sample (d), in order to reach steady-state deformation. Four different cases with sample width varying from 2 mm to 40 mm were investigated. In Case I: d=2 mm and l=10 mm; Case II: d=4 mm and l=20 mm; Case III: d=10 mm and l=55 mm; and in Case IV: d=40 mm and l=200 mm.

First, the influence of sample size on the required load has been studied. In Fig. 4.18(a), the load as a function of the ratio of displacement to the sample width is plotted for Case I. It is apparent that deformation during the ECAP process takes three steps, which is similar to the

results reported by Kim [265]. The deformation history during ECAP process has been recorded as shown in Fig. 4.19. In Step 1 the load increased rapidly from zero because the initial undeformed head part of the sample (marked as points 'AB' in Fig. 4.19) goes through the PDZ and the volume of the deformed part increases. In Step 2 the front part of the sample exits the PDZ and starts bending towards the upper surface of the exit channel and the load increases slowly to the peak load point, as shown in Fig. 4.18(a). Step 3 starts when there is enough interaction between the sample and the exit channel, where the load decreases gradually due to a decrease in the contact area within the entry channel. The load-displacement curves for four cases I-IV are compared in Fig. 4.18(b). Similar trend is observed, apart from a slight discrepancy due to the frictional effect. The frictional effect will increases as the sample becomes larger even if it is not the dominant factor in determining the ECAP load [258]. The peak loads of four cases have been summarized in Table 4.1.

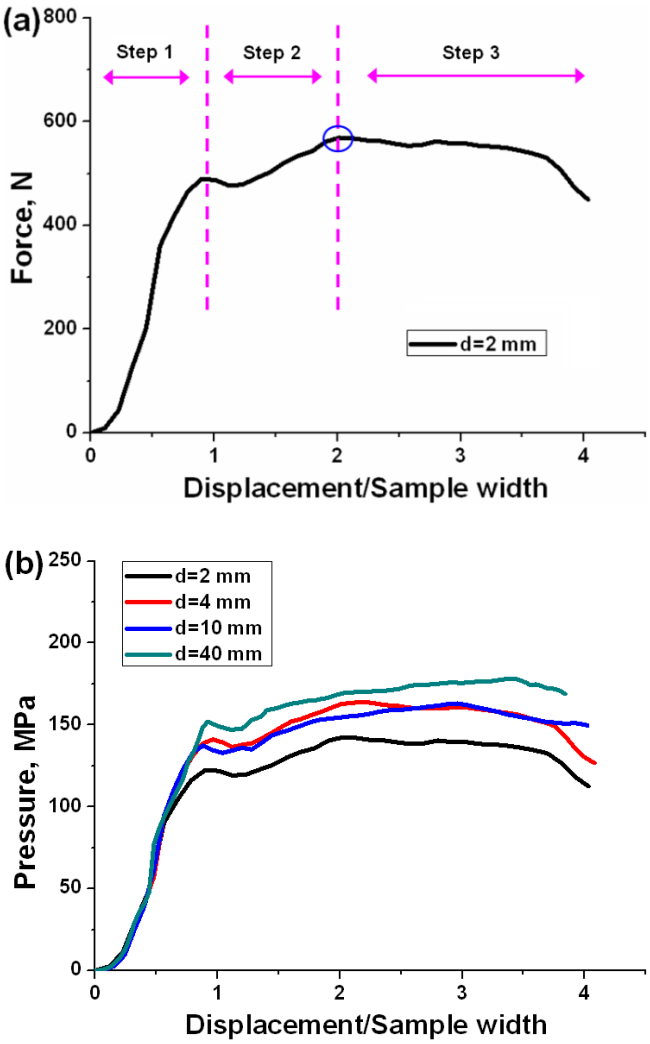

Fig. 4.18 Simulated load curves for aluminium single crystals having different sample widths varying from 2 mm to 40 mm during the ECAP process.

Fig. 4.19 shows the simulated mesh distortions in the deformed sample having a width of d=2 mm. The distortion here is not uniform along the width even in the steady-state region. In the enlarged upper and centre areas, the grids change in shape from a rectangle in the entry channel to a parallelogram after passing through the PDZ, but with different angles (θ) as shown in Fig. 4.19(d), which is about 40.3° in the upper area and 26.8° in the centre, respectively. In contrast, there is almost no shearing in the shape of the rectangular grid in the lower area as it passes through the PDZ. There are similar deformed meshes for the other three cases, but they are not presented in this section. The deformation heterogeneities in these

three regions are consistent with the work performed by Kalidindi et al. [55], where the macroscale deformation fields during ECAP were idealized as a set of equi-spaced streamlines.

Table 4.1 The average values of the effective plastic strain ($\bar{\varepsilon}$), shear strength ($\bar{\tau}_c$), von Mises stress ($\bar{\sigma}$), peak force, and the deformation inhomogeneity index (C_i) along the width of the sample after the ECAP process.

Cases	Peak force (N)	$\bar{\varepsilon}$	$\bar{\tau}_c$ (MPa)	$\bar{\sigma}$ (MPa)	C_i
I	569	1.178	46.603	92.132	1.571
II	2621	1.161	45.084	87.622	1.267
III	16307	1.205	42.709	84.717	1.456
IV	281760	1.159	40.499	82.349	1.325

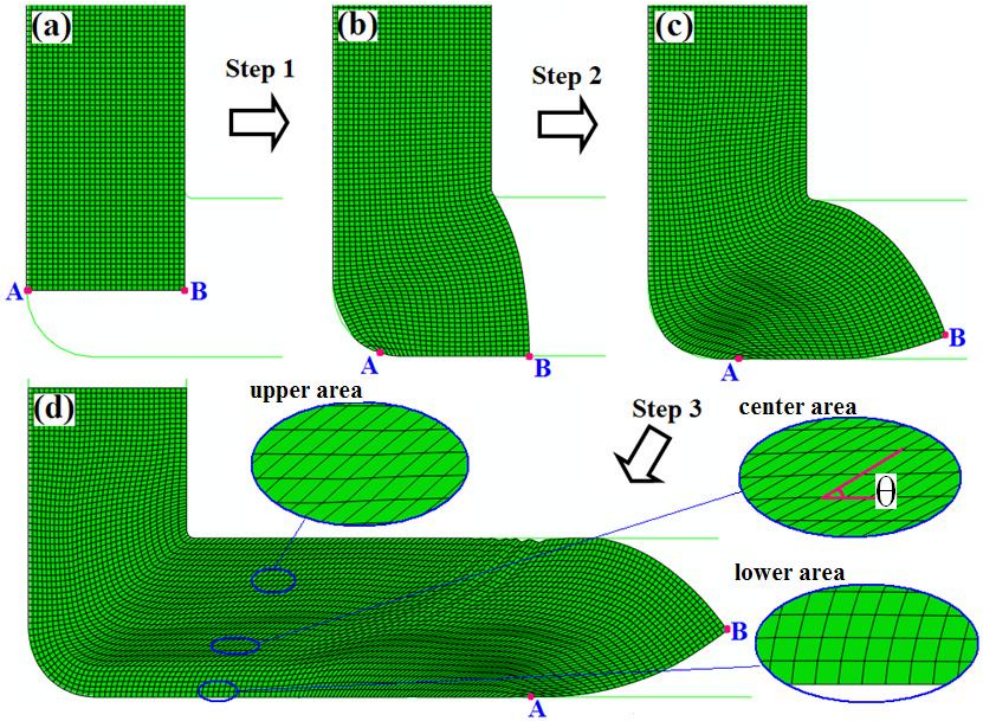

Fig. 4.19 The deformation history of the ECAP process and the simulated mesh distortions for the sample width of d=2 mm.

The distribution of the calculated shear strength (τ_c) along the width of the sample in the steady state region after ECAP have been shown in Fig. 4.20. It is obvious that approximately three deformation regions along the width of the sample, i.e. the upper half part, the centre region between 1/2 and 3/4 of the width from the top surface, and the lower quarter region, can be distinguished. The result in the upper region is relatively uniform, unlike those in the centre and lower regions. As can be seen, four cases have shown similar trends except for a slight decrease in the shear strength as the sample width increases. It is also interesting to note that almost the same results are obtained for the larger samples, e.g. case III and case IV, as shown in Fig. 4.20.

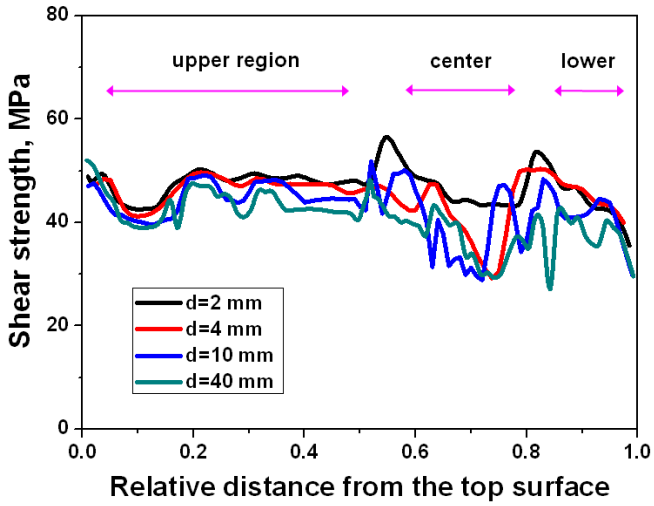

Fig. 4.20 Distribution of calculated shear strength along the width of the sample of aluminium single crystals with d=2-40 mm after the ECAP process.

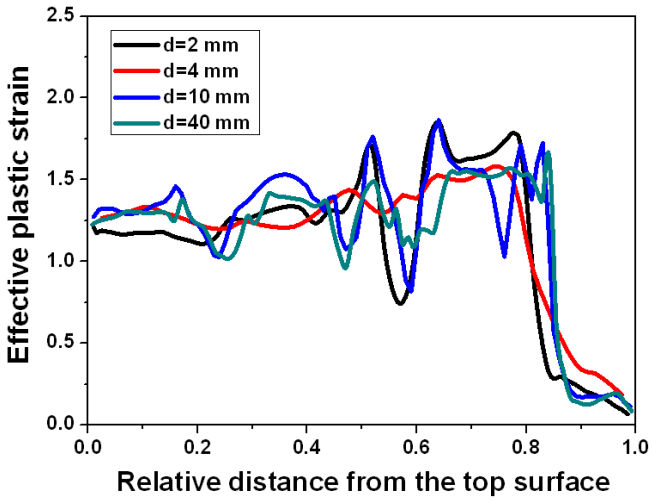

Figure 4.21 Distribution of the calculated effective plastic strain along the width of the sample of aluminium single crystals with d=2-40 mm after the ECAP process.

Fig. 4.21 and Fig. 4.22 show the distributions of the effective plastic strain and von Mises stress (σ) along the width of the sample, respectively. Very similar results are observed for all cases, except for a minor discrepancy in the smallest sample size (case I) which is affected the most by the frictional condition. The smallest strain and stress are located at the bottom of the sample, independent of the width since the deformation in this region is characterized as rigid body rotation due to the presence of an outer corner angle, as shown in Fig. 4.19.

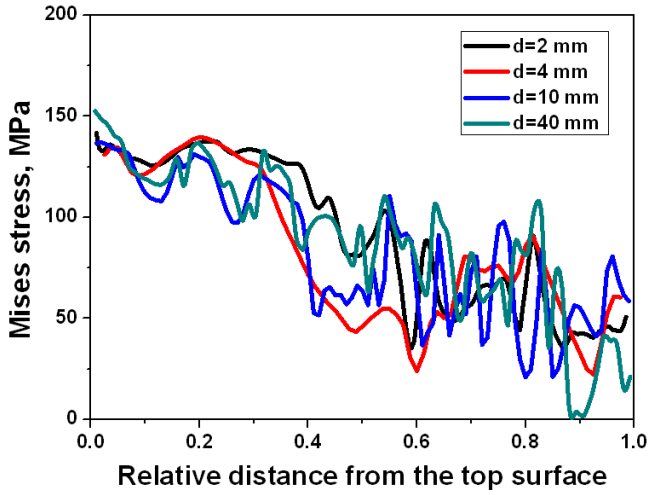

Fig. 4.22 Distribution of the calculated von Mises stress along the width of the sample of aluminium single crystals with d=2-40 mm after the ECAP process.

The deformation inhomogeneity index is calculated according to the Equation (4.1) for all four cases listed in Table 4.1. Moreover, the average values of the shear strength ($\bar{\tau}_c$) and von Mises stress ($\bar{\sigma}$) are also calculated based on the simulation results. The deformation is very inhomogeneous along the width of the sample for all four cases. The average value of simulated effective strain does not vary much among these samples. All cases have a similar deformation inhomogeneity index C_i as shown in Table 4.1. In Fig. 4.23(a), both $\bar{\tau}_c$ and $\bar{\sigma}$ show a similar tendency of decreasing as the sample width increases from 2 mm to 10 mm and dropped slightly from 10 mm to 40 mm. Fig. 4.23(b) reveals a similar trend for the average of effective plastic strain which is consistent with the theory suggested by Iwahashi [104].

To better understand the influence of the sample width on the deformation heterogeneity, the distribution of effective plastic strain rate representing the plastic deformation zone was studied. The distribution of component $\dot{\varepsilon}_X$ is shown in Fig. 4.24 for all the samples. The simulated PDZ shapes are consistent with the results for strain hardening materials in Ref. [142]. As can be seen, the magnitude of the effective plastic strain rate decreases gradually from the inner corner to the outer corner. The PDZ is a narrow banded region at the inner corner which becomes broader along the intersecting plane of the entry and exit channels, which means that the inhomogeneous PDZ leads to the three inhomogeneous plastic deformation areas shown in Fig. 4.19(d) and a non-uniform distribution of the shear strength, von Mises stress, and effective plastic strain along the width of the sample as shown from Fig. 4.20 to Fig. 4.22.

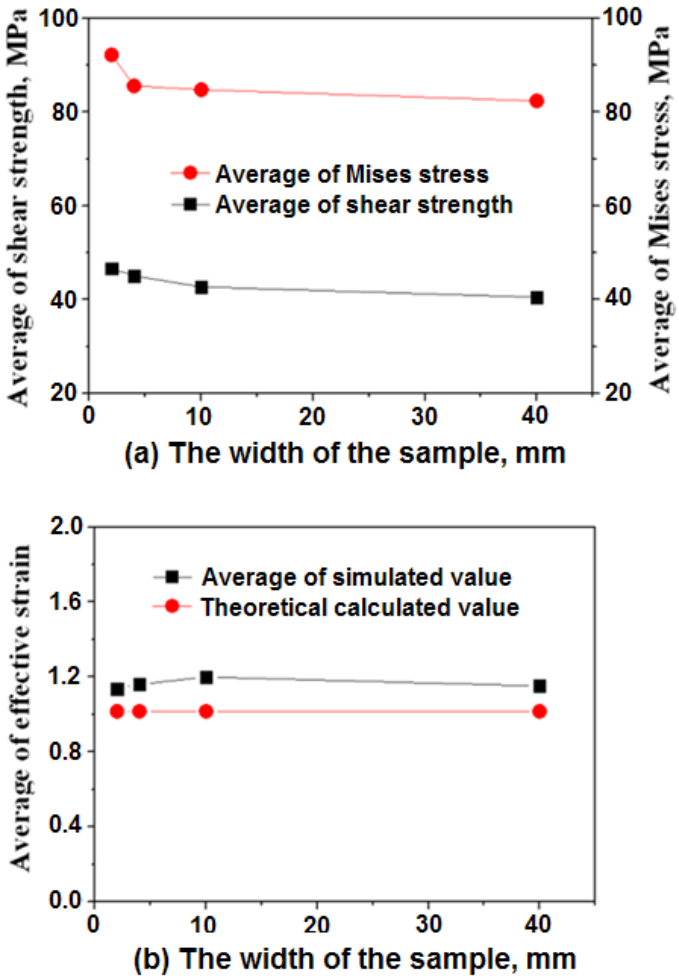

Fig. 4.23 (a) The deviation of the average values of shear strength and von Mises stress along the width of the sample for all four cases. (b) Comparison between the calculated effective strain and theoretical value during the ECAP process.

In the previous chapter the activity of slip systems of aluminium single crystal during the ECAP process were examined at a sample width of 4 mm. Here, a comparison for different sample widths has been done. According to the results shown in Fig. 4.20, the deformation is not uniform along the sample width and three macroscale deformation fields have developed. Therefore, three elements representing these regions are studied, i.e. Element I belongs to the upper region, Element II belongs to the center region, and Element III is located at the lower region.

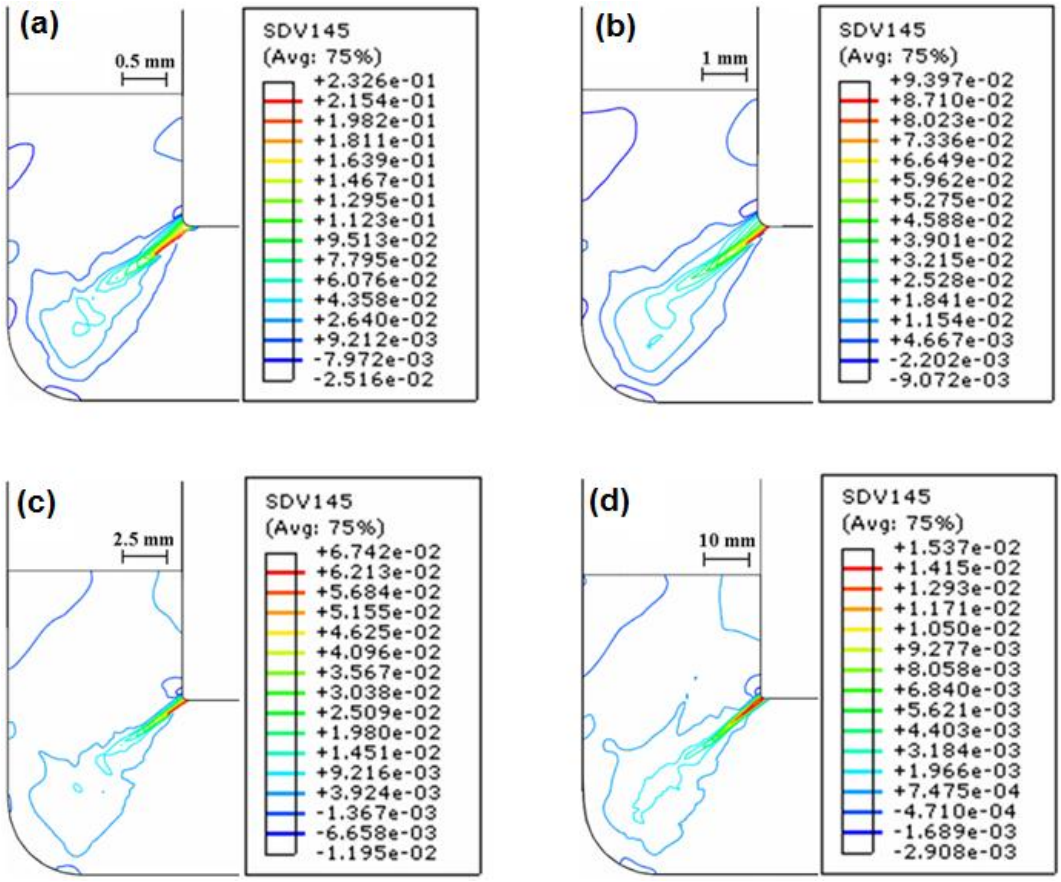

Fig. 4.24 Distribution of the effective plastic strain rate component $\dot{\varepsilon}_X$ in the plastic deformation zone for different sample widths during the ECAP process.

The results for a sample width of d=2 mm are shown in Fig. 4.25 as a function of the ECAP time, where the shear rates are zero before entering and exiting the PDZ. It also shows that it takes the shortest time to pass through the deformation zone in the upper region, which is consistent with the shape of the PDZ (a narrow banded region at the inner corner becomes wider towards the outer corner) as indicated in Fig. 4.25. For Element I in the upper region the results reveal that multi-slip systems are activated simultaneously. The slip system c1 ((1 -1 1)[0 1 1]) has the largest magnitude of shear rate of ~0.25, followed by the slip systems d1 ((1 1 -1)[0 1 1]), d2 ((1 1 -1)[1 0 1]) and b1 ((-1 1 1)[1 0 1]). It should be noted that the slip systems c1 and d1 have the same slip direction [0 1 1], and d2 and b1 have the same slip direction [1 0 1] as indicated in Table 4.2, whereas in the center region there is a single dominant slip system a3, (1 1 1)[-1 1 0],

which is consistent with the initial orientation. The shear rates of these slip systems are very small in the lower region due to the rigid body rotation in the outer corner of the ECAP die.

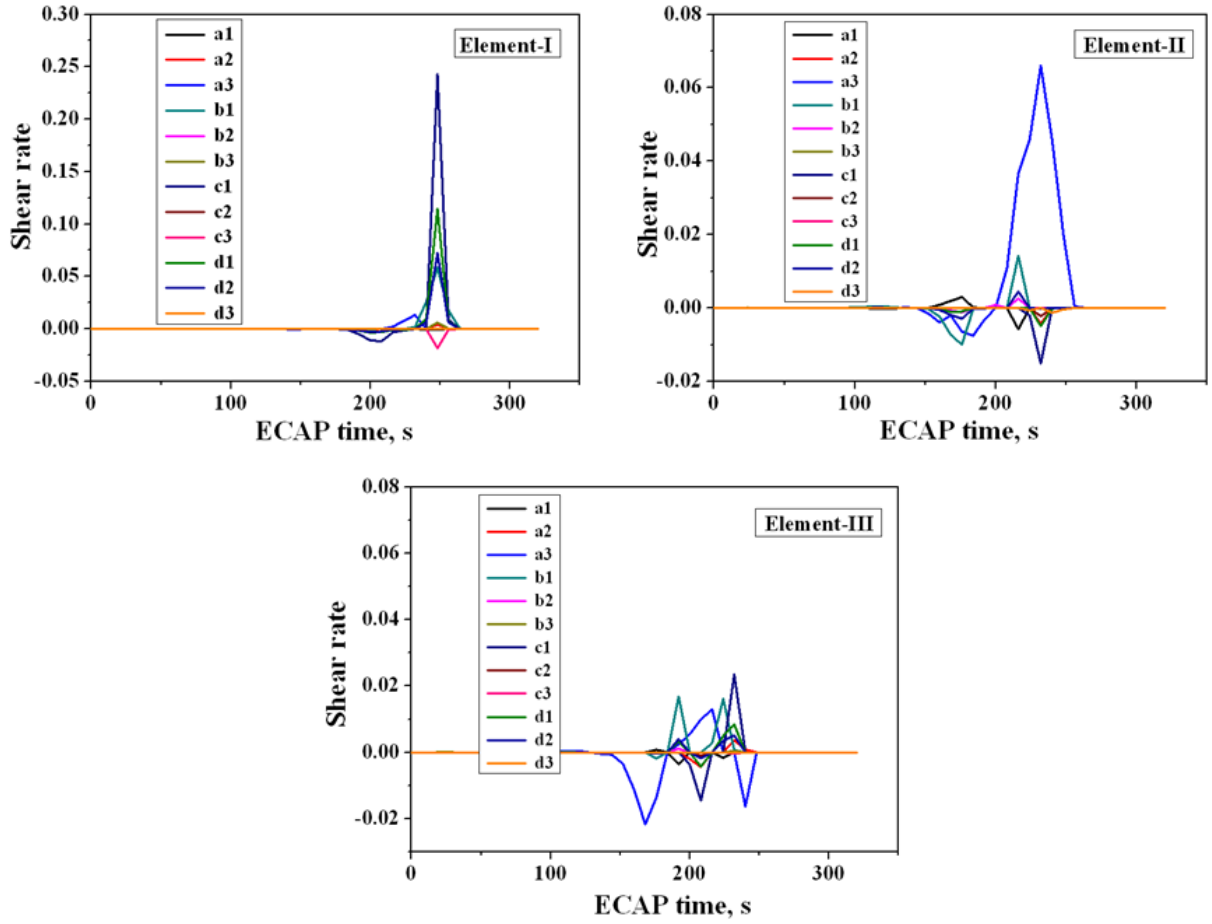

Fig. 4.25 The shear rates for three selected elements in the deformed sample with d=2 mm as a function of ECAP time: Element-I belongs to the upper region, Element-II belongs to the center region and Element-III belongs to the lower region.

The results for case II can be found in Section 4.1. Fig. 4.26 and Fig. 4.27 show similar tendency for Case III (d=10 mm) and for Case IV (d=40 mm), respectively. However, the magnitude of the shear rates decreases rapidly as the width of the sample increases, which is 0.25 at d=2 mm and 0.04 at d=40 mm for slip system c1 in the upper region of the deformed samples. The shear rate decrement is attributed to the same processing velocity being applied to all samples. It takes longer to pass through the deformation zone when the die channel is wider, and it results in a lower strain rate and strain rate gradient in the PDZ during the ECAP process.

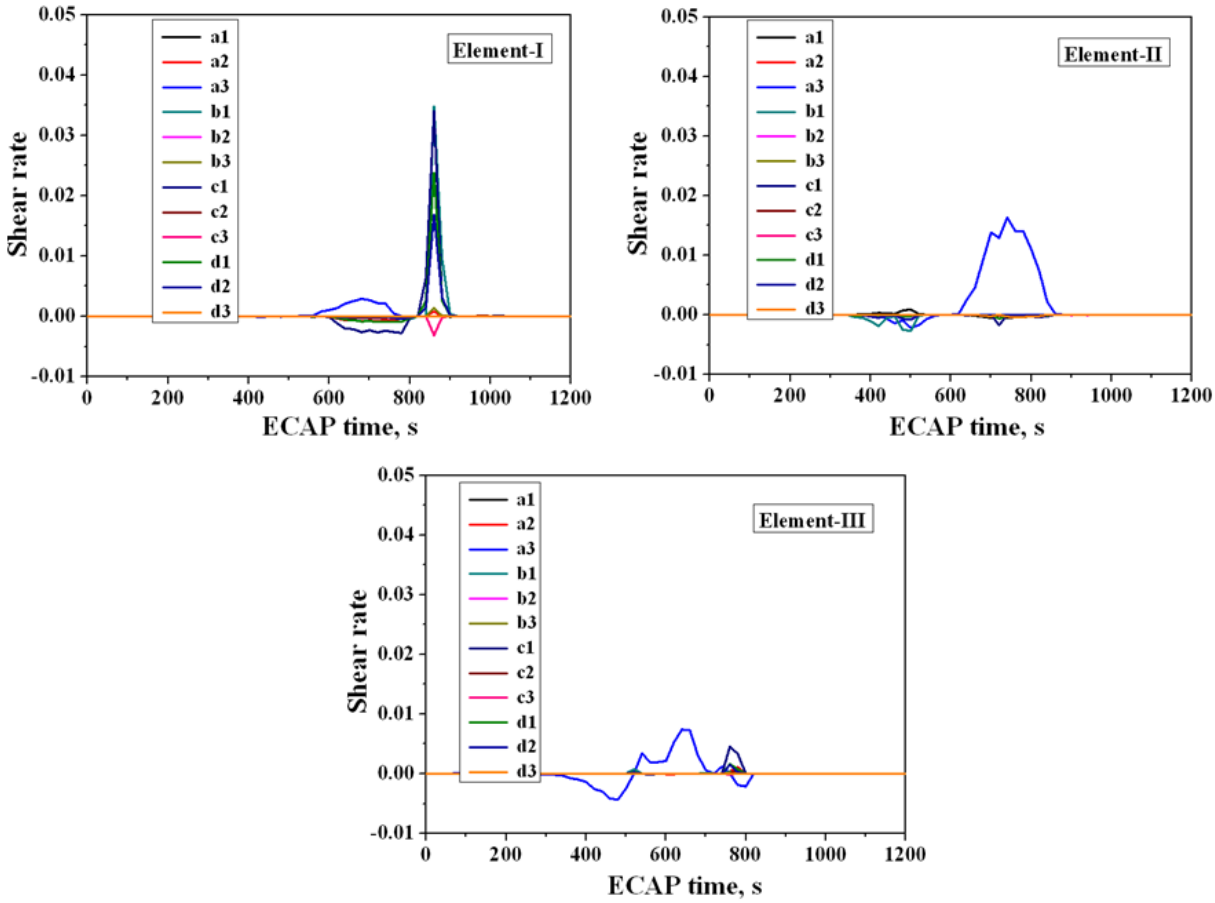

Fig. 4.26 The shear rates for three selected elements in the deformed sample with d=10 mm as a function of ECAP time: Element-I belongs to the upper region, Element-II belongs to the center region, and Element-III belongs to the lower region.

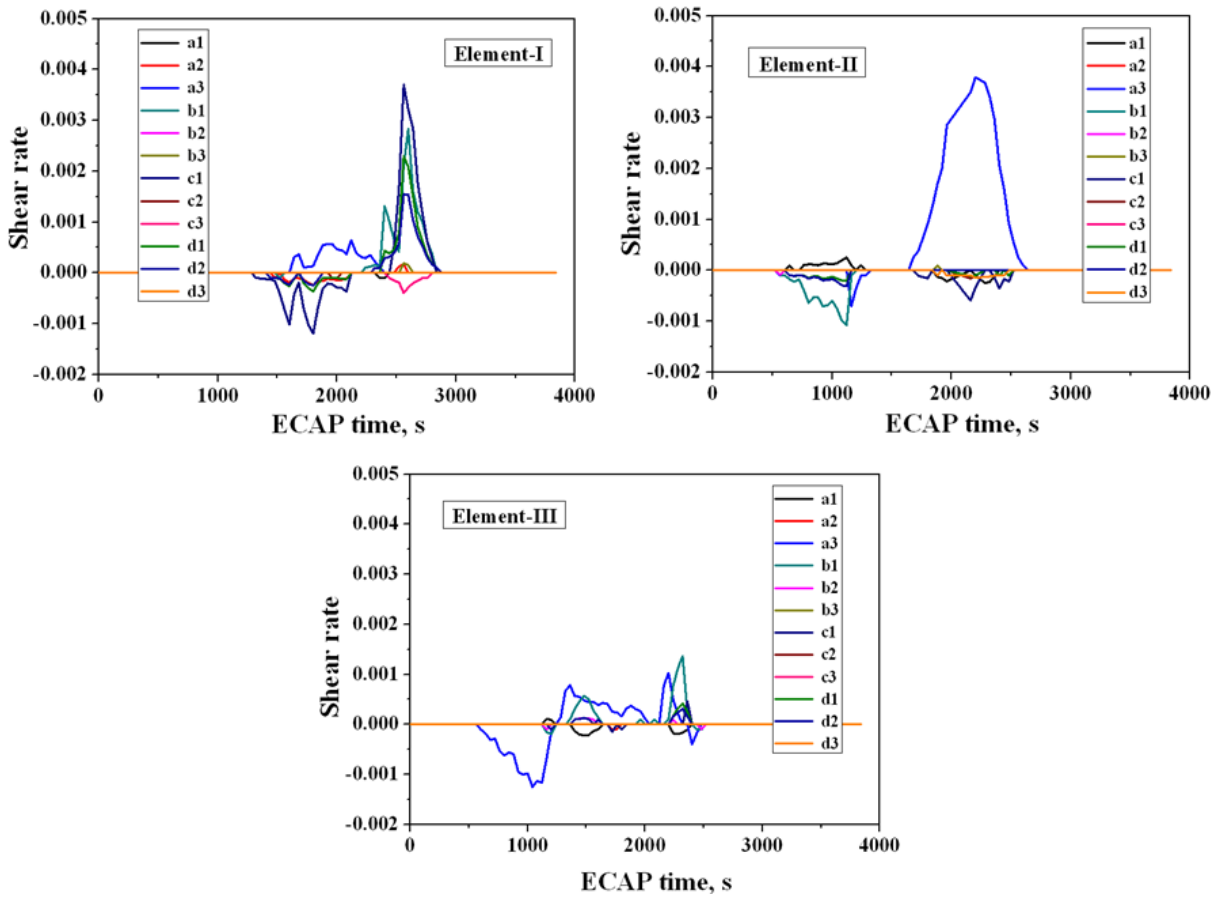

Fig. 4.27 The shear rates for three selected elements in the deformed sample with d=40 mm as a function of ECAP time: Element-I belongs to the upper region, Element-II belongs to the center region, and Element-III belongs the lower region.

Fig. 4.28 shows the contour maps of crystallographic rotation angles around Z axis for all four samples. As can be seen, the predominant Z-axis crystal rotation pattern for the initially ideal 'A' orientation is independent of the sample size and similar trends are noted for all samples. In Fig. 4.28(a) for Case I, the crystal is subdivided macroscopically into three matrix bands marked M1, M2, and M3, and two transition bands marked T1 and T2 along the width of the sample as depicted. The Z-axis rotation angles are about 60°, 0° and 90° in M1 to M3, respectively. These results are very similar to Case II, as shown in Fig. 4.2 (reproduced in Fig. 4.28(b)). Fig. 4.28(c) and (d) show the similar values of Z-axis rotation angles in these matrix bands for Cases III and IV. It should be noted that the crystal rotation angles in Fig. 4.28 are different from the angles θ

defined in Fig. 4.19, which only reflect the macroscopic distortion of the meshes during the ECAP process.

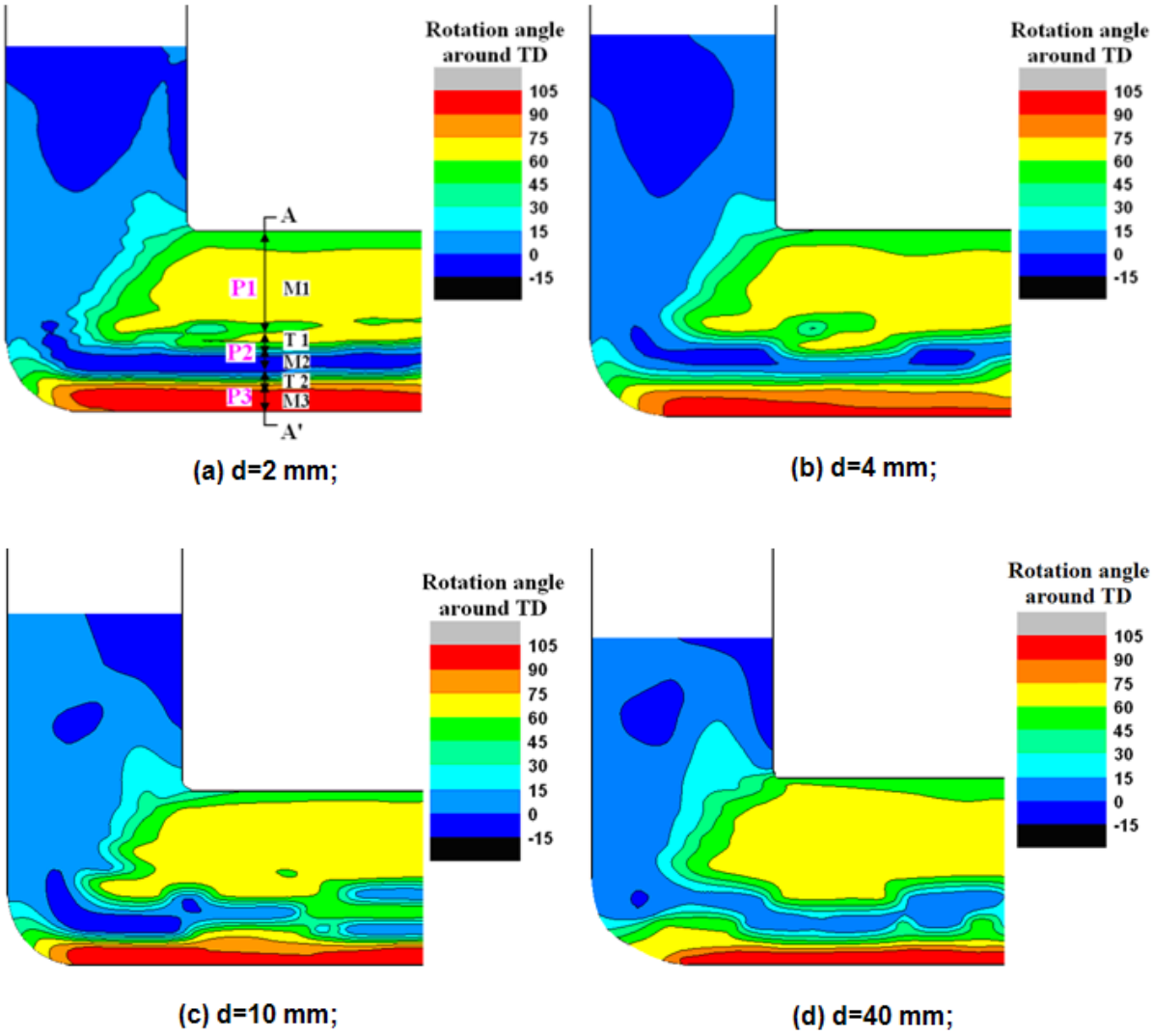

Fig. 4.28 Contour maps of crystal rotations around the Z axis during the ECAP process for all four samples. (a) d=2 mm, (b) d=4 mm, (c) d=10 mm, and (d) d=40 mm.

Fig. 4.29 shows the crystal rotation heterogeneities around three directions on the plane of AA' marked in Fig. 4.28(a) for all cases. The results indicate that the crystal rotation patterns are independent of the sample widths in the steady-state deformation region. Obviously, the X-axis rotation is characterized as clockwise rotation while the Y-axis rotation is in a counter-clockwise direction in the matrix band M1. But both rotation angles are very small compared to the Z-axis

rotation angle. The main difference in Fig. 4.29 lies in the matrix band M2, which should be attributed to the strain rate gradient in the PDZ shown in Fig. 4.24.

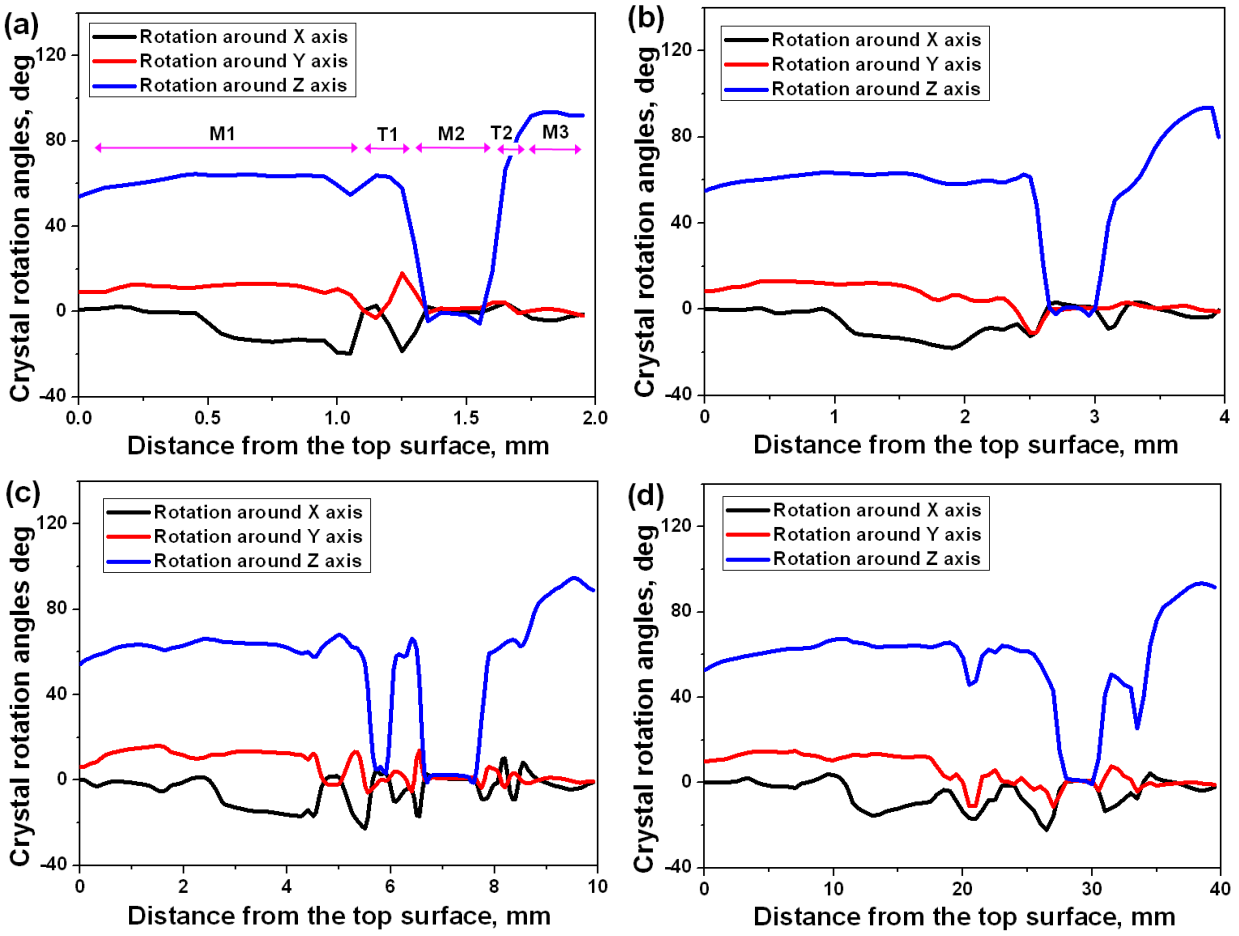

Fig. 4.29 Crystal rotations around X, Y, and Z axes along the width of the sample in the deformed aluminium single crystals with d varying from 2 mm to 40 mm during the ECAP process.

The {1 1 1} pole figures of three selected positions in each sample are plotted in Fig. 4.30, together with the initial crystallographic orientations. The selected positions are marked in Fig. 4.28(a), where Position P1 lies in M1, Position P2 lies in T1, and Position P3 lies in M3. As can be seen, all the samples lead to similar {1 1 1} pole figures, which indicate that texture evolution is independent of the dimension of the sample.

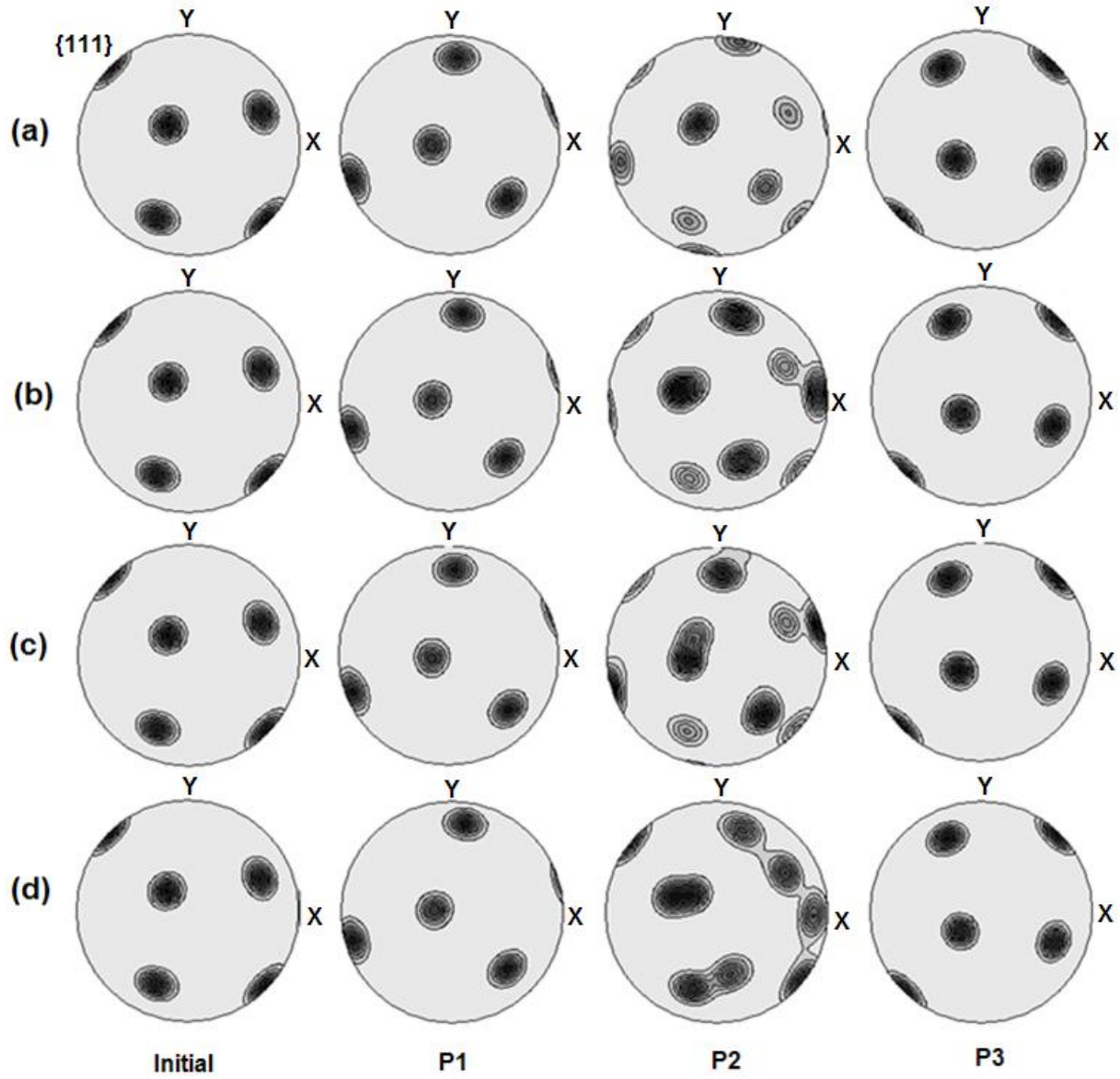

Fig. 4.30 The simulated {1 1 1} pole figures at three selected positions in the deformed samples as marked in Fig. 4.28(a). (a) d=2 mm, (b) d=4 mm, (c) d=10 mm, and (d) d=40 mm.

There are a few experimental reports on the orientation changes during the ECAP process of aluminium single crystals having the same initial crystallographic orientation and different ECAP die geometries [33, 34, 160, 164, 165]. These results can be used to validate the finding obtained in this section. According to the comparison made in Fig. 4.16, the simulation results of Case II agree with the experiment [33, 160] at d=4 mm. The samples in Ref. [34, 35, 163, 164] have a circular cross-section with 10 mm in diameter. Therefore, their experimental results can

be compared with Case III. The orientation measurements by EBSD in Ref. [34] revealed that there was no obvious crystallographic rotation in the central part of the ECAP processed billet on the ED-ND plane. As results shown in Fig. 4.28(c) and Fig. 4.29(c), the position measured in [34] should be located in the matrix band M2, where the crystallographic orientation is characterized by the initial orientation component.

4.6 Influence of Outer Corner Angle

(*This part has already been published in Computational Materials Science (2013)*)

It is well known that the ECAP process was invented by Segal in 1972 [1] and in its early design the ECAP die had very sharp angles, as shown in Fig. 4.31(a). However, it is very hard to achieve a perfectly sharp angle when manufacturing an ECAP die, so most ECAP experiments were conducted with a non-zero outer corner angle (OCA), as shown in Fig. 4.31(b) [104]. The most widely used values of OCAs are about 20° and 30°, but unfortunately no reasonable explanations have been given. Few studies have been carried out to understand the influence of the OCAs. Therefore, a systematical study of the OCAs is very essential, especially on its influence on texture evolution during the ECAP process.

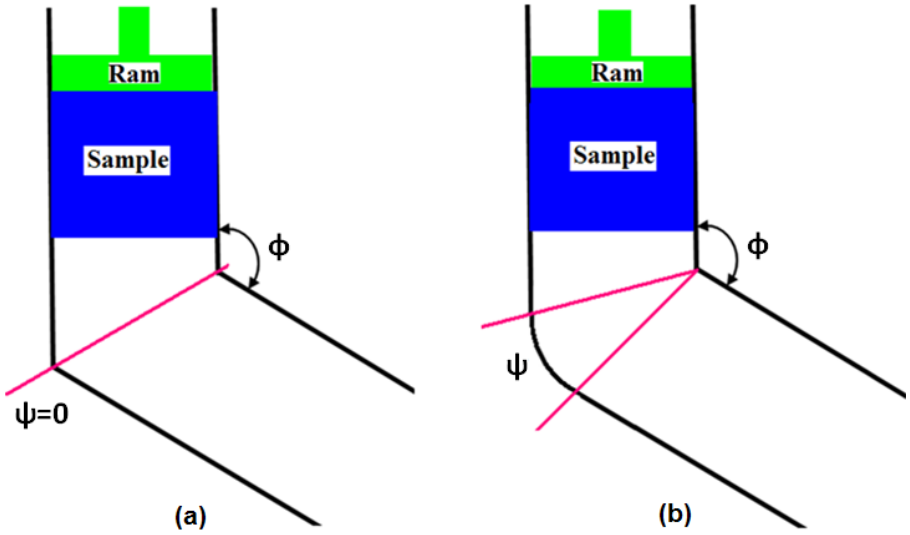

Fig. 4.31 The geometry of an ECAP die with, (a) very sharp outer corner angle [4], and (b) with a non-zero outer corner angle [104].

Table 4.2 Detailed parameters in the simulations used to study the influence of OCAs.

Case number	Value of OCA	Mesh number	Channel width	μ
I	0°	6369	4 mm	0.05
II	10°	6369	4 mm	0.05
III	20°	6369	4 mm	0.05
IV	30°	6369	4 mm	0.05
V	40°	6369	4 mm	0.05
VI	60°	6369	4 mm	0.05
VII	90°	6369	4 mm	0.05

This section will examine the influence of OCAs on the deformation behaviour and development of crystallographic orientation of aluminium single crystal subjected to the ECAP process. The simulations were two-dimensional, and the billet was 23.2 mm long and 4 mm wide. The initial crystallographic orientation is the same as described in the previous sections. The ECAP die channel angle was fixed to 90° and width of the channel was set to 4 mm. A friction coefficient of μ=0.05 was selected according to Section 4.4. Nine different OCAs varying from 0° to 90° were studied specifically and the detailed simulation parameters are listed in Table 4.2.

In Fig. 4.32, the required pressure for ECAP at different OCAs is given as a function of the deformation time. It can be seen that, most cases have a similar tendency. Three steps can be found in Fig. 4.32, i.e. (1) a rapid increment due to the undeformed head part of the sample, (2) a slow increment because the front part exits the PDZ and bends upward, and (3) a relatively steady-state deformation. It has also been found that the required maximum pressure decreases with an increasing OCA from 0° to 90°.

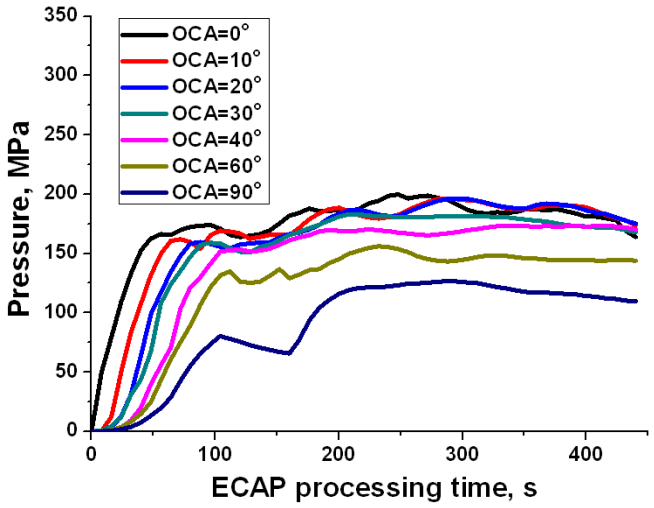

Fig. 4.32 The pressure required for processing different OCAs in terms of deformation time.

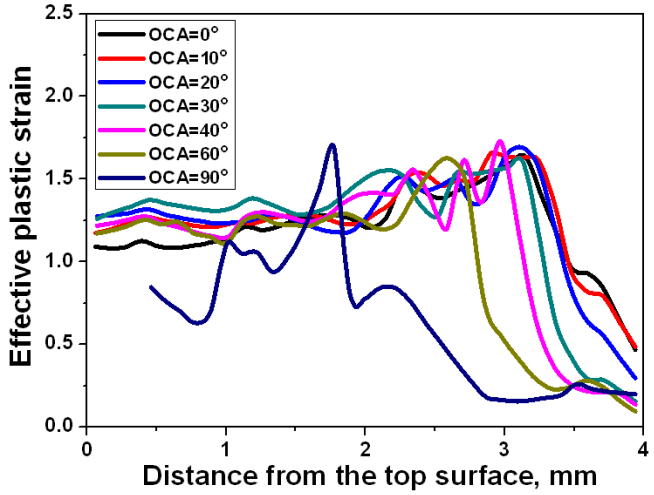

Fig. 4.33 Distribution of the effective plastic strain for different OCAs along the thickness in the deformed billet.

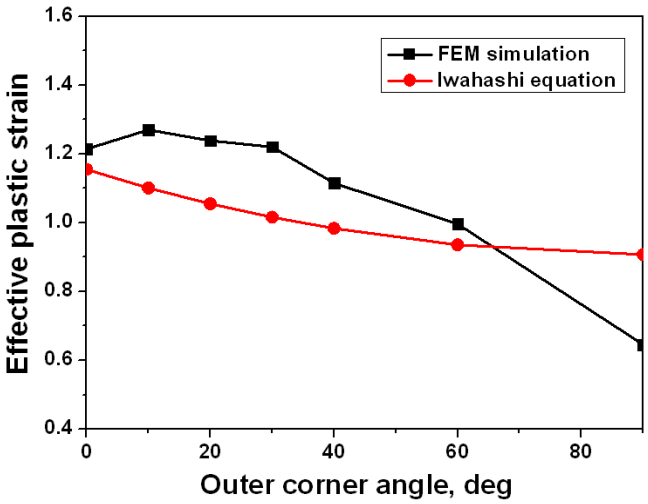

Fig. 4.34 Average values of the effective plastic strain for different OCAs during the ECAP process.

The influence of the OCA on the effective plastic strain along the thickness of the deformed samples is shown in Fig. 4.33. It is clear that the OCA has a significant influence on the distribution of plastic strain through the thickness. The lower region of the sample undergoes less deformation with an increasing OCA and the corresponding effective plastic strain obviously decreases. A larger OCA leads to a larger portion of the thickness experiencing rigid body rotation in the bottom part, and this portion reaches almost 0.5 when the OCA is 90°, as shown in Fig. 4.33. In contrast, the strains in the upper region for all cases are almost the same, except for case VII which has a large gap between the sample and the upper surface of the exit channel, as shown in Fig. 4.35(g). The average values of the effective plastic strain for different OCAs are shown in Fig. 4.34. The OCA from 0° to 30° leads to a similar effective plastic strain while the effective plastic strain decreases gradually as the OCA increases from 30° to 90°. The simulation results agree well with the calculations based on the theory [104] shown in Fig. 4.34, except that OCA=90° which should be attributed to the development of the exit channel gap not being considered in the theory [104].

Table 4.3 The average values of the effective plastic strain ($\bar{\varepsilon}$), shear strength ($\bar{\tau}_c$), von Mises stress ($\bar{\sigma}$), peak force, and the deformation inhomogeneity index (C_i) for different OCAs.

OCA	Peak force (N)	$\bar{\varepsilon}$	$\bar{\sigma}$ (MPa)	$\bar{\tau}_c$ (MPa)	C_i
0°	3195.2	1.213	114.431	46.793	0.972
10°	3128.3	1.269	102.902	46.788	0.927
20°	3115.0	1.238	106.252	47.451	1.129
30°	2927.7	1.161	87.622	45.084	1.267
40°	2769.5	1.115	93.687	45.522	1.428
60°	2498.1	0.996	85.728	42.178	1.539
90°	2030.3	0.645	101.907	40.434	2.407

Comparisons of the required processing peak force, effective plastic strain, von Mises stress, shear strength, and deformation inhomogeneity index for different OCAs have been shown in Table 4.3. It is obvious that a larger OCA results in a smaller processing force and plastic strain, but leads to more inhomogeneous deformation along the thickness direction. For example, the peak force is about 3200 N at OCA=0° and 2000 N at OCA=90°. In contrast to the von Mises stress OCA has a minor influence on the shear strength.

The influence of OCA on the PDZ has been studied in terms of the plastic strain rate components. Due to the plane strain deformation $\dot{\varepsilon}_X$=-$\dot{\varepsilon}_Y$, only the components $\dot{\varepsilon}_X$ and $\dot{\varepsilon}_{XY}$ are plotted in Fig. 4.35. The maximum value of $\dot{\varepsilon}_X$ is near the inner corner for all cases and the magnitude decreases along the intersecting plane from the inner corner to the outer corner. The maximum value of $\dot{\varepsilon}_X$ decreases with the OCA and is about 0.14 at OCA=0° and about 0.03 at OCA=90°. The dead zones are clearly shown in Fig. 4.35(a)-(c) and it decreases gradually with the OCA. After a careful examination the non-contact area between the sample and the die is also observed at OCA=30°, but the sample almost fills the ECAP die corner when OCA≥30°. However, gaps develop in the exit channel at OCA=90° as shown in Fig. 4.35(g) which was also

observed by Li et al. [142]. The PDZ shapes have been influenced significantly by the OCA as shown in Fig. 4.35. For an OCA equals to 0° and 10° in Fig. 4.35(a-b), there is a relatively narrow PDZ, but it expands quickly into the entry and exit channels when the outer corner angle rises. The PDZ can be divided into two parts; the upper part is fan shaped and covers a major portion of the PDZ, while the lower part of the PDZ includes two small deformed regions near the surface of the sample. From the distribution of strain rate component $\dot{\varepsilon}_{XY}$, there is almost negative simple shear along the intersecting plane in the upper part while the lower part is characterized as rigid body rotation due to the outer corner angle or corner gaps. However, the PDZ for OCA=30° is different from the other OCAs shown in Fig. 4.35(g).

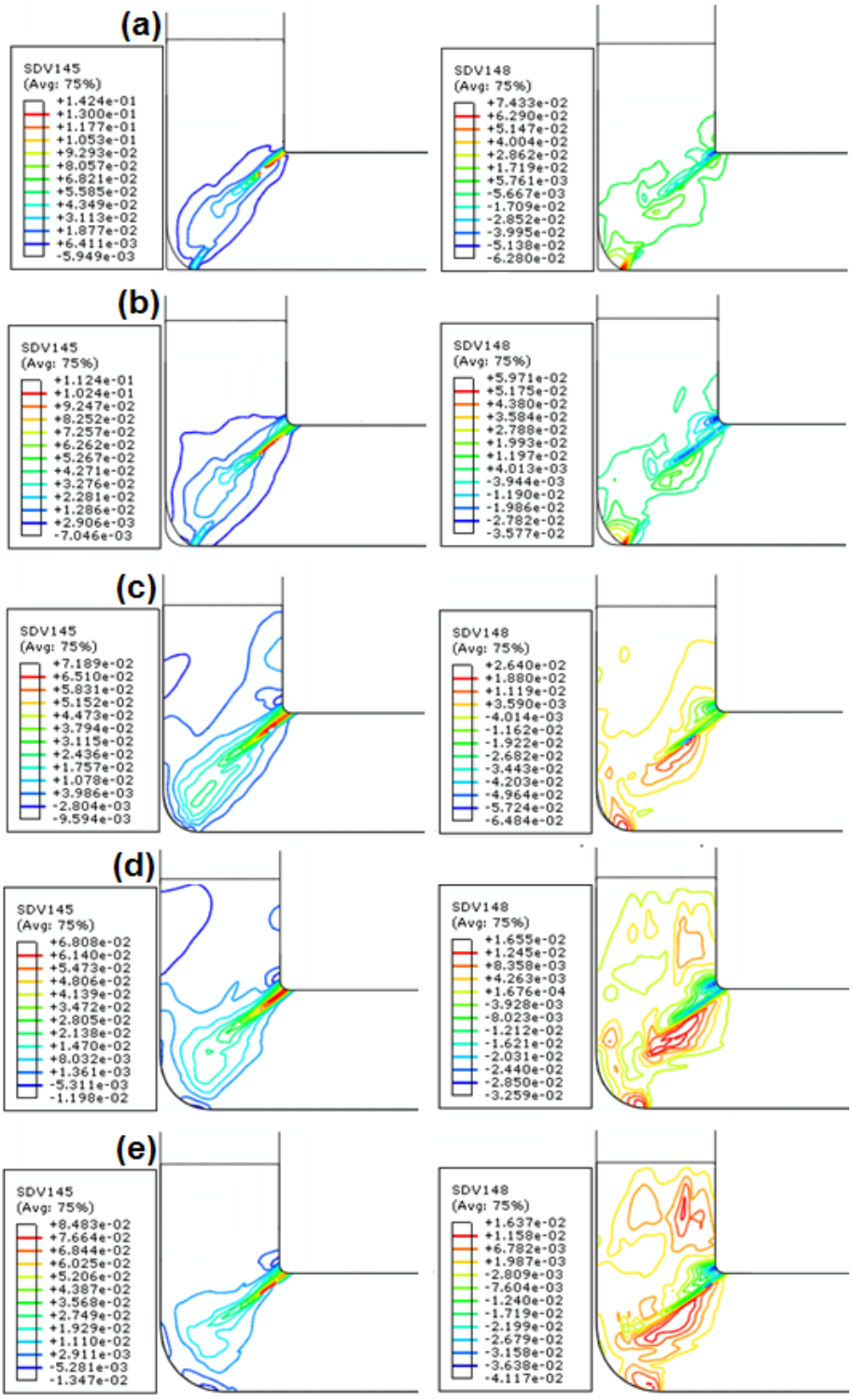

Fig. 4.35 Distribution of the plastic strain rates for different OCAs. (a) OCA=0°, (b) OCA=10°, (c) OCA=20°, (d) OCA=30°, (e) OCA=40°, (f) OCA=60°, and (g) OCA=90°.

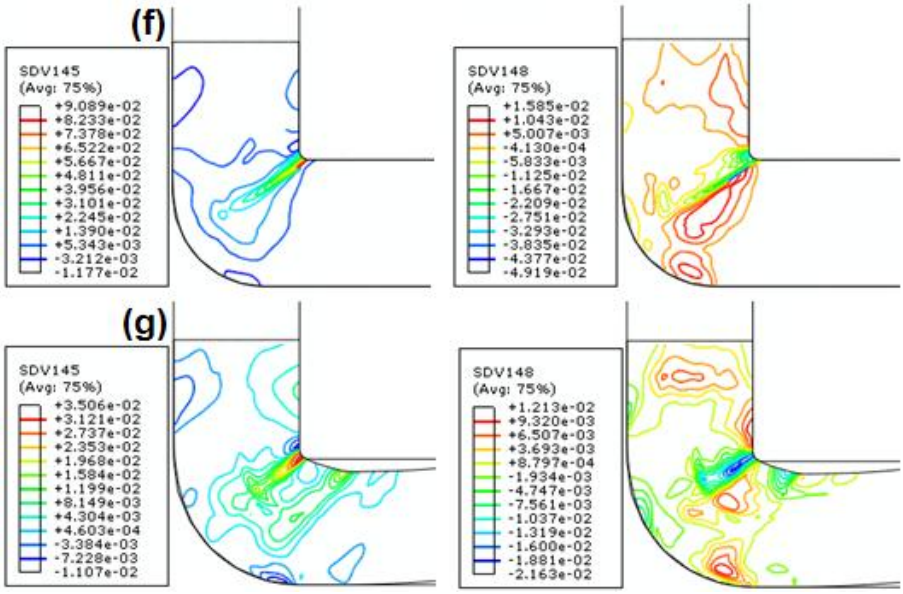

Fig. 4.35 Continued.

In order to study the influence of the OCAs on the development of crystallographic orientation in aluminium single crystals, three positions on the deformed samples (marked as P1, P2, and P3) are selected to plot the {1 1 1} pole figures, as shown in Fig. 4.36. P1 is located in the upper part, P2 is located in the middle part and P3 is located in the bottom part. As can be seen, the orientation is mainly characterized as a 60° rotated component from the initial crystallographic orientation about the transverse direction for all OCAs except where OCA=90°. The {1 1 1} pole figure at P1 in Fig. 4.36(g) indicates a 90° rotation, which should be attributed to the gaps in the exit channel as shown in Fig. 4.36(g). The pole figures at Position P2 reveal two orientation components, i.e. the initial crystallographic orientation and a 60° rotated component when OCA≤30°. In contrast, there is only a 60° rotated orientation when OCA≥40°. At Position P3, all the {1 1 1} pole figures indicate an orientation with 90° rotation from the initial one due to the rigid body rotation [172].

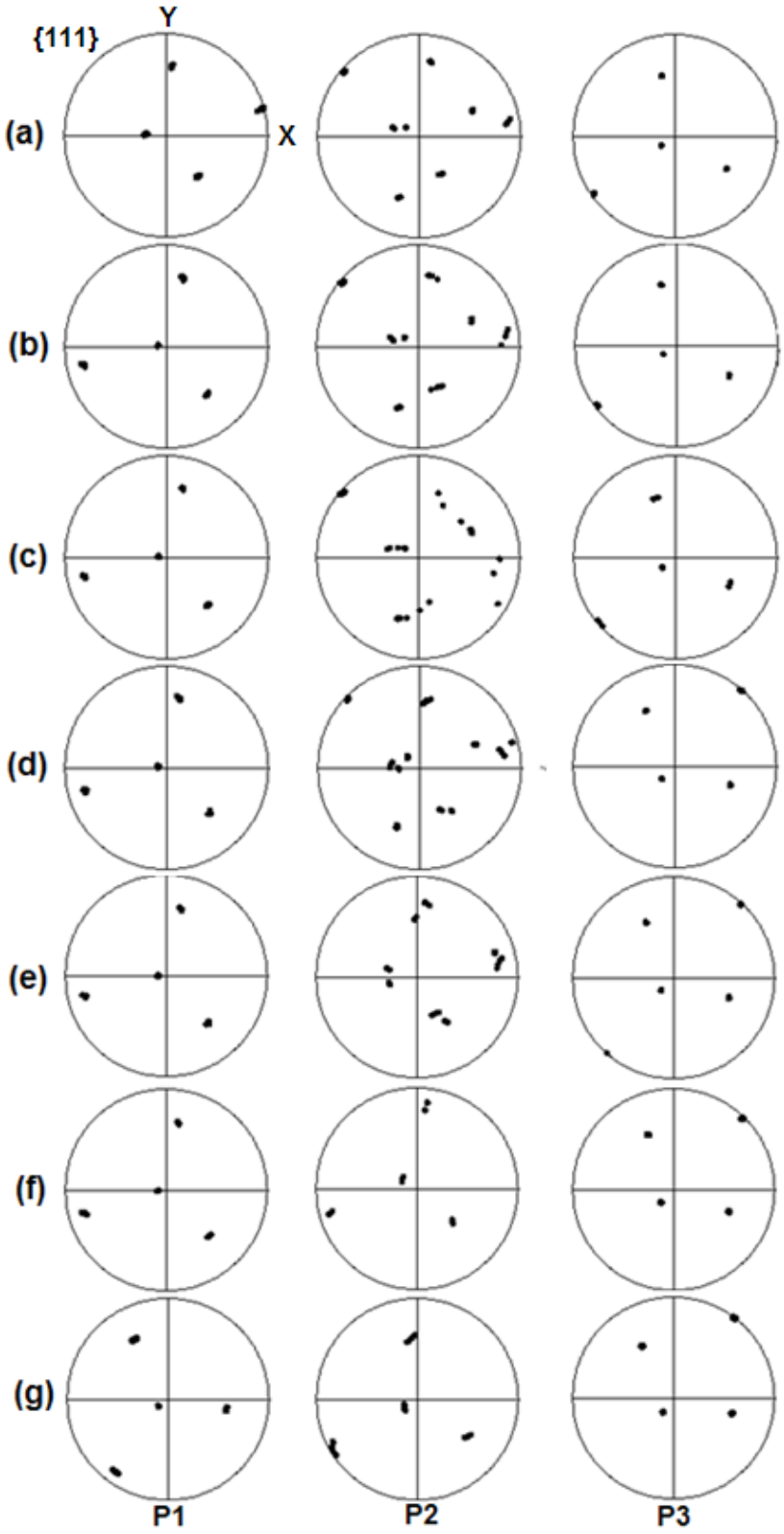

Fig. 4.36 Simulated {1 1 1} pole figures at three selected positions for different OCAs. (a) OCA=0°, (b) OCA=10°, (c) OCA=20°, (d) OCA=30°, (e) OCA=40°, (f) OCA=60°, and (g) OCA=90°.

The crystal rotation angles along the thickness direction are shown in Fig. 4.37. According to the study in Section 4.1, Z-axis rotation is the predominant crystal rotation for aluminium single crystals with an initially ideal 'A' orientation during the ECAP process. Therefore, only the Z-axis rotated component is given in Fig. 4.37. The crystal rotation pattern varies significantly for different OCAs. There are three matrix bands connected by two transition bands along the thickness direction. The crystal rotation angle in the matrix band located in the upper part is about 60°, while the rotation angle in the matrix band located in the bottom part is about 90°. Between those two matrix bands, a matrix band oriented with initial crystallographic orientation develops. Because position P2 is located in the transition band, both the initial orientation and the 60° rotated component can be observed, but with an increment of OCA from 40°, no matrix band with initial orientation developed. The majority of the sample was oriented with a 60° rotated orientation.

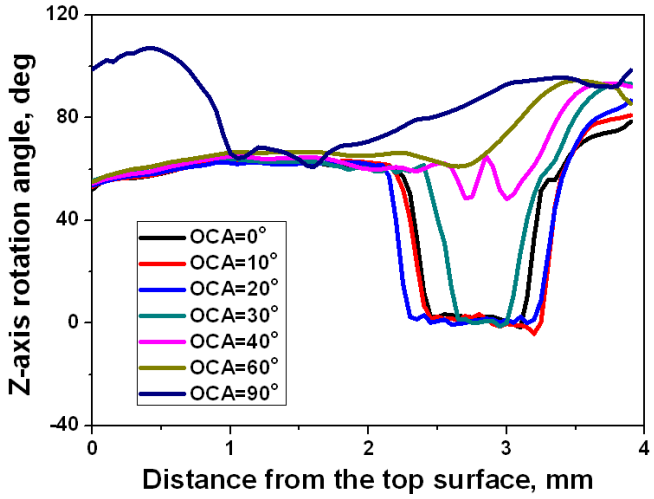

Fig. 4.37 Crystal rotation angles about the transverse direction (Z axis) along the thickness after the ECAP process.

Therefore, the OCA has a significant influence on the plastic deformation heterogeneity, distribution of strain and stress, and texture evolution during the ECAP process. In order to reduce the formation of dead zones and processing force, an ECAP die with OCA=20° or 30° would be a better choice.

4.7 Influence of Inner Corner Fillet Radius

A number of studies [126, 127, 266, 267] considering the influence of the inner corner fillet radius (ICR) have been reported. Luis [126, 127] has proposed an upper bound solution and an FEM model to determine the total load necessary to extrude the materials and proposed an improved solution of strain estimation as shown in the following equations:

$$\tan\left(\frac{x}{2}\right) = \frac{0.5(R-r)\sin(\phi)}{L_0-(R-r)\cos^2(\frac{\phi}{2})} \tag{4.2}$$

$$\gamma = 2\cot\left(\frac{\phi}{2}+\frac{x}{2}\right) + (\pi-\phi)\frac{\sin(\frac{x}{2})}{\cos(\frac{x}{2})\sin(\frac{x}{2}+\frac{\phi}{2})} \tag{4.3}$$

where r is the inner corner fillet radius, R is the outer corner fillet radius, L_0 is the ECAP die channel width and ϕ is the ECAP die channel angle.

Yoon and Kim [266] stated that a round inner corner with an angle up to 9° was acceptable in the classic finite element simulations for reproducing a sharp inner corner. In Ref. [267] the experimental results revealed that a die with two equal fillet radii at the inner and outer corner is less effective than a conventional ECAP die for producing homogeneity within the billets. Unfortunately all the studies mentioned above only focused on a limit range of ICRs so a systematically study on the influence of the ICRs is essential, especially on texture evolution during the ECAP process, which has never been reported yet.

The study in this section is an extension from the previous CPFEM simulations. In order to focus on the influence of ICRs, the ECAP die parameters will be set the same as the previous studies, namely a die channel angle of 90° and an OCA of 30°. All the samples have the same rectangular geometry of 23.2 × 4 mm^2 and were meshed into 6369 CPE4R elements. The simulated material is still an aluminium single crystal oriented with the ideal 'A' orientation. The coefficient of friction was set to 0.05 and a processing speed of 2.4 mm/min was applied. In this section, seven different ICR values will be assessed: ICR=0, 0.3, 0.5, 1, 2, 3, and 4 mm, respectively.

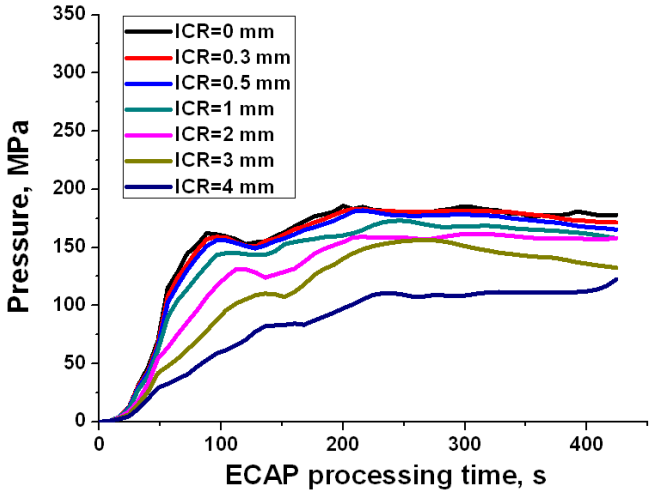

Fig. 4.38 The required processing pressures for different ICRs in terms of deformation time.

Fig. 4.38 shows the required processing pressure for different ICRs varying from 0 to 4 mm. Similar to observation in Fig. 4.18 and Fig. 4.32, three similar deformation stages can be seen in Fig. 4.38. The slop of load-time curve decreases from the first stage (the head part enters the PDZ) to the third stage (steady-state deformation) for all ICRs. It is obvious that increasing ICR leads to decreases of both the required peak load and the slope of first deformation stage.

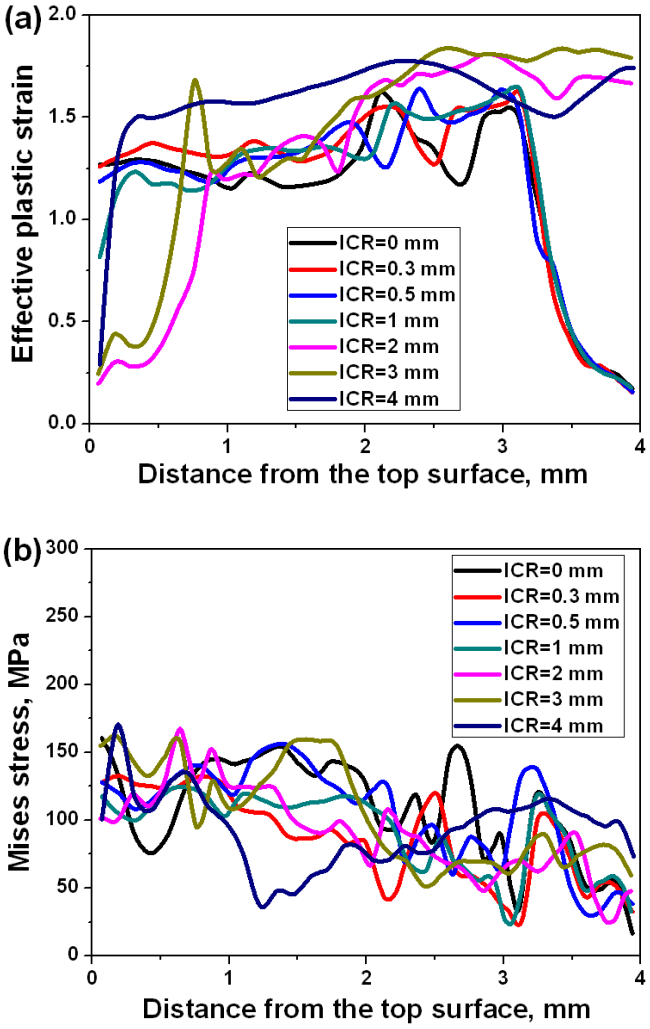

Fig. 4.39 Distribution of (a) effective plastic strain and (b) von Mises stress for different ICRs along the thickness in the deformed aluminium single crystals.

Fig. 4.39 shows the distribution of effective plastic strain and von Mises stress for different ICRs along the thickness in the deformed aluminium single crystals. It is interesting to find that the results slightly change for ICR≤1 mm in Fig. 4.39(a). The strain in the upper 3/4 region is relatively stable and decrease rapidly in the lower 1/4 region. However, the average effective plastic strain rises gradually with an increasing ICR when ICR≥2 mm. In addition, the strain increases rapidly in the upper 1/4 region and it is relatively stable in the lower 3/4 region. On the other hand, the larger ICR leads to a smaller stress in the upper part of the billet shown in Fig. 4.39(b).

Table 4.4 shows the change in the required peak force, plastic strain, stress, and shear strength. It is obvious that it is beneficial for saving the load by increasing the ICR. The required peak extrusion force decreases gradually with the Ir and it is about 2973.3 N at ICR=0 mm and about 1961.8 at ICR=4 mm. The influence of ICR on the deformation inhomogeneity can also be observed in Table 4.4. The larger ICR leads to the smaller index C_i (Equation (4.1)). It is very interesting to find that a larger ICR results in a larger plastic strain, this is opposite to the influence of OCAs studied in Section 4.6.

The simulated plastic strains have been compared with predictions by the analytical models developed by Iwahashi [104] (Equation 2.4) and Luis-Perez [126] (Equations 4.2 and 4.3) shown in Fig. 4.40. The CPFEM simulation results reveal a slight variation in the plastic strains at relatively smaller fillet radius, i.e. ICR≤1 mm. When the ICR exceeds 1 mm, the plastic strain increases gradually and there is a linear relationship, as shown in Fig. 4.40. The calculations based on Equation (2.2) indicate the same strain for all ICRs because the influence of the fillet radius is neglected. The predicted strain is acceptable at relatively small ICRs (≤0.5 mm), but the deviation becomes larger for the larger ICRs. By contrast, the calculations based on Equations (4.2) and (4.3) reveal the linear increment relationship between the plastic strain and the ICR.

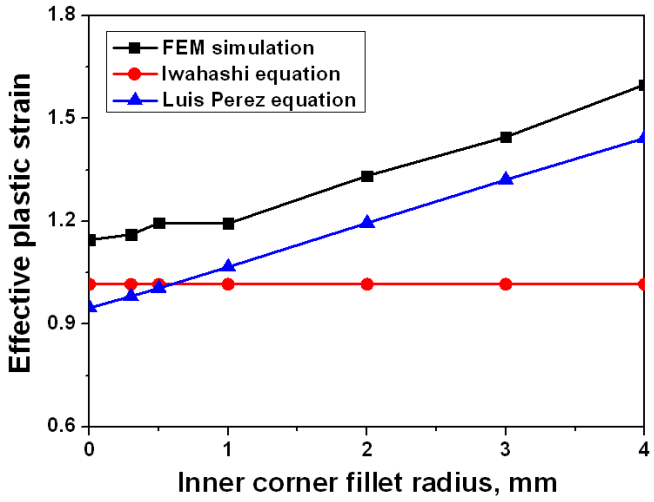

Fig. 4.40 Distribution of effective plastic strain for different ICRs along the thickness direction in the deformed billets.

Table 4.4 The required peak force, average values of effective plastic strain, von Mises stress and shear strength, and the deformation inhomogeneity index.

ICR (mm)	peak force (N)	$\bar{\varepsilon}$	$\bar{\sigma}$ (MPa)	$\bar{\tau}_c$ (MPa)	C_i
0	2973.3	1.146	109.3351	46.109	1.265
0. 3	2927.7	1.161	87.622	45.084	1.267
0. 5	2909.9	1.194	106.302	44.797	1.241
1	2767.2	1.195	92.209	42.987	1.232
2	2590.3	1.332	91.808	42.996	1.207
3	2505.4	1.445	94.712	42.504	1.015
4	1961.8	1.598	93.414	39.617	0.928

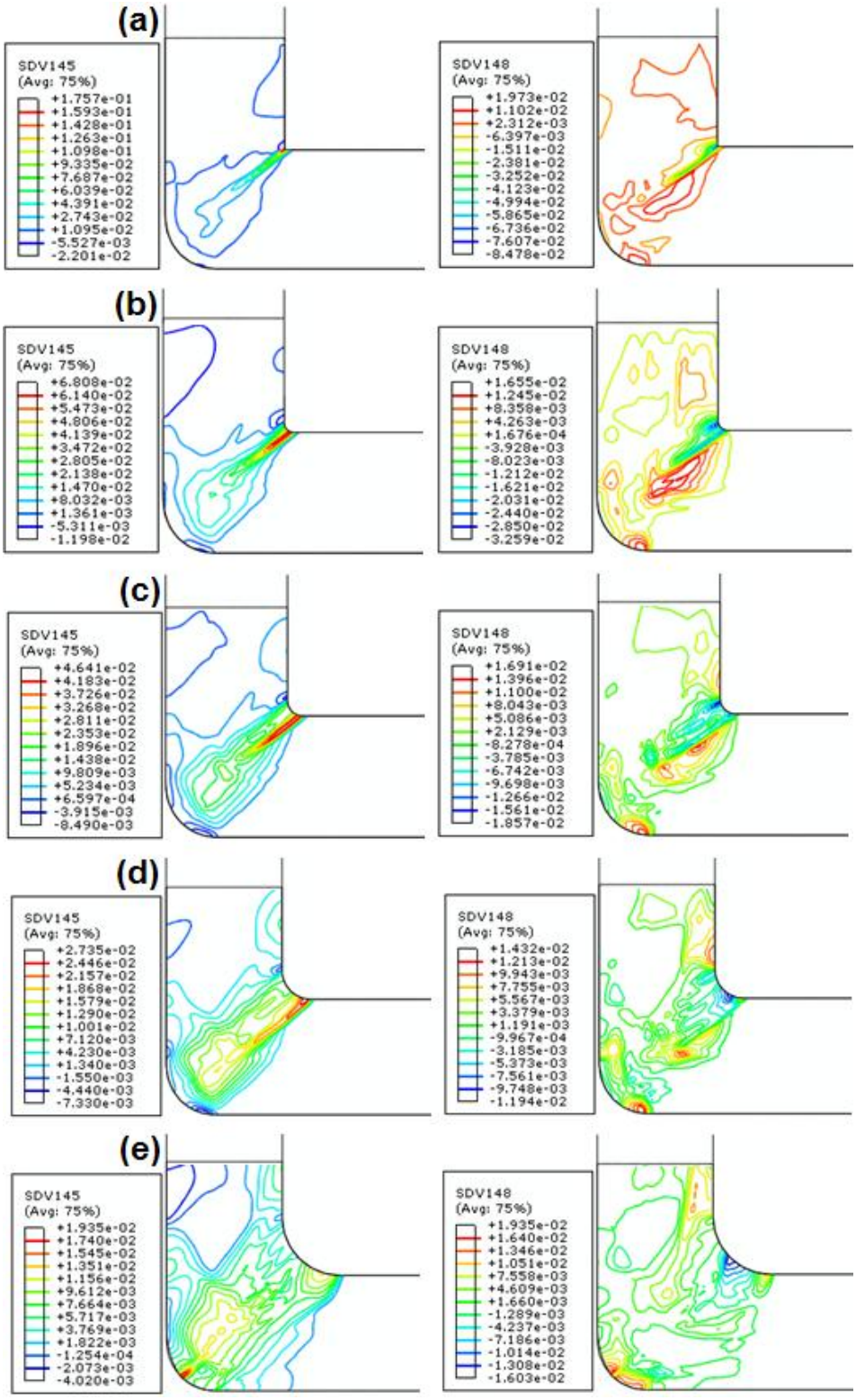

Fig. 4.41 Distribution of plastic strain rates for different ICRs. (a) ICR=0 mm, (b) ICR=0.3 mm, (c) ICR=0.5 mm, (d) ICR=1 mm, (e) ICR=2 mm, (f) ICR=3 mm, and (g) ICR=4 mm.

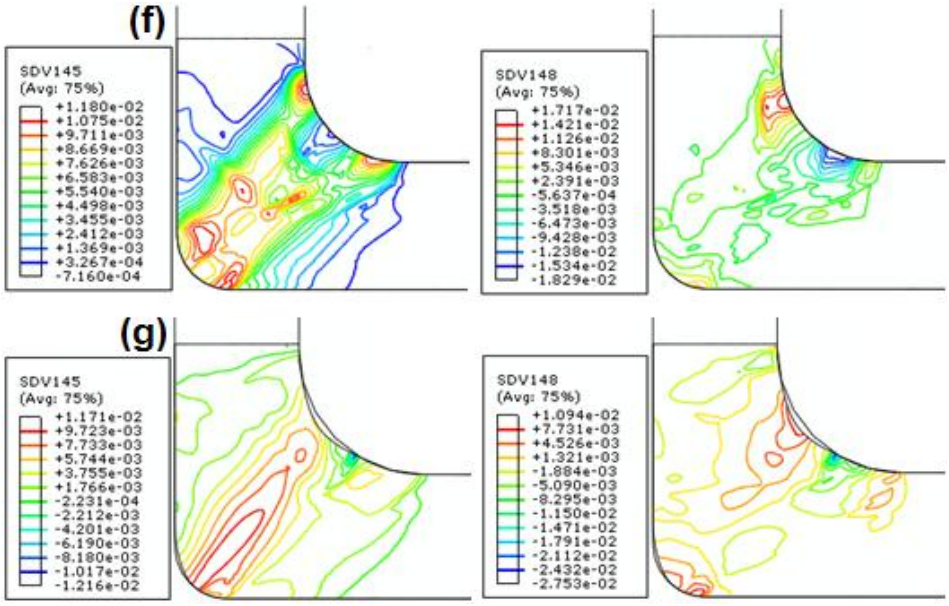

Fig. 4.41 Continued.

Fig. 4.41 shows the distribution of the plastic strain rates $\dot{\varepsilon}_X$ and $\dot{\varepsilon}_{XY}$ during ECAP process for all ICRs considered in the present study. Because the deformation was assumed to be in a plane strain condition the strain rate $\dot{\varepsilon}_Y$ has the same magnitude as $\dot{\varepsilon}_X$ but with the opposite sign. It is interesting to find that there is an obvious strain rate gradient from the inner to the outer corner. As can be seen, the aluminium single crystal undergoes more plastic deformation near the inner corner than the outer corner when ICR is less than 1 mm. The deformation pattern is characterized as simple shear along the intersecting plane close to the inner corner but rigid body rotation in the outer corner. However, the bottom region undergoes more shear deformation and the top region undergoes less shear deformation at larger ICR as shown in Fig. 4.41(e-g). The less shear deformation in the top region is attributed to the larger round inner corner angle, which induces rigid body motion flow due to less constraint against the crystal flow. According to the results shown in Fig. 4.41, for an ECAP die with an OCA given by 30°, it can be concluded that a round inner corner with an ICR up to 1 mm is acceptable to reproduce a sharp inner corner.

The influence of ICR on the crystallographic orientation development of an aluminium single crystal has been studied as shown in Fig. 4.42. Three positions in the ECAP processed samples,

marked as P1, P2, and P3 in Fig. 4.41 respectively, are selected. It is clear that the ECAP die with ICR≤1 leads to similar {1 1 1} pole figures at all three positions. The crystallographic orientation at Position P1 is a 60° rotated component from the initial ideal 'A' orientation. The {1 1 1} pole figures at Position P2 reveals the presence of both the rotated component and initial orientation. By contrast at Position P3, it has been found that the orientation development after ECAP is characterized as the 90° rotation from the initial orientation about the TD in a counterclockwise direction. The difference between the {1 1 1} pole figures at Positions P1 and P3 should be attributed to two different deformation patterns, namely there are more shear in the top region and more rigid body rotation in the bottom region.

However, different orientation developments are observed when ICR exceeds 1 mm, as shown in Fig. 4.42(e-g). When ICR=2 mm, the 90° rotated component from the initial crystallographic orientation appears at Position P1. The {1 1 1} pole figure at Position P2 reveals two orientations, i.e. the initial orientation together with a 50° rotated component, while it indicates only slight scattering from the initial orientation at Position P3. It should be noted that the pole figures at Position P1 are different even at ICR=3 mm and ICR=4 mm. Fig. 4.42(f) shows the 60° and 90° rotated orientations but only the 60° rotation from the initial orientation is observed in Fig. 4.42(g). By contrast, the {1 1 1} pole figures reveal the remains of initial orientation at Positions P2 and P3 for both ICR=3 mm and ICR=4 mm.

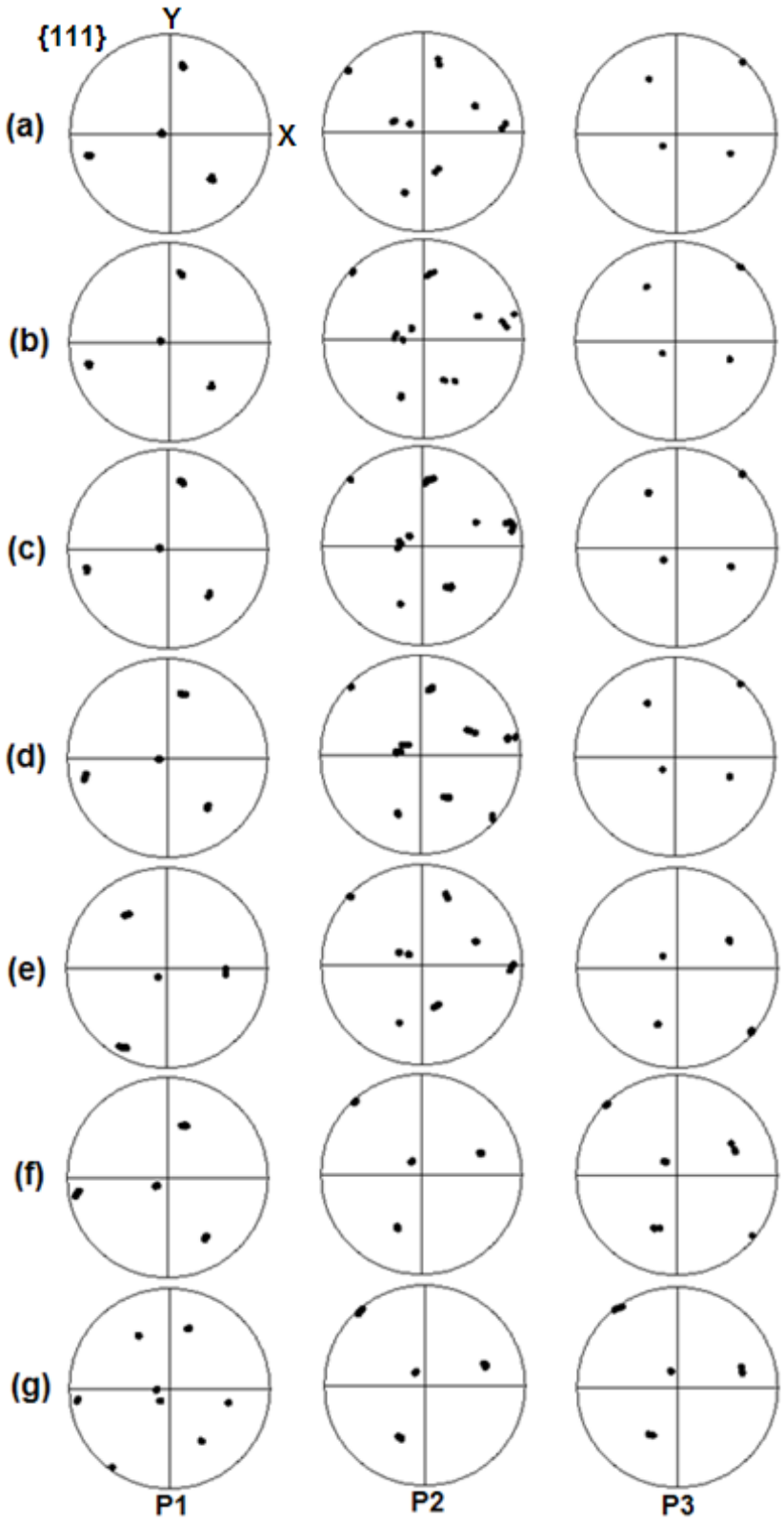

Fig. 4.42 Simulated {1 1 1} pole figures at three selected positions for (a) ICR=0 mm, (b) ICR=0.3 mm, (c) ICR=0.5 mm, (d) ICR=1 mm, (e) ICR=2 mm, (f) ICR=3 mm, and (g) ICR=4 mm.

Fig. 4.43 shows the TD component of crystal rotation angles. It is clear that the crystal rotation patterns are similar when ICR≤1 mm. There are three matrix bands connected by two transition bands. The crystal rotation angle is about 60° in the upper matrix band (the top 1/2 region), 0° in the middle matrix band (the region between 1/2 and 1/4 of the thickness from the top surface), and 90° in the lower matrix band (the bottom 1/4 region). However, the crystal rotation angle is significantly influenced by the inner corner angle when ICR>1 mm. When ICR=2 mm, five matrix bands developed along the thickness direction. The TD rotation angle is about 90° in the top 1/4 region, 60° in the region between 1/4 and 1/2 of the thickness from top, 0° in the region between 1/2 and 3/4 of the thickness from the top surface, 60° in the region between 3/4 and 7/8 of the thickness, and 20° in the bottom 1/8 region as shown in Fig. 4.43. It is obvious that the upper matrix band is characterized as 90° rotation when ICR≥2 mm, which should be attributed to the rigid body rotation in the upper region during the ECAP process. For ICR=3 mm, there are three matrix bands from the top surface and the corresponding size is 1/8, 3/8 and 1/2 of the thickness, respectively. Their rotation angles are 90°, 60° and 0°. For ICR=4 mm, the rotation angle decreases gradually along the thickness from the top surface and the lower 5/8 region is characterized by almost zero rotation.

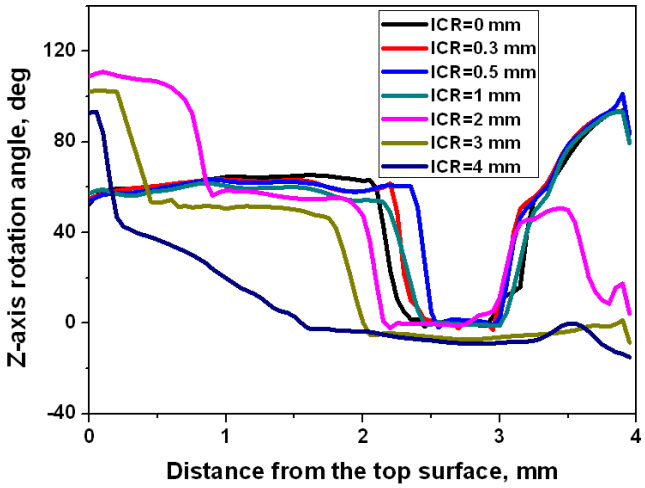

Fig. 4.43 Influence of ICR on the Z-axis rotation angles along the thickness of the deformed aluminium single crystals after the ECAP process.

The simulation results reveal that there is a significant influence of the inner corner angle or ICRs on the plastic deformation inhomogeneity and development of crystallographic orientations. For an ECAP die with OCA=30°, an inner fillet radius up to 0.5 mm can lead to similar results as having a sharp inner corner. Even larger plastic strain can be achieved by increasing the inner fillet radius, but it is less effective for grain refinement because the number of matrix bands along the thickness has been decreased.

4.8 Summary

Chapter 4 is summarized as follows:

(1) For an aluminium single crystal initially oriented with ideal 'A' orientation, the simulation results revealed that the crystallographic orientation rotates in three directions and the predominant rotation is around the Z axis during the ECAP process. The distributions of crystal rotation angles are heterogeneous through the thickness, and the sample was subdivided into three matrix bands along the thickness. The corresponding Z-axis rotation angles in three matrix bands are about 60°, 0° and 90°, respectively. According to the simulated slip traces, it has been found that multi-slip systems can be activated in the large strain gradient region and the lattice rotation dominates the material rotation. When the strain gradient is small, a single dominant slip is the main slip mechanism and the lattice remains at the initial orientation after deformation. A region of rigid body rotation was observed in the lower part of the die corner and the lattice rotation angle is about 90°.

(2) For an ECAP die with a square cross-section, deformation is inhomogeneous along the thickness but can be treated as uniform along the transverse direction. The strain components along the Z axis can be neglected. It has been found that a three-dimensional CPFEM simulation of the ECAP process gives similar results to a two-dimensional simulation. Therefore, it is reasonable to apply two-dimensional CPFEM model to study the deformation and texture evolution during the ECAP process.

(3) The results reveal the significant influence of mesh conditions on the plastic deformation and texture evolutions of aluminium single crystals during the ECAP process. The outer corner gap between the sample and ECAP die obviously decreases as the element number increases from 600 to 2400 and it will remain similar when the element number is larger than 2400. Mesh 6369 predicted similar plastic strain and textures as Mesh 12000. In contrast, Mesh 600 and Mesh 2400 fails to capture the rigid body rotation in the bottom part of the deformed billets and they are unable to predict the texture observed in the experiments [33, 268]. Therefore, the sample should be meshed fine enough to simulate texture accurately in the ECAP simulation.

(4) Four cases with different coefficient of friction of μ=0, 0.05, 0.1 and 0.15 have been simulated. It has been found that the coefficients μ=0.05 and 0.1 can capture the major texture features observed in the experiments and μ=0.05 predicts a slightly better texture than μ=0.1. The frictional condition significantly affects texture evolution in the region (Region B) between 1/2 and 3/4 of the billet thickness from the top surface. Cases of μ=0.05 and 0.1 predict a matrix band with an initial orientation in this region and the matrix band is parallel to the X axis. However, this matrix band does not appear in the simulation with μ=0. When the coefficient of friction is high (μ=0.15), Region B consists of separate small matrix bands. Friction affects texture in Region B through the PDZ. Different friction conditions changes the shape of the corner gap and in turn influences the distribution of stresses in the lower part of the PDZ. As a result, texture in Region B is different for different frictional conditions.

(5) For the first time the influence of sample size on texture evolution during the ECAP process has been studied systematically by considering a sample width varying from 2 mm to 40 mm. It has been found that the deformation (including the distribution of effective plastic strain, von Mises stress, and shear strength, and the activity of slip systems) of an aluminium single crystal is independent with the sample dimension during the ECAP process and three similar deformation steps have been observed for all cases. Larger samples for the industrial applications can be analogized by examining the smaller samples in the laboratory.

(6) Nine ECAP dies with different OCAs are simulated to study its influence on the deformation heterogeneity and texture evolution of aluminium single crystal during the ECAP process. The processing pressure decreases gradually with the OCA. A similar distribution of the effective plastic strain is obtained when OCA≤30°, while the effect plastic strain decreases with the increasing OCA when OCA>30°. A significant influence of OCA on the PDZ shape and texture evolution is observed. The thickness of the rigid body rotation part in the billet bottom rises gradually and it covers nearly 1/2 of the whole billet thickness when OCA=30°. The initial crystallographic orientation disappears after the ECAP process when OCA exceeds 30°. According to the simulation results, an ECAP die with OCA=20° or 30° will be suggested in order to reduce the formation of the dead zone and the processing force.

(7) Seven dies with different ICRs are simulated. For a die having a channel width of 4 mm, the simulation results show similar distributions of the effective plastic strains when ICR is less than 1 mm. The strain increases gradually with the ICR when the ICR exceeds 1 mm. The simulated {1 1 1} pole figures suggested a strong influence of the ICRs on texture evolutions in the upper quarter region and lower quarter region when the ICR is larger than 1 mm. The 90° rotated crystallographic orientation from the initial orientation at Position P1 has been observed at ICR≥2 mm while the rotation angle is 60° for the smaller ICRs (ICR≤1 mm). In contrast, the pole figures reveal the existence of initial orientation in the bottom at larger ICRs but 90°rotated components at smaller ICRs. Therefore, the ICR in a reasonable range (e.g. 1 mm for the die with channel width of 4 mm) can be used when manufacturing the ECAP die.

Chapter 5 Investigation of ECAP of Copper Single Crystals

In this chapter, the study has been extended to simulate the ECAP process of copper single crystals. The deformation behaviour and texture evolution of copper single crystals during ECAP will be discussed in detail.

In recent years, a few works about the ECAP processing of single crystals with different metals have been reported, including aluminium [96, 158, 159, 161, 181, 204, 264, 268-271], magnesium [198, 199], nickel [172, 174-176], niobium [177, 178], and copper single crystals [96, 159, 179, 180, 183, 185-188, 272-278]. In Refs. [198, 199], Seda and co-workers conducted ECAP experiments of magnesium single crystals with different initial orientations at 503 K. Their results showed that an orientation of [0 0 0 1] and <1 0 -1 0> axes with respect to the die geometry significantly influences the activation of various deformation modes and resulting texture evolution. Sandim et al. [177] examined the microstructure evolutions of niobium single crystals with a well chosen crystallographic orientation ([2 1 1] parallel to the ED) deformed by ECAP at room temperature using SEM and EBSD. They stated that the microstructure of the crystal following one ECAP pass was fully subdivided by regularly spaced shear bands coexisting with non-sheared regions, and the shear bands having a lamellar structure displayed misorientations of about 40-60° related to the non-sheared regions. The corresponding microstructure and texture heterogeneities in initially cube oriented nickel single crystals were investigated in Refs. [175, 176]. It has been found that the main texture after the ECAP process consists of a TD rotated cube, a split C component and a partial B fibre. Besides, copper has attracted a lot of interest. Miyamoto et al. [186] conducted the first investigation on copper single crystals deformed by ECAP. It was found that the billet exhibited shear bands after the first ECAP pass and was fragmented most in terms of grain size and orientation scattering after four passes. Then several studies on copper single crystals were reported by Miyamoto and co-workers [187, 188, 272, 273, 275]. They divided the end crystal orientations, macroscopic

heterogeneity and dislocation structures into three groups. In group I, the billet had banded structures with considerable orientation splitting and contained mainly extended, sharp and layered dislocation boundaries; in group II, the microstructures contained equiaxed cell boundaries but with a non-uniform shape and size; and in group III, the billets were macroscopically homogeneous with layered dislocation boundaries. The microstructure and texture evolution of copper single crystals after ECAP have also been examined by Fukuda and Furukawa [96, 159, 179, 180] using the optical microscopy, orientation imaging microscopy and transmission electron microscopy. Their experimental results revealed that the subgrain width (~0.2 μm) in copper is significantly smaller than that in aluminium (~1.3 μm) with the same initial crystallographic orientations after one ECAP pass. However, most studies of copper single crystals focus on the experiments and an effective modelling is essential. This chapter will investigate the ECAP process of copper single crystals by a CPFEM model. The influence of friction, die geometry and initial crystallographic orientations on the deformation behaviour and orientation development will be studied in detail.

5.1 Influence of Friction

(*This part has already been published in Materials Science and Engineering A (2012)*)

In Chapter 3, it has been proven that the developed CPFEM model is able to accurately predict texture evolution of copper single crystals during the ECAP process. This section is aiming to examine the influence of frictional conditions between the copper single crystals and ECAP die. In the simulations the channel angle is 90° and the OCA is 30°. For the initial crystallographic orientation: the crystallographic directions [-1 9 4], [-11 1 -5] and [-1 -1 2] are parallel to the X, Y and Z axes, respectively. The plane strain deformation was assumed in the simulations. The simulated sample had a rectangular shape with 20 mm in length and 4 mm in width, and was meshed into 6369 CPE4R elements. Three friction coefficients, namely μ=0.05, 0.1 and 0.15 are compared. The material parameters used in the CPFEM simulation of copper have already been given in Section 3.3. The ECAP process was simulated with a constant extrusion velocity of 0.04

mm/s along the –Y direction and the simulation was terminated when approximately three fourths of the sample was pressed through the die.

It should be noted that the friction coefficient μ=0.15 led very poor convergence and the simulation even failed to achieve a steady-state ECAP deformation. Therefore, the following analysis was only conducted for the coefficients of friction μ=0.05 and μ=0.1 at the processing time t=450 s.

Figs. 5.1(a) and (b) show the deformed meshes of copper single crystals for μ=0.05 and μ=0.1, respectively. In Fig. 5.1(a), the inhomogeneous deformations along the X and Y axes have been observed. The most significant mesh distortion is found in the bottom part of the leading head. In the entry channel, severe deformation is induced on the right side close to the inner corner while the shape of the elements is almost not changed until entering the intersecting zone of two channels. It is clear that the elements close to the bottom of the exit channel are still in rectangular shape. An outer corner gap between the sample and ECAP die exists as represented by the arc of 'AB'.

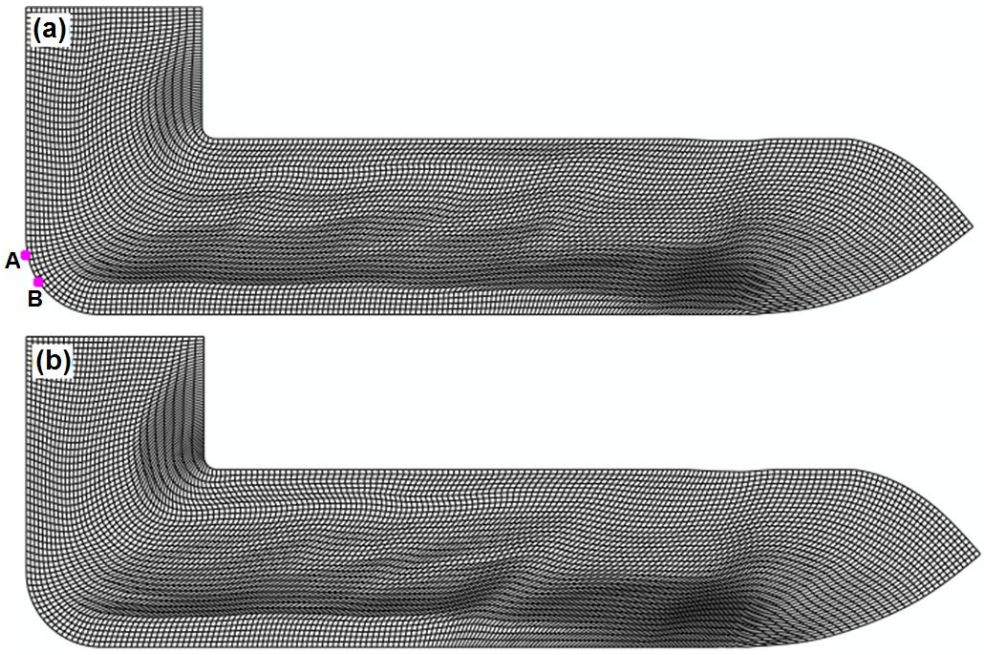

Fig. 5.1 Mesh distortions of copper single crystals during the ECAP process under frictional conditions of (a) μ=0.05, and (b) μ=0.1.

The mesh distortions for μ=0.1 shown in Fig. 5.1(b) is similar to the case of μ=0.05. The careful inspection shows that the dead zone in the outer corner observed in Fig. 5.1(a) has disappeared at the higher friction which induces the larger back pressure [279]. In addition, the larger coefficient of friction results in more extension of the induced deformation close to the inner corner of the die.

Fig. 5.2 shows the distributions of the plastic strain rates $\dot{\varepsilon}_X$, and $\dot{\varepsilon}_{XY}$ in the deformed copper single crystals with the coefficient of friction varying from 0.05 to 0.1 after a steady-state deformation is obtained. The distribution of the plastic strain rate is often used to describe the PDZ during the ECAP process. As observed in Fig. 5.2(a) for μ=0.05, deformation was first induced in the vicinity of the right side interface of the entry channel. Similar phenomenon was predicted by the flow line model and finite element analysis [48, 142, 280-282] for different materials. Material close to the inner corner is subjected to a higher strain and strain gradient than that close to the outer corner. Severe deformation near the inner corner provides a higher compressive force onto the material near the right side interface of the entry channel, which in turn results in higher friction stress at the right side interface and quite a significant plastic strain rate. It is clear that the magnitude of the strain rates significantly changes from the inner corner to outer corner. The maximum value exists near the inner corner and the value in the central area is higher than the outer corner, where the deformation is characterized as rigid body rotation. These results are consistent with the flow line model [125]. The strain rate is zero in the exit channel which indicates that the plastic deformation is finished when the material passes the lower boundary of the PDZ. The result in this study is similar to the observations by an in-situ physical modelling experiment shown in [138].

The strain rate contours for μ=0.1 are shown in Fig. 5.2(b). It has been found that an increase in the coefficient of friction leads to a slightly more expanded strain rate distribution in the vicinity of the right side of the entry channel along the vertical and horizontal directions. The distribution of the strain rate $\dot{\varepsilon}_X$ in the intersecting zone for μ=0.1 is similar to μ=0.05 but more heterogeneity of $\dot{\varepsilon}_{XY}$ in the central part for μ=0.1 has been observed.

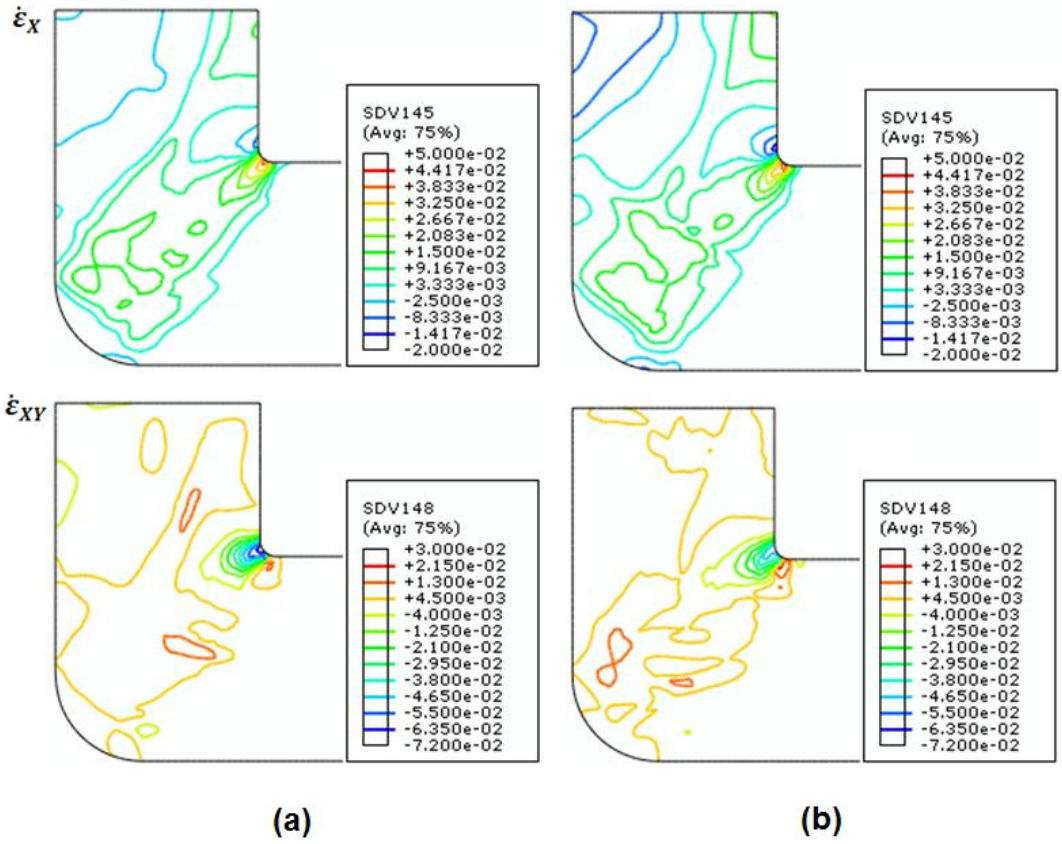

Fig. 5.2 Distributions of the simulated plastic strain rates in the deformed copper single crystals during the ECAP process with (a) μ=0.05 and (b) μ=0.1.

The deformation heterogeneity in the deformed copper single crystal along the thickness has also been investigated. Fig. 5.3 shows variations of the plastic strain through the sample thickness. Distribution of the effective plastic strain for μ=0.05 and 0.1 are compared in Figs. 5.3(a). In general, similar trend is observed for both coefficients of friction. As can be seen, the strain increases gradually with an increasing distance from the top surface and then decreases rapidly in the bottom part. It is obvious in Fig. 5.3(a) that the strain distribution in the upper 1/4 part is more sensitive to the friction than the lower half part. In contrast, the stress has been examined which shows a similar variation along the thickness for both coefficients of friction.

Figs. 5.3(b) and 5.3(c) show the variations of the plastic strain components for μ=0.05 and μ=0.1, respectively. It is clear that the values of ε_X and ε_Y are much smaller than that of ε_{XY} in the upper 1/4 part and all three components are almost zero in the bottom. In contrast, large

tension along the X axis and compression along the Y axis exist in the middle part. The different strains close to the top surface for μ=0.05 and μ=0.1 are consistent with the mesh distortions shown in Fig. 5.1 and PDZs shown in Fig. 5.2.

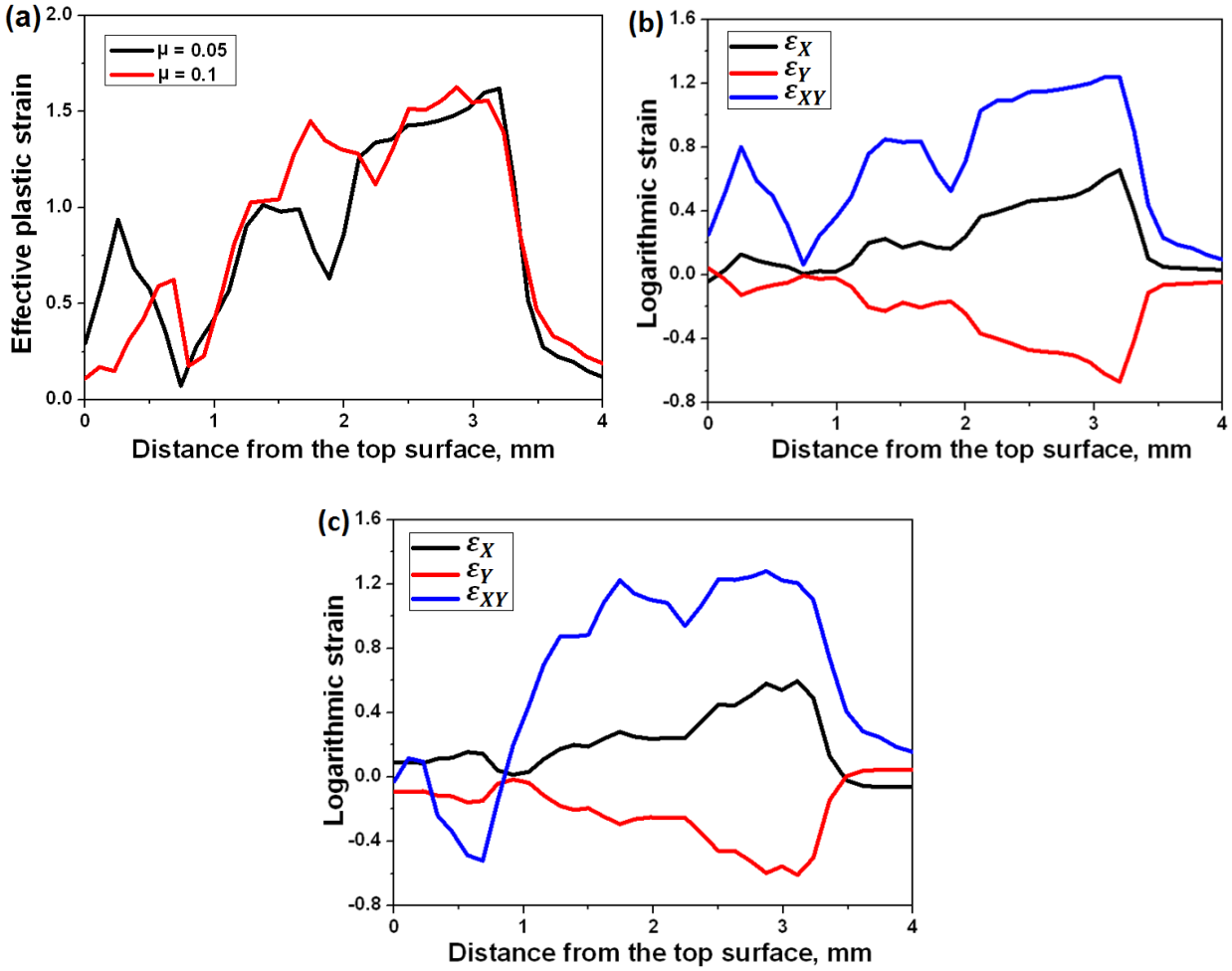

Fig. 5.3 Variation of the (a) effective plastic strain, and the logarithmic plastic strain components for (b) μ=0.05 and (c) μ=0.1 along the sample thickness in the ECAP processed copper single crystals.

Fig. 5.4 shows the simulated {1 1 1} pole figures for five positions labelled as P1, P2, P3, P4, and P5, as shown in Fig. 5.5(c). It is obvious that the pole figure at Position P1 in Fig. 5.4(a) for μ=0.05 is consistent with the simulation for μ=0.1 and the experimental results in Ref. [179]. At Position P2, the corresponding {1 1 1} pole figure for μ=0.05 revealed an initial crystallographic orientation together with a 60° rotated component which agree well with the experimental measurement [179]. In contrast, an extra orientation scattering has been observed for μ=0.1

apart from these two components observed for μ=0.05. Positions P4 and P5 are located near the top surface and bottom of the deformed samples, respectively. Both coefficients of friction lead to similar orientations at Positions P3-P5, as shown in Fig. 5.4. As can be seen, the simulated {1 1 1} pole figure is characterized by an initial crystallographic orientation at P3, a 60° rotated component at P4 and an almost 90° rotated component at P5. Therefore, it can be concluded that texture evolution in copper single crystals during the ECAP process is relevant to the frictional conditions between the sample and the die and μ=0.05 can give a better texture prediction compared to the experimentally measured pole figures [179].

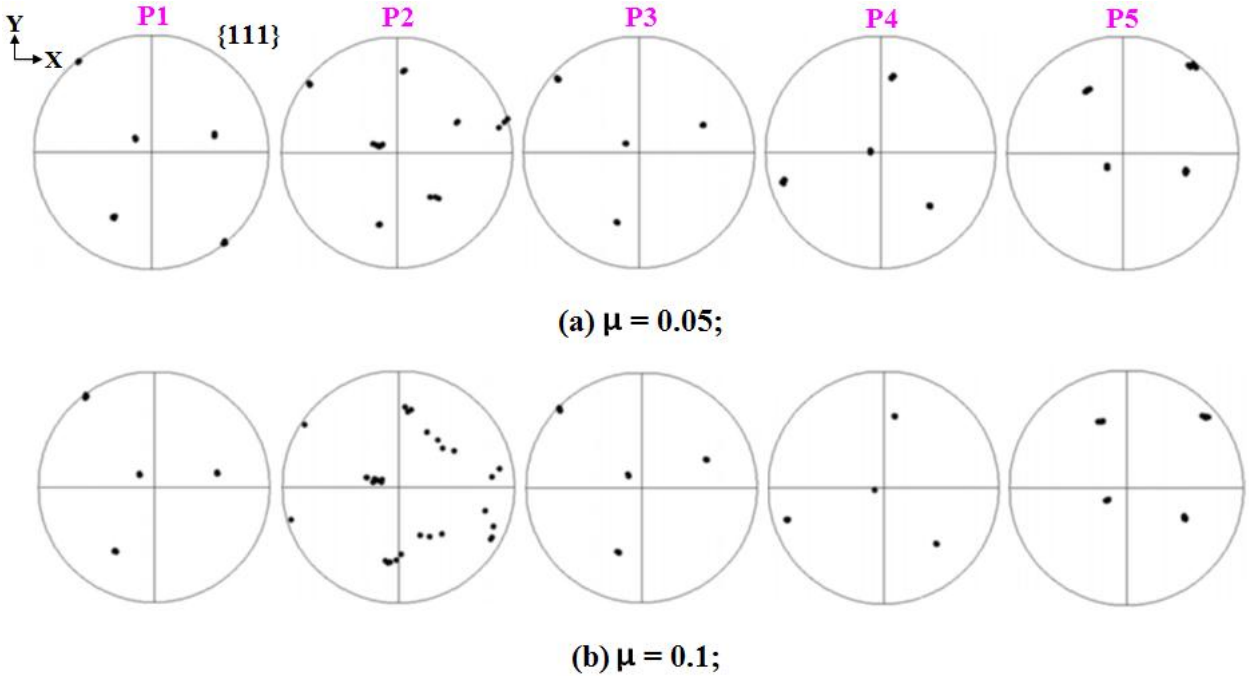

Fig. 5.4 Comparisons of the {1 1 1} pole figures for five selected positions P1-P5 marked in Fig. 5.5(c) between simulation results with different friction coefficients (a) μ=0.05 and (b) μ=0.1.

The calculated crystallographic rotation has been divided into three components around the X, Y, and Z axes. Fig. 5.5 shows the contour maps of the crystal rotation angles around all three axes in the deformed billet for μ=0.05. It is apparent in Fig. 5.5 that the crystal rotates in three-dimensions and predominantly around the Z axis for copper single crystals with the studied initial crystallographic orientation. Fig. 5.5(a) implies that the crystal rotation around the X axis is very small, varying between -5° and 5°. The positive rotation around the X axis mainly

happens in the middle part of the billet while the upper and lower parts are characterized by negative rotation. It can be seen in Fig. 5.5(b) that the crystal rotation around the Y axis is negative in the lower part and positive in the upper part. The rotation angle varies between -5° to 10° and the layer-type distribution of the rotation angle around the Y axis parallel to the X axis can be observed in Fig. 5.5(b). By contrast to the rotations around both the X and Y axes, there is a large variation in the Z-axis rotation as shown in Fig. 5.5(c). Apart from the inhomogeneous distributions in the leading head and tail of the billet, the Z-axis rotation angles can generally be divided into three parts, which are roughly parallel to the X axis, along the thickness direction. The upper part has a rotation angle of about 60°, the middle part about 0° and the lower part about 90°. This leads to splitting of the initial single crystal into three parts with different texture components.

Similar to the aluminium single crystal with the same initial orientation in Section 4.1, three matrix bands and two transition bands through the thickness developed in the copper single crystals after one pass of the ECAP process, as shown in Fig. 5.5(c). Three matrix bands are marked as M1, M2, and M3 while the transition bands are marked as T1 and T2, respectively. The rotation angles around the Z axis in three matrix bands are approximately 60°, 0° and 90°, respectively. The strain rate varies from the inner corner to the outer corner in the PDZ and multi-slip systems are activated in M1 while the single dominant slip system is activated in M2. This results in 60° rotation in M1 and zero rotation in M2. Due to the geometry of the ECAP die, the material must rotate about 90° around the Z axis in M3 and therefore, the lattices must rotate about 90°. Position P2 indicated in Fig. 5.5(c) is located in the transition band (T1) between M1 and M2, leading to both 60° and 0° rotations observed in the corresponding pole figures (Fig. 5.4(a-c)). Position P3 lies in M1, therefore only a 60° rotation is observed in the {1 1 1} pole figure.

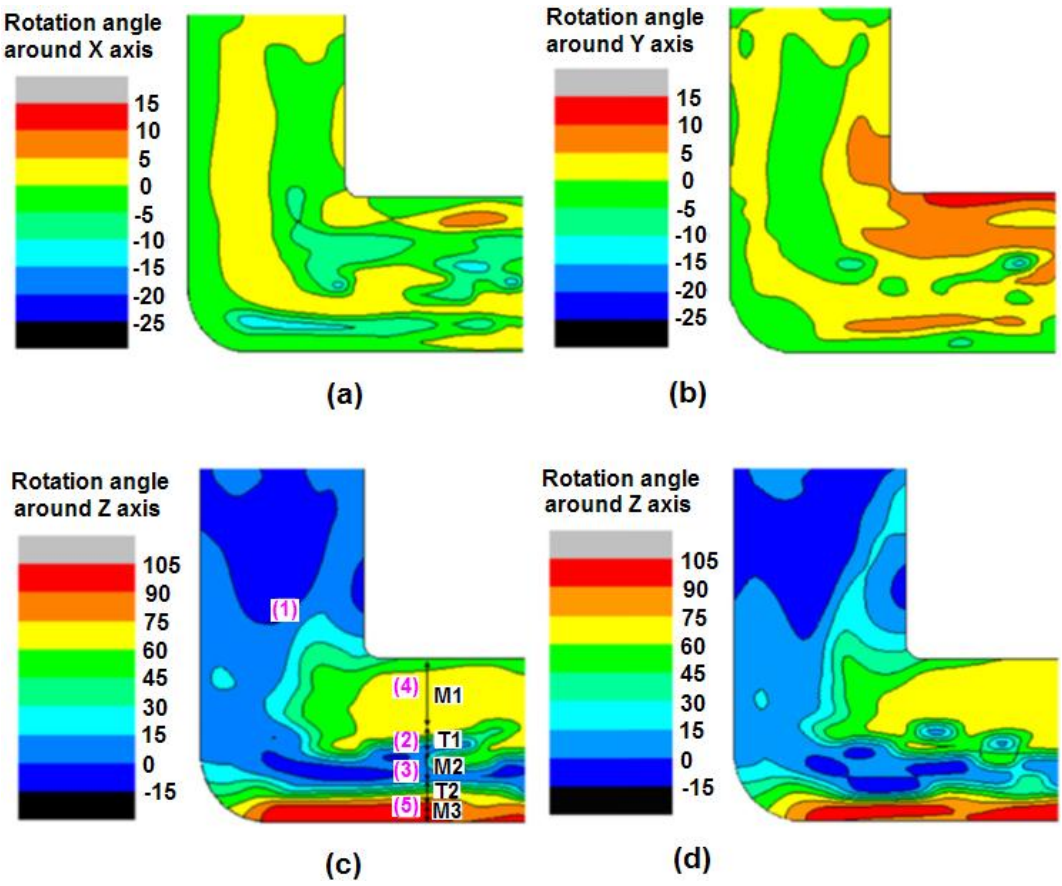

Fig. 5.5 Contour of crystal rotation angles in the steady-state deformation region of the ECAP processed copper single crystals. (a), (b), and (c) indicate the rotation components around the X, Y, and Z axes for μ=0.05, respectively and (d) indicates the rotation component around the Z axis for μ=0.1. The numbers (1)-(5) marked in (c) indicates the selected positions P1-P5. Matrix bands and transition bands are marked as 'M' and 'T', respectively.

In order to study the influence of friction on the crystal rotation patterns during the ECAP process of copper single crystal, the results for two different coefficients (μ=0.05 and μ=0.1) are compared. Since the crystal rotation components around the X and Y axes are much smaller than the rotation component around the Z axis, only the contour of the Z-axis rotation angle for μ=0.1 is plotted in Fig. 5.5(d). It can be seen that a larger friction coefficient results in more inhomogeneous crystal rotation around the Z axis. In addition, similar matrix bands and transition bands to the μ=0.05 case can be found. The Z-axis rotation angle in the vicinity of the top and bottom surfaces of the deformed samples increases slightly with the coefficient of

friction. It has also been observed that several matrix bands inclined at about 20° to the X axis developed along the billet axis.

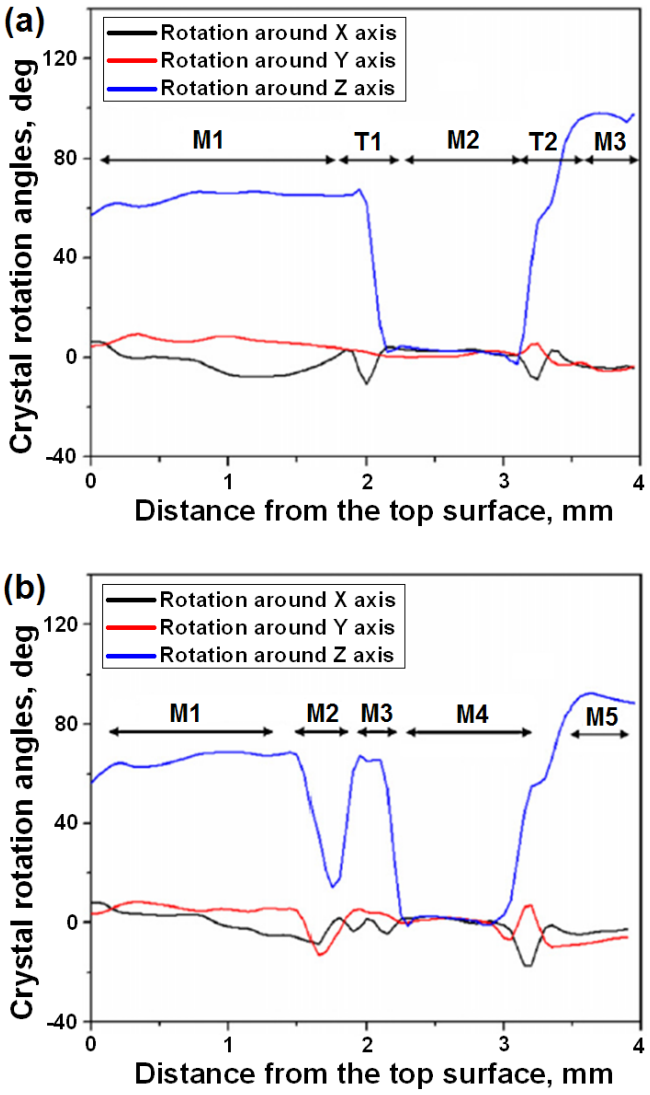

Fig. 5.6 Crystal rotation angles around the X, Y, and Z axes along the sample thickness in the exit channel at 1.5 mm away from the intersecting zone. (a) μ=0.05 and (b) μ=0.1.

Fig. 5.6(a) and (b) shows the partitioned crystal rotation angle components in the steady-state deformation region about 1.5 mm away from the main PDZ in the exit channel, as a function of the distance from the top surface for μ=0.05 and μ=0.1, respectively. It can be seen from Fig. 5.6(a) that the crystal rotation angles around both the X and Y axes are relatively small and the crystal mainly rotates around the Z axis. Three matrix bands (labelled M1, M2, and M3) and two

transition bands (labelled T1 and T2) are also shown in Fig. 5.6(a) but the crystal is split into 5 matrix bands along the thickness for the larger friction coefficient (μ=0.1), as indicated in Fig. 5.6(b). Compared to the case of μ=0.05, the matrix band in the central part has been divided into three small matrices (M2, M3, and M4) in the case of μ=0.1. This clearly indicates that the friction condition has an obvious influence on inhomogeneous texture evolution during the ECAP process.

5.2 Influence of ECAP Die Channel Angles

This section studies the influence of the ECAP die channel angles on the plastic deformation and development of crystallographic orientations of copper single crystals during the ECAP process. According to the previous studies, it has been found that the die channel angle has the most significant influence compared to the other geometry parameters including the channel width, outer corner angle and inner corner fillet radius. Therefore, this section will investigate the influence of the ECAP die channel angle during ECAP of copper single crystals.

In the previous section, a die channel angle of ϕ=90° has been studied. In this section, another two different die channel angles ϕ=75° and 105° have been analysed using the CPFEM model. Two-dimensional simulations based on plane strain assumption were conducted. The billet has an initial rectangular geometry of 26 mm (in length) by 4 mm (in width). 8000 elements have been used in the simulations. The die channels and punch are assumed to be a rigid body and the friction coefficient μ is set to 0.05 for all the simulations because it gives a better texture prediction compared with the experimental results shown in Section 5.2. Copper single crystal with the same initial crystallographic orientation, namely [-1 9 4] || ED and [-11 1 -5] || ID, is investigated. Simulations were terminated when 4/5 of the sample passed through the intersecting zone of the ECAP die.

5.2.1 ϕ = 75°

Fig. 5.7 shows the mesh distortions and distribution of plastic strain in the copper single crystal during the ECAP process with a die channel angle of 75°. Apart from inhomogeneous

deformation in the leading head part, relatively uniform steady-state region along the billet axis has been achieved. From Fig. 5.7(a), it can be observed that the mesh near the right side of the entry channel is already distorted before entering the intersecting zone due to the change of material flowing direction around the inner corner. The mesh distortions are not uniform along the sample thickness, as marked by line L-L' in Fig. 5.7(a). Compared to the shear deformation in the upper part of the sample, the elements in the bottom show that the main deformation pattern is rigid body rotation. Fig. 5.7(b) shows the plastic strain distribution in the deformed sample. There are three regions with different magnitudes of the plastic strain along the sample thickness and the plastic strain in the bottom part is very small.

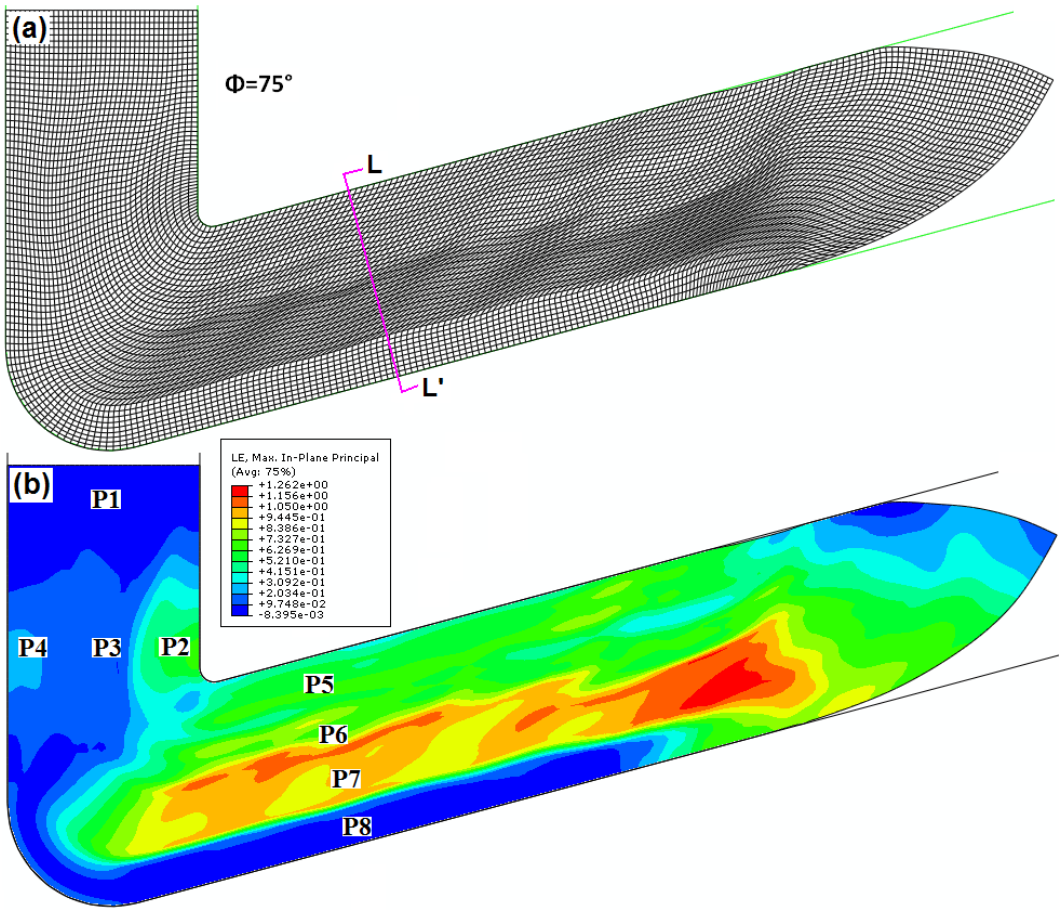

Fig. 5.7 Mesh distortions and plastic strain distribution in the deformed copper single crystal during the ECAP process with a die channel angle of 75°.

The deformation behaviour of a copper single crystal with a die channel angle of 75° was studied with the help of plastic strain rate contours as shown in Fig. 5.8. Similar to the 90° die, the magnitude of the plastic strain rate change significantly from the inner corner to the outer corner. The strain rate contours indicated a slight plastic deformation at the right side of the entry channel before entering the intersecting zone. A careful examination shows the existence of a corner gap (or dead zone) between the sample and die, represented by two points 'A' and 'B' in Fig. 5.8(a). This result is consistent with the early report [283], where a corner gap, less sheared bottom region and a front transient inhomogeneous deformation region were also observed. In addition, no corner gap developed when a sharp outer corner angle was used [284, 285].

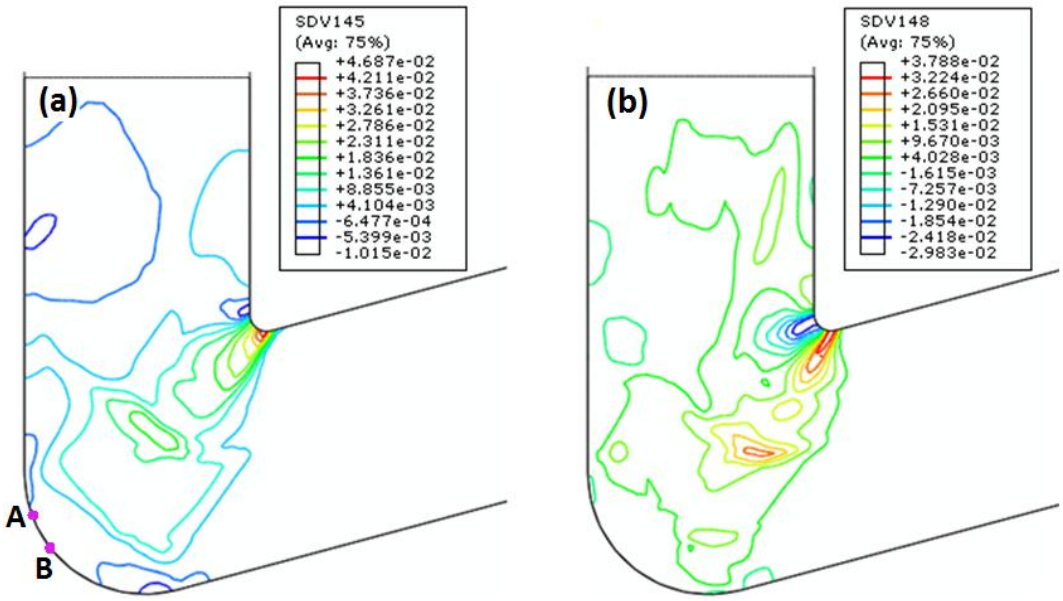

Fig. 5.8 Distribution of the plastic strain rate components (a) $\dot{\varepsilon}_X$ and (b) $\dot{\varepsilon}_{XY}$ in the deformed copper single crystal during the ECAP process with a die channel angle of 75°.

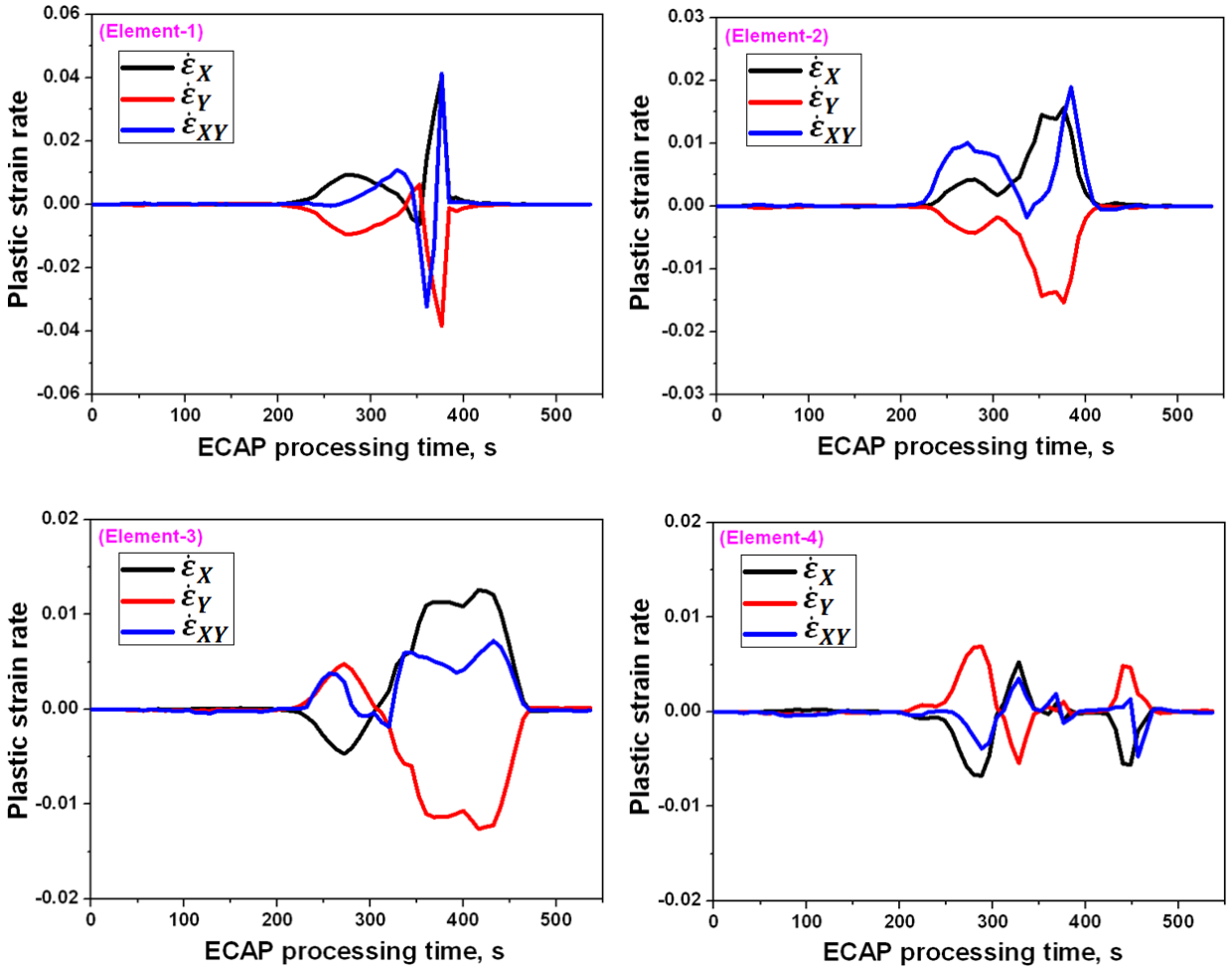

Fig. 5.9 Plastic strain rates for four tracked elements as function of the deformation time during the ECAP process with a die channel angle of 75°.

Four elements at different selected positions are tracked. The histories of the plastic strain rates and plastic strains of four elements are shown in Fig. 5.9 and Fig. 5.10, respectively. It is clear that the elements close to the inner corner (right side of the sample) start to deform earlier than the elements close to the outer corner (left side of the sample). Element-1 is tensioned in the X direction and compressed in the Y direction at the early stage, and then shear is induced which becomes the dominant deformation pattern when the element is close to the inner corner. Severe deformation is observed when the element entered into the intersecting zone where the magnitudes of all three strain rates rise rapidly and then decrease to zero when the element exit the PDZ. The sign of $\dot{\varepsilon}_{XY}$ changes from negative to positive after passing through the ideal shear plane as shown in Fig. 5.9. For Element-2, tension, compression,

and shear are induced at the same time before the element enters the PDZ, and the magnitude of $\dot{\varepsilon}_{XY}$ is larger than $\dot{\varepsilon}_X$ and $\dot{\varepsilon}_Y$. However, the magnitude of $\dot{\varepsilon}_{XY}$ of Element-2 is similar to those of $\dot{\varepsilon}_X$ and $\dot{\varepsilon}_Y$ in the PDZ. It has been found that the elements (Element-3 and Element-4) close to the outer corner are subjected to compression in the X direction and tension in the Y direction before entering the intersecting zone, and then tensioned in the X direction and compressed in the Y direction in the PDZ. This is different to Element-1 and Element-2, which are tensioned in the X direction and compressed in the Y direction during the whole plastic deformation procedure. The magnitude of $\dot{\varepsilon}_{XY}$ of Element-3 is smaller than those of $\dot{\varepsilon}_X$ and $\dot{\varepsilon}_Y$ in the PDZ. Compared to the other three elements, the strain rates of Element-4 are very small. This can be contributed to the rigid body rotation due to the presence of an outer corner angle.

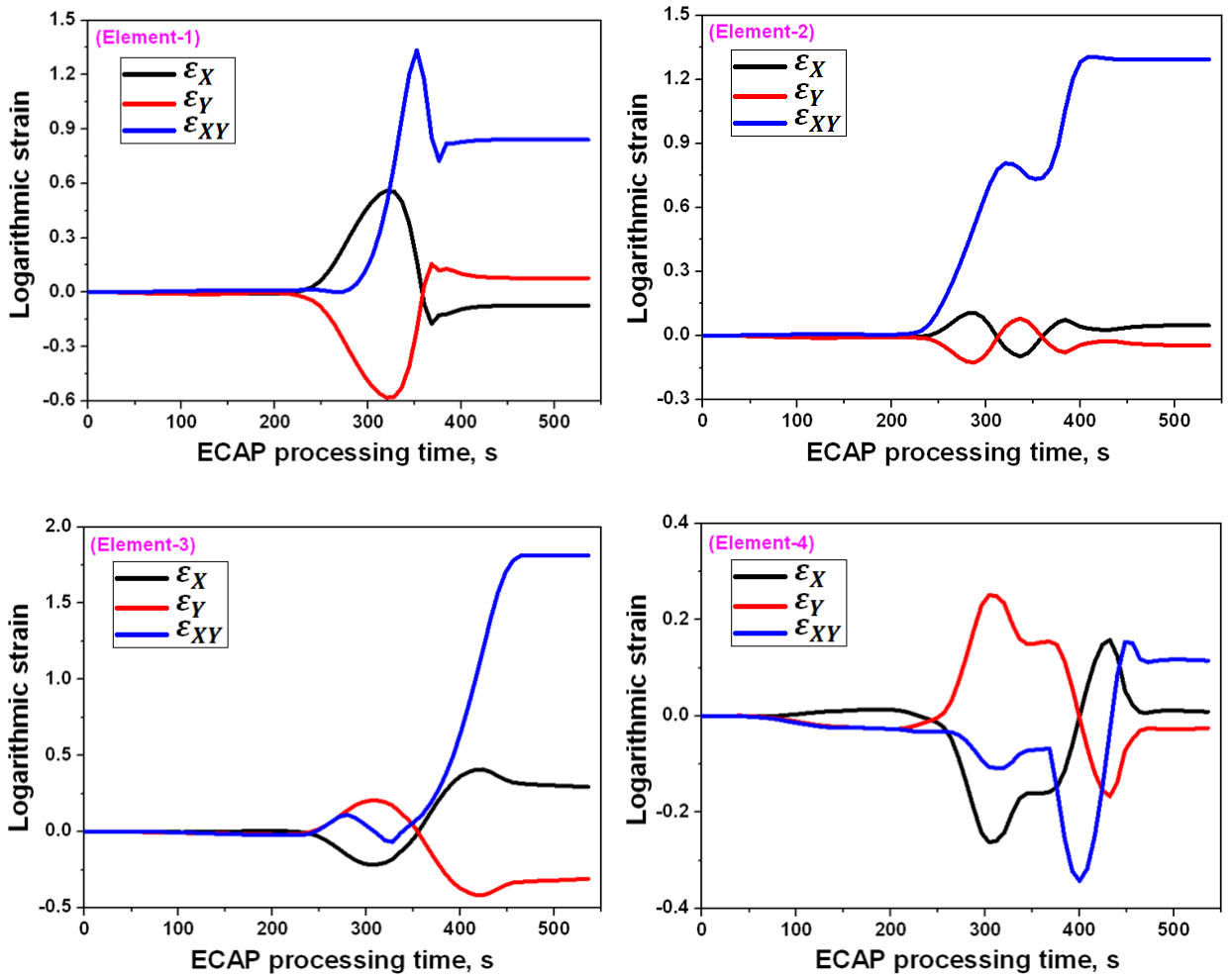

Fig. 5.10 Logarithmic plastic strain components for four tracked elements as function of the deformation time during the ECAP process with a die channel angle of 75°.

As can be seen in Fig. 5.10, the magnitude of shear strain is slightly smaller than the normal components when Element-1 is in the entry channel, but it increases rapidly when the element enters the PDZ while the normal components gradually decreases. Element-3 has the largest shear strain after ECAP process than the other three elements and the strain components for Element-4 are much smaller due to the different deformation pattern.

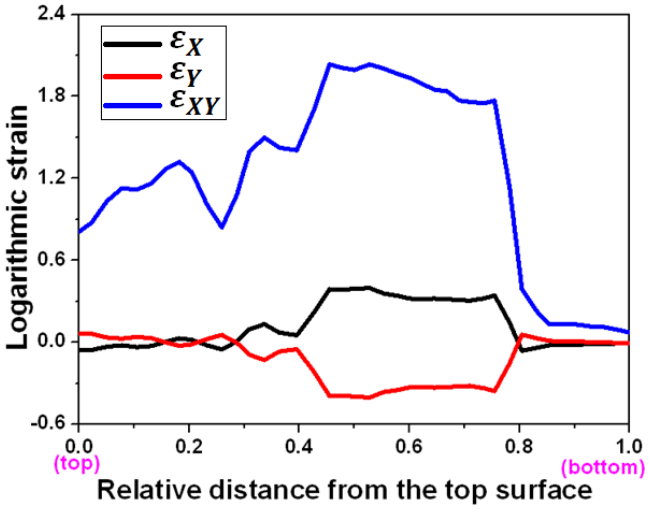

Fig. 5.11 Variations of the Logarithmic plastic strain components along the sample thickness (line L-L) in the deformed copper single crystal during the ECAP process with a die channel angle of 75°.

In order to study the deformation homogeneity of the sample, the variations in the plastic strains along the sample thickness L-L', as depicted in Fig. 5.7(a), are plotted in Fig. 5.11. The sample thickness L-L', is depicted in Fig. 5.7(a). It is obvious that there are three distinguished regions according to the strain distributions along the thickness of the sample. In the upper 40% of thickness, the shear strain component (ε_{XY}) increased slowly and the normal strain components (ε_X and ε_Y) are zero. The middle 40% of thickness has uniform results and the maximum shear strain has been observed in this region. The remaining 20% of the thickness is almost uniform with a very small plastic strain, as shown in Fig. 5.11(a). The average effective strain value was 1.407, which was slightly higher than the theoretical value (1.234) calculated by Iwahashi et al. [104].

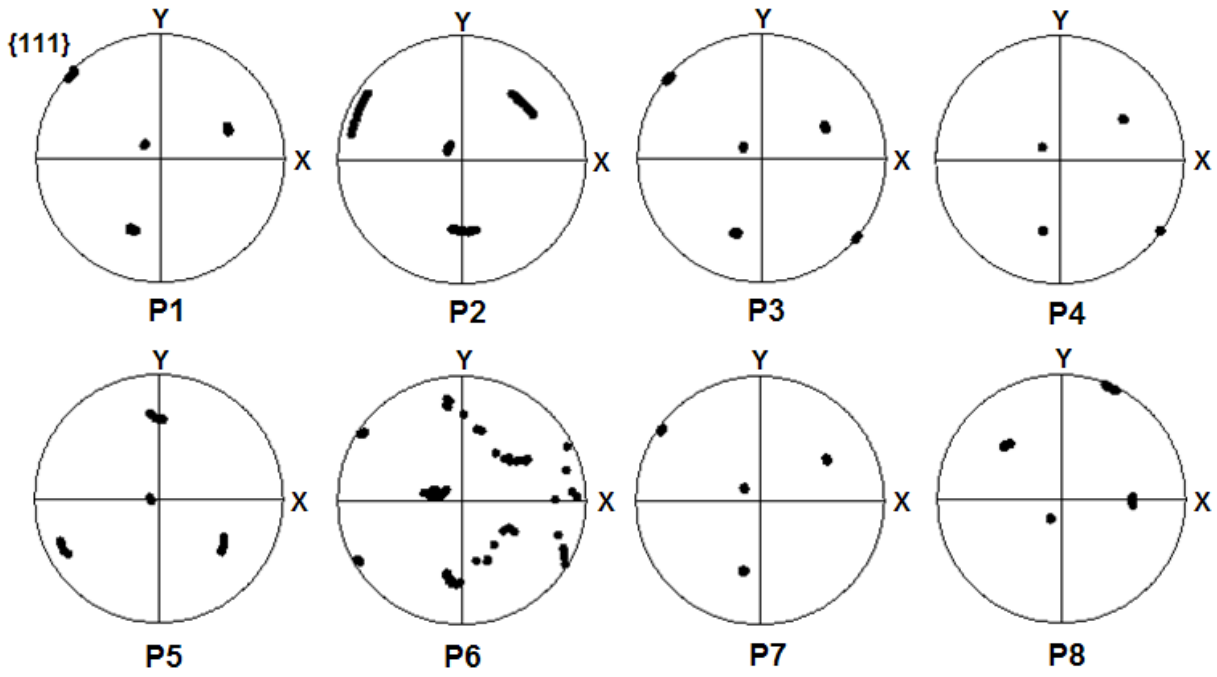

Fig. 5.12 Simulated {1 1 1} pole figures for eight selected positions in the deformed copper single crystal during the ECAP process with a die channel angle of 75°. (Positions P1-P4 are located in the entry channel and positions P5-P8 are located in the exit channel marked in Fig. 5.6(b))

Eight positions (P1-P8) are selected to study texture evolution during the ECAP process with a die channel angle of 75°. The positions are marked in Fig. 5.7(b), positions P1-P4 are located in the entry channel and positions P5-P8 are located in the exit channel. A texture analysis is conducted in terms of {1 1 1} pole figures. It is clear that the orientation does not change at position P1 which is far away from the PDZ. Plastic deformation is induced when the material gets close to the PDZ, which leads to the changes of crystallographic orientation. The {1 1 1} pole figures at positions P2-P4 reveal the variation from the initial crystallographic orientation. There is more orientation scattering at P2 than P3 and P4, as shown in Fig. 5.12, which should be attributed to the more severe plastic deformation induced on the right side of the sample. The pole figure at P5 indicates a single orientation rotated from the initial orientation by 70° around the Z axis in a counter-clockwise direction. By contrast, the pole figure at P6 reveals the presence of an initial crystallographic orientation and a rotated component. The crystallographic orientations at P7 and P8 are characterized by the initial orientation and a 105° rotated component, respectively.

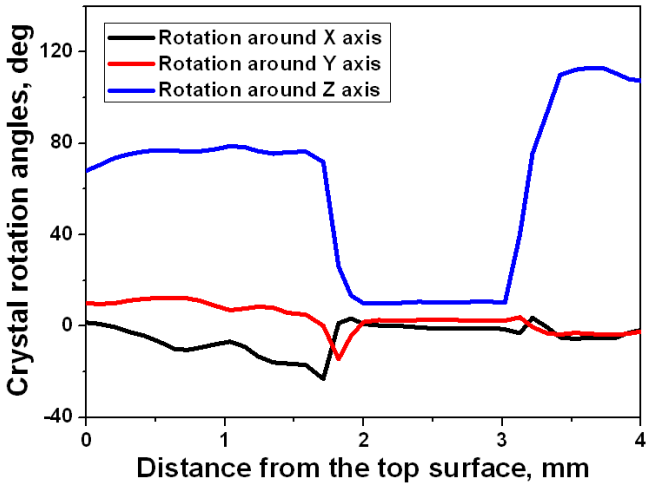

Fig. 5.13 Variation of crystal rotation angles along the thickness of the sample (line L-L) in the deformed copper single crystal during the ECAP process with a die channel angle of 75°.

The crystal rotation patterns for copper single crystal subject to ECAP with an acute channel angle die are studied shown in Fig. 5.13. Similar to the 90° die, the crystal rotates in three dimensions and the dominant rotation is around the transverse direction. There are three distinguished matrix bands along the thickness connected by two transient bands. In the upper matrix band (upper 40% of the thickness), the crystal rotation angles around X, Y, and Z axes are -20°, 15°, and 75°, respectively, where a negative sign means clockwise rotation and a positive sign means counter-clockwise rotation. The crystal rotation angles are almost zero around all three axes in the middle matrix band (about 30% of the thickness), which leads to the remaining initial crystallographic orientation at P7 in Fig. 5.12. In the lower matrix band (nearly 20% of the thickness in the bottom), the crystal only rotates around the Z axis. The deformation in the last matrix band is characterized by the rigid body rotation and the rotation angle is about (π- ϕ), which equals to 105° in this study.

5.2.2 ϕ=105°

Fig. 5.14 shows the mesh distortions and plastic strain distribution in the deformed copper single crystal during the ECAP process with the die having a channel angle of 105° and an OCA of 10°. As can be seen, the elements in this case have not been deformed as seriously as in the die with channel angles of 75° and 90°. Fig. 5.14(a) reveals a large dead zone in the outer corner

and some gaps between the sample and the exit channel, which lead to an inhomogeneous plastic strain distribution in the deformed sample, as shown in Fig. 5.14(b). The largest strain exists in the left corner of the head part. The deformation process is found to be different to the die channel angles of 75° and 90°. In this case, the left corner of the head part sticks to the bottom of the die first, and then the sample starts to fill the deformation zone and flow to the exit channel at the same time.

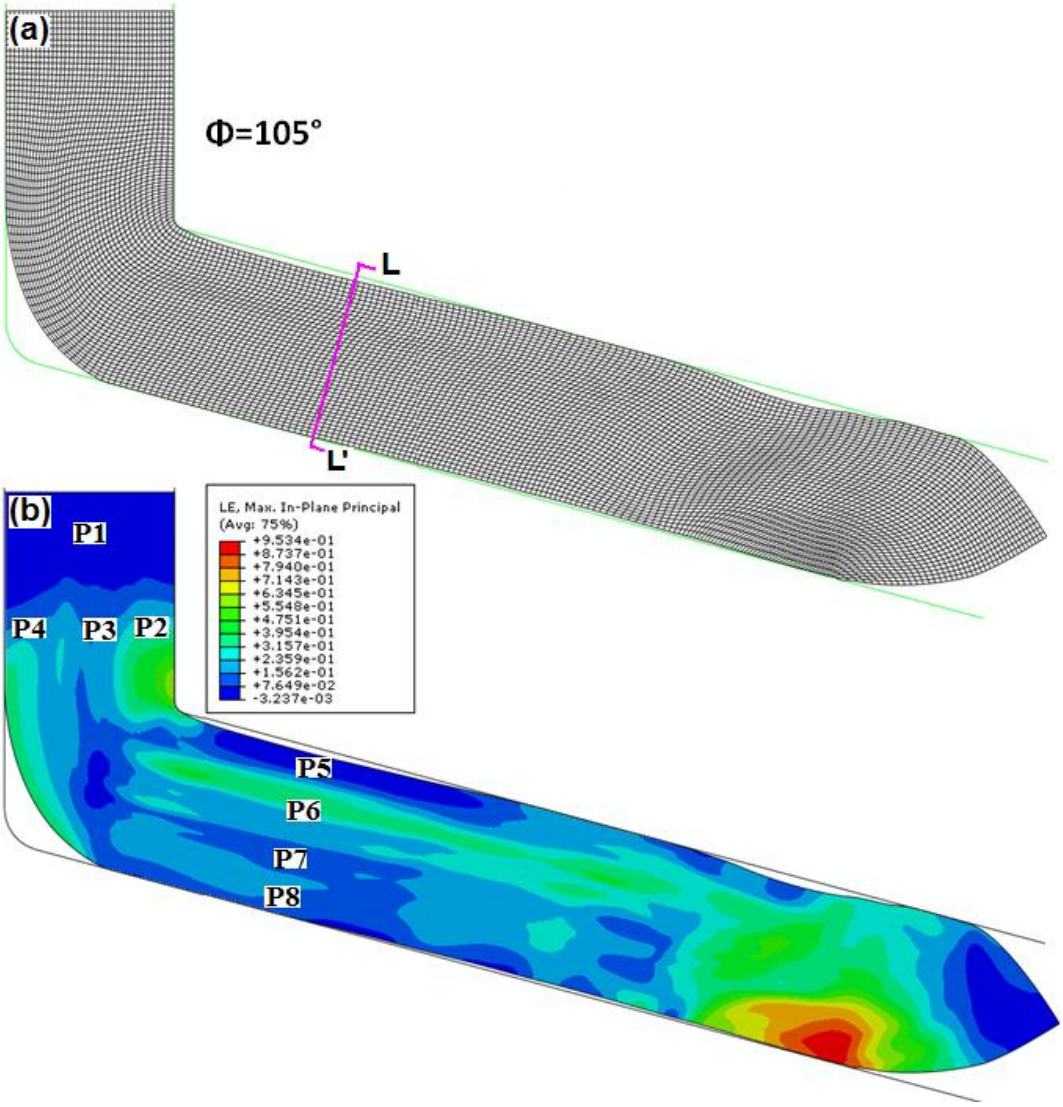

Fig. 5.14 Mesh distortions and plastic strain distribution in the deformed copper single crystal during the ECAP process with a die channel angle of 105°.

Distribution of the stress in the plastic deformation zone examined and the maximum stress is near the inner corner and decreased gradually to the outer corner. Fig. 5.15 shows the PDZ during ECAP with a die channel angle of 105° and the dead zone in the outer corner is described by the arc marked by two points 'A' and 'B'. According to the strain rates contours, plastic deformation is not symmetrical to the ideal shear plane (intersecting plane of two channels). The magnitudes of the strain rates decrease from the inner corner to the outer corner and are much smaller compared to the die channel angles of 75° and 90° as shown in Fig. 5.8 and Fig. 5.2, respectively.

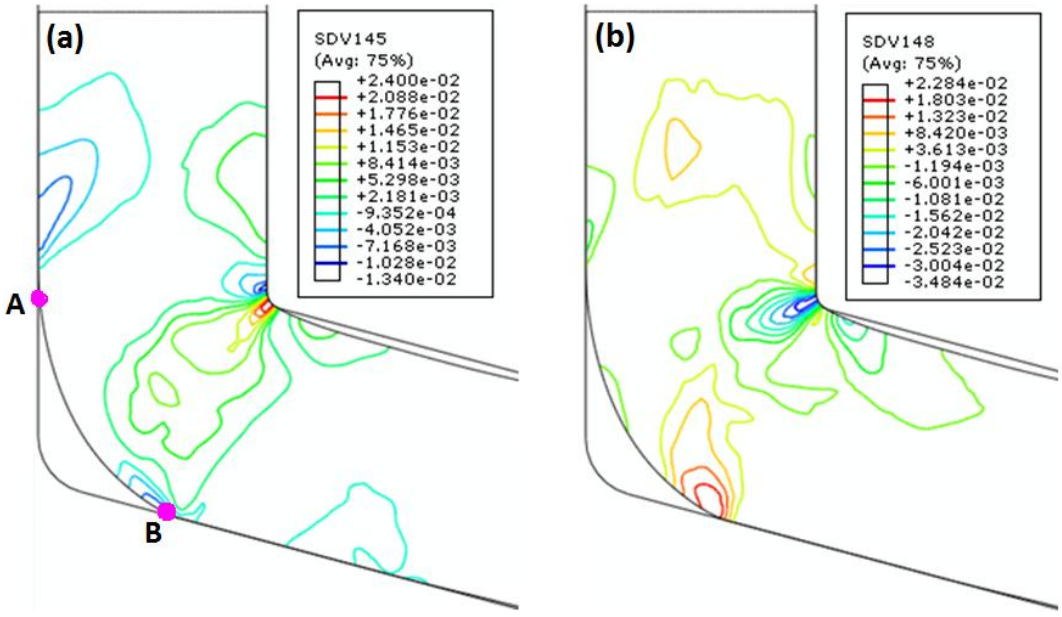

Fig. 5.15 Distribution of the plastic strain rate components (a) $\dot{\varepsilon}_X$ and (b) $\dot{\varepsilon}_{XY}$ in the deformed copper single crystal during the ECAP process with a die channel angle of 105°.

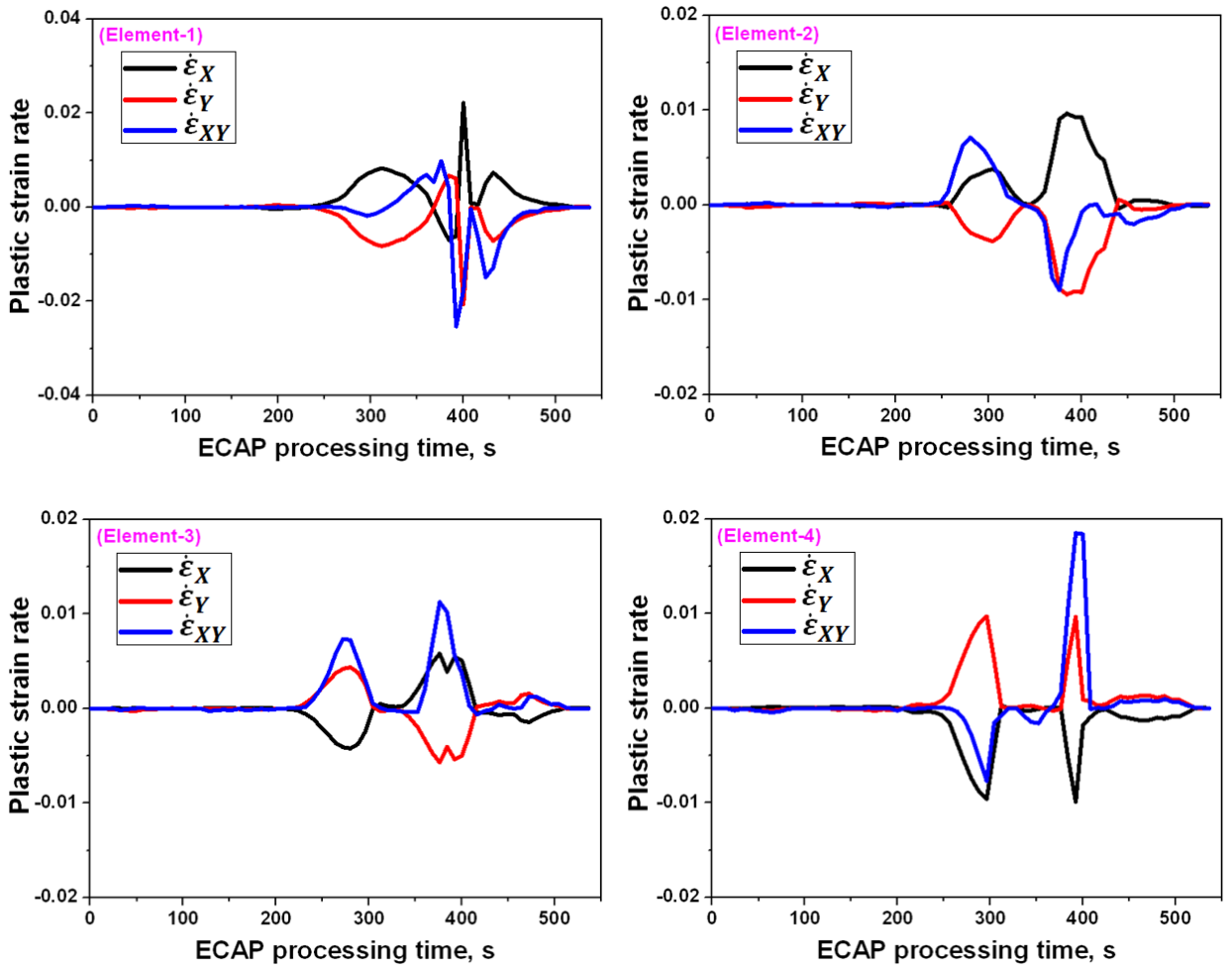

Fig. 5.16 Plastic strain rates for four tracked elements as function of the deformation time during the ECAP process with a die channel angle of 105°.

Four elements are tracked to study the deformation history during ECAP. The strain rates as functions of time for four elements are shown in Fig. 5.16. It can be seen that Element-1 and Element-2 are tensioned in the X direction and compressed in the Y direction before entering the intersecting zone, while the other two elements are tensioned in the Y direction and compressed in the X direction. The magnitudes of the strain rate components for Element-1 are slightly larger than the other three elements. In addition, the deformation time is shortest for Element-1 because it is located close to the inner corner. Element-4 undergoes the longest deformation due to its localization close to the outer corner.

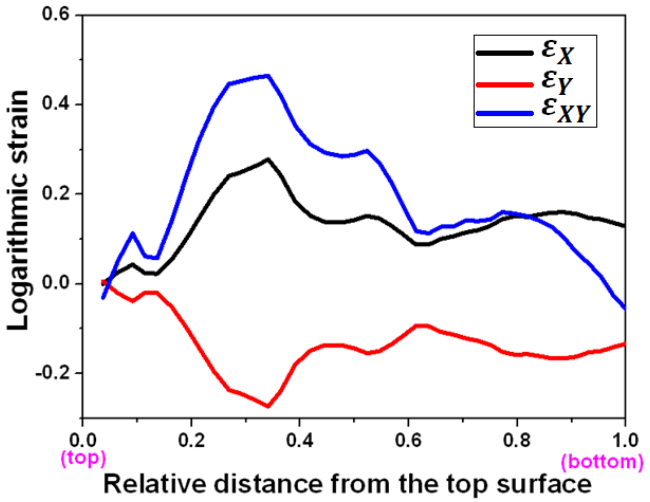

Fig. 5.17 Variation of the Logarithmic plastic strain components along the thickness of the sample (line L-L') in the deformed copper single crystal during ECAP with a die channel angle of 105°.

The deformation homogeneity along the thickness of the sample is analysed in terms of variation of the plastic strain, as shown in Fig. 5.17. It is obvious to find that the strain is very small in the upper 15% of the sample thickness due to the development of an exit channel gap as shown in Fig. 5.14 and Fig. 5.15. The gap leads to the decrement of the deformation degree. In the middle 65% of the thickness, the shear strain component (ε_{XY}) is slightly larger than the normal strain components. In the lower 20% of the thickness, the shear strain gradually decreases to zero but the normal strains remained almost constant. These results are different to the results for the die channel angles of 75° in Fig. 5.11 and 90° in Fig. 5.3.

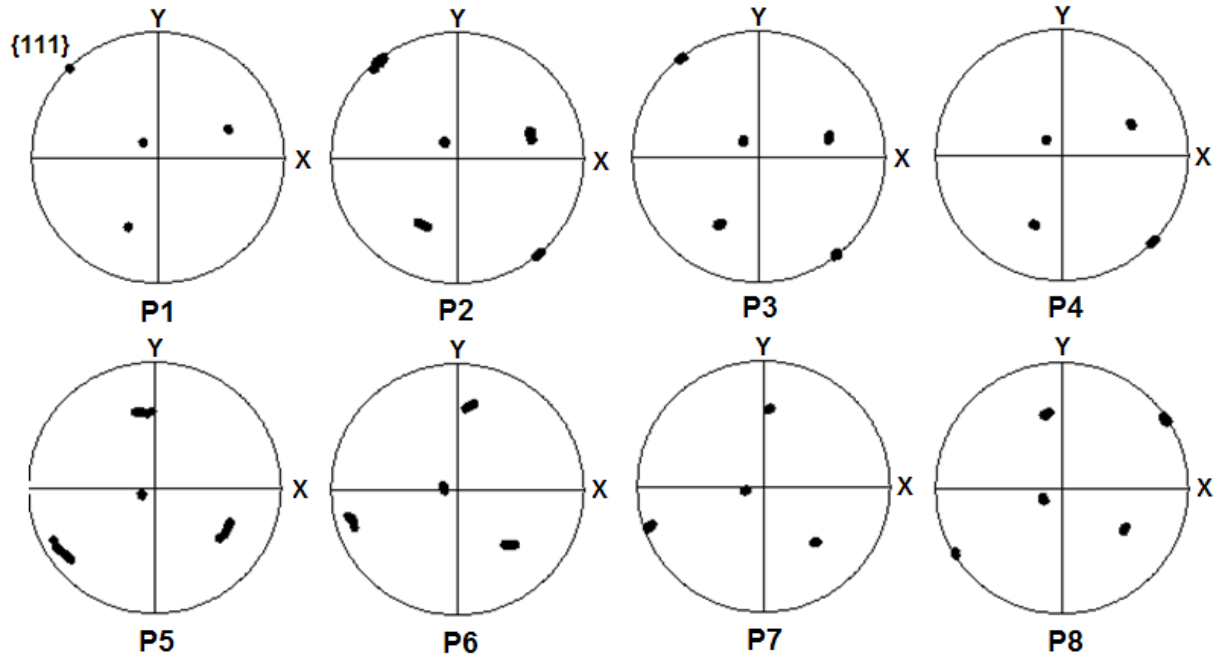

Fig. 5.18 Predicted {1 1 1} pole figures for eight selected positions in the deformed copper single crystal during the ECAP process with a die channel angle of 105°.

Eight positions (P1-P8) are selected to investigate the texture evolution of copper single crystal during ECAP with the die channel angle of 105°. The positions of eight positions are marked in Fig. 5.14(b) and the corresponding pole figures are shown in Fig. 5.18. It is obvious that only the initial crystallographic orientation is seen in the {1 1 1} pole figures at positions P1-P4, which are located in the entry channel and there is nearly no deformation. Position P5 is located close to the top surface and its pole figure indicates a rotated component (about 75°) from the initial crystallographic orientation. Positions P6 and P7 have a similar {1 1 1} pole figure which have a ~60° rotation in a counter-clockwise direction. The rotation angle at position P8 is equal to the die channel angle 75°.

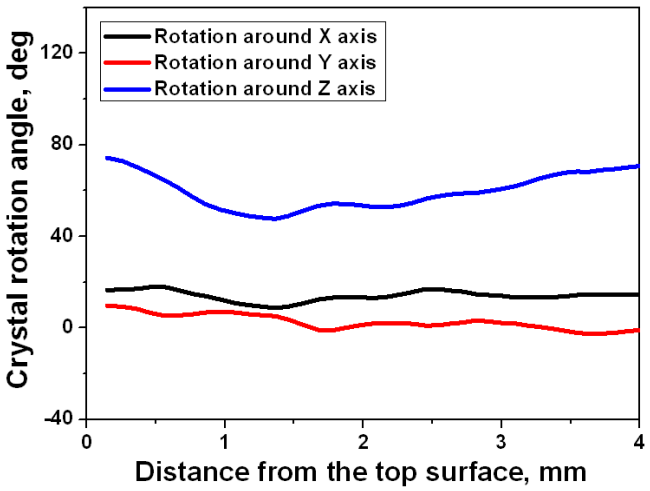

Fig. 5.19 Variation of crystal rotation angles along the thickness of the sample in the deformed copper single crystal during the ECAP process with a die channel angle of 105°.

It can be concluded from Fig. 5.19 that the crystal rotation patterns of copper single crystal in the case of ϕ=105° are very different to those of ϕ=75° and ϕ=90°, where three distinguished matrix bands were observed along the sample thickness after the ECAP process. It is clear that in this case no obvious matrix can be seen. It is clear that the predominant crystal rotation is around the transverse direction (Z axis) but the major difference between three cases lies in the X-axis rotation component. The crystal rotation angle around the X axis is much larger in this case and remains almost constant through the thickness with a value of 20° in a counter-clockwise direction. By contrast, the component around the Y axis varies slightly between 0° and 10°. There are two reasons for these observations: the first reason is that the 105° die induces less plastic deformation, and the second reason is the significant influence of the gaps developed between sample and the die (the large outer corner gap and the gaps in the exit channel as shown in Fig. 5.14).

5.3 Influence of Initial Crystallographic Orientations

(*This part has already been published in Steel Research International (2013)*)

In order to study the influence of the initial crystallographic orientation, four different copper single crystals, namely Crystal A, B, C, and D are investigated. In Crystal A, the (-1 -1 -1) slip

plane is rotated by 20° in a clockwise direction around the transverse direction from the theoretical shear plane (intersecting plane of two channels) and the [-1 1 0] slip direction is rotated by 20° in a clockwise direction around the transverse direction from the theoretical shear direction of the ECAP die. This results in that the crystallographic orientations along the X axis, Y axis and Z axis are [-0.3969 0.8849 0.244], [-0.8221 -0.2244 -0.5233] and [-1 -1 2] as listed in Table 5.1, respectively. In Crystal B, the rotation angle is the same as Crystal A but in a counter-clockwise direction. Therefore, the slip direction [-1 1 0] inclines 65° to the X direction. In Crystal C the slip plane (0 1 0) is parallel to the theoretical shear plane and the slip direction [1 0 0] is parallel to the ideal shear direction. In Crystal D the slip plane (1 1 -2) and slip direction [1 1 1] coincides with the theoretical shear plane and shear direction, respectively. The relationship between the initial crystallographic orientations of these four copper single crystals and the coordinate are listed in Table 5.1 in details.

Table 5.1 The relationship between the crystallographic orientations of four studied copper single crystals and the coordinate system X-Y-Z during the ECAP process.

Copper single crystals	X direction (ED)	Y direction (ND)	Z direction (TD)
A	[-0.3969 0.8849 0.244]	[-0.8221 -0.2244 -0.5233]	[-1 -1 2]
B	[0.224 0.8221 0.5233]	[-0.8849 0.3969 -0.244]	[-1 -1 2]
C	[1 -1 0]	[1 1 0]	[0 0 1]
D	[0.1196 0.1196 0.9856]	[0.6969 0.6969 -0.1691]	[-1 1 0]

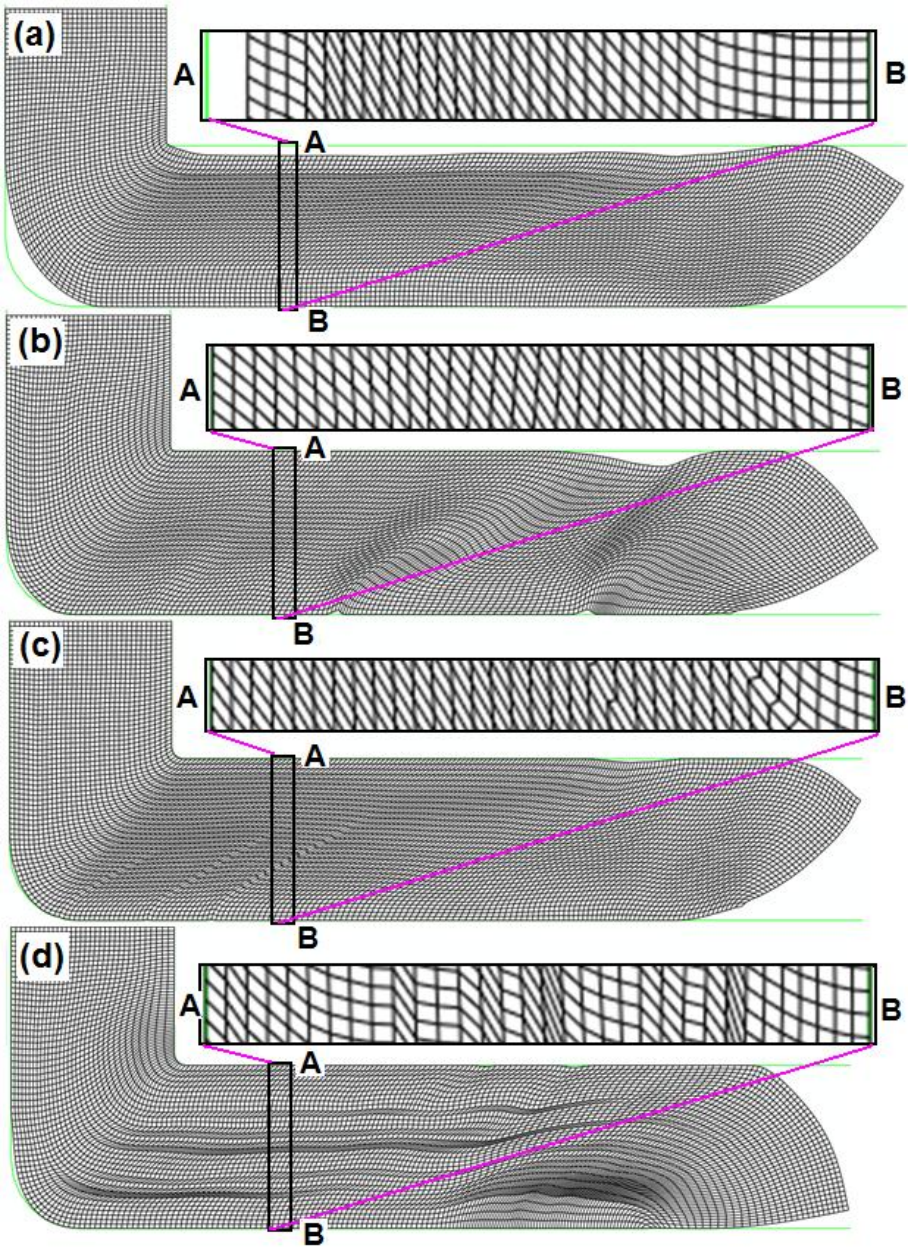

Fig. 5.20 Mesh distortions for four copper single crystals with different initial crystallographic orientation after ECAP with a 90° ECAP die: (a) Crystal A; (b) Crystal B; (c) Crystal C, and (d) Crystal D.

Four copper single crystals have the same sample size (26 mm × 4 mm) and the same meshes (8000 elements). The coefficient of friction μ=0.05. Simulations were conducted with an ECAP die channel angle of 90° and an OCA of 30°.

The mesh distortions of four copper single crystals are shown in Fig. 5.20. A significant influence of initial crystallographic orientation can be clearly observed. Different initial orientation leads to different head shape and mesh distortion after the ECAP process. A region marked 'AB' in the steady-state deformation region of each crystal is selected to examine the deformation heterogeneity along the thickness, as shown in Fig. 5.20. As the enlarged parts show, deformation is not uniform through the thickness and it depends strongly on the initial crystallographic orientation. In Crystal A a gap (called 'exit channel gap') between the sample and the upper surface of the exit channel develops. This means that the elements near the upper surface undergo less shearing than those in the middle part. Rigid body rotation without severe plastic deformation has been observed for the elements near the sample bottom. The rigid rotation angle is about 50° as indicated in Fig. 5.20(a). The deformation in Crystals B and C are much more uniform along the thickness than Crystals A and D because of the smaller dead zones in the outer corner. It is obvious that the smaller corner gap leads to a narrower rigid body rotation region at the sample bottom. The angles of the corner gaps shown in Fig. 5.20 are 15°, 10°, and 40° in Crystals B, C and D respectively. These values are compared in Table 5.2.

Table 5.2 The angle of the outer corner gap, average value of the effective plastic strain ($\bar{\varepsilon}$) and deformation inhomogeneity index (C_i) for all four copper single crystals after the ECAP process.

Crystals	Corner gap (°)	$\bar{\varepsilon}$	C_i
A	50	0.8948	1.6332
B	20	1.0605	0.9849
C	10	1.3163	0.8991
D	40	1.0787	1.2037

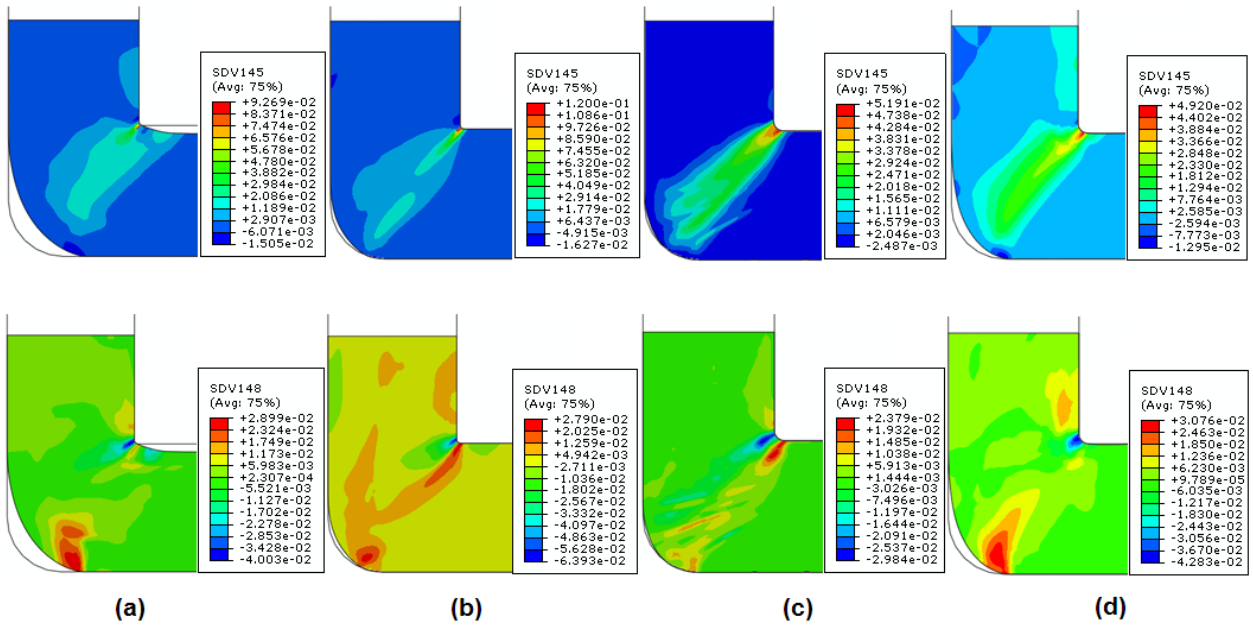

Fig. 5.21 Contour of distribution of the plastic strain rates in (a) Crystal A, (b) Crystal B, (c) Crystal C, and (d) Crystal D. (the upper panel shows the $\dot{\varepsilon}_X$ and the lower panel shows the $\dot{\varepsilon}_{XY}$)

Fig. 5.21 shows the contours of the distributions of the plastic strain rates for four copper single crystals during the ECAP process. The results indicate the deviation of deformation from an ideal simple shear along the intersecting plane of two channels for all four copper single crystals. In Crystal A there is a very wide PDZ which is attributed to the large gaps in the outer corner and exit channel, as shown in Fig. 5.21(a). In Crystals B, C, and D, the fan-shaped PDZs are observed.

The effective plastic strains along the sample thickness for all four crystals are plotted in Fig. 5.22. According to the distribution of effective plastic strain, three different regions in crystals A and D and two different regions in crystals B and C along the thickness can be seen. The deformation inhomogeneity index (C_i) in Table 5.2 indicates that crystal C leads to the most homogeneous plastic deformation along the thickness.

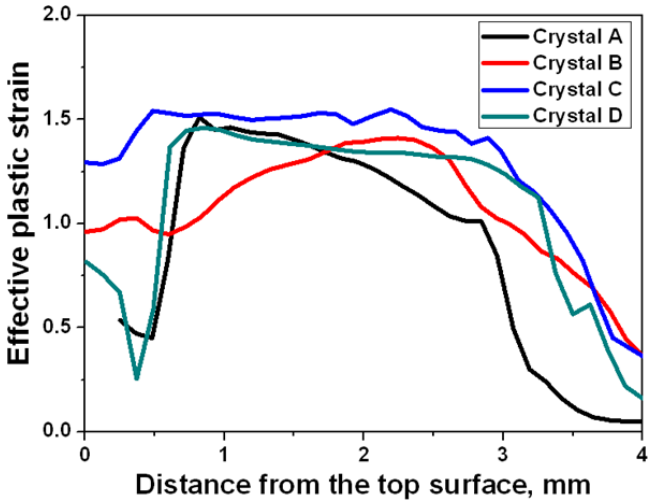

Fig. 5.22 Distribution of the effective plastic strain along the billet thickness for all four copper single crystals after ECAP.

The influence of initial crystallographic orientation on texture evolution during ECAP of copper single crystals is shown in Fig. 5.23. Four different positions marked in Fig. 5.24(a) are selected to plot the corresponding {1 1 1} pole figures. As can be seen, position P1 is located in the entry channel before entering the PDZ and positions P2-P4 are located in the exit channel after passing through the PDZ. Fig. 5.23(a) shows the textures for Crystal A. The pole figure at position P1 indicates the initial crystallographic orientations. By contrast, the pole figures at positions P2 and P3 are similar and a rotation of 20° from the initial crystallographic orientation in a counter-clockwise direction can be observed. At position P4, the pole figure reveals a component with 90° rotation. These simulation results are consistent with the experimental measurements reported by Fukuda et al. [179]. The textures for Crystal B are shown in Fig. 5.23(b) and only the initial crystallographic orientation is seen at position P1 and a 40° rotated component exists at positions P2 and P3. Fig. 5.23(c) and Fig. 5.23(d) show the simulated textures for Crystal C and Crystal D, respectively. It can be found that both the positions P2 and P3 have the similar {1 1 1} pole figures and the rotation angles are 60° in Crystal C and 20° in Crystal D. On the other hand, position P4 is located in the bottom part and the rotation angle is almost 90° which equals the ECAP die channel angle used in this study for all the copper single crystals.

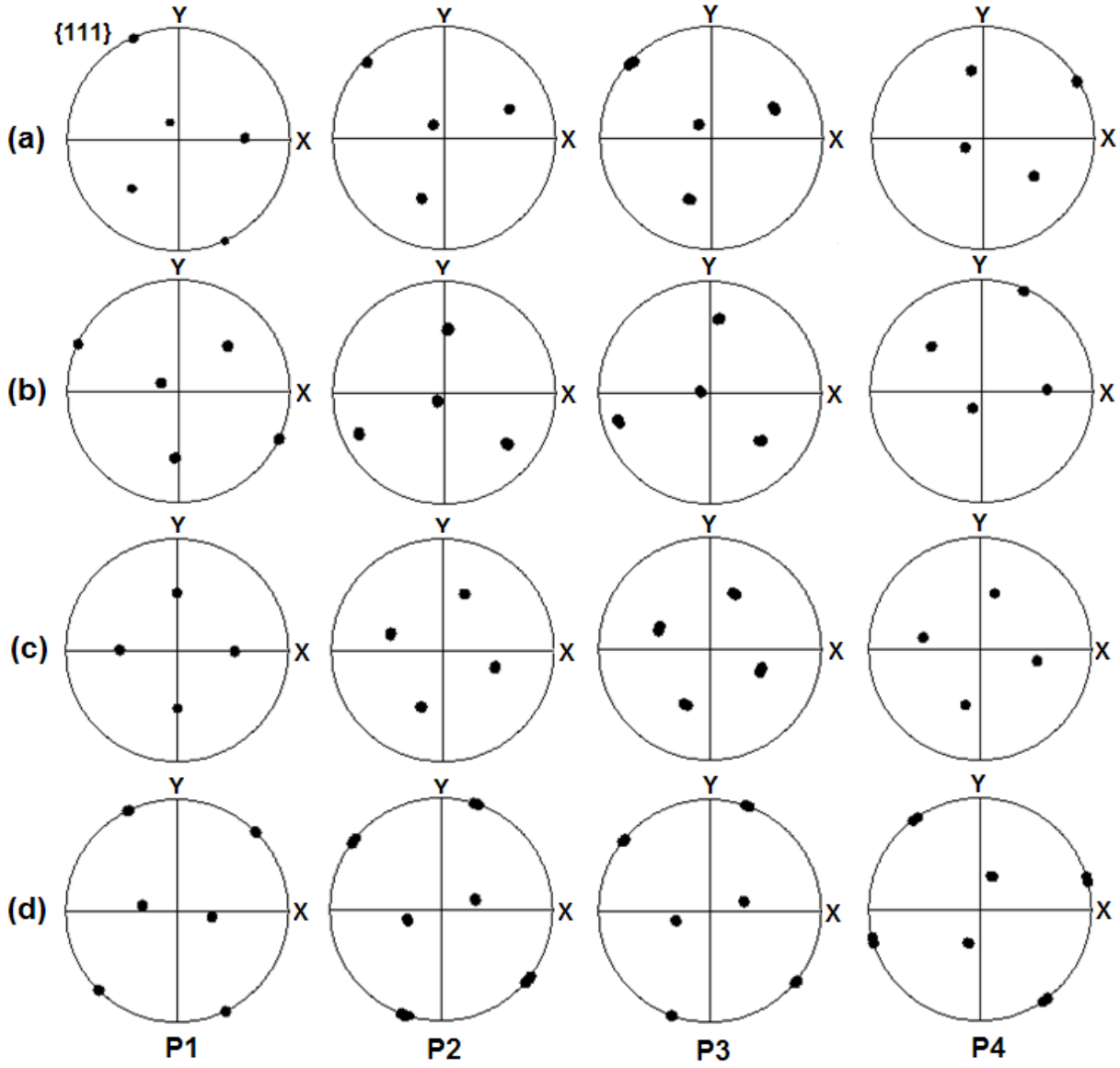

Fig. 5.23 Comparisons of the CPFEM simulated {1 1 1} pole figures at selected positions for copper single crystals during the ECAP process: (a) Crystal A, (b) Crystal B, (c) Crystal C, and (d) Crystal D.

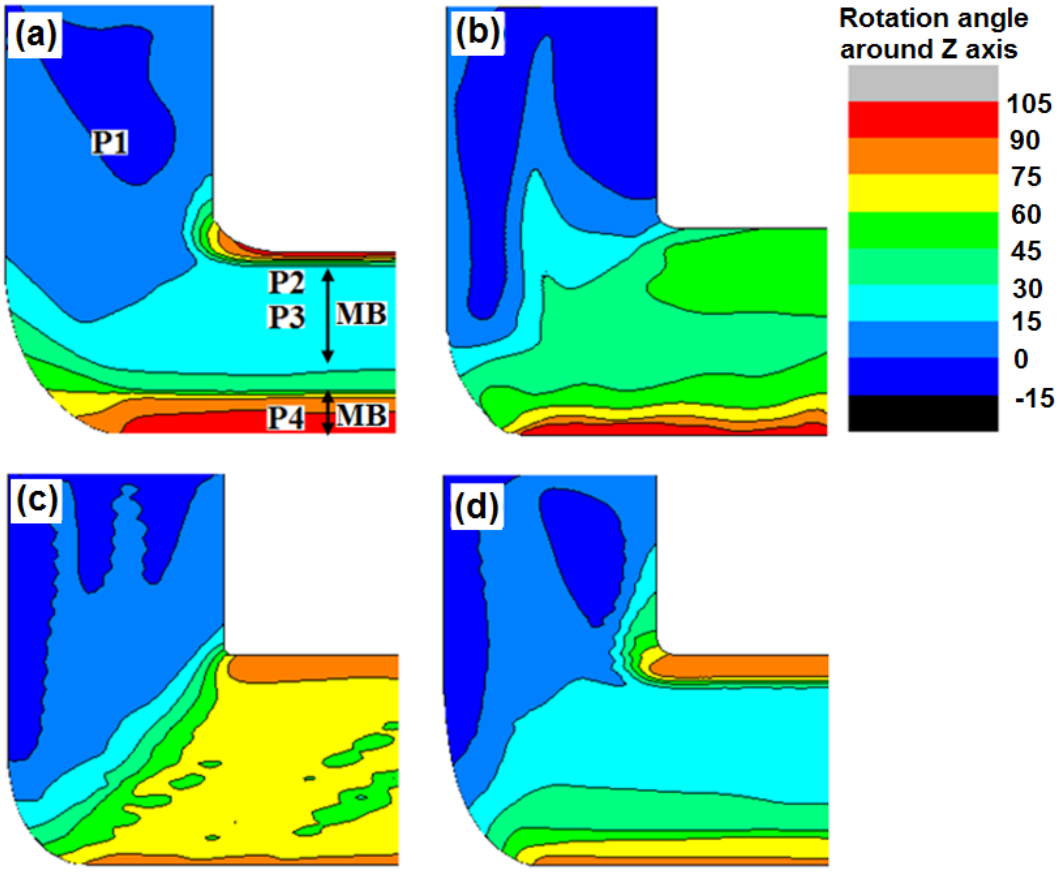

Fig. 5.24 The contour of crystal rotation angles around the Z axis in the ECAP processed copper single crystals with different initial crystallographic orientations. (a) Crystal A, (b) Crystal B, (c) Crystal C, and (d) Crystal D.

For a better understanding of the influence of initial crystallographic orientations on texture evolution of copper single crystals during the ECAP process, the crystal rotation angle for each sample was divided into three components. It has been found that the major rotation is around the Z axis for all the crystals. Therefore, only the Z-axis rotation components have been compared as shown in Fig. 5.24. As can be seen in Fig. 5.24, the rotation angle is uniform along the X axis but non-uniform along the sample thickness for all four copper single crystals. According to these results, the matrix bands (MBs) along the sample thickness can be distinguished. As shown in Fig. 5.24(a) for crystal A, positions P2 and P3 belong to the same matrix band which leads to the similar {1 1 1} pole figures in Fig. 5.23.

Distributions of the crystal rotation angles along the sample thickness are compared in Fig. 5.25 for all four copper single crystals. As can be seen, Fig. 5.25 reveals that crystal rotation is predominant around the Z axis (transverse direction) for all four crystals. These results are different to the copper single crystal studied in Section 5.1. The magnitude of crystal rotation angle is strongly dependent on the initial crystallographic orientation. In Section 5.1, a matrix band with initial crystallographic orientation has been observed but it does not exist in the four copper single crystals studied in this section. As shown in Fig. 5.25, three obvious matrix bands can be seen in crystals A and D and the misorientation angles between these matrix bands are very large. In contrast, only two matrix bands are seen in crystals B and C and the misorientation angles are much smaller.

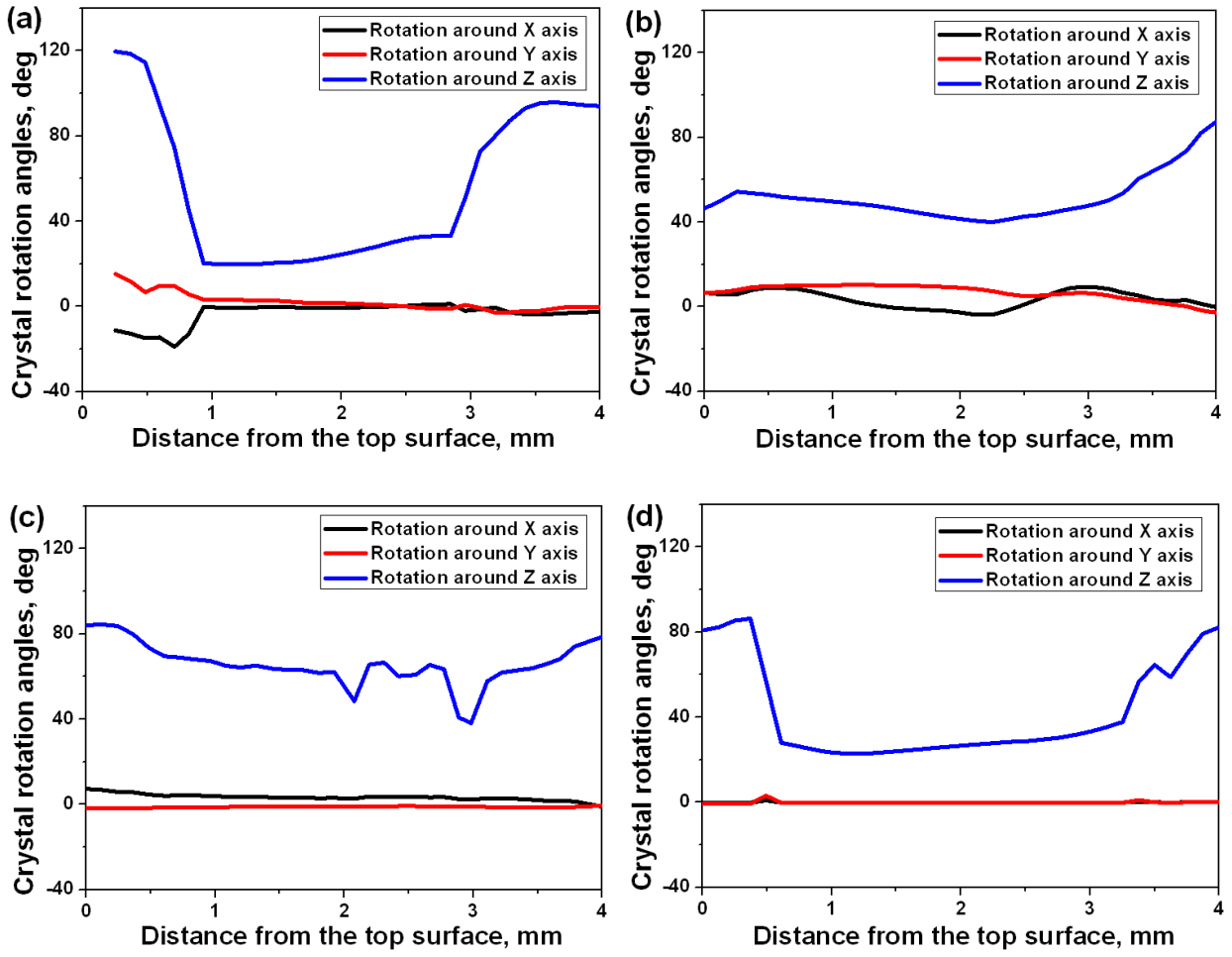

Fig. 5.25 Distribution of crystal rotation angles around three axes along the thickness of the sample during the ECAP process: (a) Crystal A, (b) Crystal B, (c) Crystal C, and (d) Crystal D.

5.5 Summary

In this chapter the deformation behaviour and texture evolution of copper single crystals during the ECAP process have been studied in detail. The summaries are listed as follows.

(1) It has been found that the friction condition has an obvious influence on the deformation heterogeneity and texture evolution in copper single crystals during the ECAP process. The plastic strain distribution is much more sensitive to the friction in the upper half part of the deformed samples than in the lower part, and μ=0.05 provided a better texture prediction than μ=0.1 compared with experimental results.

(2) The simulation results indicate that the crystallographic orientation of a copper single crystal having an initial 'A' orientation during the ECAP process with a 90° die rotates in three dimensions and the dominant rotation direction is around the Z axis. The crystal has been split into three matrix bands connected by two transition bands through the thickness of the billet at μ=0.05. The corresponding Z axis rotation angle in three matrix bands are about 60°, 0°, and 90°, respectively.

(3) The mesh distortions, stress and strain distributions, and texture evolution of copper single crystals are strongly dependent on the ECAP die channel angle. The die with an obtuse channel angle (ϕ=105° and 135°) leads to a larger outer corner gap than that with an acute channel angle (ϕ=75°), or right angle (ϕ=90°). The magnitudes of effective plastic strain and strain rate decreased gradually with the increasing die channel angle. The crystal rotation angle around the Z axis in the bottom part is dependent on the die channel angle and is equal to (180°-ϕ) where ϕ is the ECAP die channel angle.

(4) An initial crystallographic orientation of a copper single crystal had a significant influence on the development of a corner gap, inhomogeneous mesh distortion, PDZ shape, and distribution of plastic strain in the billet after ECAP. A larger corner gap leads to the decrement of the average value of plastic strain and the increment of deformation inhomogeneity index C_i along the thickness of the billet. The largest C_i in crystal A was about 1.633 and the smallest value was about 0.899 in crystal C. The simulation results also revealed that the texture evolution and

crystal rotation patterns depended strongly on the initial orientation. There were three distinguished matrix bands along the thickness in crystals A and D, but only two matrix bands in crystals B and C. The thickness of the matrix band in the bottom part increased with the larger outer corner gap.

Chapter 6 CPFEM Simulation of Multi-pass ECAP Process

In Chapters 4 and 5, CPFEM simulations of single pass ECAP process of aluminium and copper single crystals have been conducted, respectively. This chapter studies deformation behavior and texture evolution of aluminium single crystals during the multi-pass ECAP process under Routes A and C using a CPFEM model. Such work has not been reported in the published literature. The major challenge in the simulation of the multi-pass ECAP process is that the mesh becomes significantly distorted and the simulation often encounters convergence problem. In order to solve this problem, one of the adaptive meshing techniques, known as mesh to mesh solution (MTMS) mapping analysis [286], has been used in the simulation of the multi-pass ECAP process.

6.1 Adaptive Meshing Techniques

Three different adaptive meshing techniques are available in the commercial finite element software Abaqus: Arbitrary Lagrangian Eulerian (ALE) adaptive meshing, varying topology (VT) adaptive remeshing, and mesh to mesh solution (MTMS) mapping analysis [286]. A brief introduction to these three adaptive meshing techniques is given in the following text.

6.1.1 ALE Adaptive Meshing Analysis

ALE adaptive meshing provides control of mesh distortion. A single mesh definition that gradually becomes smoother within the steps of the analysis has been used. A high quality mesh can be maintained throughout the analysis by allowing the mesh to move independently of the material, even when large deformation or loss of material occurs. In an ALE analysis the element can only be defined as a single material, so a Lagrangian adaptive mesh domain will be created. The domain as a whole will follow the material originally inside it, which is the proper physical interpretation for most structural analyses. ALE analysis in Abaqus/Standard is

intended to solve Lagrangian problems and to model the effects of ablation, or wear of materials. It can also be used in geometrically nonlinear static, steady-state transport, coupled pore fluid flow, and stress, and coupled temperature-displacement procedures. However, the application of ALE analysis in Abaqus/Standard is limited due to the following four reasons. Firstly, initial mesh sweeps cannot be used to improve the quality off the initial mesh definition and secondly, the diagnostic capabilities are limited. Thirdly, this analysis is not intended to be used in general classes of large deformation problems and finally, the material properties of the fluid do not change as a result of smoothing the mesh [286].

6.1.2 VT Adaptive Remeshing Analysis

VT adaptive remeshing involves the iterative generation of multiple dissimilar meshes to determine a single, optimized mesh used throughout the analysis, with the aim of minimizing the number of elements and cost of the solution. Therefore, VT adaptive remeshing can be used to obtain a mesh which provides a balance between the cost of the analysis and the desired accuracy. When incorporating the VT adaptive remeshing into the Abaqus/CAE model, the remeshing rules and the remeshing area should be defined first. Then the error indicator output variables, the sizing method and size constraints are required. A new and smoother mesh in the specified regions will finally be created by sweeping iteratively over the adaptive mesh domain. During each sweep of the mesh, nodes in the domain are relocated based on the current positions of neighboring nodes and elements to reduce element distortion. In a typical sweep a node is moved a fraction of the characteristic length of any element surrounding the node. The increasing number of sweeps leads to the increment of the intensity in each adaptive meshing increment. The default number is one. Finally the neighboring regions will also be remeshed.

VT adaptive remeshing is very helpful to improve the quality of the simulation results, especially in conditions where: (i) it is hard to design an adequately refined mesh near a region of interest; and (ii) it is not certain how refined a mesh is required to reach a particular level of accuracy. However, several limitations of the application exist. For example, Abaqus/CAE is required and only Abaqus/Standard procedures are supported. Besides, only three kinds of elements with

special shapes including planar continuum triangles and quadrilaterals, shell triangles, and quadrilaterals and tetrahedrals can be used [286].

6.1.3 MTMS Mapping Analysis

MTMS mapping is a remeshing analysis technique where a mesh significantly deformed from its original configuration is replaced by a mesh of better quality and the analysis is able to continue. In MTMS mapping, each mesh subsequent to the initial configuration reflects a solution dependent deformed configuration of the model and indicates a component of the overall analysis history. The solution variables will be propagated from one analysis to the next.

When applying the MTMS mapping analysis, it is very important to decide when to remesh. This can be done by examining the magnitude of strains that occur during the phase of the analysis. One possible criterion for remeshing is extreme element distortion in areas where high strain gradients need to be resolved accurately. Another criterion is solution discontinuity. Significant discontinuity suggests that remeshing should have done at an earlier increment before too much distortion occurs, or the meshes are not fine enough.

During the MTMS mapping analysis, all the files needed for restart and the output database must be required for the old job. The interpolation technique is used to obtain the solution variables at the nodes of the old mesh by extrapolating all values from the integration points to the nodes of each element, and then averaging these values over all similar elements abutting each node. Then the location of each integration point in the new mesh is obtained with respect to the old mesh. The variables are interpolated automatically from the nodes of the old element to the integration points of the new element. It should be noted that the boundary conditions are not carried out over from the old mesh to the new mesh. The boundary conditions applied at the beginning of the remeshed analysis should normally be the same as those in effect at the step and increment selected from the initial analysis. Although the boundary conditions can be altered, the problem may fail to converge if the structure is a long way from an equilibrium state. There are no restrictions on applying boundary conditions and loads in the MTMS mapping analysis.

Another advantage of MTMS mapping analysis is that any of the mechanical constitutive models available in Abaqus can be used and there is no restriction on agreement between material models in the old and new analyses. The application of MTMS mapping analysis is supported for the following five procedures, such as 'Static stress analysis', 'Quasi-static analysis', 'Fully coupled thermal-stress analysis', 'Coupled pore fluid diffusion and stress analysis' and 'Geostatic stress state'. However, it is only suitable for the continuum elements [286].

There are several reasons to choose the MTMS mapping approach in this study:

(1) The ALE analysis is not good at general classes of large deformation problems, whereas the ECAP process is one of the severe plastic deformations which definitely belong to the problem of large deformation and therefore the ALE analysis is not suitable in this study [286].
(2) The VT adaptive remeshing analysis is not good at controlling distortion and is only available for the analyses submitted from Abaqus/CAE [286].
(3) The MTMS mapping is suitable to any constitutive models and there is no restriction on agreement between material models in the old and new analyses [286].

In order to examine the capability of the MTMS mapping approach, the {1 1 1} pole figures are plotted based on the data before and after the MTMS mapping. Fig. 6.1(a) shows the deformed mesh after the first-pass ECAP process. A new sample with a new mesh is then created in order to simulate the second pass, as shown in Fig. 6.1(b). The MTMS mapping approach is used to transfer all the variables from the nodes of the old mesh (the box part in Fig. 6.1(a)) to the new mesh (Fig. 6.1(b)). The new mesh with all the transferred variables will be used in the simulation of the second ECAP pass. Fig. 6.1(c) shows the {1 1 1} pole figures before the MTMS mapping (along line A-B marked in Fig. 6.1(a)) and Fig. 6.1(d) demonstrates the {1 1 1} pole figure after the MTMS mapping (along line A'-B' marked in Fig. 6.1(b)). It is obvious that excellent agreement between two pole figures has been obtained by comparing Fig. 6.1(c) and (d). This clearly indicates that the MTMS mapping approach is an adaptive remeshing method suitable for simulations of the multi-pass ECAP.

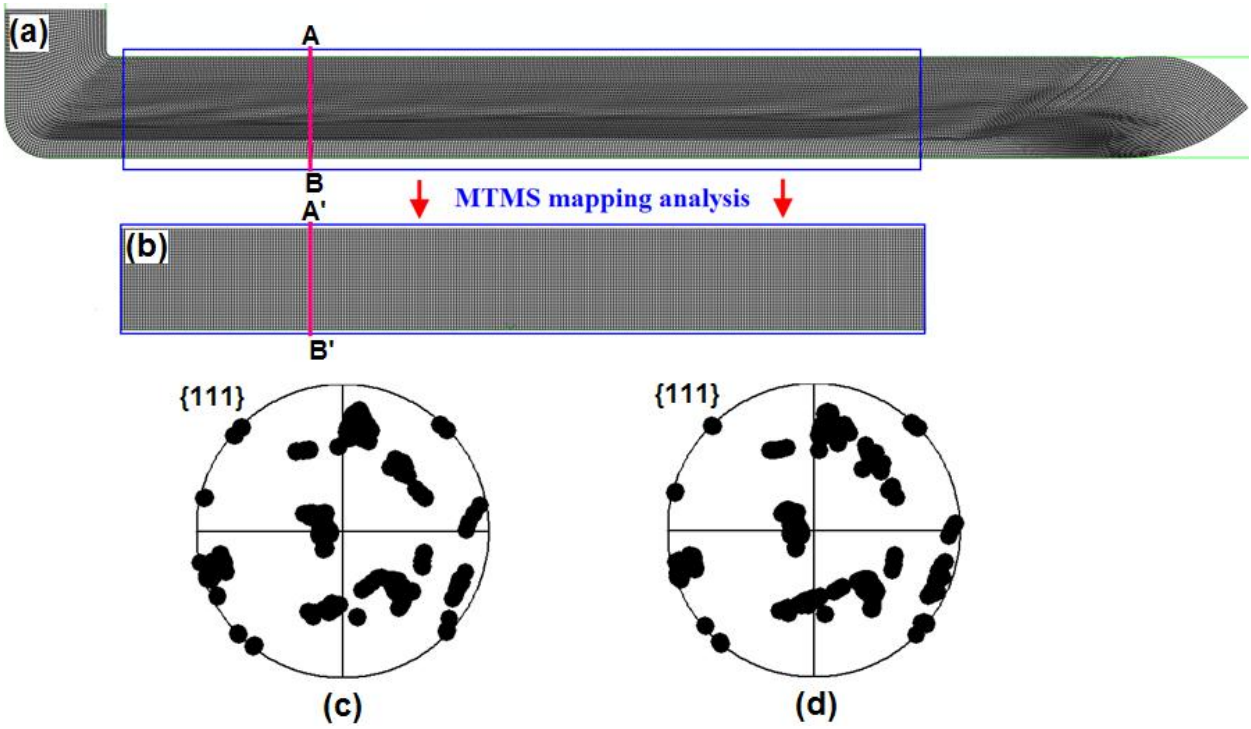

Fig. 6.1 (a) The deformed mesh after the first pass of ECAP process, (b) New mesh based on the MTMS mapping analysis from the steady-state region of deformed mesh in (a), (c) {1 1 1} pole figure along line A-B marked in (a), and (d) {1 1 1} pole figure along line A'-B' marked in (b).

6.2 CPFEM Simulation of Route A

In this section, the deformation heterogeneity and texture evolution history of an aluminium single crystal subjected to ECAP up to four passes in Route A are studied in detail.

The geometry of the ECAP die simulated in this section is the same as the one used in Section 4.1. The coefficient of friction μ was set to 0.05. The material used in these simulations was an aluminium single crystal initially oriented with: (-11 1 -5)[-1 9 4], where (-11 1 -5) parallel to the normal plane and [-1 9 4] parallel to the extrusion direction. Details of the parameters used in the simulations are given in Table 6.1. The ECAP process up to 4 passes under Route A has been simulated.

Table 6.1 The details of parameters used in the simulations of Route A.

Pass number	Length (mm)	Width (mm)	Elements	Nodes	μ
1	50	4	16000	16441	0.05
2	35.5	4	12000	12341	0.05
3	26	4	8000	8241	0.05
4	20.5	4	8000	8241	0.05

The study in Chapter 4 showed that the head and tail parts of the simulated samples are subjected the significantly distorted deformation, which often causes the convergence problem in the simulations of the following pass. Therefore, a long sample was used in the first pass simulation in order to obtain a long steady-state deformation region. Only the steady-state region will then be remeshed by the MTMS mapping approach and used for the simulation of the second pass. The similar procedure has been applied to the simulations of the consequent third and fourth passes.

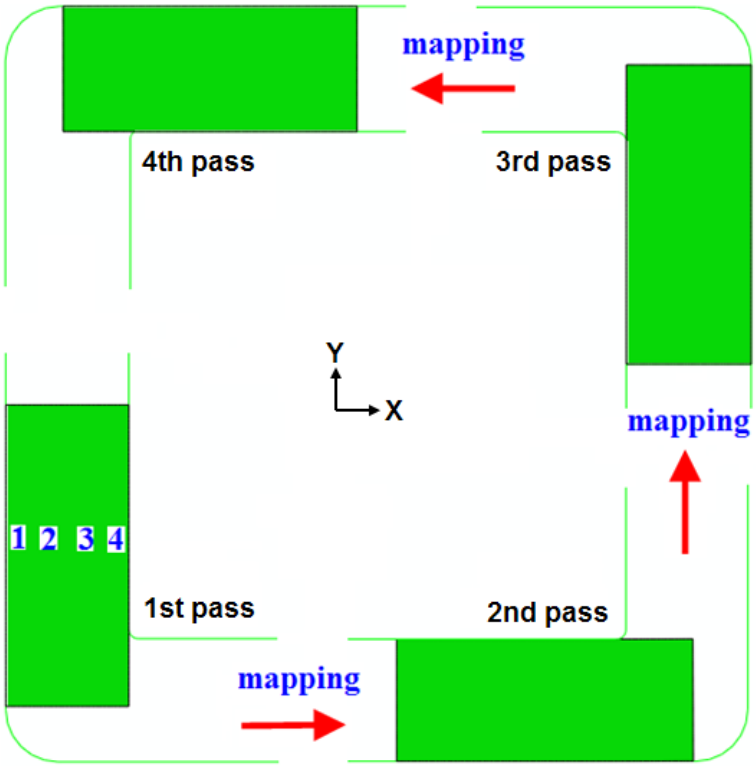

Fig. 6.2 Scheme of the Route A of the ECAP process used in the simulations.

In practice, the die remains the same position and the sample needs to be re-inserted into the die to implement the multi-pass ECAP. However, for convenience, the ECAP of Route A is simulated in this study as schematically demonstrated in Fig. 6.2. In the simulation the ECAP die was rotated by 90° around the Z axis in a counter-clockwise direction after each pass. The computing time of the first pass is about 400 hours using the HPC cluster in University of Wollongong using four CPUs at the same time.

Fig. 6.3 provides the effective plastic strain distribution along the thickness of the sample after ECAP up to four passes in Route A. It can be seen that the deformation is not uniform along the thickness and the difference between the maximum and minimum effective plastic strain increases obviously with the number of ECAP passes. The bottom part has the minimum effective plastic strain because of the smallest plastic deformation due to the outer corner angle in every pass in Route A. In contrast, the upper 75% region undergoes more severely plastic deformation and accumulates more plastic strain, as shown in Fig. 6.3. Similar results have also been seen in a published paper [141].

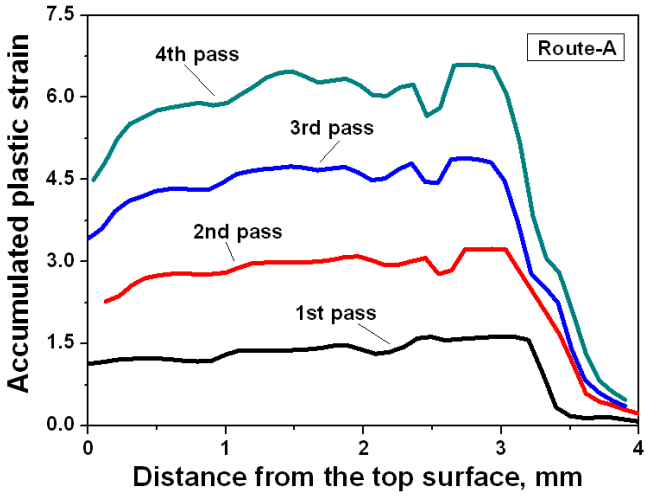

Fig. 6.3 Effective plastic strain distribution along the thickness of the billet after ECAP in Route A. ('top' means close to the inner corner and 'bottom' means close to the outer corner).

Fig. 6.4 compares the average of simulated effective plastic strain with predictions by an analytic model used in Ref. [104]. As can be seen, very good agreement has been obtained. The average simulated effective plastic strain is about 1.962 after the second pass, 2.987 after the third pass and 3.993 after the fourth pass.

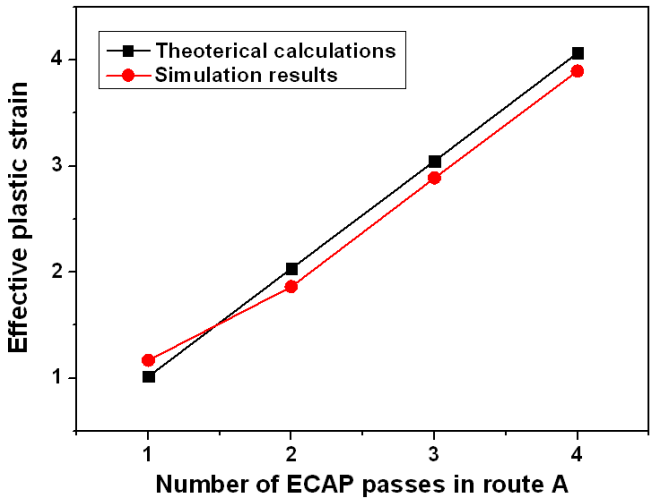

Fig. 6.4 Comparison of effective plastic strain between the FEM simulation and empirical theoretical calculations for Route A during up to 4 ECAP passes.

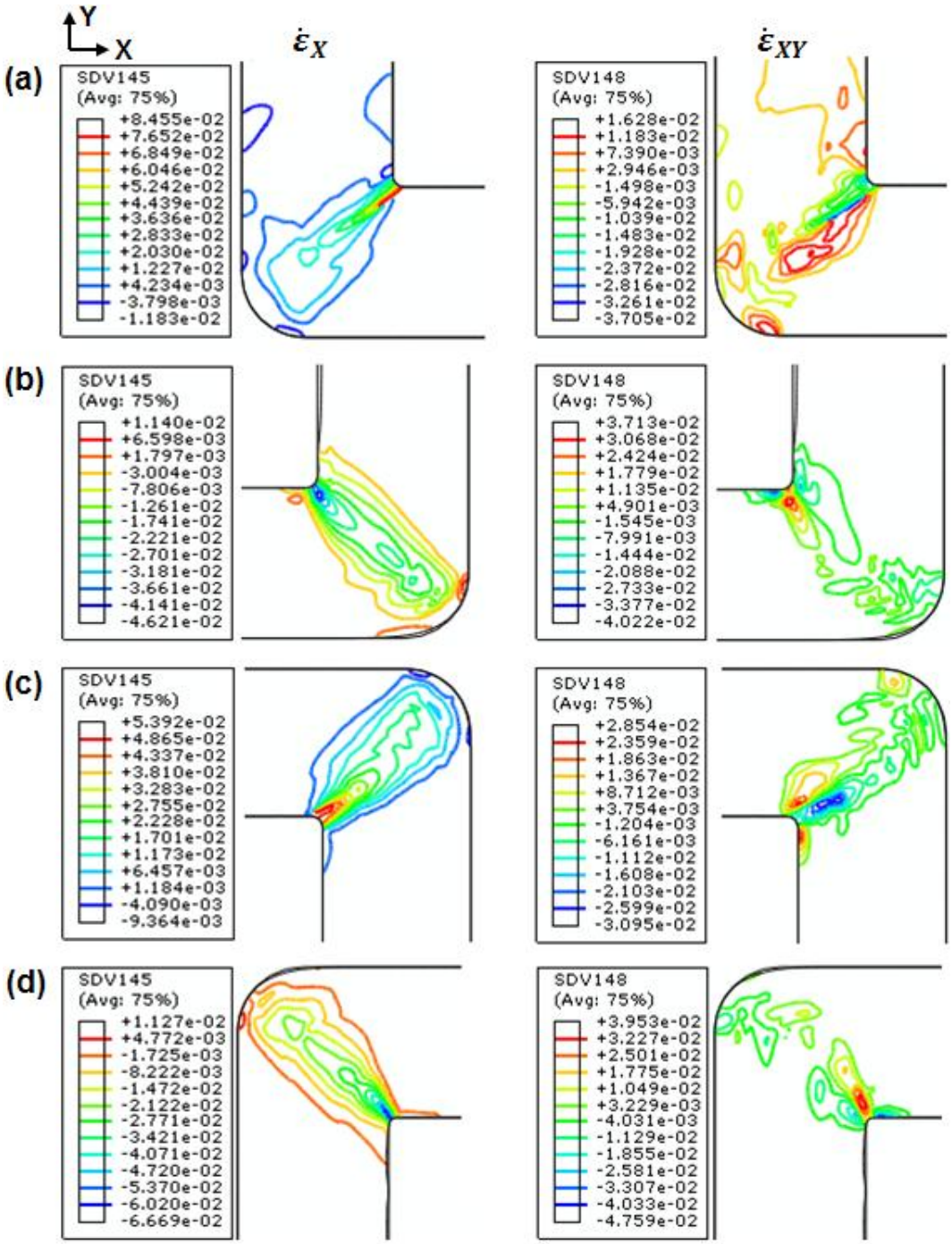

Fig. 6.5 Distribution of plastic strain rate $\dot{\varepsilon}_X$ and $\dot{\varepsilon}_{XY}$ in the deformed billet during the (a) first pass, (b) second pass, (c) third pass, and (d) fourth pass of ECAP in Route A.

Fig. 6.5 shows the distributions of plastic strain rates $\dot{\varepsilon}_X$ and $\dot{\varepsilon}_{XY}$ in the deformed billet during up to 4 ECAP passes in Route A. Similar to the first pass, the plastic deformation in other passes

deviates from the simple shearing along the intersecting plane of the entry and exit channels. It is apparent that Passes 1 and 3 have the same ideal shear plane and Passes 2 and 4 have the same ideal shear plane, as shown in Fig. 6.5. Two sets of ideal shear planes intersect at an angle of 90° [1, 287]. The magnitude of strain rates gradually decreases from the inner corner to the outer corner and a fan shape of $\dot{\varepsilon}_X$ can be observed for each pass. It is interesting to find that the sign of shear component $\dot{\varepsilon}_{XY}$ around the inner corner changes from negative to positive after passing through the intersecting plane in the odd passes (the first and third passes), while it changes from positive in the entry channel to negative in the even passes. In addition, plastic deformation is induced in the entry channel close to the intersecting zone during the first ECAP pass but it is not obvious in the consequent passes. As can be seen in Fig. 6.5, the plastic deformation is not uniform along the intersecting plane which leads to an inhomogeneous microstructure and microhardness along the thickness of the billet [200, 288]. This feature will be inherited from the former process in Route A because plastic deformation near the outer corner is always smallest in each pass. In contrast, more plastic deformation can accumulate in the upper region.

For a better understanding of the deformation history in Route A, four Elements 1-4 initially located in the cross-sectional plane of the middle length of the sample each pass (marked in Fig. 6.2) are selected to monitor the effective plastic strain, strain rate, activity of slip systems, and texture evolution. The distance of these elements from the left side (close to the outer corner) is approximately 0.3, 1.2, 1.7, and 3.7 mm, respectively.

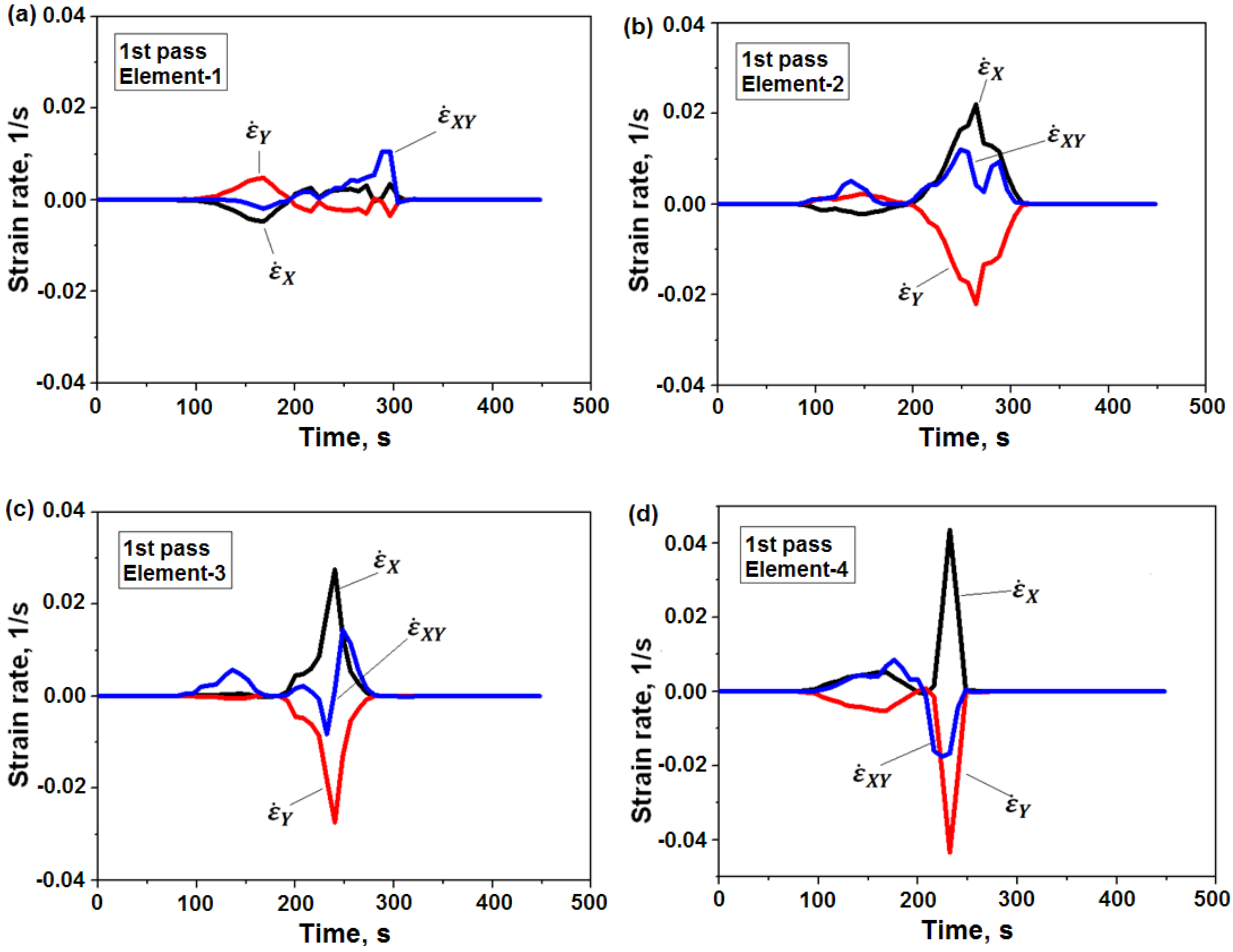

Fig. 6.6 Variation of plastic strain rates of (a) Element 1, (b) Element 2, (c) Element 3, and (d) Element 4 during the first pass of ECAP as a function of the processing time.

Fig. 6.6 shows the variation of strain rates during the first pass of the ECAP process for all four selected elements as a function of the processing time. As can be seen, the magnitude of strain rates increase from Element 1 to Element 4, which means that the gradients of the strain rates increase from the outer corner to the inner corner during the first ECAP pass. Besides the shear component $\dot{\varepsilon}_{XY}$, large normal components $\dot{\varepsilon}_X$ and $\dot{\varepsilon}_Y$ can also be observed for Elements 2-4, which indicates that deformation is not only characterized as simple shear, it is also compression along the -Y axis and tension along the X axis. The compression and tension are much larger than shear in the PDZ, especially for Element 4 near the inner corner.

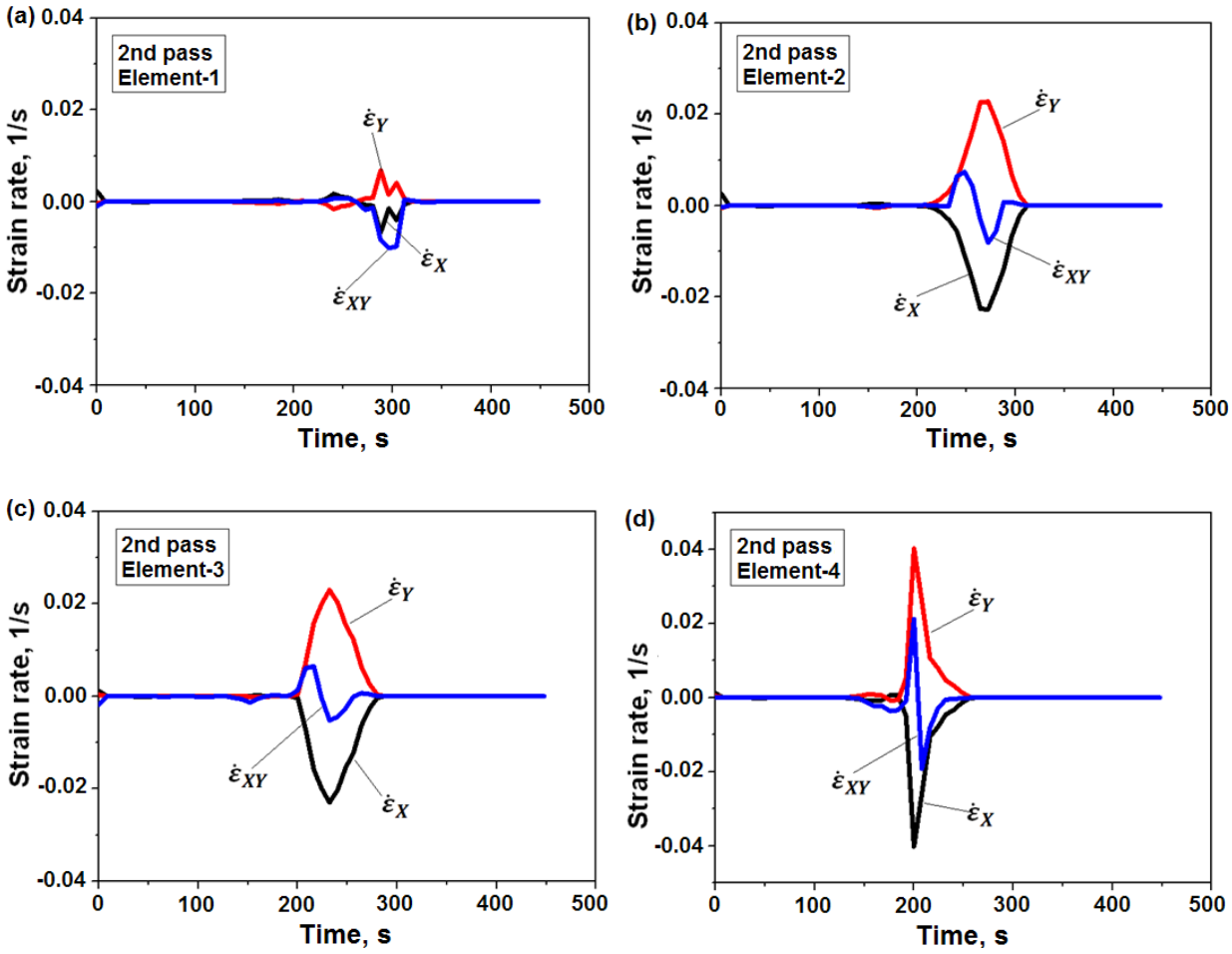

Fig. 6.7 Variation of plastic strain rates of (a) Element 1, (b) Element 2, (c) Element 3, and (d) Element 4 during the second pass of ECAP in Route A as a function of the processing time.

Fig. 6.7 shows the variation of plastic strain rates during the second ECAP pass in Route A for all four tracked elements as a function of processing time. These results indicate that the trends during the second pass in Route A are similar to the first one, as shown in Fig. 6.6. Element 1 still has the smallest strain rates and Element 4 has the largest strain rates. These elements undergo tension along the Y axis and compression along the –X axis because the ECAP die is rotated in the second pass shown in Fig. 6.2. In practice the plastic deformation mechanism is the same during the two consecutive ECAP passes in Route A [105]. Similar trends of strain rates variation for all four selected elements have been obtained in the following third and fourth passes.

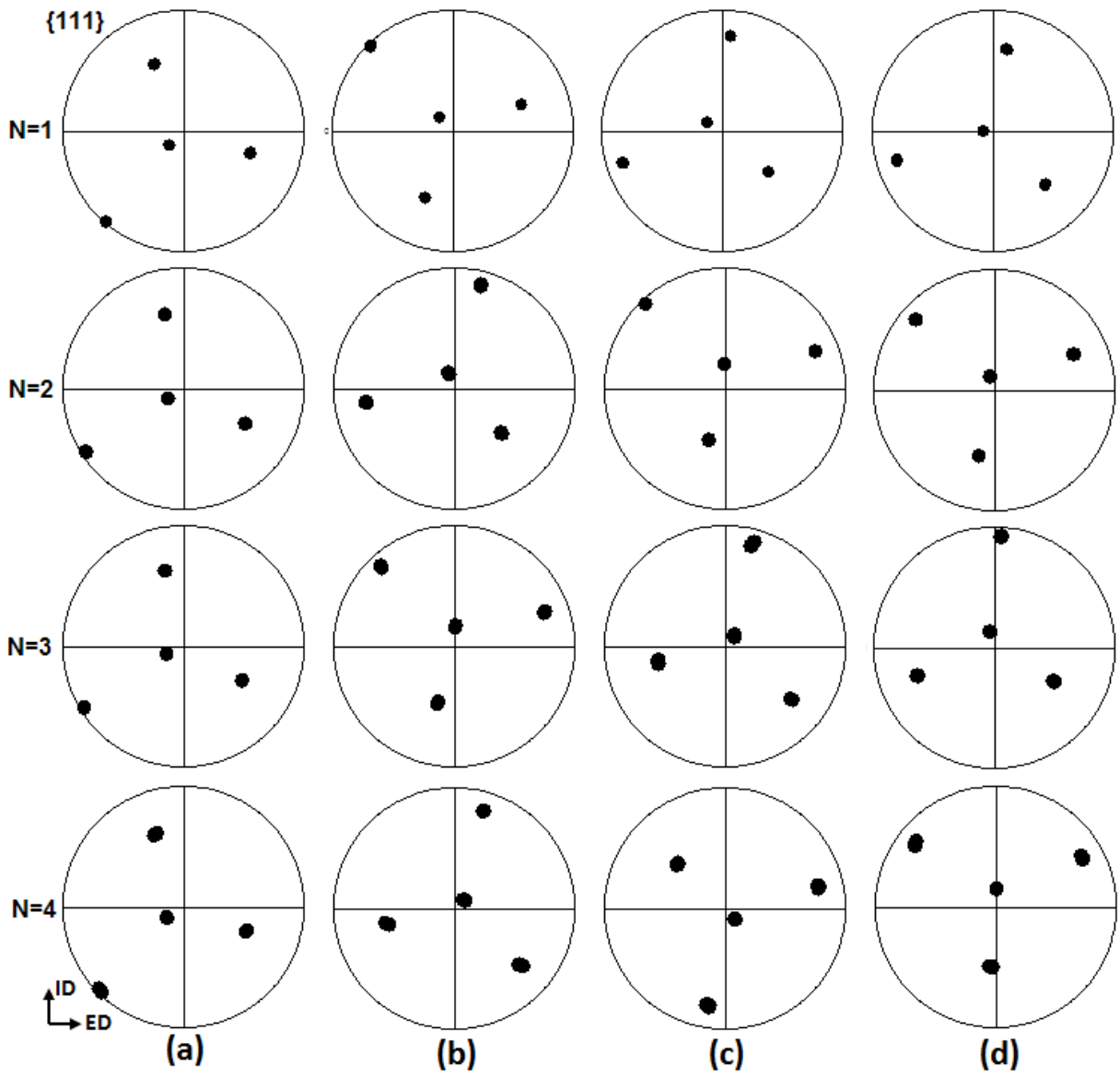

Fig. 6.8 The history of crystallographic orientations development of four tracked elements (a) Element 1, (b) Element 2, (c) Element 3, and (4) Element 4 during the ECAP process in Route A up to four passes. (N indicates the pass number)

Fig. 6.8 shows the simulated {1 1 1} pole figures for the four tracked elements in Fig. 6.2 to study the development history of their crystallographic orientations in Route A. It should be noted that all the {1 1 1} pole figures are plotted on the ED-ID plane. For Element 1, the {1 1 1} pole figures indicates a crystallographic orientation component with almost 90° rotation around the Z axis in a counter-clockwise direction from the initial orientation for all the passes. As

discussed in the previous chapters, the development of this orientation is attributed to the rigid body rotation in the outer corner. For Element 2, crystallographic orientation remains at the initial component after the first and third passes, but a 60° rotation in a clockwise direction is seen during the second and fourth passes. In addition, a rotation of almost -20° around ID during the third pass and rotations of about 15° around ED and -15° around ID during the fourth pass have been observed in Fig. 6.8(b), where positive angle means the counter-clockwise rotation and negative angle means the clockwise rotation. The {1 1 1} pole figures in Fig. 6.8(c-d) reveal that Element 3 and Element 4 have the similar crystallographic orientation, but the orientation is different from pass to pass.

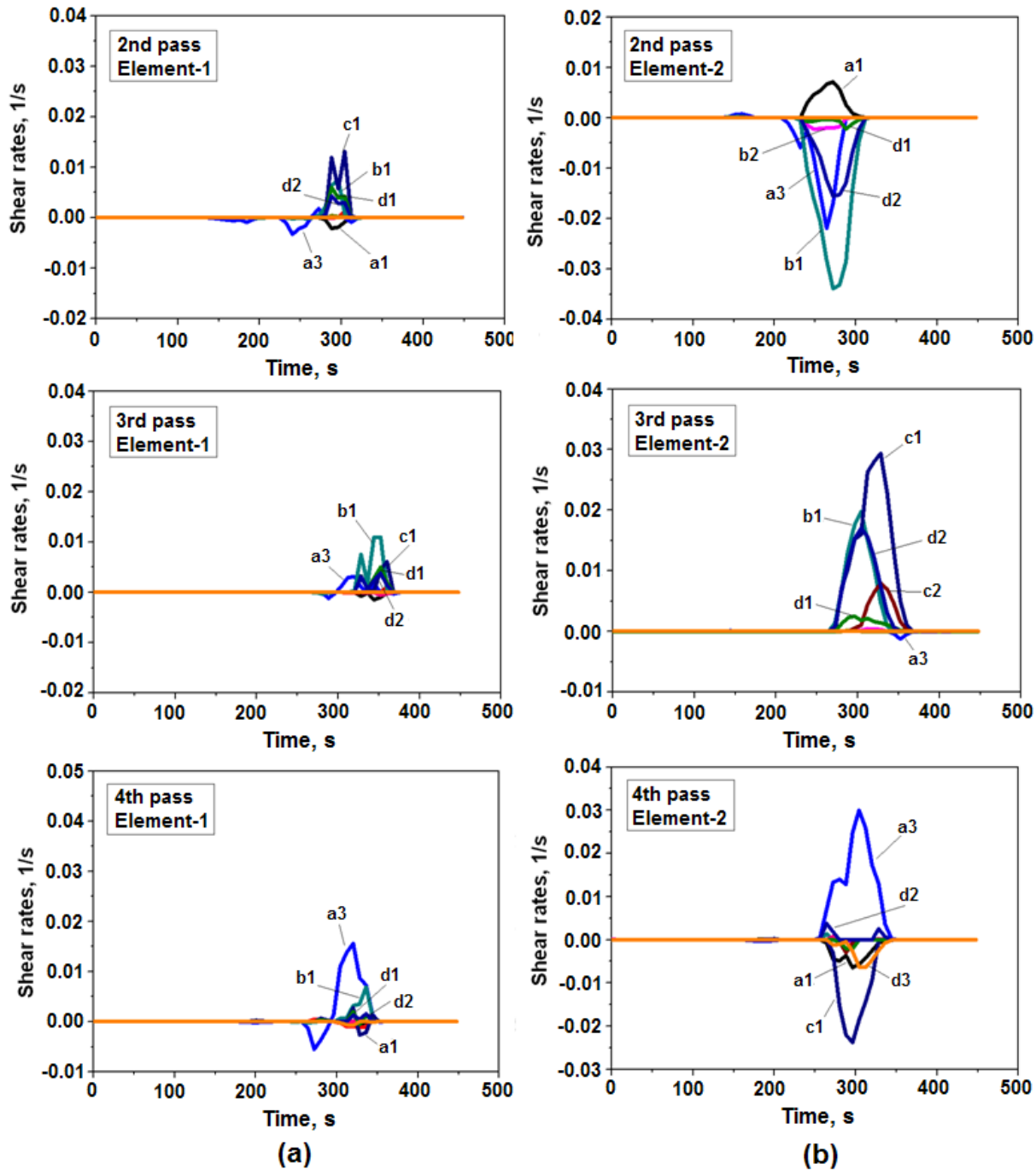

Fig. 6.9 The shear strain rates of four tracked elements (a) Element 1, (b) Element 2, (c) Element 3, and (d) Element 4 during the ECAP process of 2-4 passes in Route A.

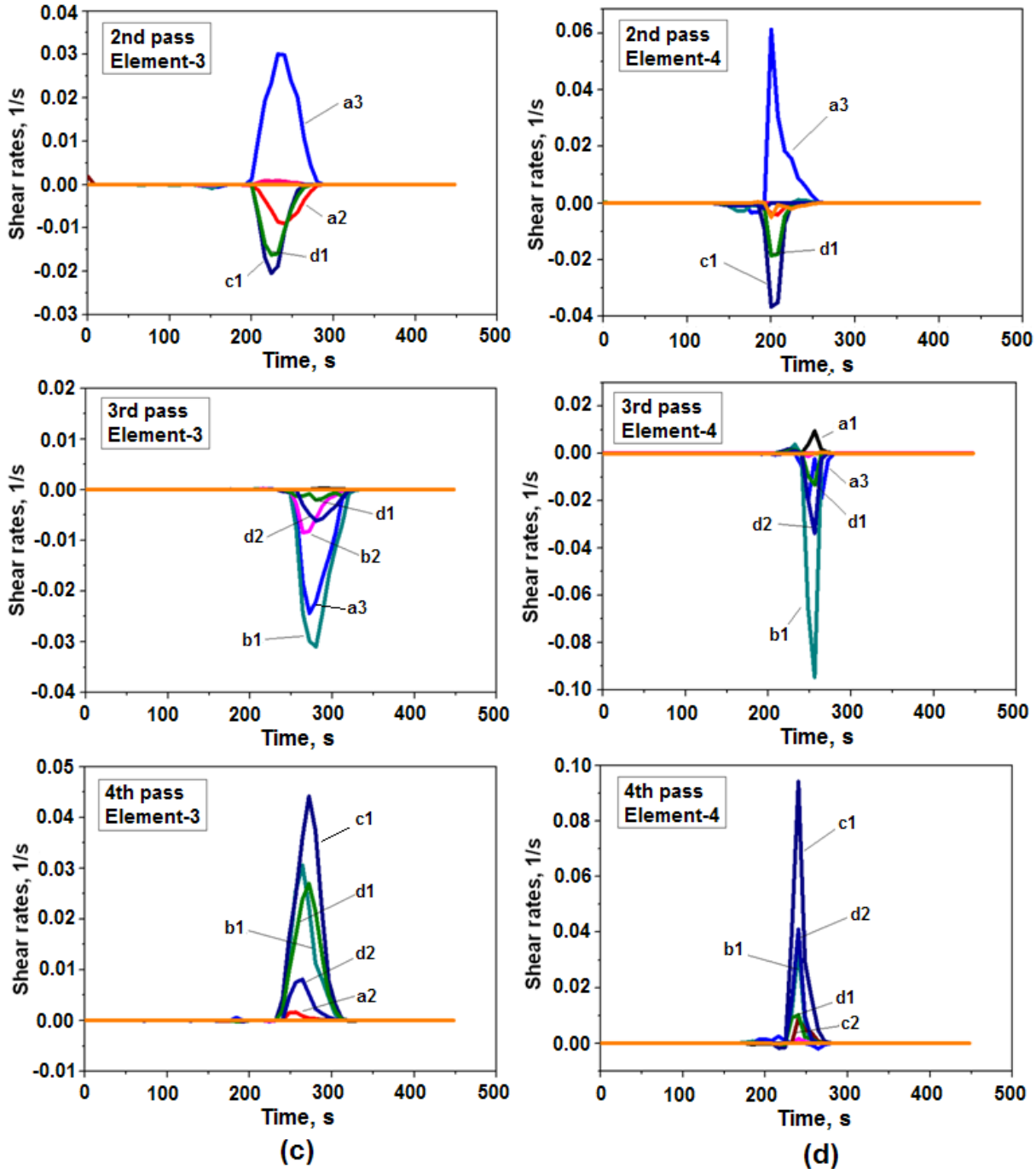

Fig. 6.9 Continued.

Why are the crystallographic orientations different for these four tracked elements during ECAP in Route A? The answer can be found from Fig. 6.9, where the activity of 12 slip systems has been studied. Fig. 6.9(a) shows the shear strain rates of 12 slip systems for Element 1 during the 2, 3 and 4 ECAP passes. As can be seen, the shear strain rates of all activated slip systems for

this element are very small during each pass. Fig. 6.9(b-d) show the shear strain rates for Elements 2, 3 and 4, respectively. It is worthy to note that the negative shear strain rate indicates the slip along the negative slip direction on the same slip plane, or the slip along the positive slip direction on the negative slip plane. As can be seen, the activated slip systems are not the same for Element 2 in each pass even though the increments of plastic strain are the same. From the theory introduced in Chapter 3, the shear strain rate of each slip system ($\dot{\gamma}^{(\alpha)}$) relates to the resolved shear stress ($\tau^{(\alpha)}$) of this slip system. According to Equations (3.50) and (3.22), the crystallographic orientation during the current configuration influences the resolved shear stress, which in turn determines the activity of this slip system. Therefore, different slip systems could be activated in two consecutive passes for the same element. Main activated slip systems in Fig. 6.9(b) for Element 2 are b1, a3, d2, a1, b2 and d1 (order from the magnitude decrement of shear strain rate) during the second pass, and c1, b1, d2, c2, d1 and a3 during the third pass, and a3, c1, d3, a1 and d2 during the fourth pass. It is obvious that the activated slip systems are almost the same for Element 3 and 4 but with different magnitudes. The predominant slip system for these two elements is a3 during the second pass, b1 during the third pass and c1 during the fourth pass as shown in Fig. 6.9(c-d).

Fig. 6.10 shows the crystal rotation angles of the four tracked elements in Route A. Because the crystal rotation angles for the first pass of aluminium single crystal has been studied in Chapter 4 already, only the rotations during the second, third and fourth passes have been shown here. In Fig. 6.10(a), three matrix bands along the billet thickness can be seen. In the upper matrix band, the crystal rotation angles are relatively small. In the middle matrix band, there is a large rotation around TD and the angle is around 60° in a clockwise direction. In the lower matrix band, the rotation is mainly around TD and the rotation angle is almost 90°. The crystal rotations for the third pass have been studied in Fig. 6.10(b), where four matrix bands along the thickness direction exist. It is obvious that the predominant rotation is still around TD but relative large rotation around ID can also be seen. Fig. 6.10(c) shows the crystal rotation angles for the fourth pass. Very large rotations around ID and TD are seen in the upper matrix band and the rotation angles are about -40° and 60°, respectively. It is obvious that there are five

matrix bands along the billet thickness. The number of matrix bands shown in Fig. 6.10 can reflect the capability of grain refinement during the ECAP process in Route A.

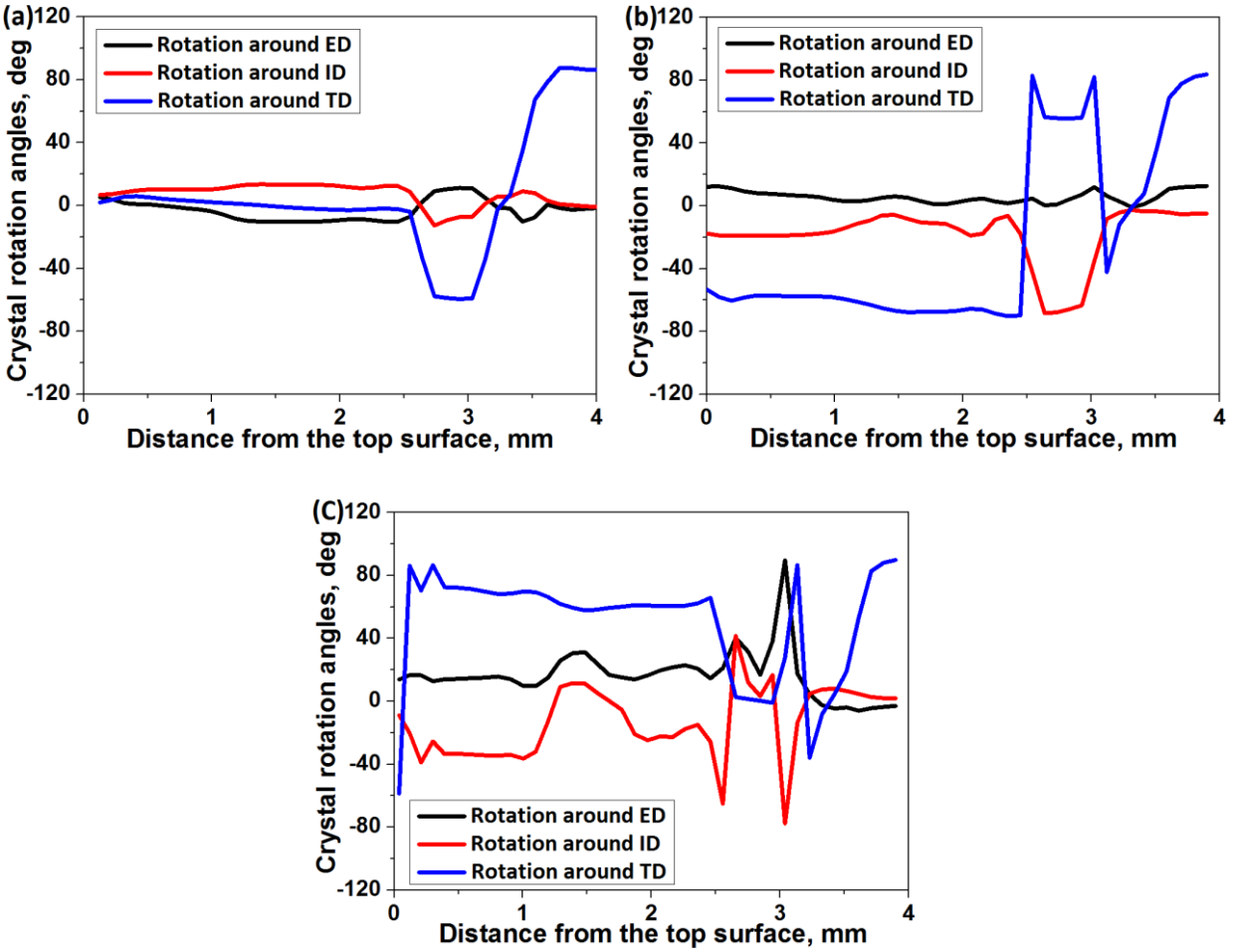

Fig. 6.10 Crystal rotation angles along the billet thickness during ECAP in Route A. (a) second pass, (b) third pass, and (c) fourth pass.

6.3 CPFEM Simulation of Route C

In this section, an extended study to Route C has been conducted. The deformation and texture evolution during up to four ECAP passes in Route C will be investigated systematically. In order to make a comparison, the same die geometry, material and initial crystallographic orientation with Route A are used in the CPFEM simulations of Route C. Fig. 6.11 is the schematically illustration of Route C used in the simulations. For convenience, the ECAP die is rotated by 180°

around the Z axis after each pass to replace the equivalent rotation of samples in Route C defined in Ref. [1]. It should be noted that the ED and ND coincide with the X and Y axes in the first and third passes but they are parallel to the –Y and –X axes respectively during the second and fourth ECAP passes in Fig. 6.11.

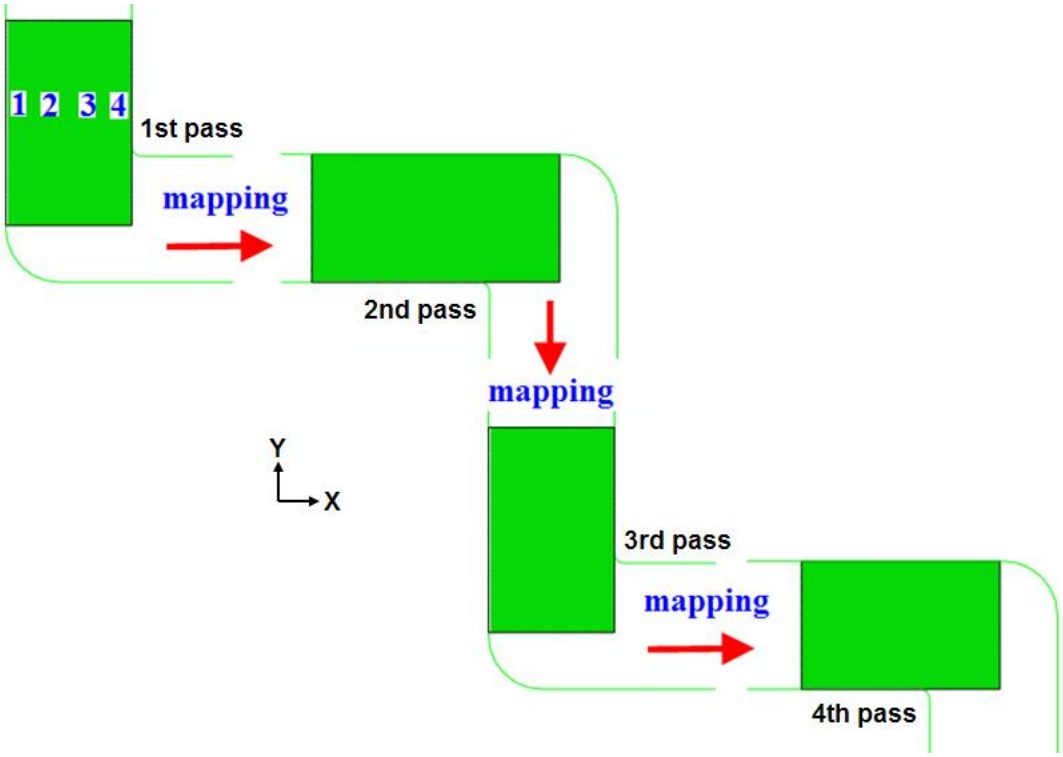

Fig. 6.11 Scheme of Route C in the ECAP process used in the simulations.

Fig. 6.12 shows the variation of effective plastic strain in the deformed billets along the thickness direction in Route C from 1 to 4 ECAP passes. The top surface and the bottom surface have almost the same level of effective plastic strain in Route C after the second ECAP pass. This is because the bottom part undergoes rigid body rotation when passing through the outer corner in the first pass and then undergoes more plastic deformation when crossing the inner corner in the second pass. However, the region close to the top surface is subject to more plastic deformation in the first pass but less deformation in the second pass. Therefore, similar plastic strain level has been obtained in these two regions after two ECAP passes. Relatively uniform distribution of strain can only be seen in the middle 50% of the thickness. It can be

found by comparisons of Fig. 6.3 and Fig. 6.12 that the influence of the ECAP route on the strain level in the middle part of the billet thickness is negligible.

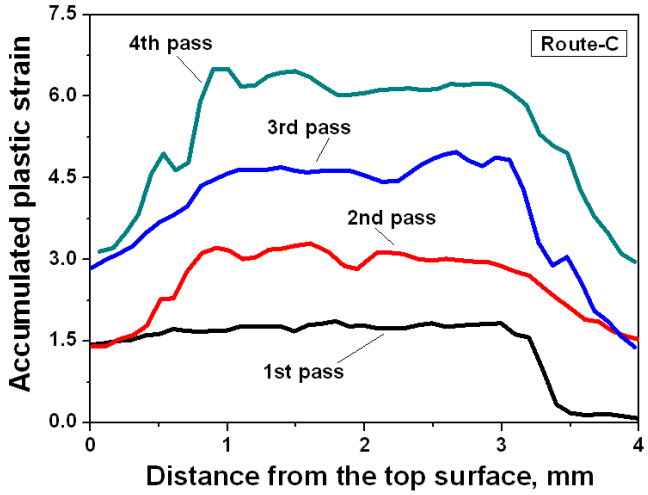

Fig. 6.12 Varitation of effective plastic strain along the sample thickness after ECAP during up to four passes in Route C. ('top surface' means close to the inner corner)

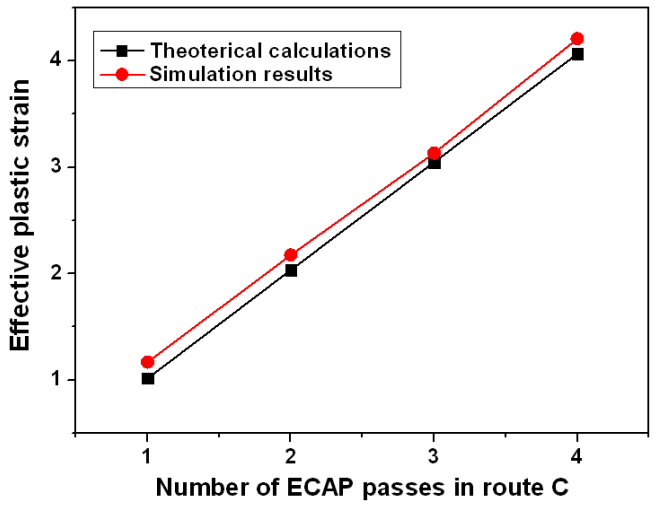

Fig. 6.13 Comparison of the effective plastic strain between the CPFEM simulations and empirical theoretical calculations after ECAP in Route C.

The effective plastic strains for up to four ECAP passes in Route C have been calculated according to the equation proposed by Iwahashi et al. [104]. Comparison of the average effective plastic strains predicted by the present simulations and the equation proposed by Iwahashi et al. [104] has been shown in Fig. 6.13. As can be seen, a good agreement has been obtained. The simulated strains are slightly larger than the preiction by Iwahashi's equation for all the passes. However, the simulation results are slightly smaller than the analtical model in Route A except for the first ECAP pass. In Fig. 6.13, the simulated effective strains are about 2.174, 3.132 and 4.206 after the second, third and fourth passes, respectively.

In Fig. 6.14, the distributions of plastic strain rates $\dot{\varepsilon}_X$ and $\dot{\varepsilon}_{XY}$ in the deformed billet from 1 to 4 ECAP passes in Route C are shown. The shapes of the strain rates distribution from the inner corner to the outer corner are similar for all passes. It should be noted that after an even number 2N (N=1 and 2 in this study) of ECAP passes in Route C, the top region and the bottom region undergoes N times of rigid body rotation respectively, which means that similar plastic strain accumulated for these two regions, as shown in Fig. 6.12. For the ideal deformation mechanism in ECAP (simple shearing along the intersecting plane), the plastic strain should be restored after every even number of passes [1]. However, from Fig. 6.14 we can see the obvious deviation of the deformation pattern from the ideal simple shearing. The microstructure evolutions observed in Ref. [60] also confirmed that deformation could not be totally recovered in Route C due to the deformation deviating from simple shear.

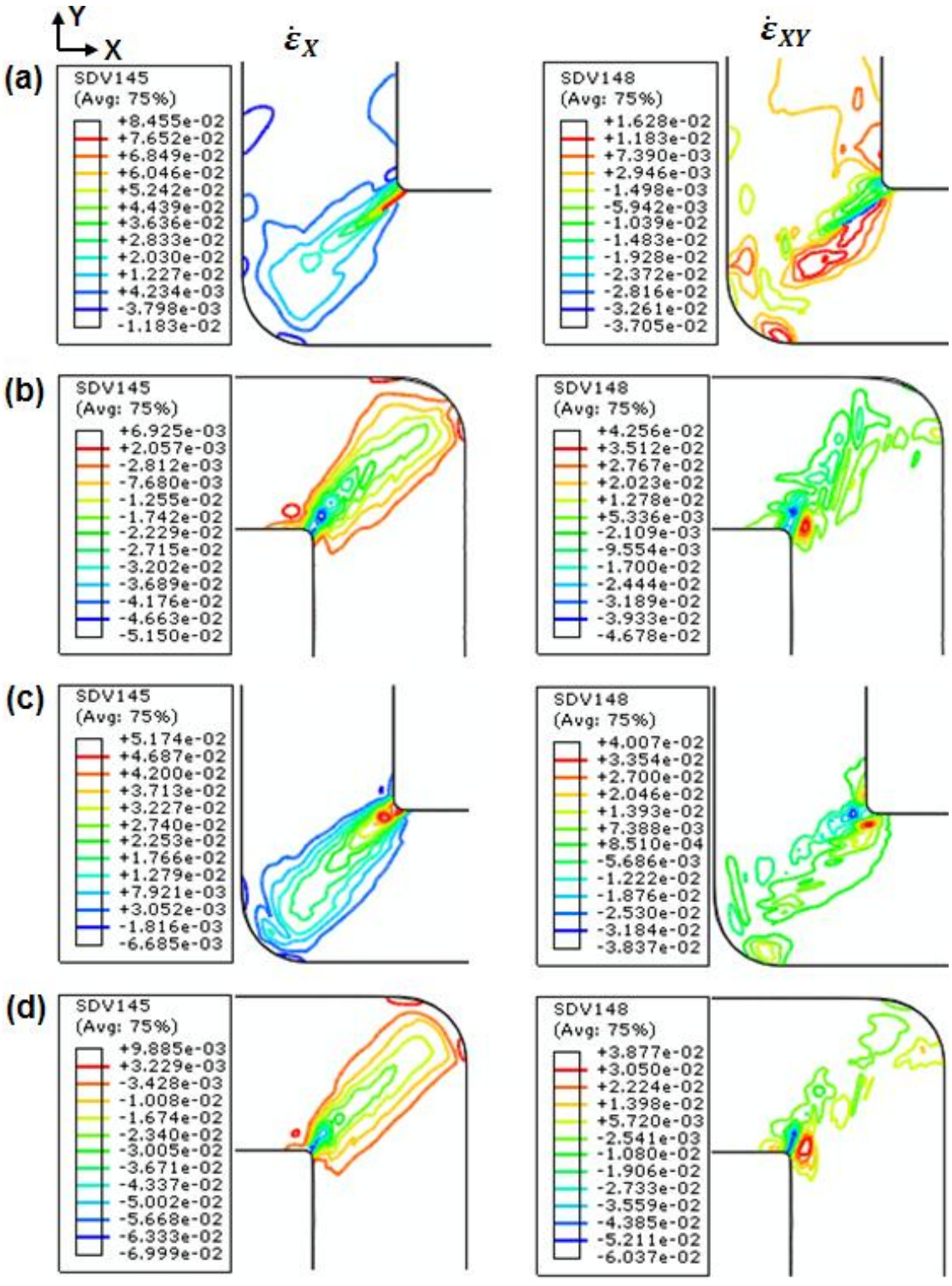

Fig. 6.14 Distribution of plastic strain rates $\dot{\varepsilon}_X$ and $\dot{\varepsilon}_{XY}$ in the deformed billet during the (a) first pass, (b) second pass, (c) third pass, and (d) fourth pass of ECAP in Route C.

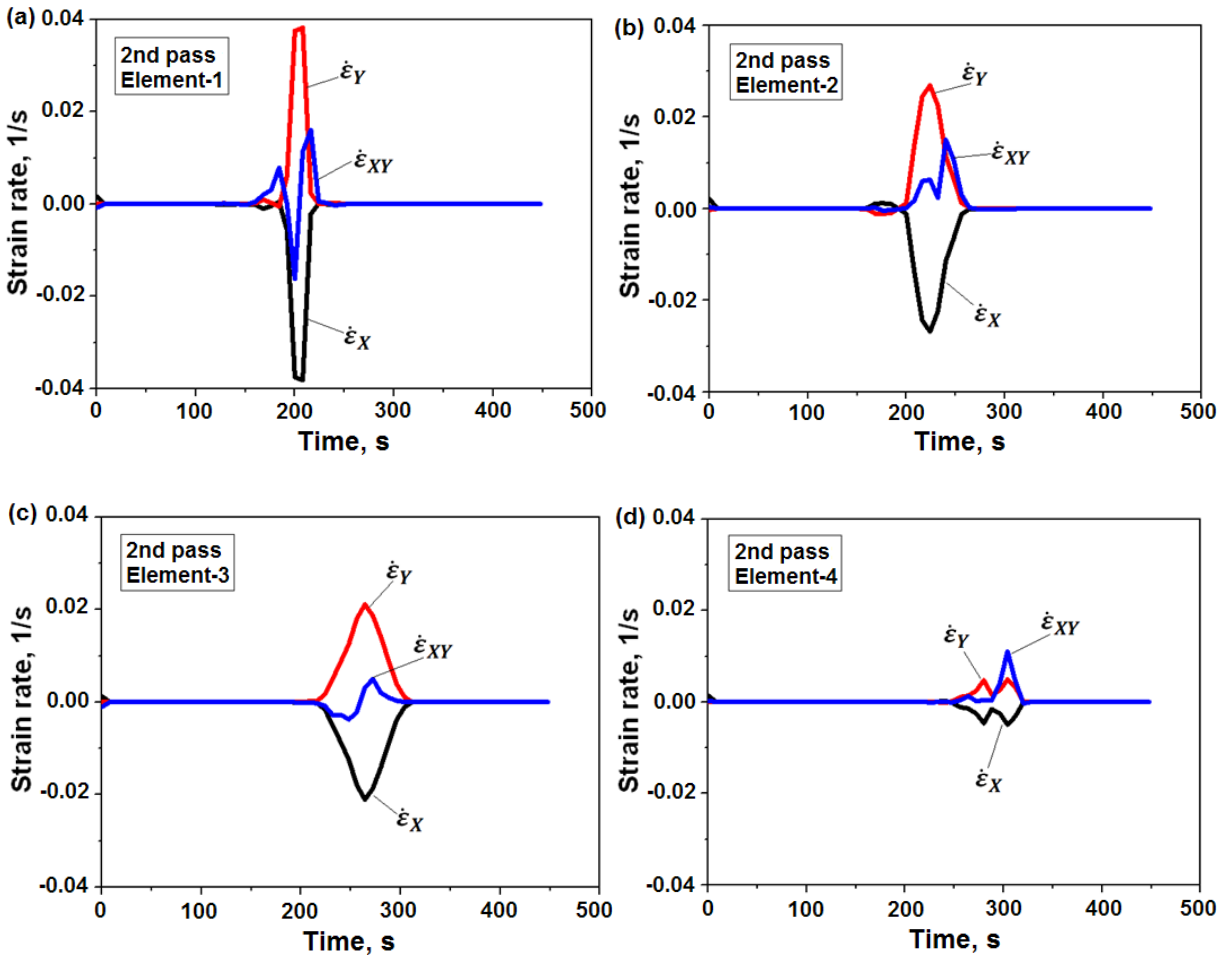

Fig. 6.15 Variation of the strain rates of (a) Element 1, (b) Element 2, (c) Element 3, and (d) Element 4 during the second pass of ECAP in Route C as a function of the processing time.

Four elements marked in Fig. 6.11 have been tracked to study the strain rate, and texture evolution in Route C. Element 1 and Element 4 are located near the edges while the Element 2 and Element 3 are in the middle region.

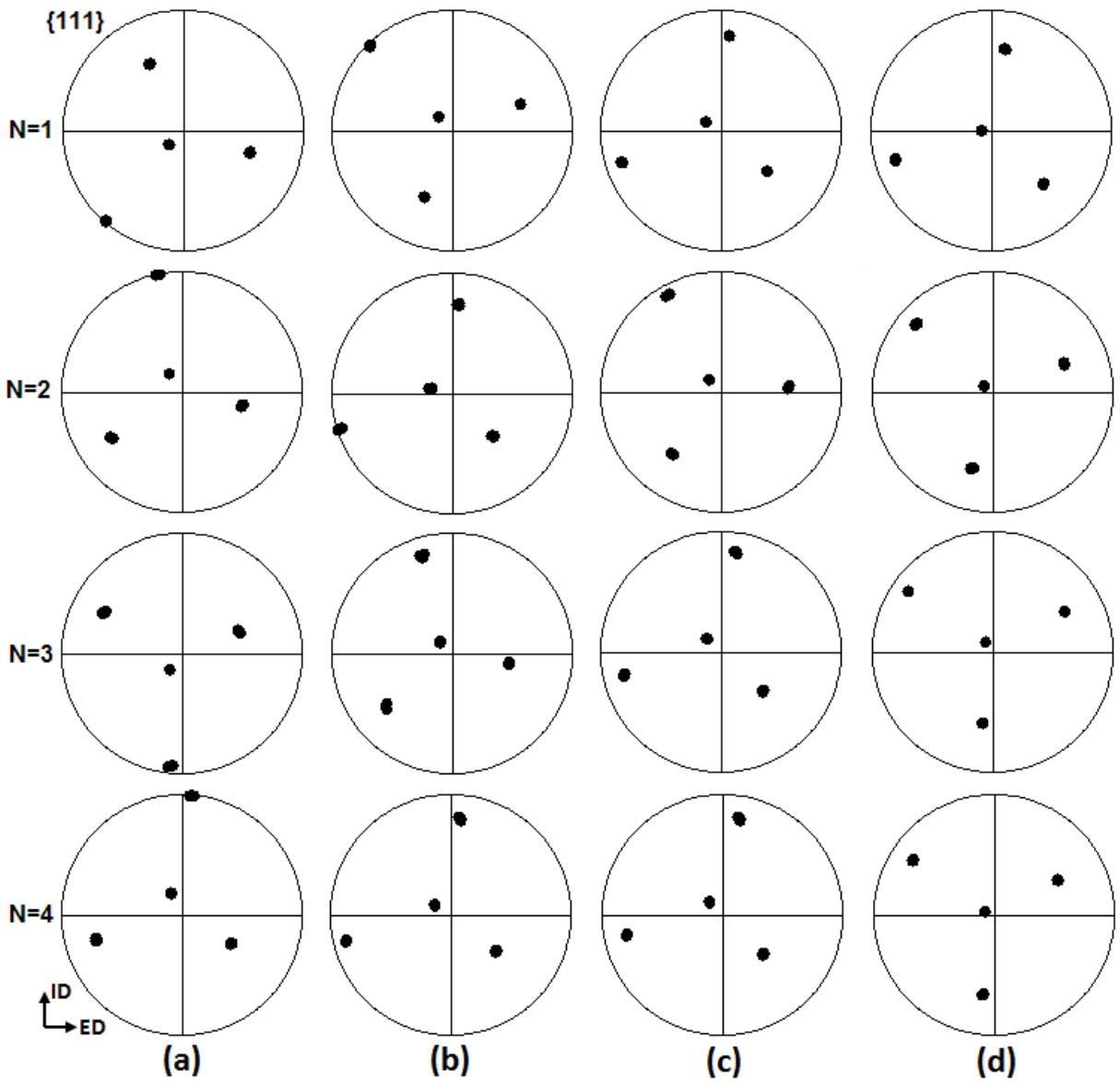

Fig. 6.16 The development history of crystallographic orientations of four selected elements (a) Element 1, (b) Element 2, (c) Element 3, and (4) Element 4 during ECAP in Route C.

Fig. 6.15 only shows the strain rates during the second ECAP pass because the results for the first pass has already been shown in Fig. 6.6. The results reveal that the biggest difference between the first and second pass exists for Elements 1 and 4. Element 1 has the smallest magnitudes of strain rates during the first pass but the largest magnitudes of strain rates during the second pass. In contrast, Element 4 has the largest strain rates during the first pass but the

smallest during the second pass. The results for the third and fourth passes are similar to the first and second passes, respectively.

Fig. 6.16 indicates the simulated {1 1 1} pole figures for the tracked elements. Fig. 6.16(a) shows the history of orientation development for Element 1. As can be seen, the orientation of Element 1 after the second pass has a 30° rotated component around TD in a clockwise direction from the initial orientation. The final crystallographic orientation of Element 1 after the fourth pass is rotated about -48° from the initial orientation around TD. As for Element 2, a 60° TD rotated component develops after the second pass and the same orientation has been obtained after the fourth pass. However, the orientation at the third pass is different to that of the first pass which remains as the initial crystallographic orientation as shown in Fig. 6.16(b). The orientation rotates around 30° in the third pass. Fig. 6.16(c-d) show the {1 1 1} pole figures for Elements 3 and 4, respectively. As discussed in Chapter 4, these two elements have the same orientation during the first pass because they are located in the same matrix band with a crystal rotation of 60° around TD. During the second pass, Element 3 has the initial crystallographic orientation while the orientation of Element 4 is slightly rotated away from the initial component around both TD and ID. The pole figures of Element 3 after three and four ECAP passes are similar. It has been seen that the orientation has rotated about 60° around TD from the initial orientation. It is interesting to find that the orientation of Element 4 almost does not change during the third and fourth passes and the {1 1 1} pole figures are similar to that of the second pass.

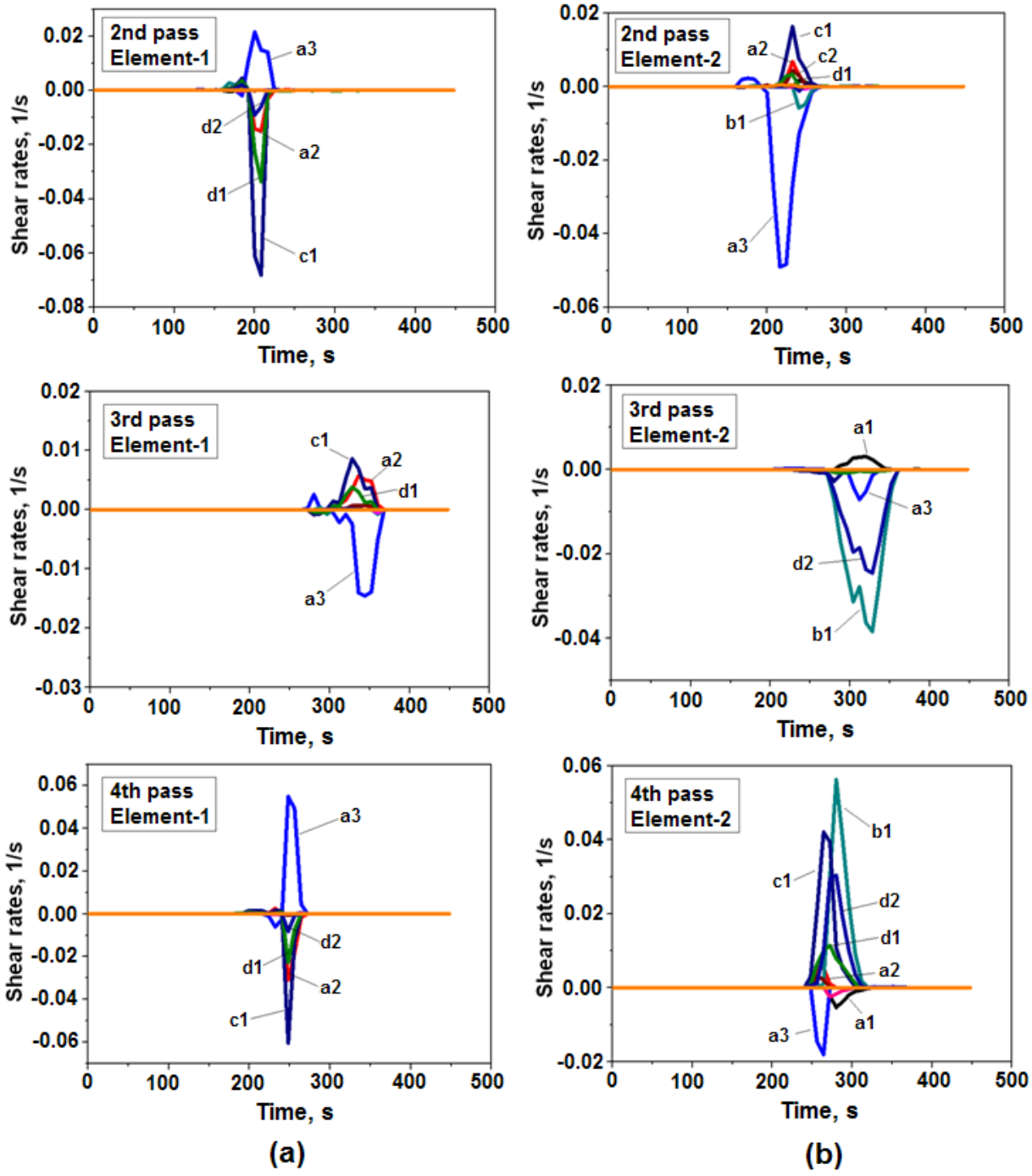

Fig. 6.17 The shear strain rates of four tracked elements during ECAP in Route C. (a) Element 1, (b) Element 2, (c) Element 3, and (d) Element 4.

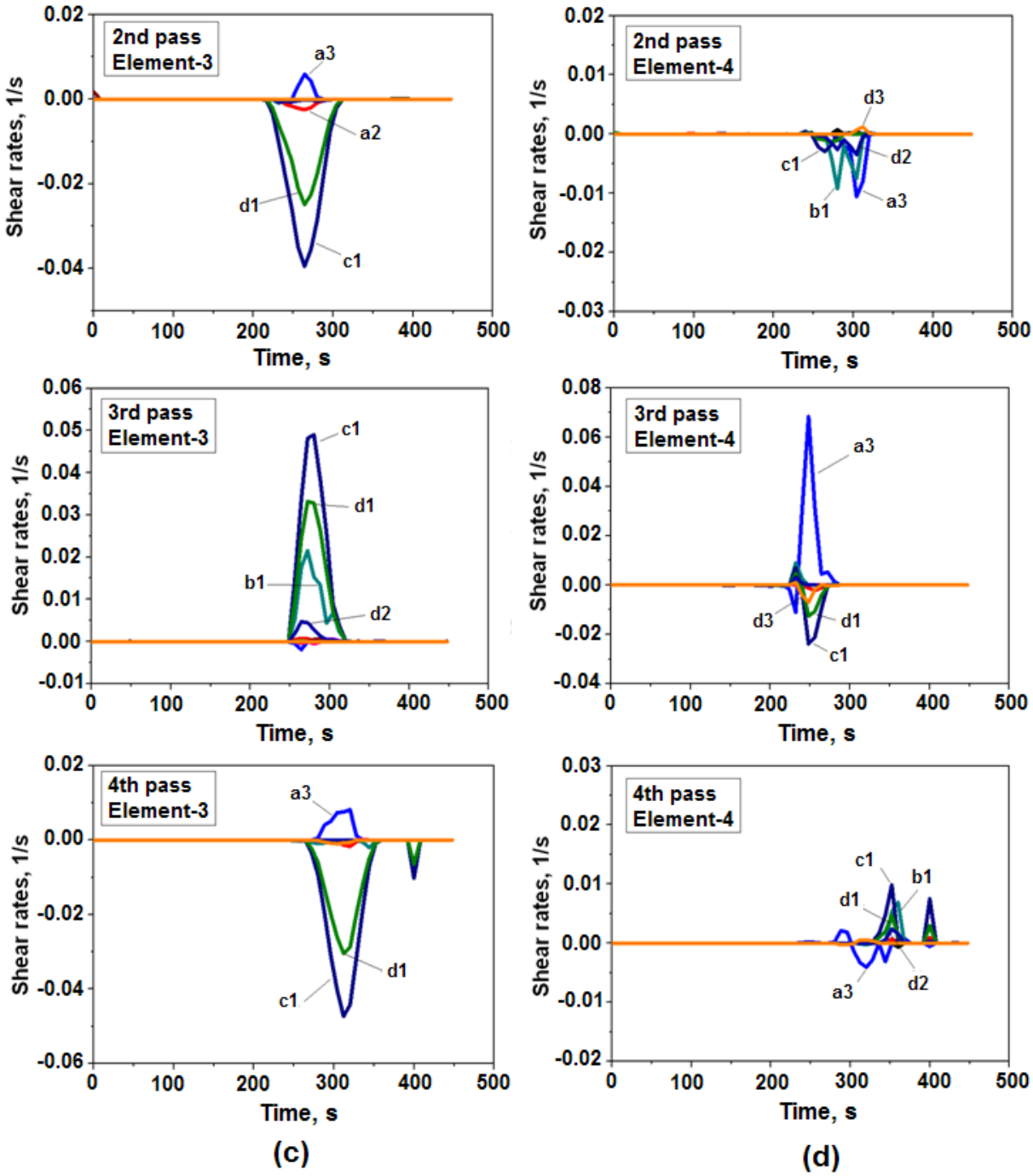

Fig. 6.17 Continued.

Fig. 6.17 shows the shear strain rates for the tracked elements during the ECAP process in Route C to study the slip systems activity. Significant differences to the results of Route A can be seen. It is obvious that the shear strain rates of Element 1 during the odd number pass and Element 4 during the even number passes are very small. This is caused by the rigid body

rotation. The results for Elements 2 and 3 reveals the activation of multi-slip systems during Passes 2-4. The predominant slip systems (with a maximum magnitude of shear strain rate) for Element 2 are a3 during the second pass, and b1 during the third and fourth passes. On the other hand, the slip systems c1 and d1 have the largest and second largest shear strain rates for Element 3 during the 2-4 ECAP passes. Therefore, it can be concluded that there is a significant influence of positions in the entry channel on the slip system activity during ECAP in Route C, which leads to different textures shown in Fig. 6.18.

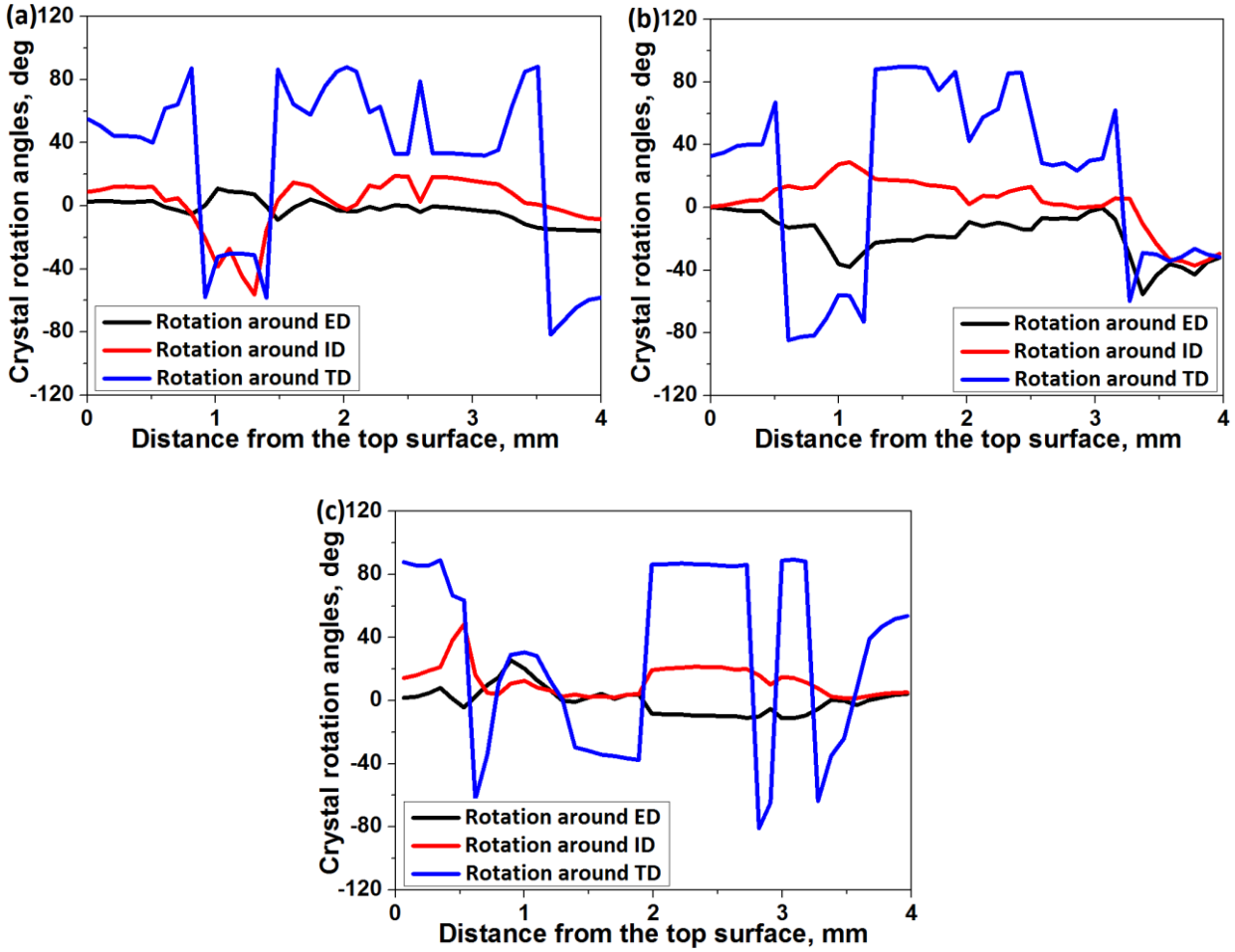

Fig. 6.18 Crystal rotation angles along the billet thickness direction during ECAP in Route C. (a) second pass, (b) third pass and (c) fourth pass.

Fig. 6.18 shows the variation of crystallographic rotation angles along the billet thickness direction in Route C. In Fig. 6.18(a), eight matrix bands are seen. Two matrix bands near the top

and bottom surfaces have the similar rotation angle of about 60° around TD, but in an opposite direction. The number of matrix bands developed during the third pass in Fig. 6.18(b) is the same as the second pass. It is worthy to note that large crystal rotations around ED and ID have been observed in the matrix band close to the sample bottom and the rotation angles are the same with the TD rotation, which is nearly 40° in a clockwise direction. Fig. 6.18(c) shows that ten matrix bands exist along the sample thickness after the fourth ECAP pass. The largest rotation angle is about 90° around TD and there is no matrix bands having the zero rotations which exists after the first ECAP pass as shown in Fig. 4.2(d). As can be seen from Fig. 6.18, the predominant crystal rotation remains around TD for all the passes in Route C, while large ID rotation exists in Route A. It can be concluded that the crystal rotation pattern is dependent on the ECAP route. Clearly, more matrix bands have developed in Route C than Route A. This indicates that Route C is more effective in grain refinement than Route A.

6.5 Summary

In this chapter, the multi-pass ECAP process of aluminium single crystal has been simulated. The following summaries can be made:

(1) Three adaptive meshing techniques available in Abaqus are introduced, namely the ALE analysis, VT adaptive meshing and MTMS mapping approach. The MTMS mapping analysis has been finally used to simulate the multi-pass ECAP process because the ALE analysis is not good at large deformation problems such as SPD techniques, and the VT adaptive remeshing analysis is not good at controlling distortion and is only available for the analyses submitted from Abaqus/CAE. Another advantage of the MTMS method is that it can be used with any material models. Capability of the MTMS mapping approach is examined by comparing the {1 1 1} pole figures before and after the MTMS mapping analysis. Good agreement suggests that this approach is suitable for texture simulations during the multi-pass ECAP of aluminium single crystals.

(2) The influence of the processing routes on the inhomogeneous deformation and texture evolution is significant by comparing the results in Routes A and C. The simulated strains for

both routes agree well with predictions by the analytical models. It has been found that the accumulated strain in Route A is slightly smaller than Route C. The strain distributions reveal that Route C leads to a more uniform deformation than Route A. Four elements have been tracked in both routes and it has been found that texture evolution and slip system activity are strongly influenced by the ECAP route and number of passes. Investigation of crystal rotation angles suggests that more matrix bands develop in Route C and Route C is more effective in grain refinement than Route A.

Chapter 7 CPFEM Simulation of ECAP Process of Aluminium Bicrystals and Polycrystal

In the previous chapters, the deformation behavior and texture evolution during the ECAP process of single crystals have been studied. In this chapter the study will be extended to investigate ECAP processing of bicrystals and polycrystal.

Bicrystals give us the chance to discern the individual influence of the grain boundary and the different crystallographic orientations of the component grains. To the best of my knowledge the study of the ECAP process of bicrystals by Han et al. [36] is the only one available in the published literatures. In their study, four Cu bicrystals with the same initial crystallographic orientations but different grain boundary positions with respect to the ECAP die were specifically designed to examine the evolution of the initial grain boundaries and development of the shear bands. However, their experimental results mainly revealed the microstructure evolutions close to the grain boundaries and developments of the shear bands and slip bands, whereas the influence of grain boundaries on the crystallographic orientation changes has not been studied in detail. The present study is the first simulation of the ECAP process of bicrystals.

Compared to the limited studies of single crystals and bicrystals, numerous experimental and modeling investigations have been conducted on the ECAP process of polycrystals. According to Beyerlein and Toth [2], the predicted texture during the ECAP process is significantly influenced by the texture models and deformation histories. As mentioned in Section 2.5, most of the texture simulations of polycrystals during the ECAP process were carried out using the Taylor-type model or VPSC model [31, 50, 59, 100], which often fail to agree with the experimental results. Even though several studies [55, 57, 58, 120] were based on the advanced crystal plasticity model, satisfactory predictions were still not obtained due to the assumption of simple shear in these models. Therefore, the present study will be the first attempt to simulate

texture evolution of polycrystals by considering the deformation history of the real full-scale ECAP process using the CPFEM model.

7.1 CPFEM Simulation of Aluminium Bicrystals

The simulated ECAP die is the same as that used in the previous studies. Two cases (Case 1 and Case 2) have been investigated. Two single crystals (Crystal1 and Crystal2) are used in the simulations. But their relative positions are different in Case 1 and Case 2 as demonstrated in Fig. 7.1. The grain boundaries were designed to be parallel to the Y axis. Two crystals have the same dimensions of 2 × 23 mm^2 which have been meshed into 4000 elements. In Crystal1, the crystallographic plane (-4 -1 2) is parallel to the normal plane (ND or Y axis) and the crystallographic direction [1 2 3] is parallel to the X axis (or ED) in Crystal 1. In Crystal2, the crystallographic plane (4 1 -2) is parallel to the ND and the crystallographic direction [1 2 3] is parallel to the ED. The corresponding Euler angles of two component grains are (-61.44°, 65.91°, 153.43°) and (61.44°, 114.09°, 26.57°), respectively. For convenience, the corresponding {1 1 1} pole figures of these two component grains have been shown in Fig. 7.1.

Like the previous studies, the die was assumed to be a rigid body and the sample was simulated as a deformable body. The coefficient of friction (μ) was set to 0.05 and the processing speed (v) was set to 2.4 mm/min.

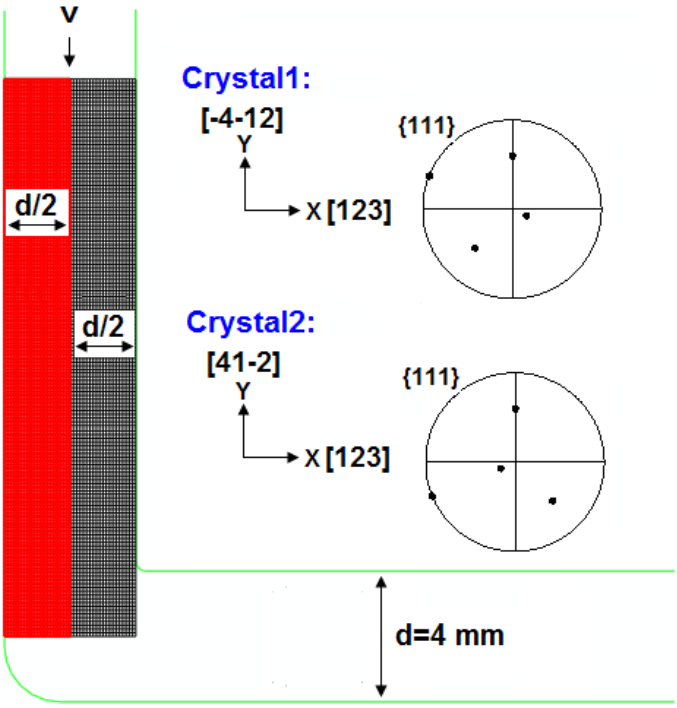

Fig. 7.1 Illustration of the sample geometry, initial crystallographic orientations of two component grains in the aluminium bicrystal (Case 1).

Fig. 7.2 shows the mesh distortions in two simulation cases. In the figure, Crystal1 is highlighted by the red color. In Case 1, as shown in Fig. 7.2(a), significant mesh distortions occur in the leading head of specimen in the vicinity of grain boundary and a small corner gap develops in the outer corner, represented by the arc of 'AB'. As can be seen, the grain boundary after deformation in Case 1 is almost parallel to the X axis in the steady state deformation region. Similar observations were reported in the experiment of the ECAP processed copper bicrystal [36]. Inhomogeneous distortions along the thickness were found in both grains in Case 1. It is interesting to observe that the mesh of Crystal2 is distorted more near the grain boundary than other locations, whereas in Crystal1, there are more distortions in the middle part than the place closer to the grain boundary.

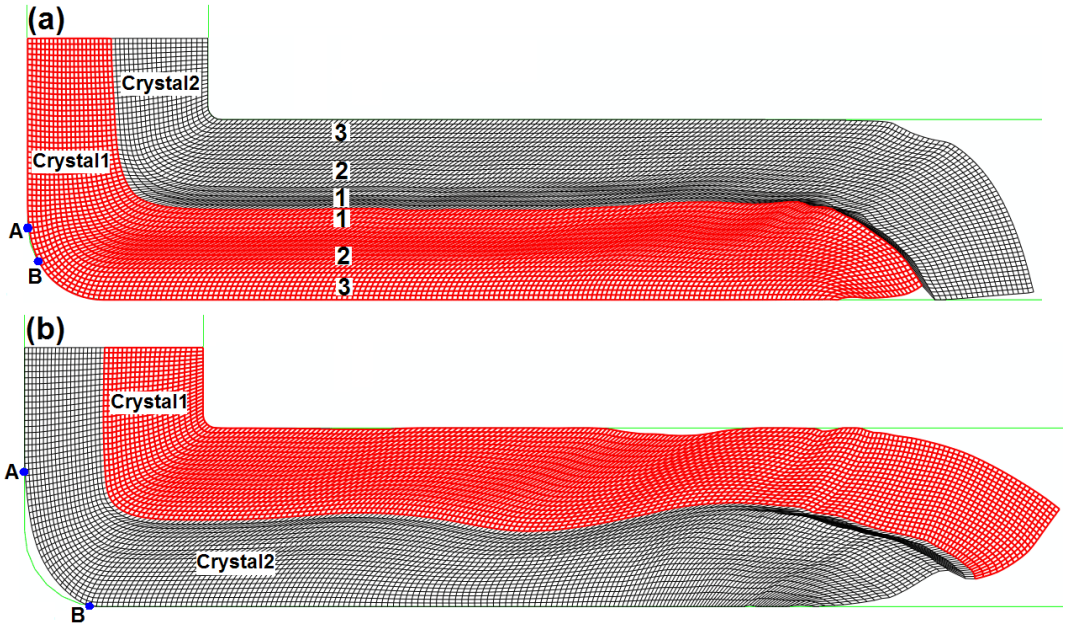

Fig. 7.2 Mesh distortions of the aluminium bicrystals: (a) Case 1 and (b) Case 2 during the ECAP process. (the grain denoted as Crystal1 is highlighted in red).

However, very different result has been observed in Case 2. Fig. 7.2(b) shows a longer inhomogeneous leading head and a larger corner gap for Case 2 compared to Case 1. In Case 2 the grain boundary is wavy in the steady state deformation region. In Crystal1 the mesh is deformed quite uniform along the thickness but in Crystal2, there was more mesh distortion around the area close to the grain boundary. It should be noted that the thickness of Crystal2 becomes slightly smaller than the initial thickness due to compression in the entry channel before entering the PDZ.

Fig. 7.3 shows the distributions of the von Mises stress and plastic strain rate components in the deformed specimen in Case 1. It is clear that the stress distribution is very inhomogeneous along the X axis and Y axis and the von Mises stress in Crystal1 is slightly larger than in Crystal2. According to Fig. 7.3(b-d), the fan-shaped PDZ has been partitioned into two sections and the strain rate gradient is larger in Crystal2 than in Crystal1. Besides, the length of Crystal2 along the intersecting line is shorter than that of Crystal1. Compared to the normal strain rates $\dot{\varepsilon}_X$ and $\dot{\varepsilon}_Y$, the shear strain rate $\dot{\varepsilon}_{XY}$ has scattered more into the entry channel and exit channel in Crystal2.

Fig. 7.4 shows the distributions of the von Mises stress and plastic strain rate components in Case 2. As can be seen, the results are different to those of Case 1. The von Mises stress in Crystal1 is still larger than that in Crystal2. In addition, the scattering of the strain rate $\dot{\varepsilon}_{XY}$ is much smaller and confined into a relatively narrow band. The length of Crystal1 along the intersecting line is longer than that of Crystal2. The distribution of strain rates around the place close to the outer corner is less uniform in Case 2 than Case 1.

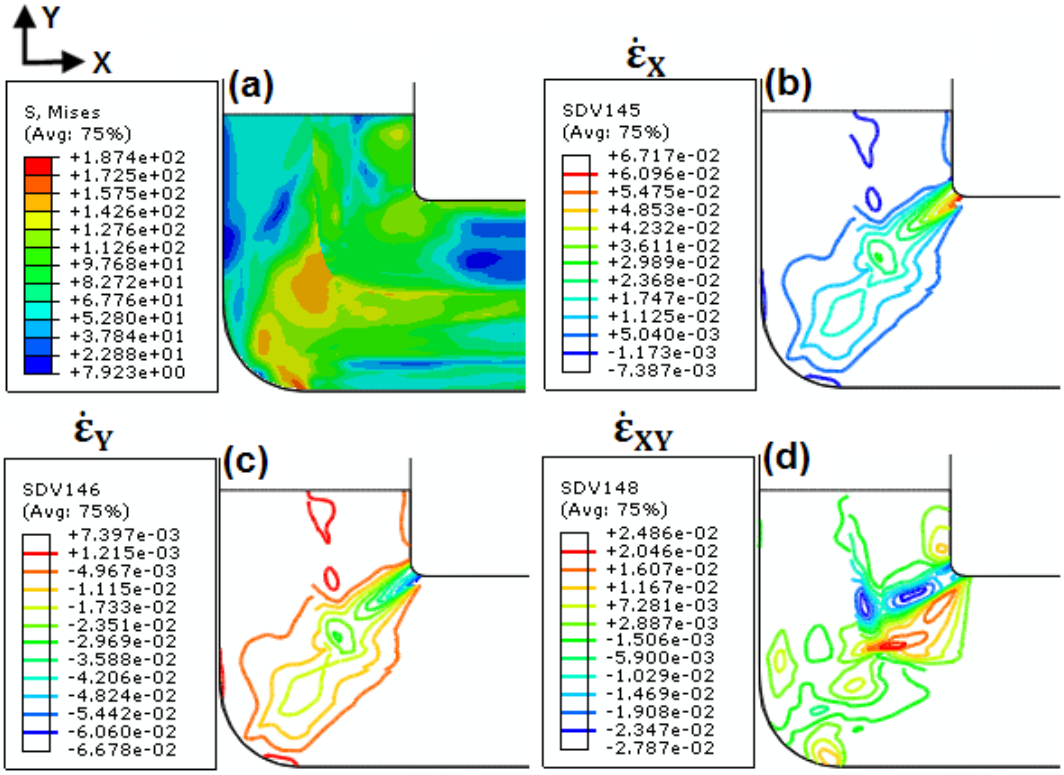

Fig. 7.3 Distributions of (a) von Mises stress and plastic strain rate components (b) $\dot{\varepsilon}_X$, (c) $\dot{\varepsilon}_Y$ and (d) $\dot{\varepsilon}_{XY}$ in the deformed specimen of Case 1.

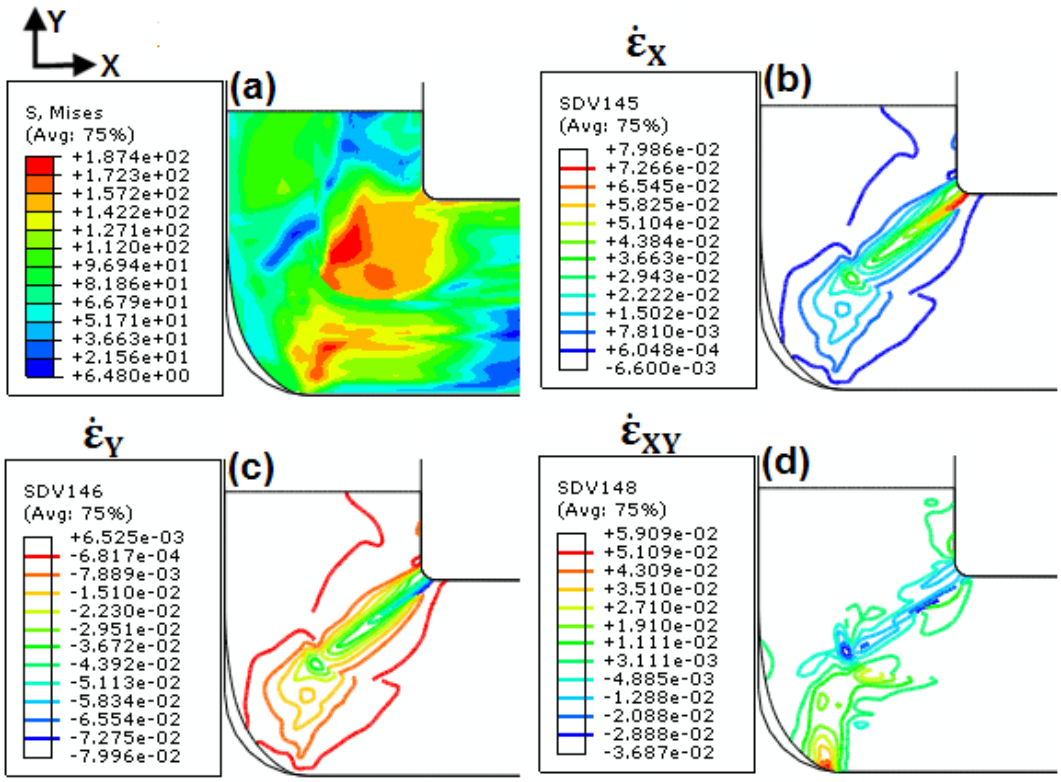

Fig. 7.4 Distributions of (a) von Mises stress and plastic strain rate components (b) $\dot{\varepsilon}_X$, (c) $\dot{\varepsilon}_Y$ and (d) $\dot{\varepsilon}_{XY}$ in the deformed specimen of Case 2.

Fig. 7.5 shows the variation of the effective plastic strain along the thickness direction as a function of the distance from the top surface in both simulation cases. In Case 1 it is clear that the strain in Crystal1 increases slowly from the top surface and increases rapidly close to the grain boundary, whereas the strain in the lower part (Crystal2) can be divided into three parts which include a rapid decrement close to the grain boundary, a relatively uniform part in the middle of the crystal, and a gradual decrement at the bottom. On the other hand, a different result can be found in Case 2. The strain in 75% of the thickness in the upper crystal (Crystal2) is similar to Case 1, and then there was a rapid decrement in the remaining 25% of the thickness close to the grain boundary. Compared to the upper crystal, the strain in the lower crystal (Crystal1) decreased gradually from the grain boundary to the bottom. The average values of the effective plastic strains along the thickness are 1.234 and 1.321 in Case 1 and Case 2, respectively.

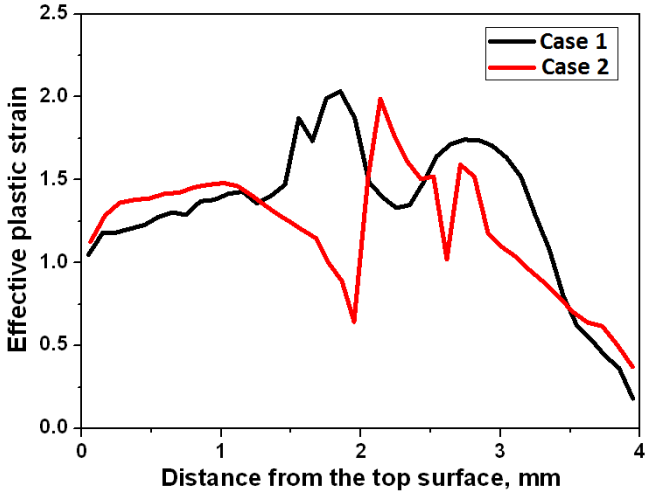

Fig. 7.5 Variation of effective plastic strains along the thickness in both bicrystals.

Fig. 7.6 shows the variations of the von Mises stress, shear component of the stress, and the shear strength along the thickness direction in both simulation cases. It is obvious that a significant influence of the grain boundaries can be observed. Fig. 7.6(a) indicates that the von Mises stresses near the grain boundaries and surfaces of the die are larger than the other locations. In addition, the upper crystal in Case 1 has a smaller von Mises stress than Case 2, but the stress in the lower crystal of Case 1 is larger than the corresponding result in Case 2. From Fig. 7.6(b) and (c), it is clear that the grain boundary leads to a large fluctuation in the shear stress and shear strength in both cases during the ECAP process. It should be noted that the results are different in the crystals with the same initial crystallographic orientation when they are located in the different positions in the ECAP die.

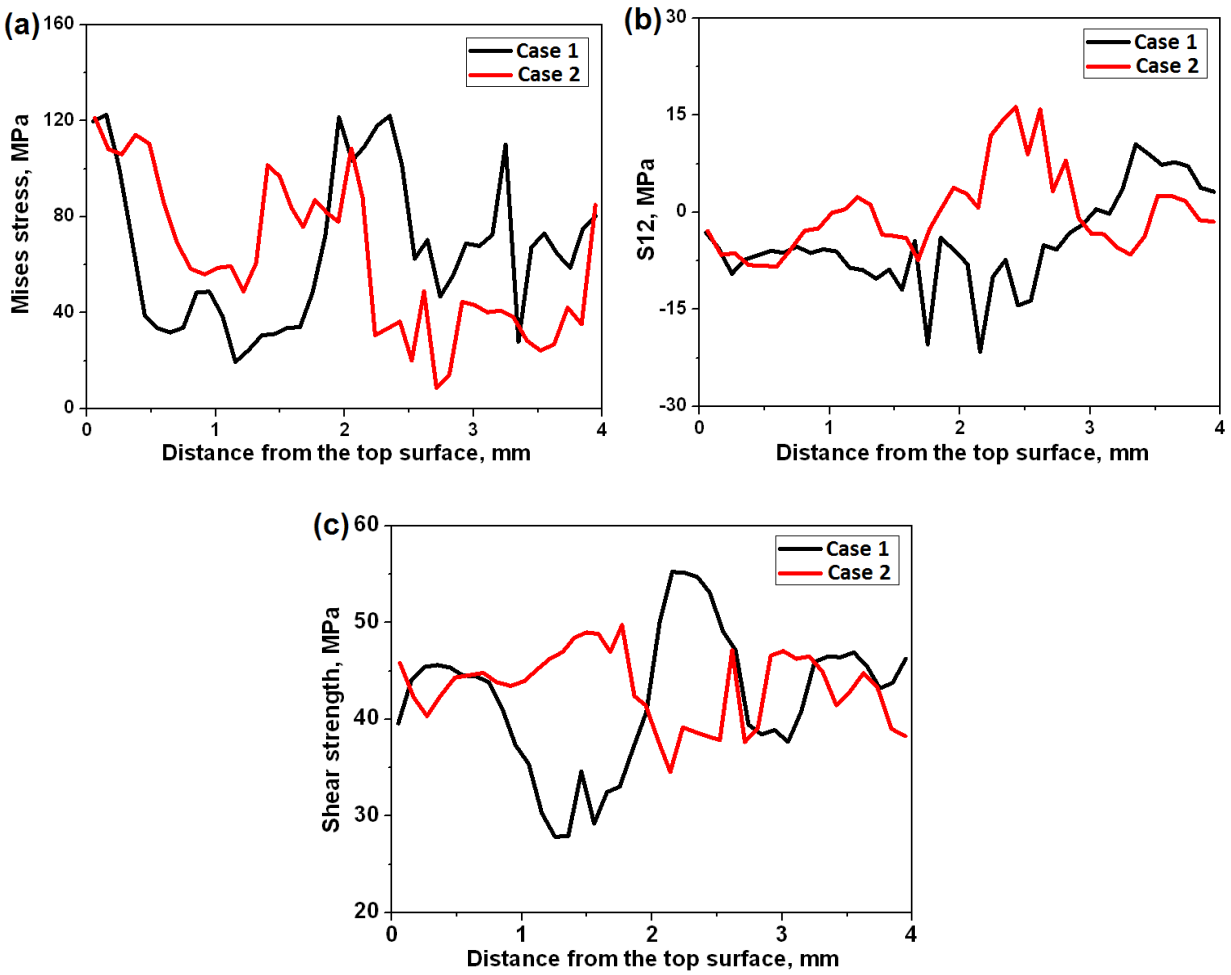

Fig. 7.6 Variation of the (a) von Mises stress, (b) shear component of the stress (S12), and (c) shear strength along the thickness in both simulation cases.

In order to study the influence of the grain boundary on texture evolution, three different positions are selected, as shown in Fig. 7.2(a), to plot the {1 1 1} pole figures. Position P1 is located in the vicinity of the grain boundary, Position P2 is in the middle part of the crystals, and Position P3 is furthest away from the grain boundary and close to the surfaces of the die. The pole figures of Case 1 are shown in Fig. 7.7. It is obvious that the {1 1 1} pole figure of Position P1 in the upper crystal (Crystal2) indicates a 40° rotated orientation from the initial crystallographic orientation around the Z axis. As can be seen, there was almost a 60° rotated orientation component at Position P2, while the rotation angle is slightly smaller and the pole figure at Position P3 indicates a 50° rotated orientation. In contrast in the lower crystal (Crystal1) the {1 1 1} pole figures for the three positions are different from those in the upper

crystal. The pole figure at Position P1 is characterized as a 60° rotated component around the Z axis from the initial crystallographic orientation and the pole figure at Position P2 indicates a 40° rotation. As for Position P3, the pole figure revealed a 90° rotation which should be attributed to the rigid body rotation due to the existence of the OCA of the ECAP die and development of a corner gap during the ECAP process.

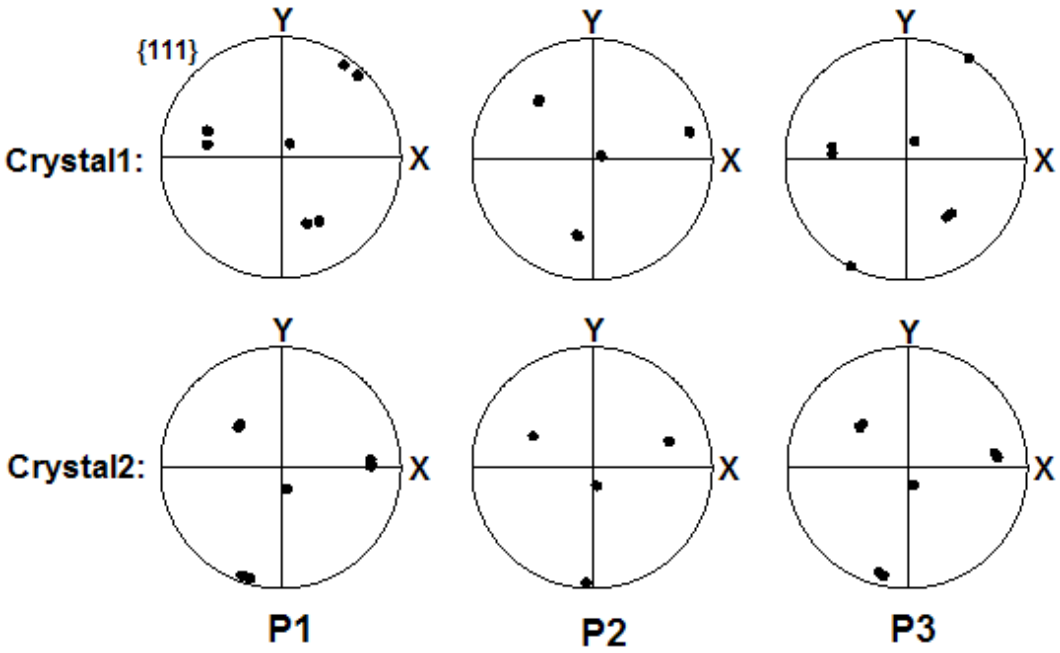

Fig. 7.7 Simulated {1 1 1} pole figures of three selected positions (P1-P3 marked in Fig. 7.2(a)) in both component grains in Case 1.

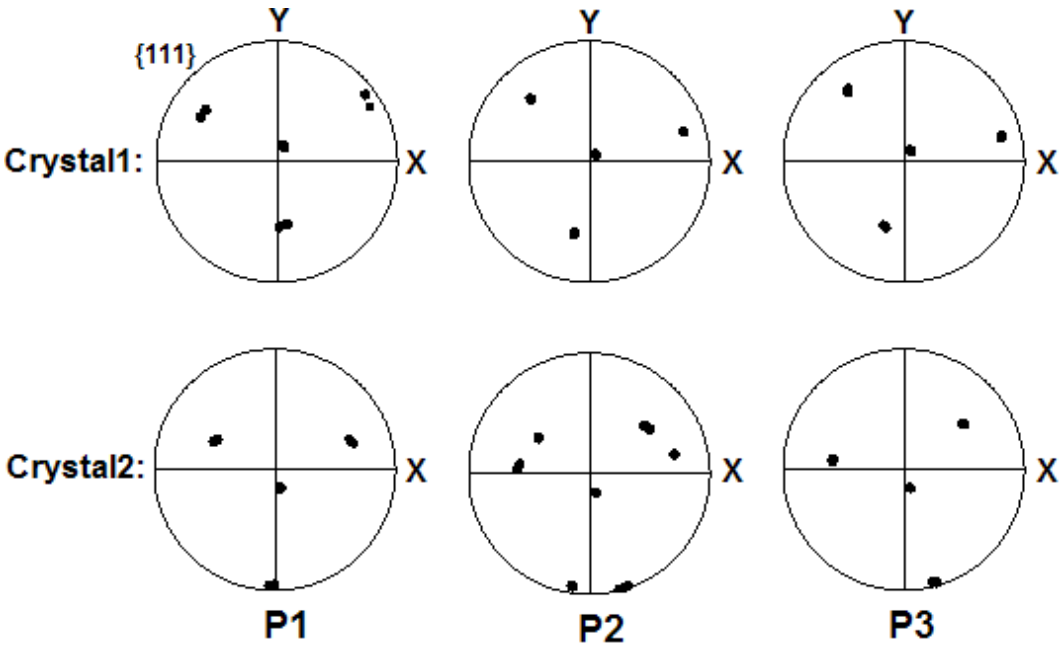

Fig. 7.8 Simulated {1 1 1} pole figures of three selected positions (P1-P3 marked in Fig. 7.2(a)) in both component grains in Case 2.

Fig. 7.8 shows the simulated {1 1 1} pole figures for Case 2. In the upper crystal (Crystal1), the pole figure at Position P1 indicates a 60° rotated component around the Z axis with a small scattering. The pole figures at Positions P2 and P3 are similar, which indicates a 40° Z-axis rotated orientation. In addition, there is a slight rotation of almost 15° around the Y axis in the pole figures at Positions P2 and P3. The {1 1 1} pole figure of the lower crystal (Crystal2) reveals a 60° Z-axis rotated orientation and a 90° Z-axis rotated orientation at Positions P1 and P3, respectively, whereas these are two orientations existing simultaneously at Position P2.

According to the above results, it can be concluded that the grain boundary has a significant influence on the plastic deformation behavior, such as mesh distortion and the shape of the PDZ, the strain and stress distributions, and the crystallographic orientation evolutions during the ECAP process.

7.2 CPFEM Simulation of Aluminium Polycrystal

The main objectives of this section is to investigate the deformation heterogeneity and texture evolution of aluminium polycrystal subjected to one pass of the ECAP process using the CPFEM simulation.

The simulated billet was rectangular and was 22 mm long by 4 mm wide, and it was meshed into 8000 elements (with 40 elements along the width). The ECAP die was the same one used in the previous section and was assumed to be a rigid body during the FEM simulation. The punch and billet were defined as a rigid body and deformable body, respectively. A constant processing speed of 2.4 mm/s was given along the –Y axis and the coefficient of friction μ was set to 0.05.

In order to validate the polycrystal simulation model developed in the present study, an ECAP experiment has been performed. The material used in ECAP was commercially pure aluminium AA1050. Billets were cast and heat treated at 456° for one hour and then air cooled to the room temperature. The chemical composition of this aluminium alloy is shown in Table 7.1 and the ECAP instrument is shown in Fig. 7.9(a). The optical microstructure of the annealed aluminium alloy was observed with a Leica DMRM microscope, where the sample was round, polished with a Struers TegraPol-21 polishing machine to an OPS finish and then etched with Barker's reagent. The grain size was measured using the linear intercept method. The textures before and after the ECAP process were measured by X-ray diffraction using X'Pert MRD goniometer with Cu Kα radiation at 45 kV and ~40 Ma, where the sample was fround and polished with a Struers OPS finish to ensure a flat surface. Pole figure and ODFs were calculated using X'Pert texture software after defocusing and background correction [22].

The ECAP die in Fig. 7.9(a) has a cross-section of 20 × 20 mm^2, an intersection angle of 90° and an OCA of 20°. The annealed AA1050 was cut into 20 × 20 × 100 mm^3 billets. In the experiment, the four longer faces of the billet were prepared to obtain a mirror like finish by grinding on abrasive paper and electro-polishing and then coated in a MoS_2 lubricant prior to processing. ECAP experiment was conducted at room temperature.

Table 7.1 Chemical composition of aluminium alloy AA1050 used in this study [22].

wt %	Si	Fe	Cu	Mn	Mg	Zn	Ti	Al
AA1050	0.25	0-0.4	0.05	0.05	0.05	0.05	0.03	Balance

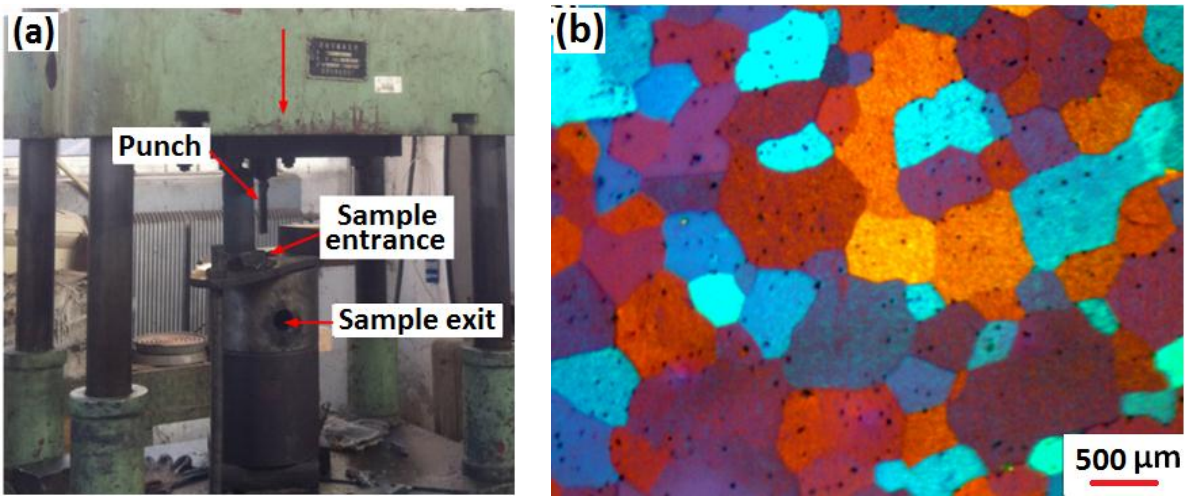

Fig. 7.9 (a) Photo of the experimental instrument for ECAP and (b) Optical microstructure of the annealed aluminium alloy AA1050 before ECAP.

Fig. 7.9(b) indicates the optical microstructure of the annealed AA1050 before the ECAP process. The average grain size measured from Fig. 7.9(a) is about 600 µm. The distribution of the grain size is shown by bars in Fig. 7.10(a). A normal distribution function is used to fit the measured grain size distribution. The fitting result is also displaced by a red line in Fig. 7.10(a). The average value and standard deviation of the measured grain size are 540 µm and 195 µm, respectively.

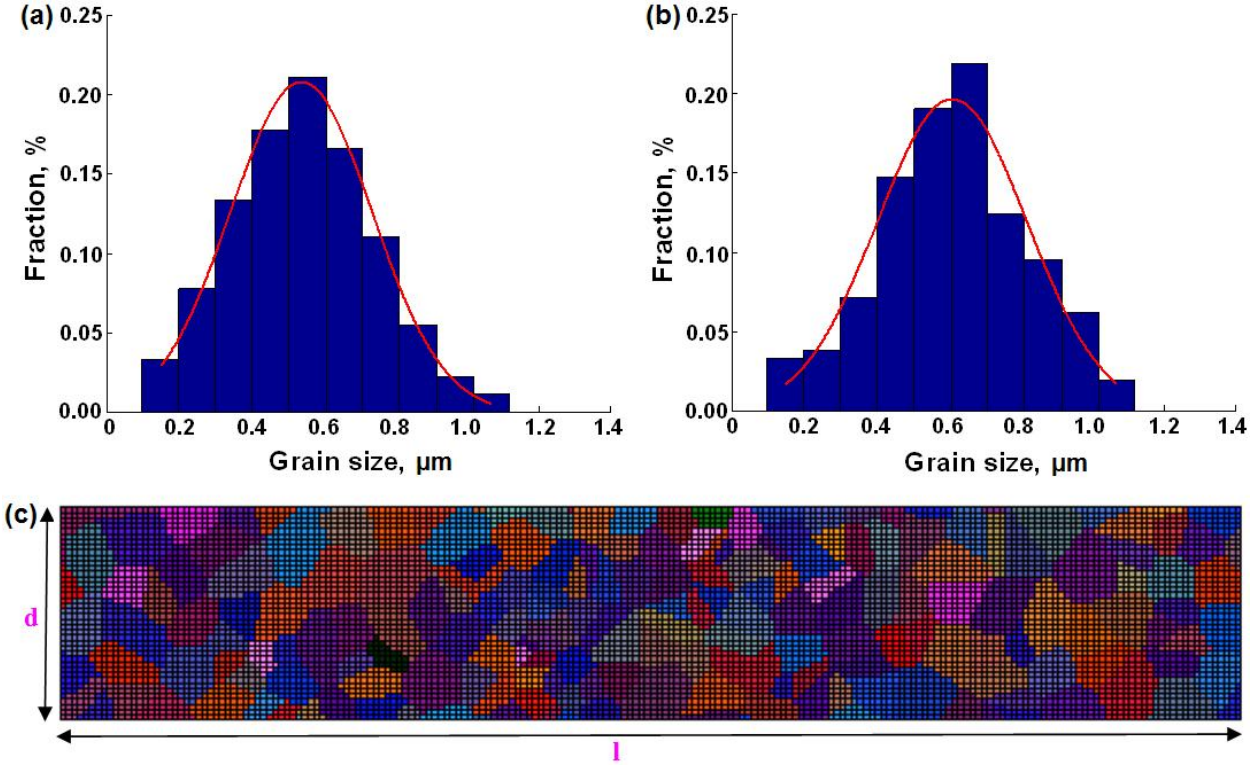

Fig. 7.10 (a) The experimental measured distribution of grain size and (b) the calculated distribution of grain size for the simulation based on the experimental result, and (c) the simulated grain shapes and initial meshes of the billet in the model before the ECAP process.

In the present study the polygons built by planar Voronoi diagram will be used to represent two-dimensional grain shapes which were found better to describe the real grain shapes than the regular circle and ellipse [240]. Each polygon contains one seed and the number of seeds will be controlled to determine the average size of the polygons. Because the total planar area was fixed as 4 × 22 =88 mm^2, the number of polygons should be about 280 to meet the measured average grain size. The polygons generated by Voronoi diagram are shown in Fig. 7.10(c) and each polygon represents one grain. The distribution of size of the generated polygons and the corresponding fitting curve are shown in Fig. 7.10(b). The average value and standard deviation of the fitting curve are 560 μm and 218 μm, respectively. These values are in good agreement with the experimental values. It is obvious from comparison of Fig. 7.9 and Fig. 7.10 that the grain sizes and shapes used in the simulation are consistent with the experimentally measured results.

Initial crystallographic orientation of the AA1050 alloy before ECAP has been shown in terms of {1 1 1} pole figure in Fig. 7.11(a) and φ_2=0° ODF section in Fig. 7.12(a). It can be seen that the initial texture of annealed AA1050 alloy can be characterized as a strong Cube texture from both the {1 1 1} pole figure and ODF section. A Matlab program has been developed to allocate the crystallographic orientation to each orientation according to the measured texture. The {1 1 1} pole figure and the ODF section generated by the Matlab program are shown in Fig. 7.11(b) and Fig. 7.12(b), respectively. It can be seen that good agreement in Fig. 7.11 and Fig. 7.12 has been obtained.

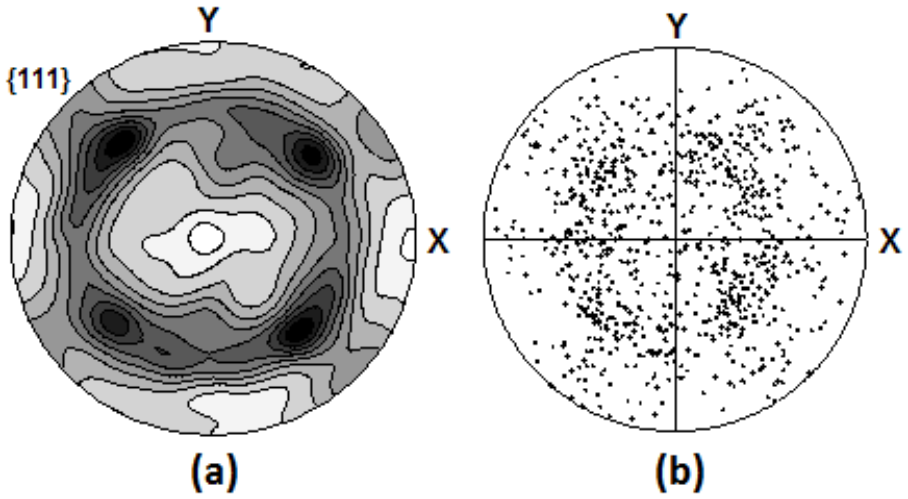

Fig. 7.11 Initial {1 1 1} pole figure of the annealed AA1050 alloy before ECAP: (a) experimental measurement [22] and (b) Matlab program generated result used for simulation.

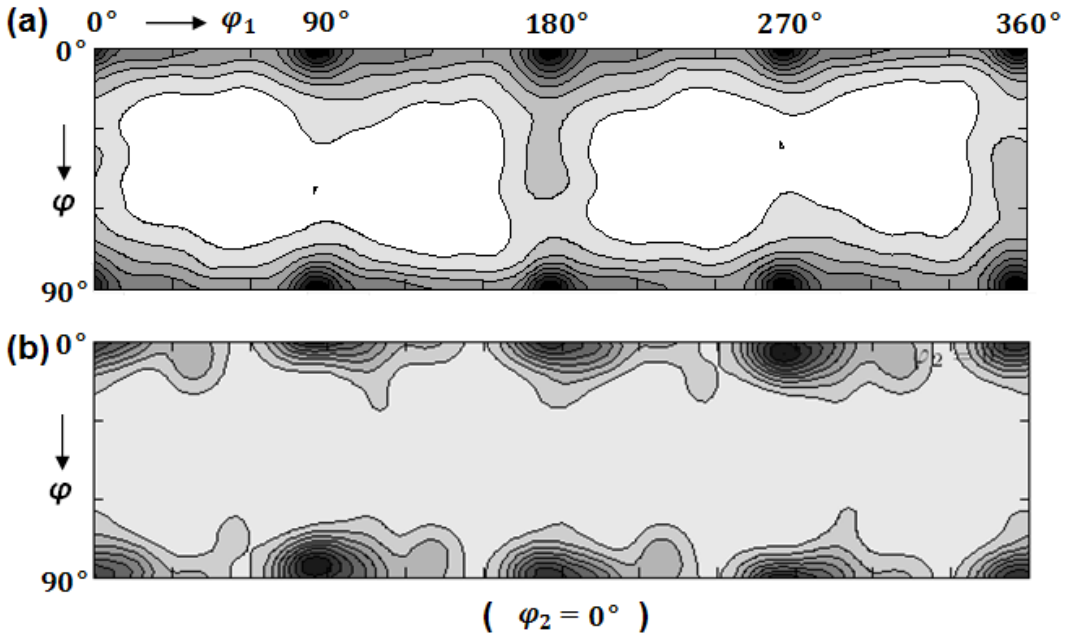

Fig. 7.12 Initial texture of the annealed AA1050 before the ECAP process in terms of φ_2=0° ODF section (a) experimental measurement [22] and (b) Matlab program generated result used for simulation.

The other material parameters used in the simulation for pure aluminium, such as the elastic moduli, Poisson ratio and density are the same as those described in Chapter 3. It takes approximately 500 hours using four CPUs to finish this simulation.

Fig. 7.13(a) shows the deformed mesh of the polycrystal after the ECAP process. As can be seen, the mesh distortion is not uniform along the billet axis and billet thickness. This result is very different to those of single crystals and bicrystals in the previous studies. Some macro-bands parallel to the intersecting line of two channels developed in this polycrystal but the mesh distortion in the bottom of the sample was different from the upper region because of the influence of the OCA. In addition, an outer corner gap is also seen in Fig. 7.13(a) as marked by the arc of 'AB'.

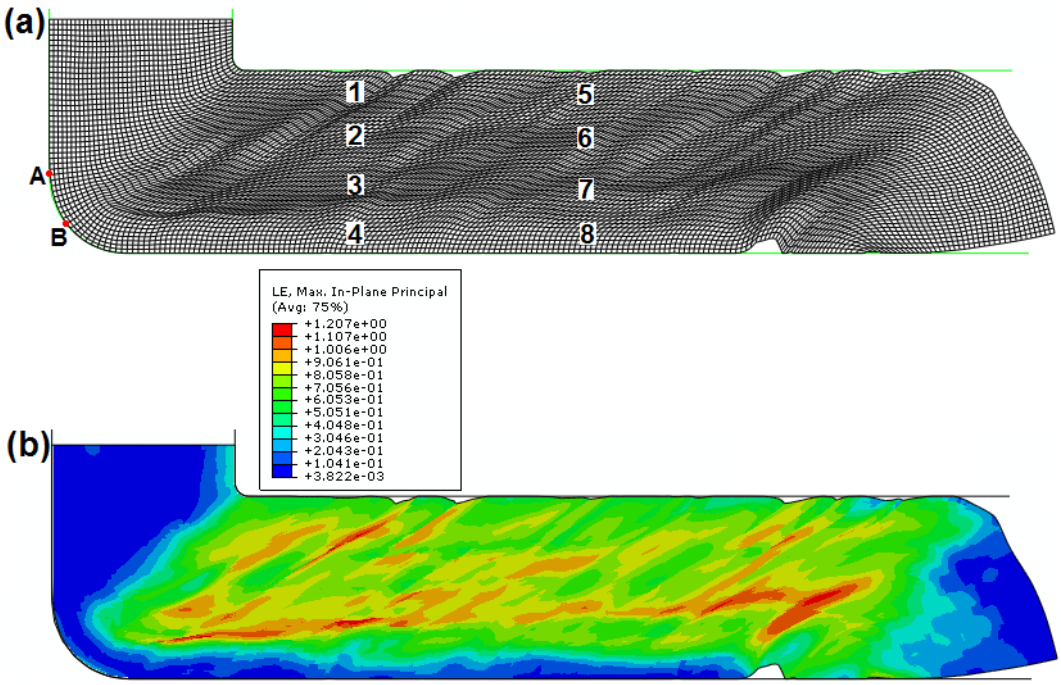

Fig. 7.13 (a) Mesh distortion and (b) Distribution of the plastic strain in the aluminium polycrystal during the ECAP process at t=480 s.

The distribution of plastic strain in the deformed aluminium polycrystal is shown in Fig. 7.13(b). It is clear that the strain is not uniform along the billet axis and the strain in the leading head and undeformed part are very small, while a larger strain has accumulated in the middle part. Along the thickness direction the strain was less in the bottom than the upper region.

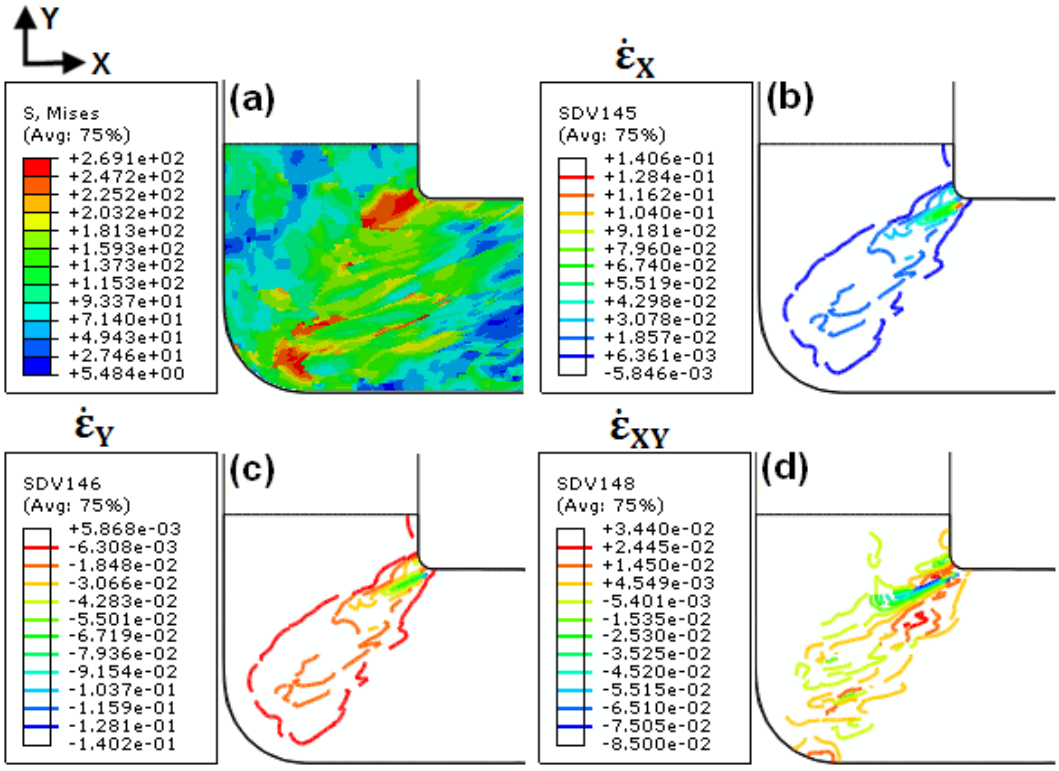

Fig. 7.14 Distributions of (a) von Mises stress and plastic strain rates (b) $\dot{\varepsilon}_X$, (c) $\dot{\varepsilon}_Y$ and (d) $\dot{\varepsilon}_{XY}$ in the deformed polycrystal during the ECAP process.

In order to gain a better understanding of the deformation behavior of this aluminium polycrystal during the ECAP process, the simulated results around PDZ has been analyzed in detail. Fig. 7.14 shows the distribution of the von Mises stress and plastic strain rates. Fig. 7.14(a) indicates that the von Mises stress at the intersecting zone of two channels is different to the case of single crystals shown in Chapter 4. The largest magnitude of stress here is about 269.1 MPa close to the inner corner. Fig. 7.14(b-d) shows the distributions of plastic strain rates $\dot{\varepsilon}_X$, $\dot{\varepsilon}_Y$ and $\dot{\varepsilon}_{XY}$, respectively. For the normal components $\dot{\varepsilon}_X$ and $\dot{\varepsilon}_Y$, the largest values are close to the inner corner and the magnitudes decrease gradually along the intersecting plane from the inner to the outer corner. Compared to the single crystal, the fan-shaped PDZ in the polycrystal only expanded slightly.

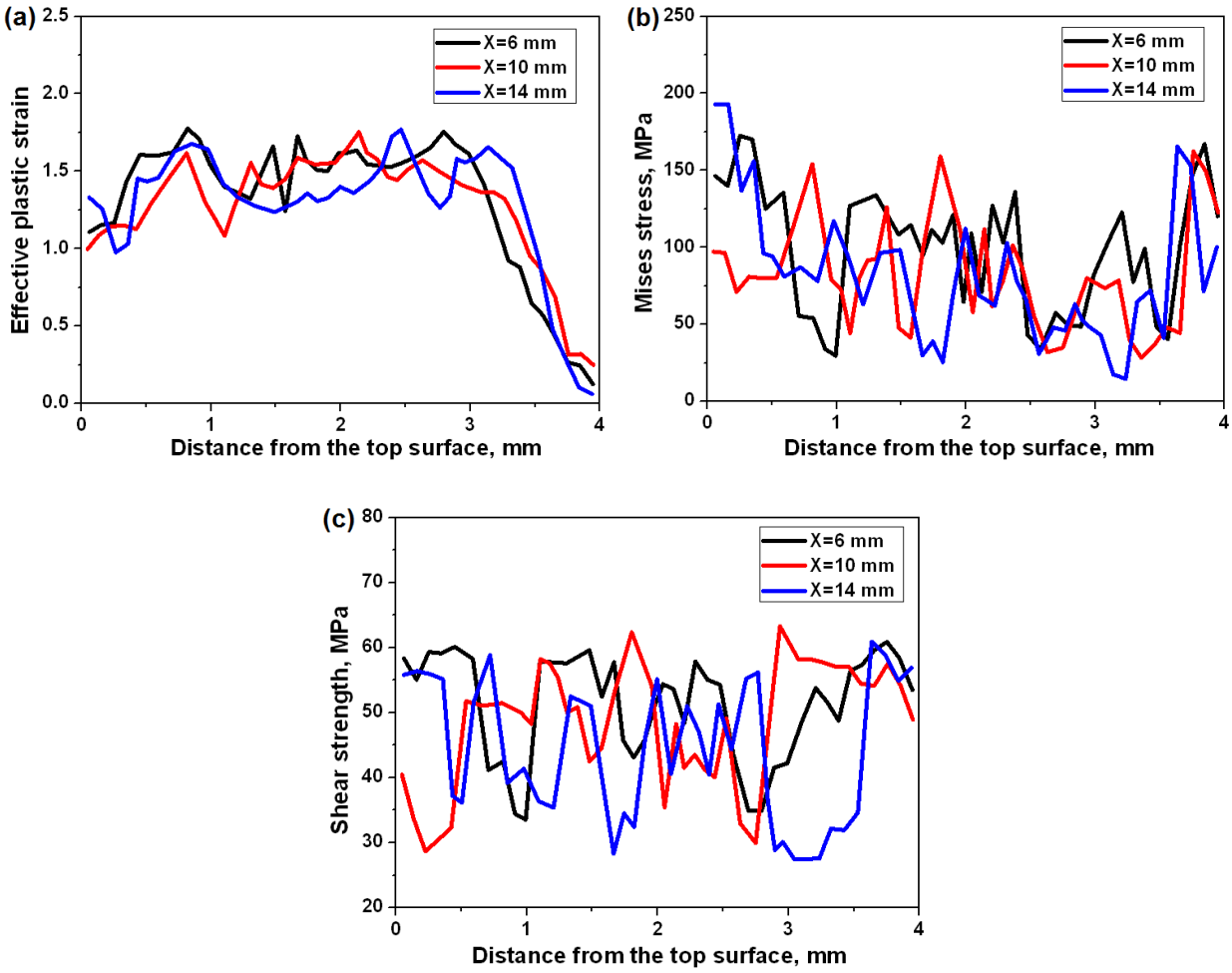

Fig. 7.15 Variation of (a) Effective plastic strain, (b) von Mises stress and (c) Shear strength along the thickness in the ECAP processed aluminium polycrystal.

As shown in Fig. 7.13(a), an inhomogeneous mesh distortion is observed in the deformed polycrystal. Therefore, three planes away from the PDZ at distances of 2 mm, 6 mm, and 10 mm, are compared. These three planes are denoted as X=6, X=10, and X=14, respectively. Fig. 7.15(a) shows the variation of the effective plastic strain along the thickness direction for three planes. The average effective plastic strains are 1.315, 1.1.267 and 1.294, respectively. In contrast, there are more differences between the planes shown in Fig. 7.15(b) for the von Mises stress, and in Fig. 7.15(c) for the shear strength. As can be seen, the planes X=6 and X=14 have the similar trends with more fluctuations than the plane X=10.

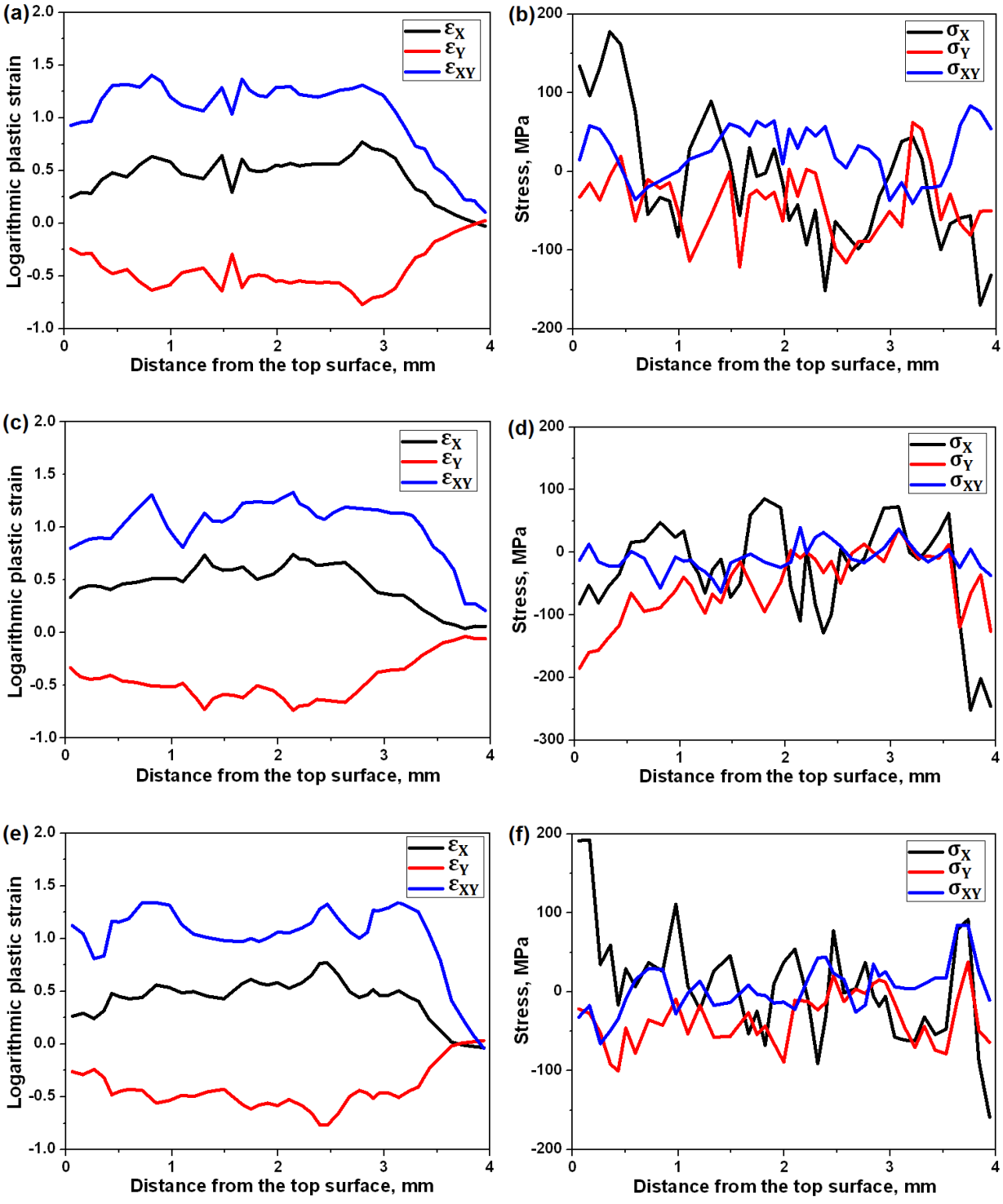

Fig. 7.16 Variation of the logarithmic plastic strains at (a) X=6, (c) X=10, and (e) X=14 and the stress components at (b) X=6, (d) X=10, and (f) X=14 along the thickness in the ECAP processed aluminium polycrystal.

Detailed information on the plastic strain and stress for three selected planes are shown in Fig. 7.16. The strains of three planes are similar and the shear component is larger than the normal components for all these planes. Nearly 75% of the thickness had relatively uniform strains at the plane X=6, as shown in Fig. 7.16(a) and at the plane X=14 in Fig. 7.16(e), while it was about 85% for the planes X=10, as shown in Fig. 7.16(c). At the plane X=6 the strains in the lower quarter are much smaller than the upper three quarters. On the other hand, the stress distributions shown in Fig. 7.16(b), (d) and (f) reveal that the stress state is complicated and different along the thickness. For example at the plane X=6, the stress state is characterized as tension along the X axis close to the top surface and compression along the X axis and shear near the bottom. The stress state at the plane X=14 is similar to the plane X=6, but different to the plane X=10 which is significantly influenced by the formation of shear bands, as shown in Fig. 7.13(a).

The average von Mises stress along the billet thickness has been calculated and it is 98.214 MPa at the plane X=6, 82.465 MPa at the plane X=10, and 81.735 MPa at the plane X=14 respectively as listed in Table 7.2. In addition, the average shear strengths of three planes are 51.055 MPa, 48.219 MPa and 43.823 MPa, respectively. It has been found that the plane X=6 has the largest von Mises stress and shear strength compared to the other two selected planes. For a better understanding of the deformation behavior along the thickness direction in the deformed polycrystal, the deformation inhomogeneity index introduced by Li et al. [142] is calculated for three planes and listed in Table 7.2. The results are consistent with the observation in Fig. 7.13(a) and the plane X=10 has the smallest index due to the least influence of the macro-bands. In contrast, the plane X=14 had the largest deformation heterogeneity index of about 1.319, while a slightly smaller index of about 1.279 is obtained at the plane X=6.

Table 7.2 The list of average values of effective plastic strain ($\bar{\varepsilon}$), von Mises stress ($\bar{\sigma}$), shear strength ($\bar{\tau}_c$), and the deformation inhomegeneity index (C_i) along the billet thickness at three selected planes in the ECAP processed aluminium polycrystal.

Selected planes	$\bar{\varepsilon}$	$\bar{\sigma}$ (MPa)	$\bar{\tau}_c$ (MPa)	C_i
X=6	1.315	98.214	51.055	1.279
X=10	1.267	82.465	48.219	1.188
X=14	1.294	81.735	43.823	1.319

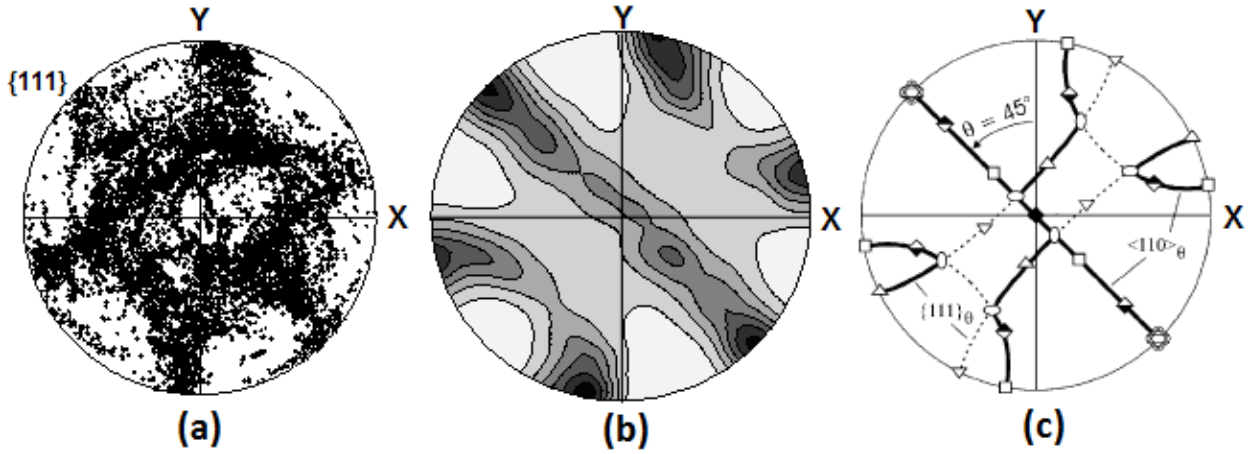

Fig. 7.17 {1 1 1} pole figures of the aluminium polycrystal of (a) CPFEM simulation result, (b) experimental measurement [22] and (c) the main ideal orientations in FCC materials after the ECAP process [31].

Texture evolution of this aluminium polycrystal during the ECAP process has been studied. Fig. 7.17(a) indicates the {1 1 1} pole figure calculated from the CPFEM simulation results and Fig. 7.17(b) shows the experimentally measured {1 1 1} pole figure after the ECAP process of the annealed AA1050. The main ideal orientations of FCC materials after the ECAP process are shown in Fig. 7.17(c) [31]. Comparison of the pole figures in Fig. 7.17(a) and Fig. 7.17(b) indicates that the CPFEM model simulated texture agrees well with the experimental measured texture. As can be seen, both the typical {1 1 1} fiber and <1 1 0> fiber of shear textures shown

in Fig. 7.17(c) for the FCC materials have been observed in the simulated texture and measured texture.

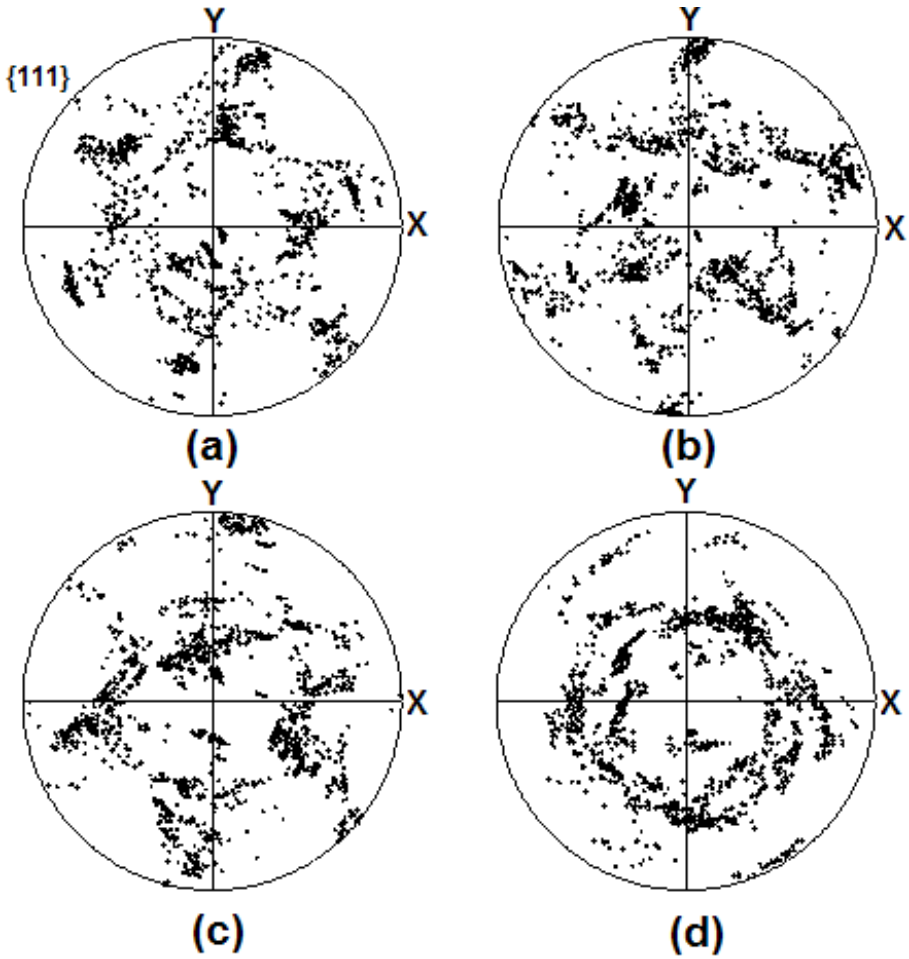

Fig. 7.18 Simulated {1 1 1} pole figures of ECAP processed aluminium polycrystal at four different positions of (a) Position P1, (b) Position P2, (c) Position P3, and (d) Position P4 as marked in Fig. 7.13(a).

In order to study the texture evolution heterogeneity along both the axis of the billet and the billet thickness, eight different positions at two different planes in the deformed billet are selected, as shown in Fig. 7.13(a), to plot the {1 1 1} pole figures. The area of each position is set to 1 mm (along the X axis) by 0.5 mm (along the Y axis).

Fig. 7.18 shows the simulated {1 1 1} pole figures at Positions P1-P4 which are located at the same plane, as shown in Fig. 7.13(a). It is obvious that texture evolution is not uniform along the thickness and there are significant differences among the four {1 1 1} pole figures. In Fig.

7.18(a) for Position P1, the pole figure shows a strong <1 1 0> fiber with slightly a weak {1 1 1} fiber. The <1 1 0> fiber becomes weaker at Position P2 in Fig. 7.18(b), while the {1 1 1} fiber is stronger than P1. In contrast, at Position P3, as shown in Fig. 7.18(c), both fibers can be observed and it is obvious that the {1 1 1} fiber is stronger than the <1 1 0> fiber. It should be noted that texture at Position P4 is different to the other three positions. At Position P4 the ideal shear components disappear and the pole figure indicates the rotated Cube orientation together with scatterings.

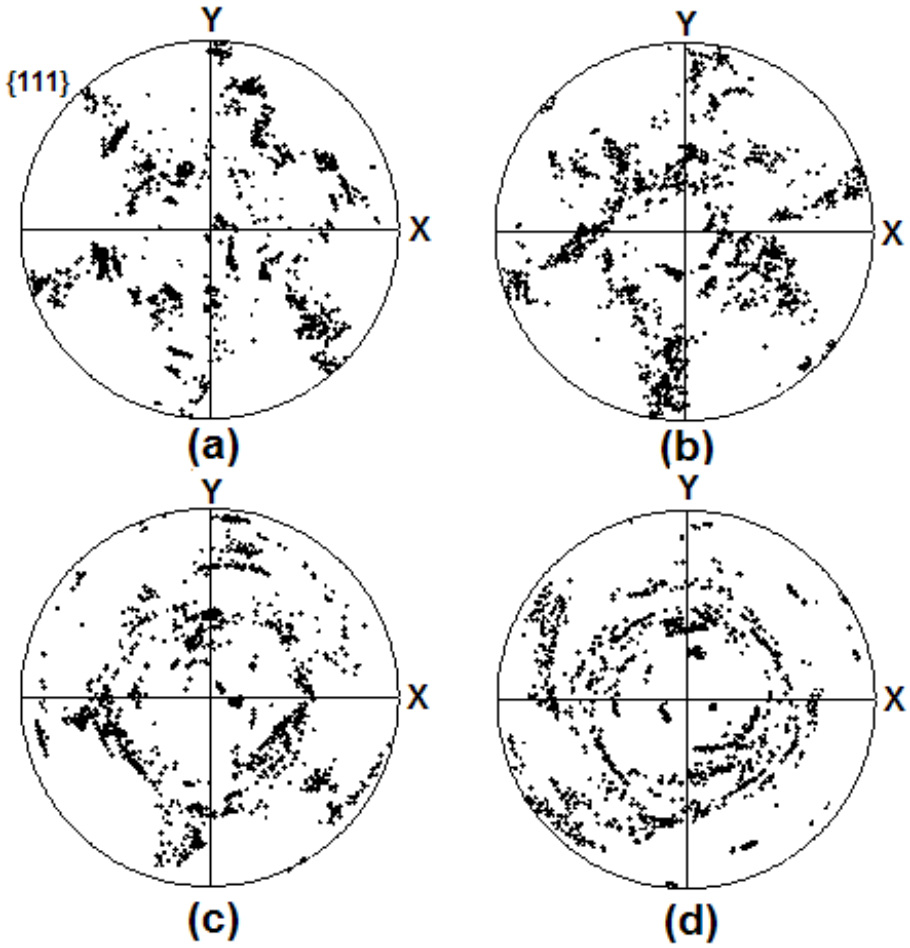

Fig. 7.19 Simulated {1 1 1} pole figures of ECAP processed aluminium polycrystal at four different positions of (a) Position P5, (b) Position P6, (c) Position P7, and (d) Position P8 as marked in Fig. 7.13(a).

Fig. 7.19 shows the simulated {1 1 1} pole figures for Positions P5-P8. It is obvious that an almost ideal shear texture can be observed at Positions P5 and P6, as shown in Fig. 7.19(a-b). At Position P7 in Fig. 7.19(c), the {1 1 1} fiber and <1 1 0> fiber are very weak and the main texture

component is the rotated Cube orientation. The {1 1 1} pole figure at Position P8 is shown in Fig. 7.19(d) where the {1 1 1} fiber and <1 1 0> fiber cannot be seen. Only the rotated Cube orientation with scattering and some other intermediate components appear. The main feature of the {1 1 1} pole figure at Position P8 is similar to P4.

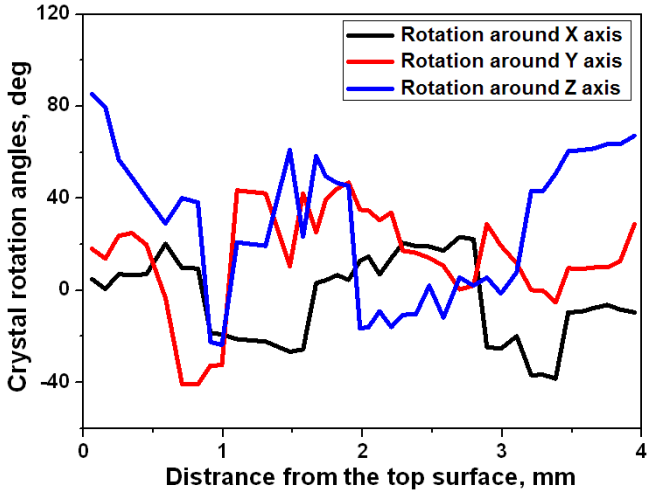

Fig. 7.20 Crystal rotation angles around three axes along the thickness in the ECAP processed aluminium polycrystal at plane X=6.

Fig. 7.20 shows the variation of crystal rotation angles along the thickness direction at the plane X=6. It is obvious that there are very large rotation angles around the Z axis, although there are also large rotations around the X and Y axes. Comparison of Fig. 7.18 and Fig. 7.19 indicates that the largest difference lies in Positions P3 and P7, both of which are located at similar thicknesses, as shown in Fig. 7.13(a). On the other hand there is also a slight difference in the upper regions at Positions P1-P2 and P5-P6, which can be attributed to the inhomogeneous PDZ and development of macro-bands. Therefore, it can be concluded that texture evolution of the aluminium polycrystal is not uniform along both the billet axis and billet thickness during the ECAP process.

7.3 Summary

In this chapter, the following conclusions can be drawn:

(1) According to the CPFEM simulation of aluminium bicrystals, significant influences of grain boundaries on the mesh distortion, development of outer corner gap, PDZ shape, and distribution of plastic stress and strain during the ECAP process have been observed. It has been found that existence of the grain boundary leads to a rapid change of the effective plastic strain, von Mises stress, and shear strength along the thickness of the billet. In addition, the simulated {1 1 1} pole figures reveal that texture evolution is not uniform in both component grains and are relevant to their locations in the ECAP die.

(2) The present study is the first attempt to conduct the simulation of the ECAP process of polycrystal using a crystal plasticity model fully coupled with modeling of the real ECAP process deformation history. The major challenge of such work is the implementation of the realistic information of material, such as grain size, grain shape, and crystallographic orientation into the CPFEM model. In order to validate the simulation, the experiment has been carried out to obtain the initial texture, microstructure and distribution of grain sizes. A Matlab program is used to implement the experimentally measured information into the CPFEM model. It has been found that the simulation results of AA1050 alloy agree well with the experimental results and the theoretical ECAP textures for FCC materials in literature. The deformation and texture evolution are not uniform along both the axis of the billet and the billet thickness in the ECAP processed polycrystal.

Chapter 8 Conclusions and Suggestions for Future Work

8.1 Conclusions

In this work, a CPFEM model of the ECAP process has been developed to simulate the deformation behavior and texture evolution of single crystals, bi-crystals, and polycrystals having FCC structures. It should be noted that the simulations of ECAP of single crystals and bicrystal have never been conducted. The influencing factors such as plane strain assumption, mesh condition, sample dimension, frictional condition, ECAP die geometry and the processing route have been examined in detail. The following conclusions can be drawn:

(1) The crystal plasticity theory and a rate-dependent hardening law were introduced and the development of the CPFEM model by implementing the crystal plasticity constitutive model into the UMAT in a commercial finite element code (Abaqus) was described. For the first time, the CPFEM simulations of the full-scale ECAP processes of aluminium and copper single crystals have been conducted. The simulated results agreed well with the experimental measurements. This indicates that the developed CPFEM model can accurately predict texture evolution during the ECAP process.

(2) The deformation behavior and texture evolution of aluminium single crystals during the ECAP process have been simulated for the first time. It has been found that for the single crystal initially oriented with ideal 'A' orientation, plastic deformation and development of crystallographic orientations were not uniform along the sample thickness. Three-dimensional crystal rotation patterns have been observed and the predominant rotation was found to be around the transverse direction. In addition, three matrix bands were obtained along the thickness connected by two transition bands. The corresponding rotation angles of these matrix bands are 60°, 0°, and 90°, respectively, from the top surface. The slip traces have been studied which revealed that multi-slip could be activated in the large strain gradient region and lattice

rotation dominated the material rotation. In contrast, single dominant slip was the main slip mechanism when the strain gradient was small and the lattice remained at the initial orientation after the deformation. At the bottom of the sample, the deformation was characterized as rigid body rotation due to the presence of the OCA of the ECAP die and development of the corner gaps between the sample and the die. It should be noted that simulation of slip traces during ECAP has never been conducted before.

(3) Comparison of the results of three-dimensional simulation and two-dimensional simulation of the ECAP process indicated that it was reasonable to assume that deformation in the ECAP die with a square cross-section satisfied the plane strain condition. It has been found that the simulated deformation behavior and textures were significantly influenced by the mesh conditions. When the mesh had less than or equal to 2400 elements, the simulations failed to capture the rigid body rotation in the bottom part. Different frictional conditions led to the different PDZs and the coefficient of friction of 0.05 performed best in predicting textures compared to the experimental results. In addition, the plastic deformation and development of crystallographic orientations were strongly influenced by the OCAs and ICRs of the ECAP die, whereas the sample width varying from 2 mm to 40 mm didn't significantly influence the simulation results. Finally, the major research conclusions obtained in the lab-scale tests are applicable for scaling up of the ECAP process for the industrial application.

(4) Simulations revealed similar textures and crystal rotation patterns of copper single crystals to aluminium single crystals during the ECAP process when they had the same initial crystallographic orientation of 'A'. It has been found that the deformation inhomogeneity was strongly influenced by the frictional conditions and the ECAP die channel angles. An obtuse channel angle (ϕ=105° and 135°) led to a larger outer corner gap than an acute channel angle (ϕ=75°) or right angle (ϕ=90°). Besides, initial crystallographic orientation was another important factor influencing the formation of outer corner gap, mesh distortion, distribution of plastic stress and strain, deformation inhomogeneity, and texture evolution and crystal rotation pattern.

(5) A mesh mapping approach is indispensable in the simulations of the multi-pass ECAP processes. It has been proved that the MTMS mapping technique in Abaqus can satisfy the requirement of the multi-pass ECAP simulation. The ECAP processes of aluminium single crystals in Route A and Route C have been successfully simulated for up to four ECAP passes. The results indicated that different slip systems were activated at different ECAP passes in both routes, which led to the different textures. Compared with Route A, Route C had more uniform deformation after even number of ECAP passes. However, Route C had a stronger grain refinement capability than Route A.

(6) CPFEM simulations of the ECAP process of aluminium bi-crystals revealed that grain boundary significantly influence deformation heterogeneity and texture evolution along both the billet axis and the billet thickness. Different PDZ, distribution of plastic stress, strain and shear strength and texture evolution have been obtained by rotating the same bi-crystal 180° around its longitudinal direction. A new construction method of polycrystal structure was introduced which can be used to accurately transfer the experimentally measured texture into simulation model. Based on this method, the ECAP process of an annealed polycrystalline AA1050 alloy has been performed. It has been found that textures were inhomogeneously distributed along both the billet axis and the billet thickness after deformation and crystal rotation patterns were different to those observed in ECAP of single crystals.

8.2 Suggestions for Future Work

The following areas are suggested to be conducted to continue the research from this work.

The experiments and simulations of the bi-crystals during the ECAP process considering the initial crystallographic orientations of the component grains need to be carried out to investigate in depth the influence of grain boundaries with different initial misorientations on the deformation behavior and texture evolutions.

Multi-pass ECAP process of polycrystals needs to be simulated to understand the influence of processing routes and number of ECAP passes on texture evolution, especially Routes Ba and Bc, which cannot be simulated using two-dimensional model.

The CPFEM model has been proved to be a very effective and powerful tool to simulate the deformation behavior and texture evolution of FCC materials during the ECAP process in this work. It is strongly recommended that the fully-coupled CPFEM simulations of the ECAP processes of BCC and HCP materials need to be conducted. The other deformation mechanism such as twinning needs to be considered in the crystal plasticity theory in order to accurately simulate the deformation of the HCP materials.

References

1. Valiev, R.Z. and T.G. Langdon, *Principles of equal-channel angular pressing as a processing tool for grain refinement.* Progress in Materials Science, 2006. **51**(7): p. 881-981.
2. Beyerlein, I.J. and L.S. Tóth, *Texture evolution in equal-channel angular extrusion.* Progress in Materials Science, 2009. **54**(4): p. 427-510.
3. Valiev, R.Z., R.K. Islamgaliev, and I.V. Alexandrov, *Bulk nanostructured materials from severe plastic deformation.* Progress in Materials Science, 2000. **45**(2): p. 103-189.
4. Segal, V.M., *Materials processing by simple shear.* Materials Science and Engineering: A, 1995. **197**(2): p. 157-164.
5. Segal, V.M., *Equal channel angular extrusion: from macromechanics to structure formation.* Materials Science and Engineering: A, 1999. **271**(1–2): p. 322-333.
6. Segal, V.M., *Severe plastic deformation: simple shear versus pure shear.* Materials Science and Engineering: A, 2002. **338**(1–2): p. 331-344.
7. Segal, V.M., K.T. Hartwig, and R.E. Goforth, *In situ composites processed by simple shear.* Materials Science and Engineering: A, 1997. **224**(1–2): p. 107-115.
8. Valiev, R., *Nanostructuring of metals by severe plastic deformation for advanced properties.* Nature Materials, 2004. **3**(8): p. 511-516.
9. Valiev, R.Z., A.V. Korznikov, and R.R. Mulyukov, *Structure and properties of ultrafine-grained materials produced by severe plastic deformation.* Materials Science and Engineering: A, 1993. **168**(2): p. 141-148.
10. Zhilyaev, A.P. and T.G. Langdon, *Using high-pressure torsion for metal processing: Fundamentals and applications.* Progress in Materials Science, 2008. **53**(6): p. 893-979.
11. Yoon, S.C., Z. Horita, and H.S. Kim, *Finite element analysis of plastic deformation behavior during high pressure torsion processing.* Journal of Materials Processing Technology, 2008. **201**(1–3): p. 32-36.
12. Wetscher, F., A. Vorhauer, and R. Pippan, *Strain hardening during high pressure torsion deformation.* Materials Science and Engineering: A, 2005. **410–411**(0): p. 213-216.
13. Kratochvíl, J., M. Kružík, and R. Sedláček, *A model of ultrafine microstructure evolution in materials deformed by high-pressure torsion.* Acta Materialia, 2009. **57**(3): p. 739-748.
14. Khatibi, G., et al., *High cycle fatigue behaviour of copper deformed by high pressure torsion.* International Journal of Fatigue, 2010. **32**(2): p. 269-278.
15. Hebesberger, T., et al., *Structure of Cu deformed by high pressure torsion.* Acta Materialia, 2005. **53**(2): p. 393-402.
16. Degtyarev, M.V., et al., *Influence of the relaxation processes on the structure formation in pure metals and alloys under high-pressure torsion.* Acta Materialia, 2007. **55**(18): p. 6039-6050.
17. Lu, C., K. Tieu, and D. Wexler, *Significant enhancement of bond strength in the accumulative roll bonding process using nano-sized SiO2 particles.* Journal of Materials Processing Technology, 2009. **209**(10): p. 4830-4834.

18. Krallics, G. and J.G. Lenard, *An examination of the accumulative roll-bonding process.* Journal of Materials Processing Technology, 2004. **152**(2): p. 154-161.
19. Saito, Y., et al., *Ultra-fine grained bulk aluminum produced by accumulative roll-bonding (ARB) process.* Scripta Materialia, 1998. **39**(9): p. 1221-1227.
20. Saito, Y., et al., *Novel ultra-high straining process for bulk materials—development of the accumulative roll-bonding (ARB) process.* Acta Materialia, 1999. **47**(2): p. 579-583.
21. Su, L., et al., *Ultrafine grained AA1050/AA6061 composite produced by accumulative roll bonding.* Materials Science and Engineering: A, 2013. **559**(0): p. 345-351.
22. Su, L.H., *Microstructure, texture and vacancy-type defects in severe plastic deformed aluminum alloys.* PhD Dissertation, University of Wollongong, Australia, 2012.
23. Tsuji, N., *Accumulative Roll-Bonding*, in *Encyclopedia of Materials: Science and Technology (Second Edition)*, K.H.J.B. Editors-in-Chief: , et al., Editors. 2011, Elsevier: Oxford. p. 1-8.
24. Lee, J.C., H.K. Seok, and J.Y. Suh, *Microstructural evolutions of the Al strip prepared by cold rolling and continuous equal channel angular pressing.* Acta Materialia, 2002. **50**(16): p. 4005-4019.
25. Saito, Y., et al., *Improvement in the r-value of aluminum strip by a continuous shear deformation process.* Scripta Materialia, 2000. **42**(12): p. 1139-1144.
26. Utsunomiya, H., et al., *Continuous grain refinement of aluminum strip by conshearing.* Materials Science and Engineering: A, 2004. **372**(1–2): p. 199-206.
27. Wei, W., et al., *Finite element analysis of deformation behavior in continuous ECAP process.* Materials Science and Engineering: A, 2009. **516**(1–2): p. 111-118.
28. Richert, M., Q. Liu, and N. Hansen, *Microstructural evolution over a large strain range in aluminium deformed by cyclic-extrusion–compression.* Materials Science and Engineering: A, 1999. **260**(1–2): p. 275-283.
29. Peng, T., Q.D. Wang, and J.B. Lin, *Microstructure and mechanical properties of Mg–10Gd–2Y–0.5Zr alloy recycled by cyclic extrusion compression.* Materials Science and Engineering: A, 2009. **516**(1–2): p. 23-30.
30. Chen, Y.J., et al., *Microstructure evolution in magnesium alloy AZ31 during cyclic extrusion compression.* Journal of Alloys and Compounds, 2008. **462**(1–2): p. 192-200.
31. Li, S., I.J. Beyerlein, and M.A.M. Bourke, *Texture formation during equal channel angular extrusion of fcc and bcc materials: comparison with simple shear.* Materials Science and Engineering: A, 2005. **394**(1–2): p. 66-77.
32. Toth, L.S., *Texture evolution in severe plastic deformation by equal channel angular extrusion.* Advanced Engineering Materials, 2003. **5**(5): p. 308-316.
33. Fukuda, Y., et al., *The application of equal-channel angular pressing to an aluminum single crystal.* Acta Materialia, 2004. **52**(6): p. 1387-1395.
34. Han, W.Z., et al., *Influences of crystallographic orientations on deformation mechanism and grain refinement of Al single crystals subjected to one-pass equal-channel angular pressing.* Acta Materialia, 2007. **55**(17): p. 5889-5900.
35. Han, W., et al., *Materials Science Forum*, Y. Zhao and X. Liao, Editors. 2010. p. 511-525.
36. Han, W.Z., et al., *Evolution of initial grain boundaries and shear bands in Cu bicrystals during one-pass equal-channel angular pressing.* Acta Materialia, 2009. **57**(4): p. 1132-1146.

37. Han, W.Z., et al., *Nature of shear flow lines in equal-channel angular-pressed metals and alloys.* Philosophical Magazine Letters, 2007. **87**(10): p. 735-741.
38. Gu, C.F. and L.S. Tóth, *The origin of strain reversal texture in equal channel angular pressing.* Acta Materialia, 2011. **59**(14): p. 5749-5757.
39. Gu, C.F., L.S. Tóth, and C.H.J. Davies, *Effect of strain reversal on texture and grain refinement in route C equal channel angular pressed copper.* Scripta Materialia, 2011. **65**(2): p. 167-170.
40. Li, S., I.J. Beyerlein, and D.J. Alexander, *Characterization of deformation textures in pure copper processed by equal channel angular extrusion via route A.* Materials Science and Engineering: A, 2006. **431**(1–2): p. 339-345.
41. Li, S., et al., *Texture evolution during multi-pass equal channel angular extrusion of copper: Neutron diffraction characterization and polycrystal modeling.* Acta Materialia, 2005. **53**(7): p. 2111-2125.
42. Li, S., et al., *Effect of processing route on microstructure and texture development in equal channel angular extrusion of interstitial-free steel.* Acta Materialia, 2006. **54**(4): p. 1087-1100.
43. Tóth, L.S., et al., *Analysis of texture evolution in equal channel angular extrusion of copper using a new flow field.* Acta Materialia, 2004. **52**(7): p. 1885-1898.
44. Li, S., *Orientation stability in equal channel angular extrusion. Part II: Hexagonal close-packed materials.* Acta Materialia, 2008. **56**(5): p. 1031-1043.
45. De Messemaeker, J., B. Verlinden, and J. Van Humbeeck, *Texture of IF steel after equal channel angular pressing (ECAP).* Acta Materialia, 2005. **53**(15): p. 4245-4257.
46. Wang, S.C., et al., *Texture evolution by shear on two planes during ECAP of a high-strength aluminum alloy.* Acta Materialia, 2008. **56**(15): p. 3800-3809.
47. Ferrasse, S., et al., *Texture evolution during equal channel angular extrusion: Part I. Effect of route, number of passes and initial texture.* Materials Science and Engineering: A, 2004. **368**(1–2): p. 28-40.
48. Hosseini, E. and M. Kazeminezhad, *The effect of ECAP die shape on nano-structure of materials.* Computational Materials Science, 2009. **44**(3): p. 962-967.
49. Gholinia, A., P. Bate, and P.B. Prangnell, *Modelling texture development during equal channel angular extrusion of aluminium.* Acta Materialia, 2002. **50**(8): p. 2121-2136.
50. Li, S., et al., *Texture evolution during equal channel angular extrusion: Effect of initial texture from experiment and simulation.* Scripta Materialia, 2005. **52**(11): p. 1099-1104.
51. Arruffat-Massion, R., L.S. Tóth, and J.P. Mathieu, *Modeling of deformation and texture development of copper in a 120° ECAE die.* Scripta Materialia, 2006. **54**(9): p. 1667-1672.
52. Skrotzki, W., et al., *Microstructure and texture gradient in copper deformed by equal channel angular pressing.* Acta Materialia, 2007. **55**(6): p. 2013-2024.
53. Tóth, L.S., *Modelling of strain hardening and microstructural evolution in equal channel angular extrusion.* Computational Materials Science, 2005. **32**(3–4): p. 568-576.
54. Jung, K.-H., et al., *Prediction of the effects of hardening and texture heterogeneities by finite element analysis based on the Taylor model.* International Journal of Plasticity, 2013. **42**(0): p. 120-140.

55. Kalidindi, S.R., B.R. Donohue, and S. Li, *Modeling texture evolution in equal channel angular extrusion using crystal plasticity finite element models.* International Journal of Plasticity, 2009. **25**(5): p. 768-779.
56. Li, S., *A crystal plasticity-based explanation for the dependencies of grain refinement on processing route and die angle in equal channel angular extrusion.* Scripta Materialia, 2009. **60**(8): p. 706-709.
57. Li, S., B.R. Donohue, and S.R. Kalidindi, *A crystal plasticity finite element analysis of cross-grain deformation heterogeneity in equal channel angular extrusion and its implications for texture evolution.* Materials Science and Engineering: A, 2008. **480**(1–2): p. 17-23.
58. Li, S., S.R. Kalidindi, and I.J. Beyerlein, *A crystal plasticity finite element analysis of texture evolution in equal channel angular extrusion.* Materials Science and Engineering: A, 2005. **410–411**(0): p. 207-212.
59. Li, S., et al., *Heterogeneity of deformation texture in equal channel angular extrusion of copper.* Acta Materialia, 2004. **52**(16): p. 4859-4875.
60. Li, S., et al., *Microstructure and texture evolution during equal channel angular extrusion of interstitial-free steel: Effects of die angle and processing route.* Acta Materialia, 2007. **55**(3): p. 1017-1032.
61. Wenk, H.R. and P.V. Houtte, *Texture and anisotropy.* Reports on Progress in Physics, 2004. **67**: p. 1367-1428.
62. Zhu, Y.T., T.C. Lowe, and T.G. Langdon, *Performance and applications of nanostructured materials produced by severe plastic deformation.* Scripta Materialia, 2004. **51**(8): p. 825-830.
63. Koch, C.C. and Y.S. Cho, *Nanocrystals by high energy ball milling.* Nanostructured Materials, 1992. **1**(3): p. 207-212.
64. Gleiter, H., *Nanocrystalline materials.* Progress in Materials Science, 1989. **33**(4): p. 223-315.
65. Segal, V.M., *Mechanics of continuous equal-channel angular extrusion.* Journal of Materials Processing Technology, 2010. **210**(3): p. 542-549.
66. Miura, H., G. Yu, and X. Yang, *Multi-directional forging of AZ61Mg alloy under decreasing temperature conditions and improvement of its mechanical properties.* Materials Science and Engineering: A, 2011. **528**(22–23): p. 6981-6992.
67. Nakao, Y. and H. Miura, *Nano-grain evolution in austenitic stainless steel during multi-directional forging.* Materials Science and Engineering: A, 2011. **528**(3): p. 1310-1317.
68. Takayama, A., et al., *Continuous static recrystallization in ultrafine-grained copper processed by multi-directional forging.* Materials Science and Engineering: A, 2008. **478**(1–2): p. 221-228.
69. Richert, J. and M. Richert, *A new method for unlimited deformation of metals and alloys.* Aluminium, 1986. **62**: p. 604-607.
70. Zaharia, L., R. Chelariu, and R. Comaneci, *Multiple direct extrusion: A new technique in grain refinement.* Materials Science and Engineering: A, 2012. **550**(0): p. 293-299.
71. Beygelzimer, Y., et al., *Useful properties of twist extrusion.* Materials Science and Engineering: A, 2009. **503**(1–2): p. 14-17.

72. Latypov, M.I., et al., *Finite element analysis of plastic deformation in twist extrusion.* Computational Materials Science, 2012. **60**(0): p. 194-200.
73. Farhoumand, A., S. Khoddam, and P.D. Hodgson, *A study of plastic deformation during axisymmetric forward spiral extrusion and its subsequent mechanical property changes.* Modelling and Simulation in Materials Science and Engineering, 2012. **20**: p. 085005.
74. Pardis, N. and R. Ebrahimi, *Deformation behavior in Simple Shear Extrusion (SSE) as a new severe plastic deformation technique.* Materials Science and Engineering: A, 2009. **527**(1–2): p. 355-360.
75. Pardis, N. and R. Ebrahimi, *Different processing routes for deformation via simple shear extrusion (SSE).* Materials Science and Engineering: A, 2010. **527**(23): p. 6153-6156.
76. Tork, N.B., N. Pardis, and R. Ebrahimi, *Investigation on the feasibility of room temperature plastic deformation of pure magnesium by simple shear extrusion process.* Materials Science and Engineering: A, 2013. **560**(0): p. 34-39.
77. Tóth, L.S., et al., *Severe plastic deformation of metals by high-pressure tube twisting.* Scripta Materialia, 2009. **60**(3): p. 175-177.
78. Pougis, A., et al., *Stress and strain gradients in high-pressure tube twisting.* Scripta Materialia, 2012. **66**(10): p. 773-776.
79. Arzaghi, M., et al., *Microstructure, texture and mechanical properties of aluminum processed by high-pressure tube twisting.* Acta Materialia, 2012. **60**(11): p. 4393-4408.
80. Zhang, Z. and H.W. Zhang, *Numerical studies on controlling of process parameters in friction stir welding.* Journal of Materials Processing Technology, 2009. **209**(1): p. 241-270.
81. Mishra, R.S. and Z.Y. Ma, *Friction stir welding and processing.* Materials Science and Engineering: R: Reports, 2005. **50**(1–2): p. 1-78.
82. Heurtier, P., et al., *Mechanical and thermal modelling of Friction Stir Welding.* Journal of Materials Processing Technology, 2006. **171**(3): p. 348-357.
83. Cavaliere, P., et al., *2198 Al–Li plates joined by Friction Stir Welding: Mechanical and microstructural behavior.* Materials & Design, 2009. **30**(9): p. 3622-3631.
84. Zhao, X., et al., *A new SPD process for spheroidal cast iron.* Materials Letters, 2004. **58**(19): p. 2335-2339.
85. Wang, W., et al., *Properties of a gray cast iron with oriented graphite flakes.* Journal of Materials Processing Technology, 2007. **182**(1–3): p. 593-597.
86. Wang, J.T., et al., *Principles of severe plastic deformation using tube high-pressure shearing.* Scripta Materialia, 2012. **67**(10): p. 810-813.
87. Zhilyaev, A.P., et al., *Experimental parameters influencing grain refinement and microstructural evolution during high-pressure torsion.* Acta Materialia, 2003. **51**(3): p. 753-765.
88. Bridgman, P.W., *On Torsion Combined with Compression.* Journal of Applied Physics, 1943. **14**: p. 273-283.
89. Zhilyaev, A.P., et al., *Microhardness and microstructural evolution in pure nickel during high-pressure torsion.* Scripta Materialia, 2001. **44**(12): p. 2753-2758.
90. Xu, C., Z. Horita, and T.G. Langdon, *The evolution of homogeneity in processing by high-pressure torsion.* Acta Materialia, 2007. **55**(1): p. 203-212.

91. Reza Toroghinejad, M., F. Ashrafizadeh, and R. Jamaati, *On the use of accumulative roll bonding process to develop nanostructured aluminum alloy 5083.* Materials Science and Engineering: A, 2013. **561**(0): p. 145-151.
92. Valiev, R.Z., et al., *Producing bulk ultrafine-grained materials by severe plastic deformation.* Jom, 2006. **58**(4): p. 33-39.
93. Berbon, P.B., et al., *Influence of pressing speed on microstructural development in equal-channel angular pressing.* Metallurgical and Materials Transactions a-Physical Metallurgy and Materials Science, 1999. **30**(8): p. 1989-1997.
94. Komura, S., et al., *Influence of stacking fault energy on microstructural development in equal-channel angular pressing.* Journal of Materials Research, 1999. **14**(10): p. 4044-4050.
95. Qu, S., et al., *Microstructural evolution and mechanical properties of Cu–Al alloys subjected to equal channel angular pressing.* Acta Materialia, 2009. **57**(5): p. 1586-1601.
96. Furukawa, M., Z. Horita, and T.G. Langdon, *Microstructures of Aluminum and Copper Single Crystals Processed by Equal-Channel Angular Pressing*, in *Thermec 2009, Pts 1-4*, T. Chandra, et al., Editors. 2010. p. 1946-1951.
97. Nakashima, K., et al., *Influence of channel angle on the development of ultrafine grains in equal-channel angular pressing.* Acta Materialia, 1998. **46**(5): p. 1589-1599.
98. Huang, W.H., et al., *Effect of die angle on the deformation texture of copper processed by equal channel angular extrusion.* Materials Science and Engineering: A, 2001. **307**(1–2): p. 113-118.
99. Iwahashi, Y., et al., *The process of grain refinement in equal-channel angular pressing.* Acta Materialia, 1998. **46**(9): p. 3317-3331.
100. Li, S., I.J. Beyerlein, and C.T. Necker, *On the development of microstructure and texture heterogeneity in ECAE via route C.* Acta Materialia, 2006. **54**(5): p. 1397-1408.
101. Yamaguchi, D., et al., *Significance of adiabatic heating in equal-channel angular pressing.* Scripta Materialia, 1999. **41**(8): p. 791-796.
102. Chen, Y.C., et al., *The effect of extrusion temperature on the development of deformation microstructures in 5052 aluminium alloy processed by equal channel angular extrusion.* Acta Materialia, 2003. **51**(7): p. 2005-2015.
103. Yamashita, A., et al., *Influence of pressing temperature on microstructural development in equal-channel angular pressing.* Materials Science and Engineering: A, 2000. **287**(1): p. 100-106.
104. Iwahashi, Y., et al., *Principle of equal-channel angular pressing for the processing of ultra-fine grained materials.* Scripta Materialia, 1996. **35**(2): p. 143-146.
105. Nakashima, K., et al., *Development of a multi-pass facility for equal-channel angular pressing to high total strains.* Materials Science and Engineering: A, 2000. **281**(1–2): p. 82-87.
106. Furukawa, M., et al., *The shearing characteristics associated with equal-channel angular pressing.* Materials Science and Engineering: A, 1998. **257**(2): p. 328-332.
107. Liu, Z.Y., et al., *The effect of cumulative large plastic strain on the structure and properties of a Cu–Zn alloy.* Materials Science and Engineering: A, 1998. **242**(1–2): p. 137-140.

108. Raab, G.I., *Plastic flow at equal channel angular processing in parallel channels.* Materials Science and Engineering: A, 2005. **410–411**(0): p. 230-233.
109. Liu, Z.Y. and Z.J. Wang, *Finite-element analysis of the load of equal-cross-section lateral extrusion.* Journal of Materials Processing Technology, 1999. **94**(2–3): p. 193-196.
110. Nishida, Y., et al., *Rotary-die equal-channel angular pressing of an Al – 7 mass% Si – 0.35 mass% Mg alloy.* Scripta Materialia, 2001. **45**(3): p. 261-266.
111. Ma, A., et al., *Impact toughness of an ultrafine-grained Al–11mass%Si alloy processed by rotary-die equal-channel angular pressing.* Acta Materialia, 2005. **53**(1): p. 211-220.
112. Ma, A., et al., *Characteristics of plastic deformation by rotary-die equal-channel angular pressing.* Scripta Materialia, 2005. **52**(6): p. 433-437.
113. Azushima, A. and K. Aoki, *Properties of ultrafine-grained steel by repeated shear deformation of side extrusion process.* Materials Science and Engineering: A, 2002. **337**(1–2): p. 45-49.
114. Lee, J.-C., et al., *Controlling the textures of the metal strips via the continuous confined strip shearing(C2S2) process.* Materials Research Bulletin, 2001. **36**(5–6): p. 997-1004.
115. Park, J.-W., J.-W. Kim, and Y.-H. Chung, *Grain refinement of steel plate by continuous equal-channel angular process.* Scripta Materialia, 2004. **51**(2): p. 181-184.
116. Arzaghi, M., B. Beausir, and L.S. Tóth, *Contribution of non-octahedral slip to texture evolution of fcc polycrystals in simple shear.* Acta Materialia, 2009. **57**(8): p. 2440-2453.
117. Li, C.K.Y., Z.Y. Xia, and H.J. Sue, *Simple shear plastic deformation behavior of polycarbonate plate II. Mechanical property characterization.* Polymer, 2000. **41**(16): p. 6285-6293.
118. Mahesh, S., I.J. Beyerlein, and C.N. Tomé, *Loading- and substructure-induced irreversibility in texture during route C equal channel angular extrusion.* Scripta Materialia, 2005. **53**(8): p. 965-969.
119. Oh-ishi, K., A.P. Zhilyaev, and T.R. McNelley, *Effect of strain path on evolution of deformation bands during ECAP of pure aluminum.* Materials Science and Engineering: A, 2005. **410–411**(0): p. 183-187.
120. Wu, P.D., Y. Huang, and D.J. Lloyd, *Studying grain fragmentation in ECAE by simulating simple shear.* Scripta Materialia, 2006. **54**(12): p. 2107-2112.
121. Segal, V.M., *Slip line solutions, deformation mode and loading history during equal channel angular extrusion.* Materials Science and Engineering: A, 2003. **345**(1–2): p. 36-46.
122. Altan, B.S., G. Purcek, and I. Miskioglu, *An upper-bound analysis for equal-channel angular extrusion.* Journal of Materials Processing Technology, 2005. **168**(1): p. 137-146.
123. Beyerlein, I.J. and C.N. Tomé, *Analytical modeling of material flow in equal channel angular extrusion (ECAE).* Materials Science and Engineering: A, 2004. **380**(1–2): p. 171-190.
124. Eivani, A.R. and A. Karimi Taheri, *An upper bound solution of ECAE process with outer curved corner.* Journal of Materials Processing Technology, 2007. **182**(1–3): p. 555-563.
125. Hasani, A. and L.S. Tóth, *A fan-type flow-line model in equal channel angular extrusion.* Scripta Materialia, 2009. **61**(1): p. 24-27.
126. Luis Pérez, C.J., *On the correct selection of the channel die in ECAP processes.* Scripta Materialia, 2004. **50**(3): p. 387-393.

127. Luis Pérez, C.J., *Upper bound analysis and FEM simulation of equal fillet radii angular pressing.* Modelling and Simulation in Materials Science and Engineering, 2004. **12**: p. 205-214.
128. Luri, R., et al., *A new configuration for equal channel angular extrusion dies.* Journal of Manufacturing Science and Engineering, Transactions of the ASME, 2006. **128**(4): p. 860-865.
129. Milind, T.R. and P.P. Date, *Analytical and finite element modeling of strain generated in equal channel angular extrusion.* International Journal of Mechanical Sciences, 2012. **56**(1): p. 26-34.
130. Reihanian, M., R. Ebrahimi, and M.M. Moshksar, *Upper-bound analysis of equal channel angular extrusion using linear and rotational velocity fields.* Materials & Design, 2009. **30**(1): p. 28-34.
131. Silva, F.R.F., et al., *Upper-bound and finite-element analyses of non-isothermal ECAP.* Materials Science and Engineering: A, 2012. **546**(0): p. 180-188.
132. Talebanpour, B. and R. Ebrahimi, *Upper-bound analysis of dual equal channel lateral extrusion.* Materials & Design, 2009. **30**(5): p. 1484-1489.
133. Zhernakov, V.S., et al., *A numerical modelling and investigations of flow stress and grain refinement during equal-channel angular pressing.* Scripta Materialia, 2001. **44**(8–9): p. 1765-1769.
134. Wu, Y. and I. Baker, *An experimental study of equal channel angular extrusion.* Scripta Materialia, 1997. **37**(4): p. 437-442.
135. Shan, A., et al., *Direct observation of shear deformation during equal channel angular pressing of pure aluminum.* Scripta Materialia, 1999. **41**(4): p. 353-357.
136. Manna, R., et al., *Physical modeling of equal channel angular pressing using plasticine.* Scripta Materialia, 2005. **53**(12): p. 1357-1361.
137. Kamachi, M., et al., *A model investigation of the shearing characteristics in equal-channel angular pressing.* Materials Science and Engineering: A, 2003. **347**(1–2): p. 223-230.
138. Han, W.Z., et al., *Investigation on the geometrical aspect of deformation during equal-channel angular pressing by in-situ physical modeling experiments.* Materials Science and Engineering: A, 2008. **476**(1–2): p. 224-229.
139. Prangnell, P.B., C. Harris, and S.M. Roberts, *Finite element modelling of equal channel angular extrusion.* Scripta Materialia, 1997. **37**(7): p. 983-989.
140. Bowen, J.R., et al., *Analysis of the billet deformation behaviour in equal channel angular extrusion.* Materials Science and Engineering: A, 2000. **287**(1): p. 87-99.
141. Yang, Y.-L. and S. Lee, *Finite element analysis of strain conditions after equal channel angular extrusion.* Journal of Materials Processing Technology, 2003. **140**(1–3): p. 583-587.
142. Li, S., et al., *Finite element analysis of the plastic deformation zone and working load in equal channel angular extrusion.* Materials Science and Engineering: A, 2004. **382**(1–2): p. 217-236.
143. Wei, W., et al., *Origin of inhomogenous behavior during equal channel angular pressing.* Scripta Materialia, 2006. **54**(11): p. 1865-1869.

144. Balasundar, I. and T. Raghu, *Effect of friction model in numerical analysis of equal channel angular pressing process.* Materials & Design, 2010. **31**(1): p. 449-457.
145. Mahallawy, N.E., et al., *3D FEM simulations for the homogeneity of plastic deformation in Al–Cu alloys during ECAP.* Materials Science and Engineering: A, 2010. **527**(6): p. 1404-1410.
146. Jin, Y.G., et al., *Three-dimensional finite element analysis of multi-pass equal-channel angular extrusion of aluminum AA1050 with split dies.* Materials Science and Engineering: A, 2009. **503**(1–2): p. 152-155.
147. Djavanroodi, F. and M. Ebrahimi, *Effect of die channel angle, friction and back pressure in the equal channel angular pressing using 3D finite element simulation.* Materials Science and Engineering: A, 2010. **527**(4–5): p. 1230-1235.
148. Jiang, H., Z. Fan, and C. Xie, *3D finite element simulation of deformation behavior of CP-Ti and working load during multi-pass equal channel angular extrusion.* Materials Science and Engineering: A, 2008. **485**(1–2): p. 409-414.
149. Lu, S.K., et al., *3D FEM simulations for the homogeneity of plastic deformation in aluminum alloy HS6061-T6 during ECAP.* Procedia Engineering, 2011. **12**(0): p. 35-40.
150. Suo, T., et al., *The simulation of deformation distribution during ECAP using 3D finite element method.* Materials Science and Engineering: A, 2006. **432**(1–2): p. 269-274.
151. Kim, W.J. and J.C. Namkung, *Computational analysis of effect of route on strain uniformity in equal channel angular extrusion.* Materials Science and Engineering: A, 2005. **412**(1–2): p. 287-297.
152. Zhernakov, V.S., et al., *Comparison of the plastic strain distribution during equal-channel angular pressing (ECAP) using 2D and 3D FEM modeling.* International Journal of Materials Research, 2007. **98**: p. 178-183.
153. Engler, O. and V. Randle, *Introduction to Texture Analysis: Macrotexture, Microtexture and Orientation Mapping-Second Edition.* CRC Press, 2010.
154. Bunge, H.J., *Texture Analysis in Materials Science Mathematical Methods.* Butterworths, 1982.
155. El-Danaf, E.A., *Mechanical properties, microstructure and texture of single pass equal channel angular pressed 1050, 5083, 6082 and 7010 aluminum alloys with different dies.* Materials & Design, 2011. **32**(7): p. 3838-3853.
156. Ferrasse, S., V.M. Segal, and F. Alford, *Effect of additional processing on texture evolution of Al0.5Cu alloy processed by equal channel angular extrusion (ECAE).* Materials Science and Engineering: A, 2004. **372**(1–2): p. 44-55.
157. Fukuda, Y., et al., *Influence of crystal orientation on ECAP of aluminum single crystals.* Materials Science and Engineering: A, 2006. **420**(1–2): p. 79-86.
158. Furukawa, M., et al., *An investigation of deformation in aluminum single crystals using equal-channel angular pressing*, in *Thermec'2003, Pts 1-5*, T. Chandra, J.M. Torralba, and T. Sakai, Editors. 2003. p. 2711-2716.
159. Furukawa, M., Z. Horita, and T.G. Langdon, *Application of equal-channel angular pressing to aluminum and copper single crystals*, in *THERMEC 2006, Pts 1-5*, T. Chandra, et al., Editors. 2007. p. 2853-2858.

160. Furukawa, M., Z. Horita, and T.G. Langdon, *Principles of deformation in single crystals of two different orientations processed by equal-channel angular pressing.* Materials Science and Engineering: A, 2009. **503**(1–2): p. 21-27.
161. Furukawa, M., et al., *An investigation of the deformation process during equal-channel angular pressing of an aluminum single crystal.* Materials Science and Engineering: A, 2005. **410–411**(0): p. 194-200.
162. Han, J.-H., et al., *Effects of the deformation history and the initial textures on the texture evolution in an Al alloy strip during the shear deforming process.* Acta Materialia, 2004. **52**(16): p. 4907-4918.
163. Han, W.Z., et al., *Response to comments on "Influences of crystallographic orientations on deformation mechanism and grain refinement of Al single crystals subjected to one-pass equal-channel angular pressing".* Scripta Materialia, 2008. **59**(4): p. 385-386.
164. Han, W.Z., et al., *Reply to comments on "Influences of crystallographic orientations on deformation mechanism and grain refinement of Al single crystals subjected to one-pass equal-channel angular pressing".* Scripta Materialia, 2008. **59**(4): p. 421-423.
165. Han, W.Z., et al., *Corrigendum to "Influences of crystallographic orientations on deformation mechanism and grain refinement of Al single crystals subjected to one-pass equal-channel angular pressing" [Acta Mater 55 (2007) 5889–5900].* Acta Materialia, 2008. **56**(9): p. 2163.
166. Langdon, T.G., *The principles of grain refinement in equal-channel angular pressing.* Materials Science and Engineering a-Structural Materials Properties Microstructure and Processing, 2007. **462**(1-2): p. 3-11.
167. Li, S., *Orientation stability in equal channel angular extrusion. Part I: Face-centered cubic and body-centered cubic materials.* Acta Materialia, 2008. **56**(5): p. 1018-1030.
168. Li, S., *Comments on "Influences of crystallographic orientations on deformation mechanism and grain refinement of Al single crystals subjected to one-pass equal-channel angular pressing".* Scripta Materialia, 2008. **59**(4): p. 418-420.
169. Park, J.Y. and D.N. Lee, *Deformation and annealing textures of equal-channel angular pressed 1050 Al alloy strips.* Materials Science and Engineering: A, 2008. **497**(1–2): p. 395-407.
170. Suwas, S., et al., *Evolution of texture during equal channel angular extrusion of commercially pure aluminum: Experiments and simulations.* Materials Science and Engineering: A, 2009. **520**(1–2): p. 134-146.
171. Zhilyaev, A.P., et al., *Microtexture and microstructure evolution during processing of pure aluminum by repetitive ECAP.* Materials Science and Engineering: A, 2006. **429**(1–2): p. 137-148.
172. Goran, D., et al., *Local texture and microstructure in cube-oriented nickel single crystal deformed by equal channel angular extrusion.* Philosophical Magazine, 2011. **91**(2): p. 291-309.
173. Goran, D., et al., *Pure Ni single crystal of cube orientation deformed by equal channel angular extrusion*, in *Texture and Anisotropy of Polycrystals Ii*, C. Esling, et al., Editors. 2005. p. 333-338.

174. Goran, D., et al., *Heterogeneity of deformation in pure Ni single crystal of cube orientation deformed by equal channel angular extrusion*, in *Icotom 14: Textures of Materials, Pts 1and 2*, P.V. Houtte and L. Kestens, Editors. 2005. p. 833-838.
175. Grosdidier, T., et al., *On microstructure and texture heterogeneities in single crystals deformed by equal channel angular extrusion.* Scripta Materialia, 2008. **59**(10): p. 1087-1090.
176. Skrotzki, W., et al., *Texture after ECAP of a cube-oriented Ni single crystal.* Acta Materialia, 2008. **56**(14): p. 3439-3449.
177. Sandim, H.R.Z., et al., *Equal channel angular extrusion of niobium single crystals.* Materials Science and Engineering: A, 2007. **467**(1–2): p. 44-52.
178. Zhu, L.A., et al., *EBSD characterization of an ECAP deformed Nb single crystal.* Journal of Materials Science, 2010. **45**(17): p. 4672-4681.
179. Fukuda, Y., et al., *Influence of crystal orientation on the processing of copper single crystals by ECAP.* Journal of Materials Science, 2007. **42**(5): p. 1501-1511.
180. Furukawa, M., et al., *An investigation of deformation in copper single crystals using equal-channel angular pressing*, in *Nanomaterials by Severe Plastic Deformation*, Z. Horita, Editor. 2006. p. 113-118.
181. Furukawa, M., Z. Horita, and T.G. Langdon, *Principles of deformation in single crystals of two different orientations processed by equal-channel angular pressing.* Materials Science and Engineering a-Structural Materials Properties Microstructure and Processing, 2009. **503**(1-2): p. 21-27.
182. Gazder, A.A., et al., *Progressive texture evolution during equal channel angular extrusion.* Materials Science and Engineering: A, 2006. **437**(2): p. 259-267.
183. Han, W.Z., et al., *Orientation Design for Enhancing Deformation Twinning in Cu Single Crystal Subjected to Equal Channel Angular Pressing.* Advanced Engineering Materials, 2008. **10**(12): p. 1110-1113.
184. Haouaoui, M., K.T. Hartwig, and E. Andrew Payzant, *Effect of strain path on texture and annealing microstructure development in bulk pure copper processed by simple shear.* Acta Materialia, 2005. **53**(3): p. 801-810.
185. Katayama, S., et al., *Influence of a slip plane orientation with respect to the shear plane of ECAP on microstructure of copper single crystal subject to one pressing at room temperature*, in *Nanomaterials by Severe Plastic Deformation Iv, Pts 1 and 2*, Y. Estrin and H.J. Maier, Editors. 2008. p. 387-392.
186. Miyamoto, H., et al., *Deformation structure and crystal orientation of copper single crystals deformed by equal channel angular pressing*, in *Thermec'2003, Pts 1-5*, T. Chandra, J.M. Torralba, and T. Sakai, Editors. 2003. p. 2795-2800.
187. Miyamoto, H., et al., *Microstructure and texture development of copper single crystals deformed by equal-channel angular pressing.* Philosophical Magazine Letters, 2004. **84**(4): p. 235-243.
188. Miyamoto, H., et al., *Reversible nature of shear bands in copper single crystals subjected to iterative shear of ECAP in forward and reverse directions.* Materials Science and Engineering: A, 2011. **528**(6): p. 2602-2609.

189. Salimyanfard, F., et al., *Textural evaluation of copper produced by equal channel angular pressing with routes A and B30.* Materials Science and Engineering: A, 2010. **527**(23): p. 6260-6269.
190. Salimyanfard, F., et al., *Investigation of texture and mechanical properties of copper processed by new route of equal channel angular pressing.* Materials & Design, 2013. **44**(0): p. 374-381.
191. Gazder, A.A., et al., *Microstructure and texture evolution of bcc and fcc metals subjected to equal channel angular extrusion.* Materials Science and Engineering: A, 2006. **415**(1–2): p. 126-139.
192. Li, S., *Orientation stability in equal-channel angular extrusion of body-centered cubic materials by {110}<111> and {112}<111> slip.* Materials Science and Engineering: A, 2009. **503**(1–2): p. 118-121.
193. Li, S., *Dependencies of grain refinement on processing route and die angle in equal channel angular extrusion of bcc materials.* Computational Materials Science, 2009. **46**(4): p. 1044-1050.
194. Al-Maharbi, M., et al., *Microstructure, crystallographic texture, and plastic anisotropy evolution in an Mg alloy during equal channel angular extrusion processing.* Materials Science and Engineering: A, 2011. **528**(25–26): p. 7616-7627.
195. Beausir, B., et al., *Analysis of texture evolution in magnesium during equal channel angular extrusion.* Acta Materialia, 2008. **56**(2): p. 200-214.
196. Kim, H.K. and W.J. Kim, *Microstructural instability and strength of an AZ31 Mg alloy after severe plastic deformation.* Materials Science and Engineering: A, 2004. **385**(1–2): p. 300-308.
197. Koike, J., et al., *The activity of non-basal slip systems and dynamic recovery at room temperature in fine-grained AZ31B magnesium alloys.* Acta Materialia, 2003. **51**(7): p. 2055-2065.
198. Seda, P., A. Jager, and P. Lejcek, *Microstructure and Texture of Magnesium Single Crystals Processed by ECAP*, in *Nanomaterials by Severe Plastic Deformation: Nanospd5, Pts 1 and 2*, J.T. Wang, R.B. Figueiredo, and T.G. Langdon, Editors. 2011. p. 355-360.
199. Seda, P., et al., *Texture evolution in oriented magnesium single crystals processed by equal channel angular pressing.* Philosophical Magazine, 2012. **92**(10): p. 1223-1237.
200. Zhang, X.-h., S.-j. Luo, and Z.-m. Du, *Uniformity and continuity of effective strain in AZ91D processed by multi-pass equal channel angular extrusion.* Transactions of Nonferrous Metals Society of China, 2008. **18**(1): p. 92-98.
201. Boulahia, R., et al., *Deformation behaviour and mechanical properties of polypropylene processed by equal channel angular extrusion: Effects of back-pressure and extrusion velocity.* Polymer, 2009. **50**(23): p. 5508-5517.
202. Stolyarov, V.V., et al., *Influence of ECAP routes on the microstructure and properties of pure Ti.* Materials Science and Engineering: A, 2001. **299**(1–2): p. 59-67.
203. Stolyarov, V.V., et al., *Microstructure and properties of pure Ti processed by ECAP and cold extrusion.* Materials Science and Engineering: A, 2001. **303**(1–2): p. 82-89.
204. Fukuda, Y., et al., *Influence of crystal orientation on ECAP of aluminum single crystals.* Materials Science and Engineering a-Structural Materials Properties Microstructure and Processing, 2006. **420**(1-2): p. 79-86.

205. Taylor, G.I., *Plastic strain in metals.* Journal of the Institute of Metals, 1938. **62**: p. 307-324.
206. Canova, G.R., U.F. Kocks, and J.J. Jonas, *Theory of torsion texture development.* Acta Metallurgica, 1984. **32**(2): p. 211-226.
207. Raphanel, J.L. and P. Van Houtte, *Simulation of the rolling textures of b.c.c. metals by means of the relaxed taylor theory.* Acta Metallurgica, 1985. **33**(8): p. 1481-1488.
208. Kocks, U.F. and H. Chandra, *Slip geometry in partially constrained deformation.* Acta Metallurgica, 1982. **30**(3): p. 695-709.
209. Lebensohn, R.A. and C.N. Tomé, *A self-consistent anisotropic approach for the simulation of plastic deformation and texture development of polycrystals: Application to zirconium alloys.* Acta Metallurgica et Materialia, 1993. **41**(9): p. 2611-2624.
210. Pithan, C., et al., *Microstructure and texture evolution in ECAE processed A5056.* Materials Science and Engineering: A, 2000. **280**(1): p. 62-68.
211. Suh, J.-Y., et al., *Effect of deformation histories on texture evolution during equal- and dissimilar-channel angular pressing.* Scripta Materialia, 2003. **49**(2): p. 185-190.
212. Yapici, G.G., I. Karaman, and H.J. Maier, *Mechanical flow anisotropy in severely deformed pure titanium.* Materials Science and Engineering: A, 2006. **434**(1–2): p. 294-302.
213. Mishra, A., et al., *High-strain-rate response of ultra-fine-grained copper.* Acta Materialia, 2008. **56**(12): p. 2770-2783.
214. Gubicza, J., et al., *Correlation between microstructure and mechanical properties of severely deformed metals.* Journal of Alloys and Compounds, 2009. **483**(1–2): p. 271-274.
215. Tóth, L.S., et al., *A model of grain fragmentation based on lattice curvature.* Acta Materialia, 2010. **58**(5): p. 1782-1794.
216. Hill, R., *Continuum micro-mechanics of elastoplastic polycrystals.* Journal of the Mechanics and Physics of Solids, 1965. **13**(2): p. 89-101.
217. Hutchinson, J.W., *Elastic-plastic behavior of polycrystalline metals and composites.* Proceedings of the Royal Society of London Series a-Mathematical and Physical Sciences, 1970. **319**: p. 247-272.
218. Iwakuma, T. and S. Nemat-Nasser, *Finite elastic-plastic deformation of polycrystalline metals.* Proceedings of the Royal Society of London Series a-Mathematical and Physical Sciences, 1984. **394**: p. 87-119.
219. Molinari, A., G.R. Canova, and S. Ahzi, *A self consistent approach of the large deformation polycrystal viscoplasticity.* Acta Metallurgica, 1987. **35**(12): p. 2983-2994.
220. Beyerlein, I.J., R.A. Lebensohn, and C.N. Tomé, *Modeling texture and microstructural evolution in the equal channel angular extrusion process.* Materials Science and Engineering: A, 2003. **345**(1–2): p. 122-138.
221. Beyerlein, I.J. and C.N. Tome, *Modeling compression reloads in copper prestrained by equal channel angular extrusion (ECAE).* Materialwissenschaft Und Werkstofftechnik, 2005. **36**(10): p. 541-545.
222. Agnew, S.R., D.W. Brown, and C.N. Tome, *Validating a polycrystal model for the elastoplastic response of magnesium alloy AZ31 using in situ neutron diffraction.* Acta Materialia, 2006. **54**(18): p. 4841-4852.

223. Yapici, G.G., I. Karaman, and Z.-P. Luo, *Mechanical twinning and texture evolution in severely deformed Ti–6Al–4V at high temperatures.* Acta Materialia, 2006. **54**(14): p. 3755-3771.
224. Beyerlein, I.J., D.J. Alexander, and C.N. Tome, *Plastic anisotropy in aluminum and copper pre-strained by equal channel angular extrusion.* Journal of Materials Science, 2007. **42**(5): p. 1733-1750.
225. Beyerlein, I.J., et al., *Role of twinning on texture evolution of silver during equal channel angular extrusion.* Philosophical Magazine, 2007. **87**(6): p. 885-906.
226. Kommel, L., I. Hussainova, and O. Volobueva, *Microstructure and properties development of copper during severe plastic deformation.* Materials & Design, 2007. **28**(7): p. 2121-2128.
227. Cazacu, O. and I.R. Ionescu, *Augmented Lagrangian method for Eulerian modeling of viscoplastic crystals.* Computer Methods in Applied Mechanics and Engineering, 2010. **199**(9–12): p. 689-699.
228. Figueiredo, R.B., et al., *Evolution of texture in a magnesium alloy processed by ECAP through dies with different angles.* Materials Science and Engineering: A, 2010. **527**(7–8): p. 1709-1718.
229. Suwas, S., et al., *Texture evolution in commercially pure titanium after warm equal channel angular extrusion.* Acta Materialia, 2011. **59**(3): p. 1121-1133.
230. Ostapovets, A., et al., *New misorientation scheme for a visco-plastic self-consistent model: Equal channel angular pressing of magnesium single crystals.* International Journal of Plasticity, 2012. **29**(0): p. 1-12.
231. Roters, F., et al., *Overview of constitutive laws, kinematics, homogenization and multiscale methods in crystal plasticity finite-element modeling: Theory, experiments, applications.* Acta Materialia, 2010. **58**(4): p. 1152-1211.
232. Roters, F., et al., *Crystal Plasticity Finite Element Methods in Materials Science and Engineering.* Wiley-VCH, 2010.
233. Si, L.Y., et al., *Simulation of rolling behaviour of cubic oriented al single crystal with crystal plasticity FEM.* Journal of Materials Processing Technology, 2008. **201**(1–3): p. 79-84.
234. Wert, J.A., Q. Liu, and N. Hansen, *Dislocation boundary formation in a cold-rolled cube-oriented Al single crystal.* Acta Materialia, 1997. **45**(6): p. 2565-2576.
235. Kalidindi, S.R., *Incorporation of deformation twinning in crystal plasticity models.* Journal of the Mechanics and Physics of Solids, 1998. **46**(2): p. 267-290.
236. Staroselsky, A. and L. Anand, *Inelastic deformation of polycrystalline face centered cubic materials by slip and twinning.* Journal of the Mechanics and Physics of Solids, 1998. **46**(4): p. 671-696.
237. Hill, R., *Generalized constitutive relations for incremental deformation of metal crystals by multislip.* Journal of the Mechanics and Physics of Solids, 1966. **14**(2): p. 95-102.
238. Asaro, R.J., *Crystal plasticity.* Journal of Applied Mechanics-Transactions of the Asme, 1983. **50**(4B): p. 921-934.
239. Asaro, R.J. and J.R. Rice, *Strain localization in ductile single crystals.* Journal of the Mechanics and Physics of Solids, 1977. **25**(5): p. 309-338.

240. Huynh, N.N., *A modelling of Microstructure Evolution and Crack Opening in FCC Materials under Tension.* PhD Dissertation, University of Wollongong, Australia, 2009.
241. Peirce, D., R.J. Asaro, and A. Needleman, *An analysis of nonuniform and localized deformation in ductile single crystals.* Acta Metallurgica, 1982. **30**(6): p. 1087-1119.
242. Asaro, R.J., *Micromechanics of crystals and polycrystals.* Advances in Applied Mechanics, 1983. **23**: p. 1-115.
243. Asaro, R.J. and A. Needleman, *Texture development and strain hardening in rate dependent polycrystals.* Acta Metallurgica, 1985. **33**(6): p. 923-953.
244. Toth, L.S., P. Gilormini, and J.J. Jonas, *Effect of rate sensitivity on the stability of torsion textures.* Acta Metallurgica, 1988. **36**(12): p. 3077-3091.
245. Huynh, N.N., et al., *A modelling of tensile deformation around the notch tip in single crystal aluminium.* Computational Materials Science, 2010. **48**(1): p. 179-186.
246. Hutchinson, J.W., *Bounds and self-consistent estimates for creep of polycrystalline materials.* Proceedings of the Royal Society of London Series a-Mathematical and Physical Sciences, 1976. **348**(1652): p. 101-127.
247. Wu, T.Y., J.L. Bassani, and C. Laird, *Latent hardening in single crystals: Theory and experiments.* Proceedings of the Royal Society of London Series a-Mathematical Physical and Engineering Sciences, 1991. **435**(1893): p. 1-19.
248. Basinski, S.J. and Z.S. Basinski, *Dislocations in solids.* North-Holland, 1979: p. 263.
249. *Abaqus User Subroutines Reference Manual.* Abaqus 6.9 Documentation.
250. Huang, Y.G., *A user-material subroutine incorporating single crystal plasticity in the Abaqus finite element program.* Division of Applied Sciences, Harvard University, Cambridge, Massachusetts, 1991.
251. Franciosi, P., M. Berveiller, and A. Zaoui, *Latent hardening in copper and aluminium single crystals.* Acta Metallurgica, 1980. **28**(3): p. 273-283.
252. Bassani, J.L. and T.Y. Wu, *Latent hardening in single crystals. 2. Analytical characterization and predictions.* Proceedings of the Royal Society of London Series a-Mathematical Physical and Engineering Sciences, 1991. **435**(1893): p. 21-41.
253. Beyerlein, I.J. and L.S. Toth, *Texture evolution in equal-channel angular extrusion.* Progress in Materials Science, 2009. **54**(4): p. 427-510.
254. Figueiredo, R.B., M.T.P. Aguilar, and P.R. Cetlin, *Finite element modelling of plastic instability during ECAP processing of flow-softening materials.* Materials Science and Engineering: A, 2006. **430**(1–2): p. 179-184.
255. Liu, Q., et al., *Heterogeneous microstructures and microtextures in cube-oriented Al crystals after channel die compression.* Metallurgical and Materials Transactions a-Physical Metallurgy and Materials Science, 1998. **29**(9): p. 2333-2344.
256. Smolyakov, A.A., et al., *Three-dimensional numerical simulations of multi-pass equal-channel angular pressing by a variation difference method and comparison with experiment.* Materials Science and Engineering: A, 2008. **493**(1–2): p. 148-159.
257. Xu, S., et al., *Finite element analysis and optimization of equal channel angular pressing for producing ultra-fine grained materials.* Journal of Materials Processing Technology, 2007. **184**(1–3): p. 209-216.

258. Horita, Z., T. Fujinami, and T.G. Langdon, *The potential for scaling ECAP: effect of sample size on grain refinement and mechanical properties.* Materials Science and Engineering: A, 2001. **318**(1–2): p. 34-41.
259. Srinivasan, R. and P. Chaudhury, *Forging studies with severe plastic deformation processed aluminum alloy 6061*, in *Thermec'2003, Pts 1-5*, T. Chandra, J.M. Torralba, and T. Sakai, Editors. 2003. p. 267-272.
260. Chaudhury, P.K., B. Cherukuri, and R. Srinivasan, *Scaling up of equal-channel angular pressing and its effect on mechanical properties, microstructure, and hot workability of AA 6061.* Materials Science and Engineering: A, 2005. **410–411**(0): p. 316-318.
261. Srinivasan, R., B. Cherukuri, and P.K. Chaudhury, *Scaling up of equal channel angular pressing (ECAP) for the production of forging stock*, in *Nanomaterials by Severe Plastic Deformation*, Z. Horita, Editor. 2006. p. 371-378.
262. Suo, T., Y.L. Li, and F. Zhao, *Influence of billet size on the deformation inhomogeneity of material processed by equal channel angular pressing.* International Journal of Modern Physics B, 2008. **22**(31-32): p. 6088-6093.
263. Ferrasse, S., et al., *Scale up and application of equal-channel angular extrusion for the electronics and aerospace industries.* Materials Science and Engineering: A, 2008. **493**(1–2): p. 130-140.
264. Lu, C., et al., *Crystal plasticity modeling of texture evolution and heterogeneity in equal channel angular pressing of aluminum single crystal.* Acta Materialia, 2011. **59**(9): p. 3581-3592.
265. Kim, H.S., *Finite element analysis of equal channel angular pressing using a round corner die.* Materials Science and Engineering: A, 2001. **315**(1–2): p. 122-128.
266. Yoon, S.C. and H.S. Kim, *Finite element analysis of the effect of the inner corner angle in equal channel angular pressing.* Materials Science and Engineering: A, 2008. **490**(1–2): p. 438-444.
267. Duan, Z.C. and T.G. Langdon, *An experimental evaluation of a special ECAP die containing two equal arcs of curvature.* Materials Science and Engineering a-Structural Materials Properties Microstructure and Processing, 2011. **528**(12): p. 4173-4179.
268. Fukuda, Y., et al., *The application of equal-channel angular pressing to an aluminum single crystal.* Acta Materialia, 2004. **52**(6): p. 1387-1395.
269. Han, W.Z., et al., *Influences of crystallographic orientations on deformation mechanism and grain refinement of Al single crystals su ected to one-pass equal-channel angular pressing.* Acta Materialia, 2007. **55**(17): p. 5889-5900.
270. Deng, G.Y., et al., *Crystal plasticity investigation of friction effect on texture evolution of Al single crystal during ECAP.* Journal of Materials Science, 2010. **45**(17): p. 4711-4717.
271. Deng, G.Y., et al., *Crystal Plasticity Investigation of Texture Evolution of Al Single Crystal During Extrusion Through a Bent Channel.* Journal of Computational and Theoretical Nanoscience, 2012. **9**(9): p. 1481-1484.
272. Miyamoto, H., et al., *Dislocation structures and crystal orientations of copper single crystals deformed by equal-channel angular pressing.* Materials Science and Engineering: A, 2005. **405**(1–2): p. 221-232.

273. Miyamoto, H., et al., *The effect of the initial orientation on microstructure development of copper single crystals subjected to equal-channel angular pressing*, in *Nanomaterials by Severe Plastic Deformation*, Z. Horita, Editor. 2006. p. 799-804.
274. Han, W.Z., et al., *Combined effects of crystallographic orientation, stacking fault energy and grain size on deformation twinning in fcc crystals.* Philosophical Magazine, 2008. **88**(24): p. 3011-3029.
275. Miyamoto, H., et al., *Formation of Deformation Twins and Related Shear Bands in a Copper Single Crystal Deformed by Equal-Channel Angular Pressing for One Pass at Room Temperature.* Materials Transactions, 2009. **50**(8): p. 1924-1929.
276. Vinogradov, A., M. Maruyama, and S. Hashimoto, *On the role of dislocation hardening in the monotonic and cyclic strength of severely plastically deformed metals.* Scripta Materialia, 2009. **61**(8): p. 817-820.
277. Deng, G.Y., et al., *Modeling texture evolution during ECAP of copper single crystal by crystal plasticity FEM.* Materials Science and Engineering a-Structural Materials Properties Microstructure and Processing, 2012. **534**: p. 68-74.
278. Vinogradov, A., et al., *Effect of dislocation hardening on monotonic and cyclic strength of severely deformed copper.* Philosophical Magazine, 2012. **92**(6): p. 666-689.
279. Kim, H.S., M.H. Seo, and S.I. Hong, *On the die corner gap formation in equal channel angular pressing.* Materials Science and Engineering: A, 2000. **291**(1–2): p. 86-90.
280. Aour, B., et al., *Experimental and numerical study of ECAE deformation of polyolefins.* Computational Materials Science, 2009. **45**(3): p. 646-652.
281. Aour, B., et al., *Numerical investigation on equal channel angular extrusion process of polymers.* Computational Materials Science, 2006. **37**(4): p. 491-506.
282. Son, I.H., et al., *Sensitivity of friction condition in finite element investigations of equal channel angular extrusion.* Materials Science and Engineering: A, 2007. **445–446**(0): p. 676-685.
283. Kim, H.S., *On the effect of acute angles on deformation homogeneity in equal channel angular pressing.* Materials Science and Engineering: A, 2006. **430**(1–2): p. 346-349.
284. Nagasekhar, A.V., *Reply to the comments of article—On the effect of acute angles on deformation homogeneity in equal channel angular pressing.* Materials Science and Engineering: A, 2008. **472**(1–2): p. 358-359.
285. Nagasekhar, A.V., et al., *Effect of acute tool-angles on equal channel angular extrusion/pressing.* Materials Science and Engineering: A, 2005. **410–411**(0): p. 269-272.
286. *Abaqus Analysis User's Manual.* Abaqus 6.9 Documentation.
287. Furukawa, M., Z. Horita, and T.G. Langdon, *Factors influencing the shearing patterns in equal-channel angular pressing.* Materials Science and Engineering: A, 2002. **332**(1–2): p. 97-109.
288. Tham, Y.W., et al., *Study of deformation homogeneity in the multi-pass equal channel angular extrusion process.* Journal of Materials Processing Technology, 2007. **192–193**(0): p. 121-127.